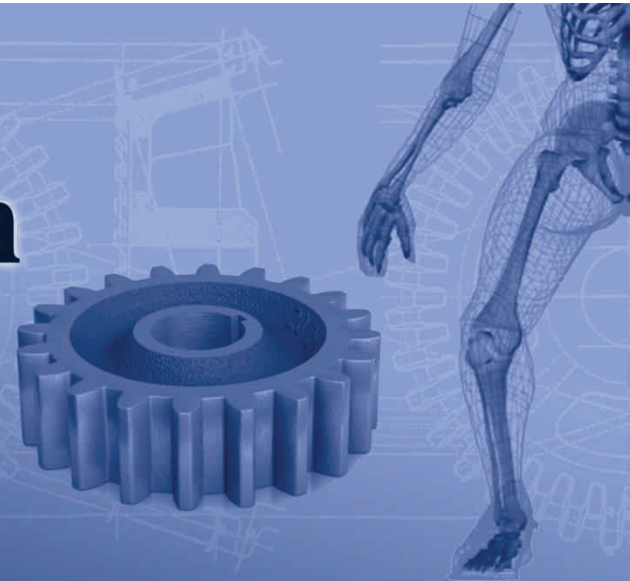UNIVERSITEIT
GENT

Sustainable Construction & Design

Volume 2, 2011

Metal Structures Centre   –   2011

Sustainable Construction & Design

Volume 2, 2011
Issue 3

Sustainable Construction & Design, volume 2, issue 3, 2011

Research activities at
Laboratory Soete

UNIVERSITEIT GENT

UGent
LS
LABORATORY SOETE

Fracture mechanics

Experts in pipeline weld research.
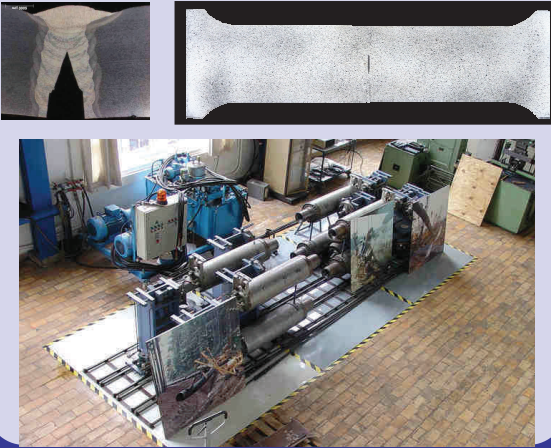
Tribology

Small to large scale experimental testing.
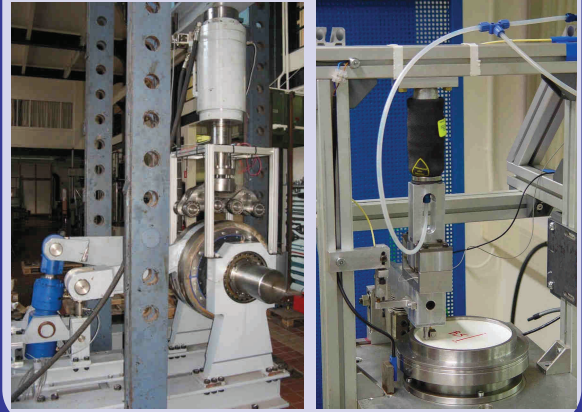
Labo Soete

LABO SOETE – GHENT UNIVERSITY
Dept. of Mechanical Construction & Production
Technologiepark 903
9052 Zwijnaarde – BELGIUM

http://www.tribology-fatigue.ugent.be
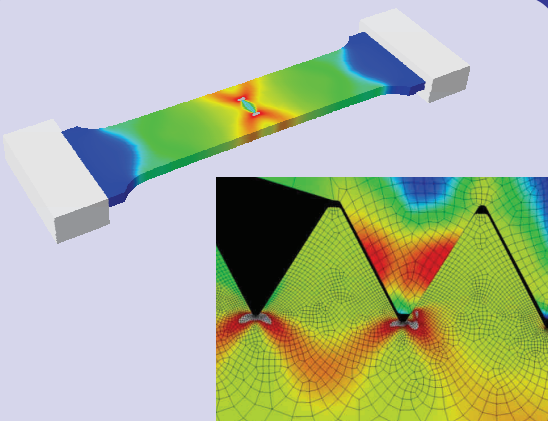
Modelling of engineering structures and applications.

Finite Element Analysis
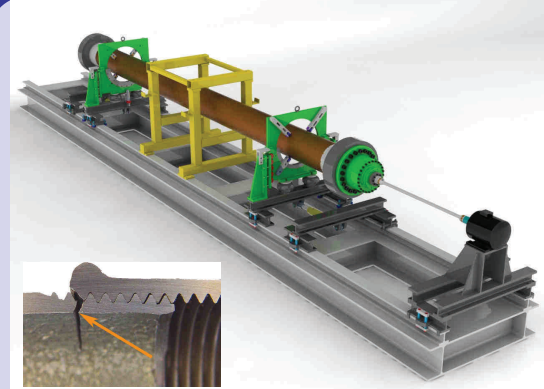
Fatigue testing and analysis. E.g. research on pipe joints in a full scale resonant bending fatigue setup.

Fatigue

Contents

Editorial

The final issue of the 2011 volume of the SCAD journal comprises selected student papers from the 2011 edition of the SCAD conference. Fields covered in this issue include fracture mechanics, fatigue, tribology, joining techniques, design of mechanical engineering systems and kinematics. The studies are carried out by either experimental or numerical studies.

On February 13, 2012 the SCAD Symposium will take place. The symposium is focussing at the research carried out by both master and PhD students at the Laboratory Soete and their partner institutions. More information about the 2012 SCAD symposium can be found on http://www.scad.ugent.be/.

Jeroen Van Wittenberghe

SCAD journal editor

KINEMATICS OF THE KNEE JOINT

W. Sampers[1], T. Sierens[1]

[1] Ghent University, Belgium

Abstract In 2006 a test rig was built by Ghent University to measure patellofemoral pressures. The main goal of the current study is to improve and upgrade the Ghent Knee Rig (GKR). The improvement consists of a better approach of the Q angle. The mechanical connection between the linear actuator and the rectus femoris tendon represents the force of the quadriceps. To validate the results of measurement, it is necessary the connection approaches the direction of the real muscle. The patella is bond with the body by use of ligaments and retinacula, which have a unknown influence on the stability of the patella. Also quadriceps and the trochlea are important stabilizers. The upgrade of the GKR is a tool to measure the patella stability, which is done by pulling the patella out of the trochlea and measure the force needed for a certain displacement. It is important the patella has five degrees of freedom (DOF) so no extra force but the stability is measured and the effect of dysplasia and trochleoplasty can be examined. In the near future the GKR will be expanded to the possibility of measuring patella tracking. The relative movements of the different components of the knee will be followed by high speed cameras.

Keywords: Ghent Knee Rig, patellofemoral pressure, patella stability, patella tracking

1   INTRODUCTION

This paper contains the different steps taken and methods used to improve and upgrade a knee kinematics simulator. The rig, designed by Ghent University and based on the Oxford model, was built in 2006. It is possible to simulate a squat movement. Due to the complexity of the knee joint and variation of medical expressions, a small description of the anatomy will be given. It is not the intension of the authors to give a complete anatomical explanation of the functioning of the knee joint. Further the GKR will be discussed because to understand the functioning of the rig and the improvements. How these improvements of the rig will be realized, is considered afterwards. It is necessary to approach the reality to verify the results with those in literature.

A frequent problem is dysplasia of the trochlea which results in lack of stability of the patella. Trochleoplasty is a medical intervention to solve this problem, but is yet not imminent. Different steps are taken to change the rig, to facilitate further research which might improve the treatment of trochleodysplasia. Patella stabilization and tracking are therefore introduced in the GKR. These are discussed in 2.5 and 2.6.

2   BODY

2.1   Anatomy

The anatomy will be explained by Fig. 1. The knee is a joint which connects the femur (2), better known as the thighbone, with the tibia (3), also called the shinbone, and fibula (4). To prevent contact between the femur and tibia, they are separated by the menisci. The patella is connected with the quadriceps on one side and with the patellar tendon on the other side (Fig. 2). By contraction of the quadriceps, the patella slides into the trochlea (Fig. 1 and Fig. 2) and the leg will bend. During this sliding the contact area between
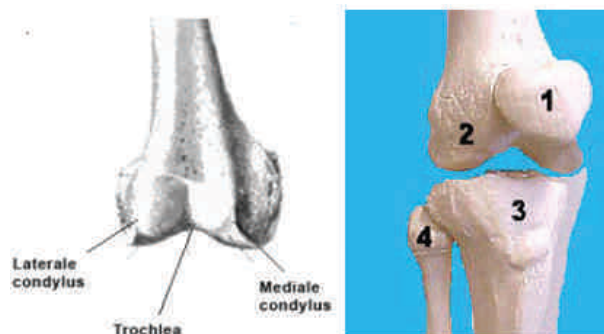
Fig. 1 Ventral view of the knee joint [1]

these two will change and the patella will disappear deeper into the groove. Some knees have problems with the stability of the patella. Stabilizers of the patella are the trochlea and all ligaments, retinacula and muscles connected with the patella [1]. Every source of stabilization has a specific point of application and an own share of the force to do that. If the trochlea is not deep enough to ensure the stability of the patella, the problem is called dysplasia. It is logic that more force is needed to pull the patella out of a deeper groove, so a bigger stability is acquired. A medical operation to enlarge the trochlea, called trochleoplasty, is not yet imminent. Due to lack of information about this problem, it is very hard to recover this problem. Another problem that should be taken into account is that a small contact area between the trochlea and the patella leads to high pressure contacts and to unsatisfied patients. Due to the fact a knee has 6 DOF [3], a lot of parameters will change during this flexion-extension movement. The patellofemoral pressure and contact area, the force in the quadriceps, the stability of the patella, the relative movement of all the components, bones as well as the muscles all changes as a function of the flexion angle. To measure all these unknown parameters, it was indispensable to construct a test rig and so simulate the squat.
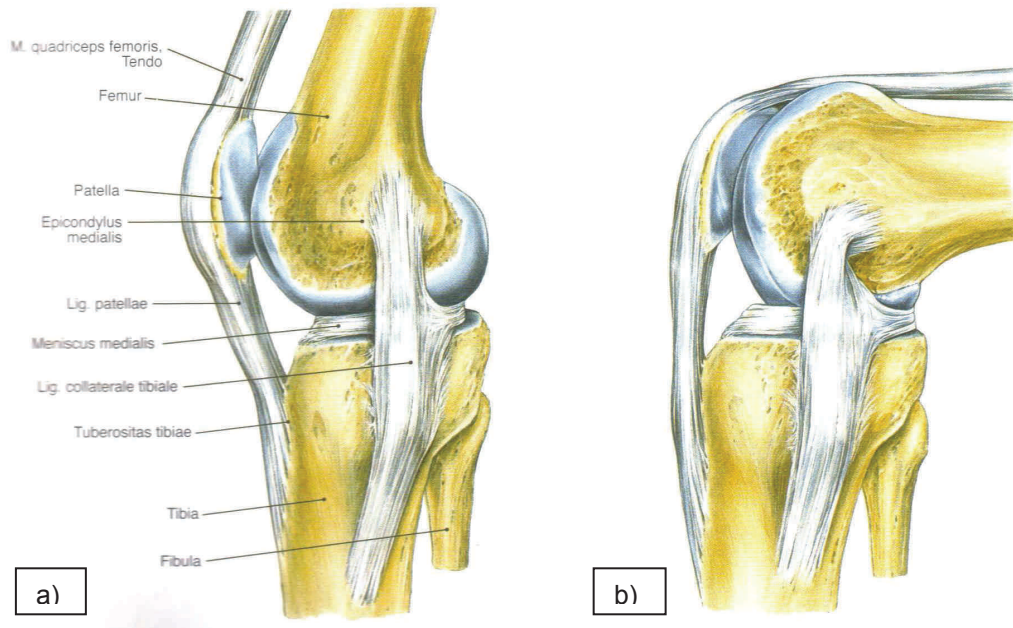
Fig. 2 medial view of the a) extension b) flexion position [2]

2.2 Existing test rig

Since the building of the GKR in 2006 (**Fig. 3**), it was possible to measure the patellofemoral pressures by the use of a sensor while the knee is making a flexion-extension motion. This is a simplified movement which people use daily e.g. walking, go up-and downstairs, cycling, etc.

The fresh frozen legs are defrost and disconcerted from the skin. To connect the specimen with the GKR, tibia and femur are cemented in two cylinders. These cylinders can easily be mounted in the rig with bolts (**Fig. 3**). The ankle and hip joint are substituted by two mechanical joints (D and H) which take care of the desired position of the knee. The hip has 3 DOF: one vertical translation and two rotations (flexion-extension movement and internal-external rotation). The ankle has 5 DOF: two translations in the horizontal plane and 3 rotation movements. It is mathematical proven that this testing station allows 6 freedoms [4]. The horizontal translations of the ankle however are never used, but if necessary for tests, they are available. The quadriceps femoris tendon is connected to a linear actuator (C) by way of a clamp system (E) and a steel cable (F). This cable, which is the replacement of the quadriceps, is guided through a pulley (G). When the actuator comes into operation, the steel cable pulls the tendon and the flexion-extension movement of the knee will start. The actuator and hip joint are mounted in such a way they move up and down with the knee, which is loaded through this by approximate 30kg. So they are subjected to inertia forces, which implies extra vibrations and less accurate measurements. However, this has to be nuanced, the speed of the actuator is only 2,75mm/s what will result in negligible inertia forces. A loadcell, connected to the end of the motor, measures the force to stretch the leg. The mechanical hip joint, the actuator and the horizontal profile (B) will move up and down and take care of the weight, carried by the leg. The patellofemoral pressures are measure by the use of a sensor (I), which is mounted between the femur and patella in a gap of approximate 5cm on the lateral side of the knee.
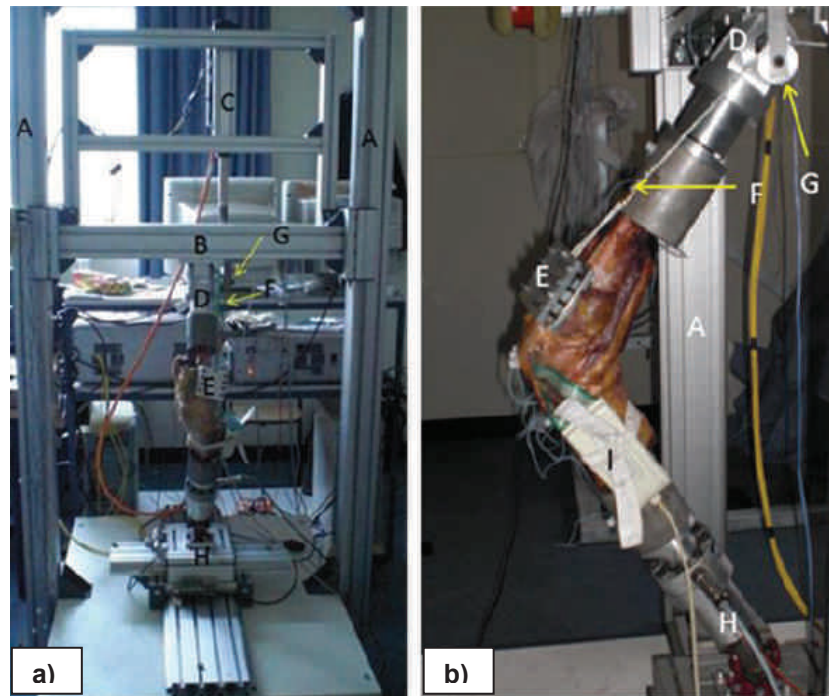
Fig. 3 a) front-view b) side-view of the specimen in the GKR [5]

2.3   Problems and solutions

The main problem of the original rig is the direction of the force, acting on the patella. As already mentioned, the quadriceps is replaced by a steel cable. To have accurate results of the test, it is necessary to approach the direction of the real muscle. The pulley (G), which is leading the cable, is placed next to the hip joint (D) (**Fig. 3**). This is not in agreement with reality due a wrong the Q angle (a measure for the angle between quadriceps, which is more lateral situated, and the patella ligament [1]). The use of a steel cable and related tailpieces is not user-friendly and inaccurate due to strain.

To make the Q angle more realistic, some alterations on the test rig are necessary. The actuator (green) is moved to the other side of the frame (**Fig. 4**) so motor and specimen (orange) are oriented to the same side of the rig. Due to the incapacity of the motor to take forces other than linear, the pulley (blue) is moved in such a way the acting force of the cable is lying perfect in line with the actuator. Because the vector of the quadriceps force is oriented towards the hip, the best position of the pulley is as close as possible to the mechanical rotation point. Due to the fact all specimen are different and left as well as right knees are tested, it is necessary the pulley is adjustable stationed. This is solved by milling grooves in the pulley system for mounting it with 4 prestressed bolts in the horizontal profile, so the wanted height can be established. Before testing, an optimal position of the pulley is chosen, during the test remains the position unchanged.

The cable problem is solved by replacing the wire by a chain which has a higher stiffness and can easily be connected to the motor on one side and the clamp system on the other side. A chain however is difficult and time-consuming to vary in length. To meet this deficiency, the actuator is no longer mounted fixed with regard to the horizontal profile to which it was initial fastened (**Fig. 4**). The motor is placed on a rail system which is connected with the hip joint and thus is moving up and down. The same principles count as for the pulley are valid. The linear actuator is mounted to a rail plate with 4 prestressed bolts. The relative position of the motor with regard to the rail plate is chosen so that the chain is not hanging loose, in other words, the motor is placed in the highest position the chain allows.

.
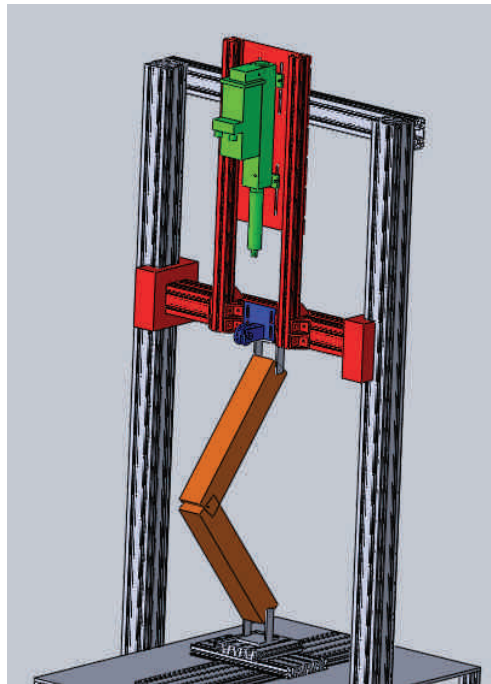
Fig. 4 Drawing changes in GKR

2.4   Protocol of the patellofemoral pressure

To ensure the accuracy of the test results, it is necessary to write an unambiguous protocol so results of different specimen can be compared with each other and with literature. Specimen are numbered and all available information (age, time post mortum, temperature, transport method, etc.) is carefully hold out. An incision is made on the lateral side of the knee, to place a pressure sensor between patella and femur. The Tekscan sensor is able to measure pressures up to 13 MPa and is designed to measure contact surfaces and pressure distributions in joints [6]. It is the industry standard for applications where real-time dynamic joint simulations are required. The system exists of a sensor, an interface and an extensive software packet for the processing of the data. The sensor is 0,1mm thick and is built up by pressure sensitive pixels which are brought into matrix formation[1]. Due to the small thickness, a small layer of Teflon is added to strengthen the film so it can easily be placed. The Teflon also helps to prevent the rise of creases.

 The positioning of the specimen in the GKR happens as described in 2.2.

2.5   Patella stabilisation

As discussed in 2.1 the stability of the patella is dependent of the trochlea, all ligaments, retinacula and muscles connected with the patella. To examine the influence of these stabilizers a new tool has to be built on the GKR. This is done by pulling the patella in the lateral and medial direction. During this procedure, the force needed to displace the patella 1cm is measured. The experiment is repeated for different flexion angles to compare. The system introduced in the GKR is based on methods used in the rig from the Departments of Mechanical Engineering and of Musculoskeletal Surgery from the Imperial College in London [7].

According to experiments in literature, the specimen is placed in horizontal plane, with the lateral side oriented upwards (**Fig. 5**). The knee is positioned in the desired flexion angle and femur is completely fixed to the test rig and has no degrees of freedom left. But for the flexion-extension movement, the tibia has all degrees of freedom. The quadriceps are connected with weights which have a total weight of 30N or 175N [8]. The force acting on the quadriceps is divided in different parts, to approach reality (**Fig. 5**). Every muscle is surrounded by linen which in turn are connected to the weights. The different parts of the quadriceps, with each its own direction and weight is summarized in **Table 1**. The patella is connected with a mounting device which has 3 DOF: anterior-posterior, proximal-distal and flexion-extension rotation. The crosshead itself is connected with Instron 1122 Materials. This is comparable with a tensile testing machine with a capacity of 5kN [9]. The tensile testing machine is provided with a load cell. The connection between patella and mounting device is a ball-and-socket joint which has a diameter of 10mm and is cemented into

---

[1] The pixel is an electrical resistance, its value being dependent on pressure.
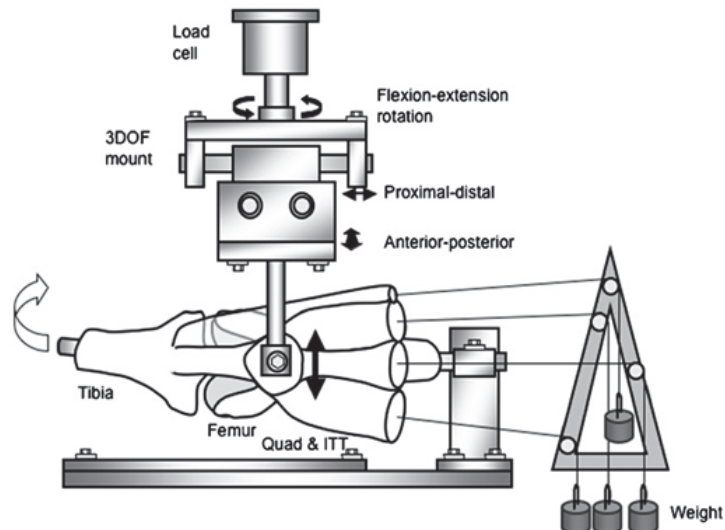
Fig. 5 Test rig patella stabilisation [10]

the patella, 10 mm deep with regard to the anterior surface (Fig.). The ball-and-socket joint are necessary to allow the natural rotations of the patella. The connection between the tensile testing machine and the patella has 5 DOF; only the medial-lateral movement is prohibited. While this movement is enforced by the tensile testing machine by a chosen flexion angle, the required force is each millimeter measured. The speed of the displacement is 100mm/min [7].

However the patella stability tool in the GKR is based on the one discussed above, the design is certainly not the same. Because there is no space enough to place it and due to the little movement and forces needed, the tensile testing machine will be replaced by a linear actuator. The 5 DOF from the ankle will, due to the current rig, be reduced to two (ab –and adduction; internal-external rotation). The 5 DOF of the connection between the patella and the mounting device will be kept. More information cannot be given because this project is only in the initial stage.

		Lateral	Medial	Anterior	Posterior	Load	Load 1	Load 2
quadriceps 30N/175N	VL longus	14°		0°		33 %	9,9 N	57,75 N
	VL obliquus	35°			33°	9 %	2,7 N	15,75 N
	VM longus		15°	0°		14 %	4,2 N	24,5 N
	VM obliquus		47°		44°	9 %	2,7 N	15,75 N
	RF+VI	0°		0°		35 %	10,5 N	61,25 N
Tractus 5N/30N	ITB	0°			6°		5 N	1 N

Table 1 Directions and forces on quadriceps [2] [10]

---

[2] VL = Vastus Lateralis, VM = Vastus Medialis, RF = Rectus Femoris, VI = Vastus Intermedius, ITB = iliotibial band
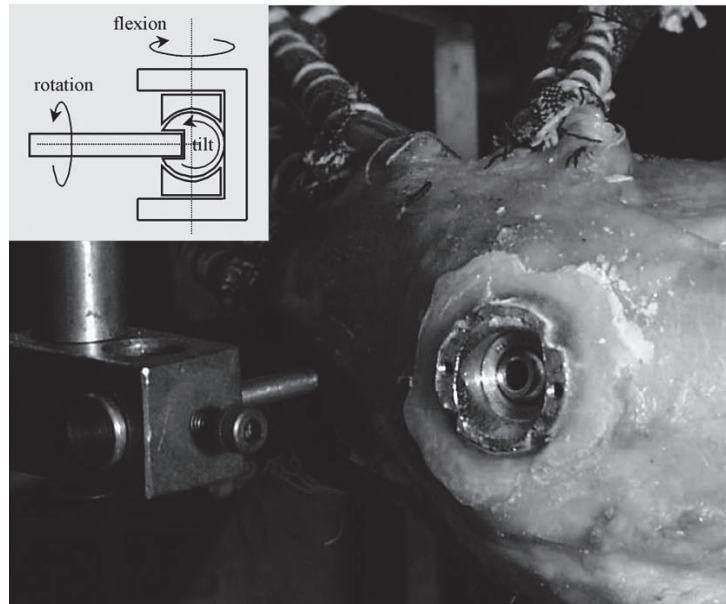
Fig. 6 Ball-and-socket joint in patella [11]

2.6 Patella tracking

For completion patella tracking is mentioned however less information can be given. This is a measurement of the relative movement of all components of the knee. While the specimen is making a walking motion (or a squat), the kinematics of all parts can be registered by the use of a camera system in function of the flexion angle.

3 CONCLUSIONS

The main goal of this study is to improve and to update the GKR. The results should be more accurate due to the better approach of reality by improve of the Q angle and the possibility to place the pulley closer to the hip joint. Because the use of a steel cable is replaced by a chain, the test rig should be more user-friendly. However we cannot confirm these assumptions because the completion of the construction is not ready. Plans to operate and measure the patellofemoral pressure should be possible from March 2011.

The concept and rough sketches for the patella stability tool is in the making. We expect at the latest to test early April 2011. Completing the patella tracking is the next step in this research.

4 NOMENCLATURE

P	Pressure	Pa
t	Time	s
m	Mass	kg
v	Velocity	m/s
s	Distance	m
F	Force	N
DOF	Degrees of freedom	
GKR	Ghent Knee Rig	

5 ACKNOWLEDGEMENTS

First of all we want to thank P. De Baets for his help in general. As the promotor for the project, he helped us with the planning, progress and technical support. Secondly we want to mention W. Ost for the advice

he gave us and helping to order all parts. We must not forget A. Van Haver, who is copromotor for this project. She was helpful for the medical part of this study.

6   REFERENCES

[1]   Stevens and Dockers. Onderzoek naar de krachtwerking van het patellofemoraal gewricht en ontwerp en constructie van een experimenteel belastingsmodel, 2006.

[2]   F.H. Netter, Atlas of human anatomy, RR Donnelley, 2007

[3]   J.A. Fisk, evaluating the accuracy of knee kinematics measured in six degree freedom using surface markers, 2004

[4]   A.B. Zavatsky. The importance of quadriceps and hamstring muscle loading on knee kinematics and in-situ forces in the ACL. Journal of Biomechanics, 32:395 – 400, 1999.

[5]   A. Van Haver, J. Quintelier, P. Verdonck, F. Almqvist, M. De Beule and P. De Baets, Patellofemoral contact during squat simulation on cadaveric knees, Day of research 2010, 2010

[6]   K-scan website: http://www.tekscan.com/medical/system_kscan.htms, 2006

[7]   W. senavongse, F. Farahmand, J. Jones, H. Andersen, A.M.J. Bull, A.A. Amis, Quantitative measurement of patellofemoral joint stability: force-displacement behavior of the human patella in vitro, Journal of orthopaedic Research 21, 780-786, 2003

[8]   W. senavongse, C. Oguz, A.M.J. Bull, A.A. Amis, D. Dejour, The effect of trochleoplasty on patellar stability and kinematics, the journal of bone and joint surgery, 2008

[9]   Instron website: http://www.instron.com/wa/product/used-equipment.aspx, 2010

[10]   A.M. Merican, E. Kondo, A.A. Amis, The effect on patellofemoral joint stability of selective cutting of lateral retinacular and capsular structures, Journal of biomechanics, 291-296, 2009

[11]   J. Christoforakis, A.M.J. Bull, R.K. Strachan, R. Shymkiw, W. Senavongse, A.A. Amis, Effects of lateral retinacular release on the lateral stability of the patella, 2006

DENTAL IMPLANTS, WHAT SHOULD BE KNOWN BEFORE STARTING AN *IN VITRO* STUDY

K. Verplancke[1], W. De Waele[2] and H. De Bruyn[3]

[1] Ghent University, Belgium
[2] Ghent University, Laboratory Soete, Belgium
[3] Ghent University, Periodontology & Oral Implantology, Belgium

Abstract Dental implant–abutment systems are used as anchors to support single or multi-unit prostheses for partially or fully edentulous patients. *In vitro* experiments and finite element analyses can be used to investigate their mechanical performance. Accurate information is needed on the geometry, material properties and friction coefficients of different implant-abutment components, on real loading conditions, and elastic properties of human jawbone. Information can be retrieved from previously reported studies or experiments. This paper provides a summary of a small but representative part hereof. Research has shown that the elastic properties of human jawbone are direction dependent and that the Young's modulus (E) also depends on the bone type. Other studies investigated the maximum bite forces and reported a broad range of results, from 200 to 2000 N. Static experiments are typically performed with axial or bending loads to evaluate the performance of dental implant systems. Dynamic tests simulate chewing cycles and are used to evaluate the fatigue endurance. The supporting structure of the implant system should be representative for the bone structure. Finite element models are ideally suited to evaluate the biomechanical behaviour of implant systems. Accurate representation of the supporting bone and its interaction with the implant is crucial.

Keywords dental implants, *in vitro* experiments, human bite force, elastic properties

1   INTRODUCTION

Dental implant–abutment systems are used as anchors to support single or multi-unit prostheses for partially or fully edentulous patients. If a fixed partial denture (FPD) on implants is to be constructed in the premolar and/or molar region, where the implants stand approximately on a straight line, it is advisable to select an implant system with high strength values. Implant systems with lower values would suffice if a full arch fixed prosthesis (for fully edentulous patients) is planned. In the latter situation, the implants are approximately placed in a horseshoe formation, which favours strength and stability. A dental implant system consists of an implant that is surgically implanted in maxilla (upper jawbone) or mandible (lower jawbone), and an abutment that mates with the implant. In the 2-stage protocol the placement of the abutment happens once the implant successfully osseo-integrates to the bone. This is after a 3 to 4 months submerged healing period. In the immediate loading protocol, the placement of the abutment happens at the same time as the surgical placement of the implant. Research has shown that micro motion less than 150 to 200 µm does not cause failure in osseo-integration [1-2]. However, most studies have reported that to achieve successful outcomes, the maximum safe motion would be 100 to 150 µm [3]. Depending on the specific system used, an abutment can include a machined connection mechanism within itself (tapered implant) or can be clamped onto the implant by means of an abutment screw. The dental prosthesis is then fabricated over the abutment. The restoration for a fully edentulous mandible consists mainly of a U-shaped prosthesis, supported by anteriorly (front) placed fixtures and with posterior (back) extensions (cantilever) (Figure 1) [3-7].
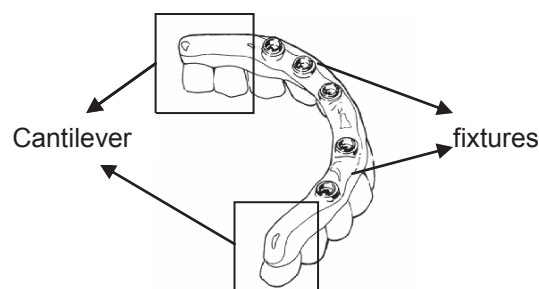

Figure 1: A typical complete-arch prosthesis [7].

Successful implant therapy requires a dynamic equilibrium between biological and mechanical factors. The biological factors are generally considered multi-factorial, whereas mechanical failure has been associated with screw joint instability between the abutment and the implant [4, 6, 8-10]. In tightening the abutment screw, a compressive force is generated that maintains contact between the bearing surfaces of implant and abutment. The success of this screw joint is directly related to the stretch of the abutment screw or the preload achieved from the tightening torque and maintenance of this preload over time. If the screw loosens and the preload falls below a critical level, joint stability may be compromised and may potentiate clinical failure. This includes soft tissue complications, abutment screw fracture, framework fracture, and abutment screw loosening. In most follow-up studies this screw loosening is reported as the most common complication. Overall, most investigators claim the better the maintenance of preload, the better the long-term stability of the joint. Factors that may result in screw joint instability or micro motion include inadequate preload, inadequate (screw) design, poor component fit, settling of surface micro roughness, excessive loading, and elasticity of bone. When tapered interference fits are used, abutment loosening seems to be less of a problem. The biting force acts in the direction of the abutment insertion, hence aids to secure the connection.

Any external tension load that is less than the preload will be taken up as a small increase in the screw tension and a larger decrease of the compression force on the cylinders. To obtain this favourable function in the screw joint, the preload must be maintained so that the screw joint will not open up. As soon as opening occurs, all of the external tension load has to be taken entirely by the screw. The opening of the screw joint, or its loosening, is the primary cause of screw breakage. If fracture occurs, it should preferably be the screw, since this component is the easiest to replace. The process of screw loosening has been described as occurring in 2 phases, both involving loss of preload. The first phase occurs as the preload is eroded because of slippage between threads as a result of functional forces. The second phase of loosening occurs when the preload has been eroded to the extent that any external load or vibration causes the threads to turn or "back off" [9]. To accomplish the desired function of the screw joint, the following conditions should be met: (*1*) optimal preload should be achieved and (*2*) there should be a precise fit between the implant and the abutment [7].

2   ELASTIC PROPERTIES OF THE HUMAN YAWBONE

The experimental measurement of the mandibular mechanical characteristics, although not impossible, is limited due to the restriction in cost, patient availability and other factors. The elastic constants quantify the relationship between a load (stress) placed on a structure and the resulting deformation of that structure (strain), within its elastic range. Elastic constants and ultimate strength can be related in bone. For instance, in the mandible, cortical bone is most resistant to deformation in the direction in which it is also the strongest. However, if a wider variety of bone types are examined, there is an overall inverse relationship between stiffness and strength which is related to the degree of mineralization [11-12].

Values of bone strain along the human mandibular corpus of up to 800 µε in human mandibles loaded with artificial muscle forces up to 60 kilopounds (±270 kN) haven been published. Densities for each sample were determined using Archimedes' principle, the result was a bone density of 1.768 ± 0.115 g/cm³ (= 1768 ± 115 kg/m³) [11].

Because bone is an anisotropic material, its elastic properties vary with direction. The most significant differences in elastic moduli were found between the longitudinal direction and the other two directions tested in the mandible (Table 1 and Figure 2). Significant differences in shear moduli were found for different orientations (Table 1). Mandibular bone samples were not taken from the edentulous individuals, as data from several specimens suggest that edentulation renders mandibular bone slightly less dense and less stiff [11].
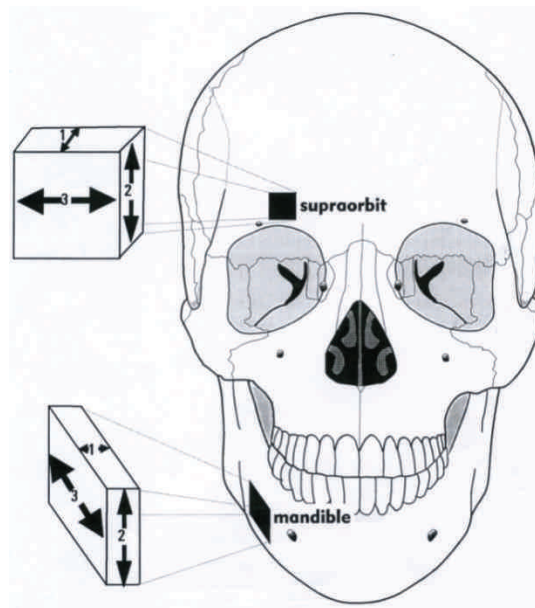
Figure 2: Orientations in bone samples taken from the mandible [11]

$E_1 =$	11.3 ± 2.4 GPa	$G_{12} =$	4.5 ± 1.0 GPa
$E_2 =$	13.8 ± 2.8 GPa	$G_{13} =$	5.2 ± 1.0 GPa
$E_3 =$	19.4 ± 4.0 GPa	$G_{23} =$	6.2 ± 0.7 GPa

Table 1: Elastic moduli and shear moduli measured on bone in the mandible [11]

The differences between edentulous and dentate mandibles were studied in [13]. The results show that throughout most of the edentulous mandibles, cortical bone was significantly thinner than in dentate mandibles. No significant differences in density between edentulous and dentate mandibles were found. This suggests that cortical bone density following edentulation is maintained despite changes in structure, stiffness and anisotropy. The differences in elastic moduli and shear moduli between the edentulous and dentate mandibles are shown in Table 2. This suggests that three-dimensional structural changes can occur within cortical bone, while density changes little [13].

Edentulous:	Dentate:		Edentulous:	Dentate:
$E_1 = 12.5 ± 2.3$ GPa	$E_1 = 12.7 ± 1.8$ GPa		**$G_{12} = 4.5 ± 0.9$ GPa**	**$G_{12} = 5.0 ± 0.6$ GPa**
$E_2 = 17.9 ± 3.3$ GPa	$E_2 = 17.9 ± 2.5$ GPa		$G_{31} = 5.3 ± 1.0$ GPa	$G_{31} = 5.5 ± 0.7$ GPa
$E_3 = 26.6 ± 5.9$ GPa	**$E_3 = 22.8 ± 5.4$ GPa**		$G_{23} = 7.1 ± 1.1$ GPa	$G_{23} = 7.4 ± 0.8$ GPa

Table 2: A comparison of elastic moduli and shear moduli for edentulous and dentate mandibles [13]

According to the index of Lekholm and Zarb, the jawbone can be divided into four different classes of bone quality, where class 4 represents the poorest quality with a high proportion of trabecular bone (Figure 3). In the maxilla (upper jaw), the dominant bone type is trabecular bone. The thin layer of cortical bone can make it difficult to achieve primary stability, which is a prerequisite for successful osseo-integration. Several studies report lower implant success rates in the maxilla than in the mandible, which often has a higher proportion of cortical bone. Other authors are of the opinion that the high proportion of trabecular bone in the maxilla makes bone tissue more sensitive to optimal healing conditions [14].

231 **Classification of bone quality according to Lekholm and Zarb (1985)**

Class I Jaw consists almost exclusively of homo-geneous compact bone

Class II Thick compact bone surrounds highly trabe-cular core

Class III Thin cortical bone sur-rounds highly trabecular core

Class IV Thin cortical bone sur-rounds loose, spongy core
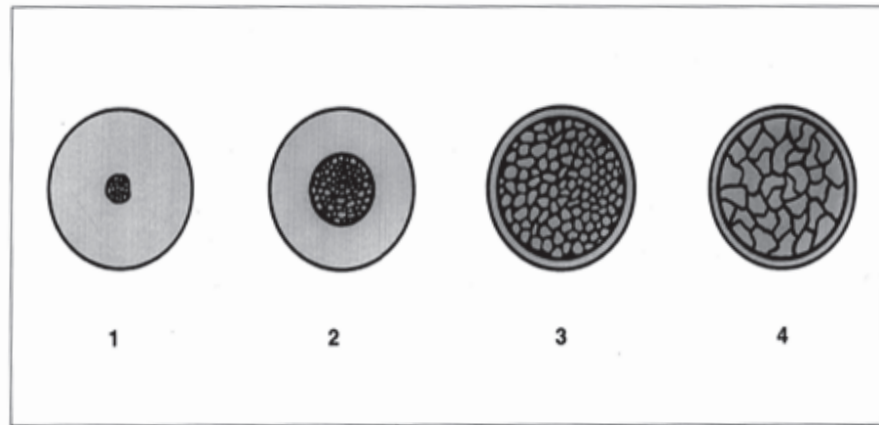
Figure 3: Classification of bone quality according to Lekholm and Zarb (1985) [15].

3   HUMAN BITE FORCE

Mastication mainly induces vertical forces in the dentition. However, transverse forces are also created by horizontal motion of the mandible and the inclination of tooth cusps (Figure 4). These forces are transferred through the prosthesis into the fixture, and finally into the bone. During this force flow, a given occlusal force creates completely different patterns of strain and stress because of the geometric configuration of the prosthesis in question [7].
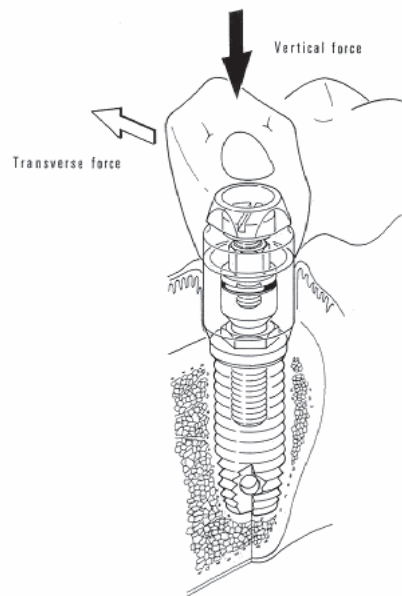
Figure 4: Vertical and transverse forces from occlusion acting on an implant prosthesis [7].

Two completely different types of loading are axial forces and bending moments. The axial force is more favourable, as it distributes stresses more homogeneously throughout the implant. The bending moment exerts stress gradients in the implant as well as in the bone. Axial forces can be of a compressive or a tensile nature. A compressive force presses the components of the system together and normally does not introduce any mechanical problems in the anchorage unit itself. On the other hand, tensile loading refers to a force that tends to separate components. Therefore, this force is of the greatest concern in regard to mechanical failure. The most essential aspect of this situation is the significance of the ratio of cantilever length relative to interfixture distance (a/b) (Figure 5). How this ratio approximately influences the tension load on an implant resulting from an occlusal force is shown in Figure 6 [7].
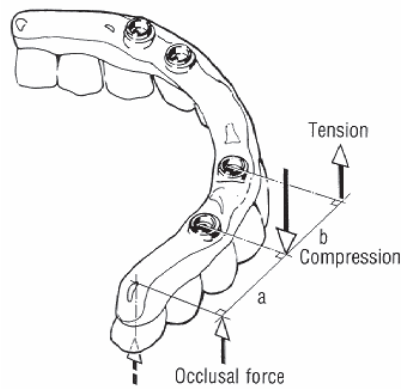
Figure 5: The implant loads induced by an occlusal force [7].
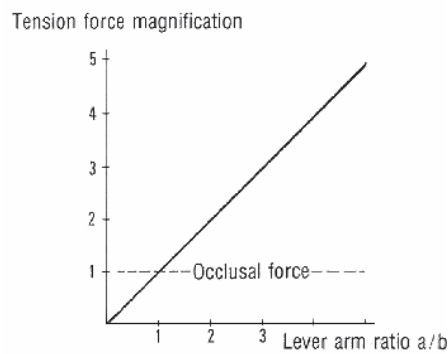
Figure 6: Tension force magnification as a function of the lever arm ratio (a/b) [7].

Forces are usually supported by first and second molars and second premolars in each arch (Figure 7) [16-17]. The greatest bite force recorded in a study was 435 N, but the teeth of the test person were abraded in evidence of his bruxing-clenching habit. This proves that the bite strength in some bruxer-clenchers can be as much as six times that of the non-bruxer. In Table 3 the bite force of other (normal) subject groups are listed [16].

Subject group	N	Range	Average	Reference and year
Natural teeth	20	55 to 280 lbs (25 to 127 kg)	162 lbs (74 kg)	Gibbs et al.,[6] 1981
Complete denture	5	22 to 47 lbs (10 to 21 kg)	35 lbs (16 kg)	Colaizzi et al.,[7] 1984
Maxillary complete denture-mandibular overdenture	6	14 to 159 lbs (6 to 72 kg)	51 lbs (23 kg)	Sposetti et al.,[8] 1985

Table 3: Bite force in other subject groups [16]
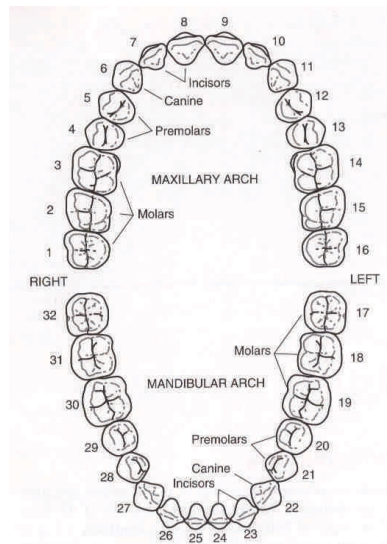
Figure 7: Numbering of the teeth (http://www.toothmingle.com/information/what-is-tooth-numbering/)

Generally, both bite force and occlusal contact area of male patients are greater than those of female patients (Table 4) [18]. Research has shown that the maximum human bite force can range from 200 N to 2440 N and that the lateral component is about 20 N [9].

	male	female	mean
Bite force of healthy subjects (N)	721.0 ± 505.5	530.7 ± 204.6	625.9 ± 387.9
Occlusal contact area of healthy subjects (mm²)	16.6 ± 13.0	11.5 ± 5.1	14.1 ± 10.0

Table 4: Bite force and occlusal contact area of healthy persons [18]

4   *IN VITRO* STUDIES

4.1   Static loading

Static failure conditions occur when bending or axial force causes stresses larger than the yield strength of the screw, resulting in a permanent deformation of the screw. In such situations, there is a loss of preload (tensile force) in the screw stem, thus the implant–abutment joint opens and/or the abutment screw loosens [10].

In a first experimental study, clinical conditions were simulated. The crowns were provided with a V-formed notch 6mm from the crown margin. A compressive force was applied to the notch, resulting in a bending load on the system (Figure 8). The whole sample, consisting of implant, abutment, gold crown and one (or in certain cases two) screw was embedded in auto-polymerizing acrylic resin in a well fitting brass pipe. Once aligned in a universal test machine, a compressive load was applied to the sample at a rate of 0.1mm/s until failure (screw loosening, screw fracture, screw deformation or abutment fracture) of the sample was evident [6].
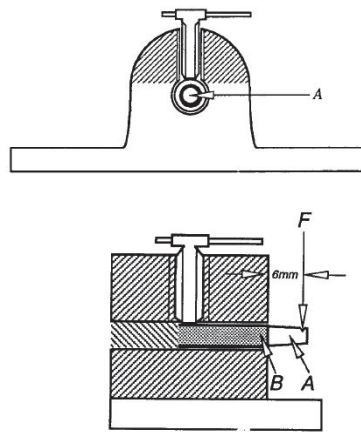
Figure 8: Experimental setup for static loading of dental implants [6]

The failure forces ranged from 138N to 693N. In this investigation, the load was a pure bending force, being perpendicular relative to the longitudinal axis of the sample, which is not clinically relevant. If a more axially oriented loading had been applied, then the samples would probably have tolerated a greater load before failure, and the failure forces would consequently have been larger [6].

In a second experimental study the tests were done using artificial bone (with representative mechanical properties) made of glass fibre reinforced composite and structural foam (Figure 9). The cross section dimensions of the artificial bone are for a typical mandible (Figure 9). An axial load was applied onto the implant head until failure was reached. For the classical geometry this was at approximately 50-55kg (±500 N), for the special geometry this was at approximately 70kg (±700 N) [19].
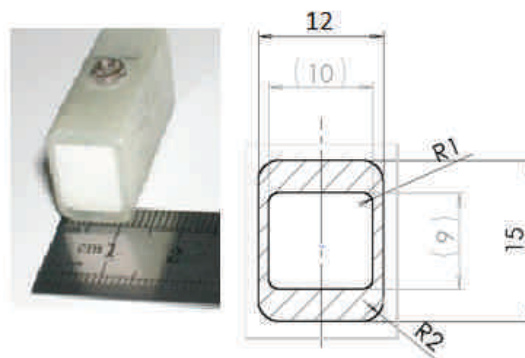
Figure 9: Artificial bone specimen and the dimensions [19].

4.2   Dynamic loading

Fatigue failure can occur when a force below the ultimate strength of the abutment screw is cyclically exerted on the system. Micro motion in the screw system can lead to cracks in the material at the implant surface as well as at the abutment and screw joint interfaces [10].

In a first experimental study, dynamic loading was applied to the 25-degree offset angulated platform of each abutment by a unidirectional vertical piston, cycling between 20 and 200N (Figure 10). A sinusoidal waveform was applied at a frequency of 8 cycles per second to simulate values found in human mastication. Cyclic loading continued for 5000000 cycles, or the approximate equivalent of 5 years of in vivo mastication [8]. The number of loading cycles were based on the assumption that an individual has 3 episodes of chewing per day, each 15 minutes in duration at a chewing rate of 60 cycles per minute (1Hz). This is equivalent to 2700 chewing cycles per day or roughly 10^6 cycles per year [9].
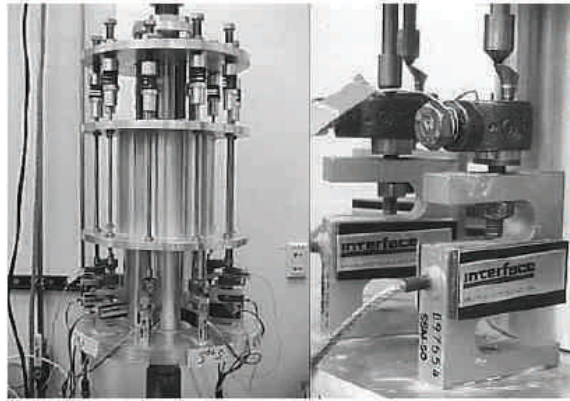
Figure 10: Carousel-type fatigue testing device [8]

In a second experimental study, the experimental device uses a linear solenoid to create a magnetic field that cycles the loading stylus at a user-defined rate (Figure 11). The solenoid chosen for this project allowed the device to cycle from 0 to more than 20 cycles per second while providing a load in the range of 0 to greater than 200 N for a duty of 500,000 cycles. The advantage of this device is its capacity to cycle at a faster rate than a conventional screw or hydraulic testing machine. The relative disadvantage of this device is the need to calibrate each specimen each time a loading period is performed. Loading was localized on the cantilever side of the implant joint opening, 4 mm from the center (Figure 11). The loading position of 4 mm off-axis was chosen to simulate a force applied to a cusp on a molar [10].
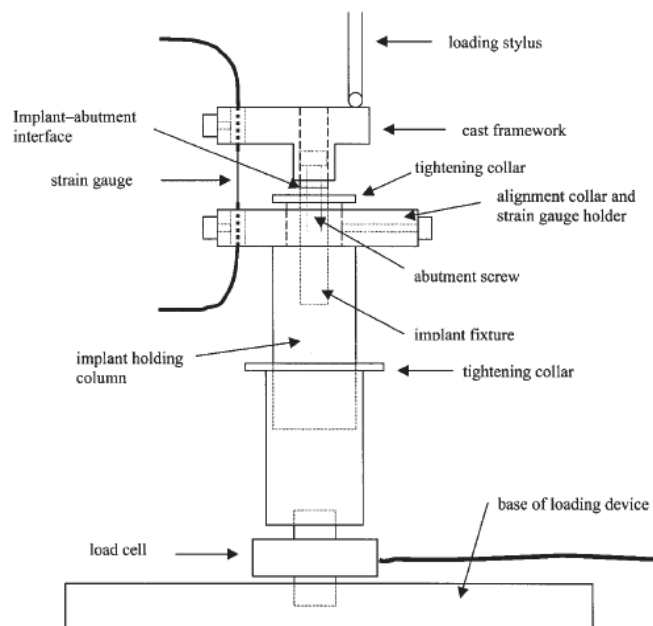
Figure 11: Solenoid driven dynamic loading test apparatus (schematic) [10]

5   FINITE ELEMENT ANALYSIS (FEA)

Different studies agree that biomechanical behaviour plays an important role in the survival of an implant, and that the finite element method (FEM) can be a reliable tool for studying this phenomenon. The degree of accuracy of the FEM is related to the knowledge of real load and supporting conditions. But it should be noted that the validity of simulation highly depends on assumptions made in modeling geometry, material properties, boundary conditions and the bone–implant interface. So that is why the results obtained from finite element simulations need substantiation by clinical research [20]. This paragraph shortly discusses the modeling of the supporting bone and its interaction with the implant.

As discussed higher, bone is an inhomogeneous anisotropic material. However, most data on the elastic properties suggest that cortical bone can be effectively modeled as either an orthotropic or transversely isotropic material. In most FEA studies the model structures were assumed to be homogeneous, isotropic and to possess linear elasticity. To describe such mechanical behaviour, knowledge of the value of two parameters is sufficient: Young's elastic modulus (E) and Poisson's ratio (v) [11-12, 20-23].

In a first FEA, the modeled section of the mandible was composed of spongiosa with a thickness of 7mm in the bucco-lingual direction (this is the cheek-tongue direction), surrounded by 2mm of cortical bone bilaterally (Figure 12). The elastic properties used in this FEA are listed in Table 5. In this study, the basic loading conditions, biting with occlusal contact at the site of the molars and premolars was investigated. This site corresponds quite well with the focal point of masticatory forces. A wide range of magnitudes for chewing forces has been reported in the literature. The magnitude of the vertical load in this study was set at 500N, the loading forces on the models were static [3, 12].
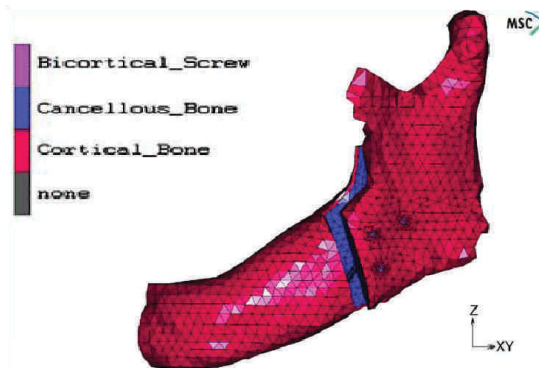
Figure 12: Modeled section of the mandible [12].

Material	Modulus of elasticity	Poisson's ratio
Cortical layer	13.7-14.8 GPa	0.3
Spongiosa/trabecular bone/cancellous bone	1.37-1.85 GPa	0.3

Table 5: Elastic properties used in the FEA [12, 20-22]

To investigate the initial stability for the situation immediately after implantation, the implant-bone interface was assumed as before the occurrence of osse-ointegration and simulated by non-linear contact zones with friction. The coefficient of friction was set to 0.3. This means that the contact zones transfer only pressure and tangential frictional forces (shear forces), whereas tension is not transferred [20].

Literature information on the precise material properties of maxillary trabecular bone is scarce. Trabecular bone is the dominant type in the maxilla, especially in the posterior regions where the surrounding compact bone often has a thickness less than 1mm. In a second FEA model, the maxilla was designed to be of homogeneous trabecular bone (Table 6) and to be isotropic and linearly elastic [14].

	Young's Modulus (E) [MPa]	Poisson's Ratio [/]
Trabecular bone I	560	0.3
Trabecular bone II	273	0.3

Table 6: Material properties used in the FE Model of [14].

6 CONCLUSIONS

Based on an extensive literature review, this paper summarizes the main observations concerning the information needed to design and perform *in vitro* experiments and finite element simulations of dental implant-abutment systems. The real elastic properties of a human jawbone are provided. Reported studies showed that the properties are direction dependant. This is difficult to realise in FEA, and therefore the materials are mostly modelled as homogeneous isotropic and linear elastic. Also provided is the range of human bite forces, 200 to 2000 N. These forces are used in *in vitro* studies to simulate the static performance of implant systems or to simulate chewing cycles in fatigue tests. Based on this information, new *in vitro* experiments and finite element models will be designed and evaluated.

7 ACKNOWLEDGEMENTS

8   REFERENCES

[1]   Pilliar, R.M., J.M. Lee, and C. Maniatopoulos, *Observations on the Effect of Movement on Bone Ingrowth into Porous-Surfaced Implants.* Clinical Orthopaedics and Related Research, 1986(208): p. 108-113.

[2]   Viceconti, M., et al., *Large-sliding contact elements accurately predict levels of bone-implant micromotion relevant to osseointegration.* Journal of Biomechanics, 2000. **33**(12): p. 1611-1618.

[3]   Fazel, A., et al., *Micromotion and Stress Distribution of Immediate Loaded Implants: A Finite Element Analysis.* Clinical Implant Dentistry and Related Research, 2009. **11**(4): p. 267-271.

[4]   Bozkaya, D. and S. Muftu, *Mechanics of the tapered interference fit in dental implants.* Journal of Biomechanics, 2003. **36**(11): p. 1649-1658.

[5]   Taylor, T.D. and J.R. Agar, *Twenty years of progress in implant prosthodontics.* Journal of Prosthetic Dentistry, 2002. **88**(1): p. 89-95.

[6]   Mollersten, L., P. Lockowandt, and L.A. Linden, *Comparison of strength and failure mode of seven implant systems: An in vitro test.* Journal of Prosthetic Dentistry, 1997. **78**(6): p. 582-591.

[7]   Rangert, B., *Forces and Moments on Brαnemark Implants.* International Journal of Oral and Maxillofacial Implants, 1989. **4**(3): p. 7.

[8]   Cibirka, R.M., et al., *Examination of the implant-abutment interface after fatigue testing.* Journal of Prosthetic Dentistry, 2001. **85**(3): p. 268-275.

[9]   Gratton, D.G., S.A. Aquilino, and C.M. Stanford, *Micromotion and dynamic fatigue properties of the denial implant-abutment interface.* Journal of Prosthetic Dentistry, 2001. **85**(1): p. 47-52.

[10]   Hoyer, S.A., et al., *Dynamic fatigue properties of the dental implant-abutment interface: Joint opening in wide-diameter versus standard-diameter hex-type implants.* Journal of Prosthetic Dentistry, 2001. **85**(6): p. 599-607.

[11]   Dechow, P.C., et al., *ELASTIC PROPERTIES OF HUMAN SUPRAORBITAL AND MANDIBULAR BONE.* American Journal of Physical Anthropology, 1993. **90**(3): p. 291-306.

[12]   Erkmen, E., et al., *Comparison of different fixation methods following sagittal split ramus osteotomies using three-dimensional finite elements analysis - Part 1: advancement surgery posterior loading.* International Journal of Oral and Maxillofacial Surgery, 2005. **34**(5): p. 551-558.

[13]   Schwartz-Dabney, C.L. and P.C. Dechow, *Edentulation alters material properties of cortical bone in the human mandible.* Journal of Dental Research, 2002. **81**(9): p. 613-617.

[14]   Bergkvist, G., et al., *A finite element analysis of stress distribution in bone tissue surrounding uncoupled or splinted dental implants.* Clinical Implant Dentistry and Related Research, 2008. **10**(1): p. 40-46.

[15]   Spiekermann, D., *Implantology*. Color atlas of dental medicine. 1995, Stuttgart: Thieme.

[16]   Gibbs, C.H., et al., *LIMITS OF HUMAN BITE STRENGTH.* Journal of Prosthetic Dentistry, 1986. **56**(2): p. 226-229.

[17]   Olmsted, M.J., et al., *Human bite force: the relation between EMG activity and bite force at a standardized gape.* American Journal of Physical Anthropology, 2005: p. 160-161.

[18]   Harada, K., et al., *Measure of bite force and. occlusal contact area before and. after bilateral sagittal split ramus osteotomy of the mandible using a new pressure-sensitive device: A preliminary report.* Journal of Oral and Maxillofacial Surgery, 2000. **58**(4): p. 370-373.

[19]   Uri Arni, I.W., Oved Gihon, *Hybrid Dual Thread Screw Implant - Analytical and Experimental Research.* 2007.

[20]   Ding, X., et al., *Effect of Diameter and Length on Stress Distribution of the Alveolar Crest around Immediate Loading Implants.* Clinical Implant Dentistry and Related Research, 2009. **11**(4): p. 279-287.

[21]   Cehreli, M., M. Akkocaoglu, and K. Akca, *Numerical simulation of <it>in vivo </it>intraosseous torsional failure of a hollow-screw oral implant.* Head & Face Medicine, 2006. **2**(1): p. 36-36.

[22]   Borchers, L. and P. Reichart, *3-DIMENSIONAL STRESS-DISTRIBUTION AROUND A DENTAL IMPLANT AT DIFFERENT STAGES OF INTERFACE DEVELOPMENT.* Journal of Dental Research, 1983. **62**(2): p. 155-159.

[23]   Abu-Hammad, O., et al., *Effect of dental implant cross-sectional design on cortical bone structure using finite element analysis.* Clinical Implant Dentistry and Related Research, 2007. **9**(4): p. 217-221.

CONCEPTUAL DESIGN OF A FRETTING FATIGUE TESTING DEVICE

N. Borms[1], D. De Schamphelaere[1], J. De Pauw[2], P. De Baets[2], W. De Waele[2]

[1] Ghent University, Belgium
[2] Ghent University, Laboratory Soete, Belgium

Abstract Fretting fatigue occurs in contacting parts which are simultaneously subjected to fluctuating loads and very small sliding movements. This phenomenon can significantly reduce the fatigue life of components. This paper focuses on the conceptual design of an advanced, especially in functionality and human engineering, test rig for fretting fatigue experiments. Different designs of test rigs are evaluated by weighing their advantages and disadvantages.

Keywords Fretting, fatigue, test rig

1   INTRODUCTION

When two mating components exercise a relative movement, in a loaded condition, wear can be caused. When these movements are relatively small, in the order of microns, this is called fretting wear. As a result, small cracks occur which will shorten the life span of the material. This relative movement can be caused by elastic deformation of the material or machine and construction vibrations [1][2]. In this paper, fretting is related to fatigue because both phenomena are important to the life span of materials and constructions.
A practical example, Figure 1, in which fretting fatigue has been observed is the connection of two plates by means of a bolt [3]. Fretting can occur between the bolt and the plates or between de plates itself. The bolted connection will typically be calculated to resist both static and fatigue loads. There are no simple means to take fretting wear into account. Figure 2 shows fretting wear observed on the thread of a bolt. By small movements, applied by elastic deformation of the plate material from fatigue or vibrations, the dimensioned bolt can premature break due to fretting in combination with fatigue. In this case the preload of the bolt was less than required.
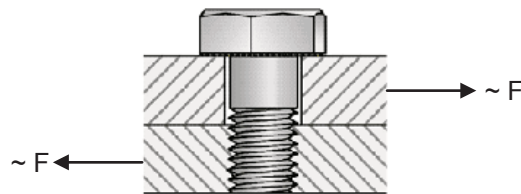
Figure 1: Two plates connected by a bolt and loaded in fatigue [4]
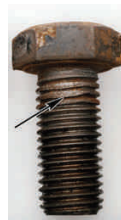
Figure 2: Fretting wear [5]

Apart from the described problem with the bolt connection, several other applications have been reported where fretting fatigue and failure appears such as leave springs [6], dovetail joints [3] used in the rotors of aircraft engines, prostheses [7]. This highlights the importance of the study into fretting and its properties and consequences. The aim of this work is the design of a test rig for fretting fatigue experiments, meeting the requirements postulated in section 4. As a source of inspiration, existing test rigs were studied and their major drawbacks evaluated. The future design is based on a coupon test rig which is a test facility used to perform universal research. This design is in contrast to full-scale test rigs which are limited to one application, such as dovetail joints.
In the next section the combination of the fretting and metal fatigue phenomena and their interrelations are discussed.
Section 3 addresses some existing test rigs and their limitations. In section 4 the main requirements for a new set-up are postulated. It further focuses on the current status of three conceptual designs and the last section gives a conclusion on the acquired knowledge.

2   COMBINING FRETTING AND FATIGUE

The loads and displacements corresponding to fatigue and fretting are independently illustrated for the case of a clamped beam (Figure 3). Hereby a fatigue load is imposed by an oscillating force F_{fat}. Apart from the fatigue load F_{fat} also a constant normal load F_N, perpendicular on the cross-section of the beam has to be introduced. To realize the fretting movement on the clamped beam, caused by the indenter (fretting pad), a micro displacement d must be available.
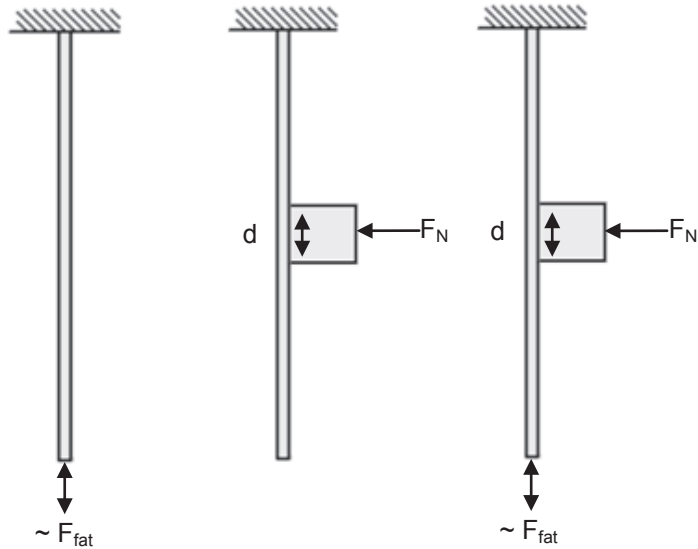
Figure 3: a) Fatigue b) Fretting c) Fretting fatigue

3   DISCUSSION OF EXISTING FRETTING FATIGUE SET-UPS

Literature on fretting fatigue clearly demonstrates that the test set-up based on the proving ring [8] is a widely used method for the creation of the normal force F_N (Figure 4).
Through a ring, which serves as a calibrated spring, and a clamping screw a force F_N is applied across the specimen. As a result of fretting wear, material particles will break loose from the test specimen. If these particles get caught between the test specimen and the fretting path, the applied normal force F_N will fluctuate. This is to be avoided what is necessary in order to obtain representative test results. Due to this test rig is displacement controlled, trough the ring mechanism, instead of force controlled a disadvantage is caused.
A similar construction exists where the normal force F_N is delivered by preloaded springs but it has the same disadvantages.
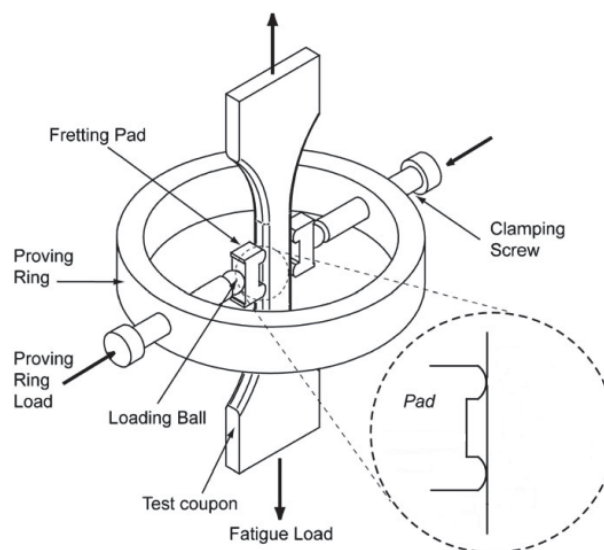
Figure 4: Proving ring test equipment

Fretting fatigue can only be accurately studied if the required slip, the relative displacement d of the fretting pad in relation to the specimen, is controllable and independent from the elastic deformation of the test specimen due to the fatigue load.

In the above figure (Figure 4) each pad is contains two contact surfaces. The elastic deformation (due to fatigue load) of the specimen creates frictional force between pad and test specimen. The deformation of the fretting pad influences the minuscule slip that takes place between the two parts. However, the achieved slip is hard to predict and impossible to control which is a drawback of this test rig. The shape and dimensions of the fretting pad are crucial.

In order to control the relative displacement d, once more calibrated and interchangeable springs have been used (Figure 5). The generated tangential force F_T, between pad and specimen, is absorbed by the spring [9] and causes a small additional slip. Here as well, the slip is hard to control and predict.
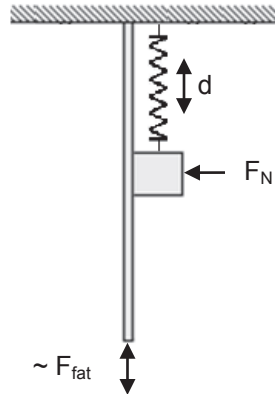
Figure 5: Impose of the relative displacement d through a spring system

This discussion clearly reveals the crucial attention points for the design of an advanced fretting fatigue test rig.

4   DESIGN OF THE FRETTING FATIGUE TEST FIXTURE

The main goal of this work is to design an advanced fretting fatigue test set-up which addresses the shortcomings of the existing set-ups. The concepts proposed in section 4.2 are based on a pad holder system with a very high tangential stiffness. The test coupon will be (elastically) elongated by the fatigue force F_{fat}, which has to be compensated by a global displacement of the test coupon. In contrast with the proving ring test rig, is the fretting pad in this case fully fixed and the fretting movement is realized by the global displacement of the specimen. These displacements can be controlled by means of one actuator that is force controlled and one that is displacement controlled respectively.

The design has to meet certain requirements to obtain efficient operation and results:
   (i)   the ability to produce a constant normal force F_N of maximum 5 kN between pad and specimen
         (value based on research of existing fretting fatigue set-ups),
   (ii) very high stiffness of the fixture in order to minimize pad movements to a few microns,
   (iii) visibility of the pad and the specimen,
   (iv) high precision techniques to measure forces, displacements and fretting slip.

A general view of the available frame and an impression of the future test set-up design is depicted in. The set-up consists of 5 parts : (i) the load frame, (ii) the hydraulic group, (iii) the two specimen grip systems, (iv) the fretting fixture, (v) the measuring tools.
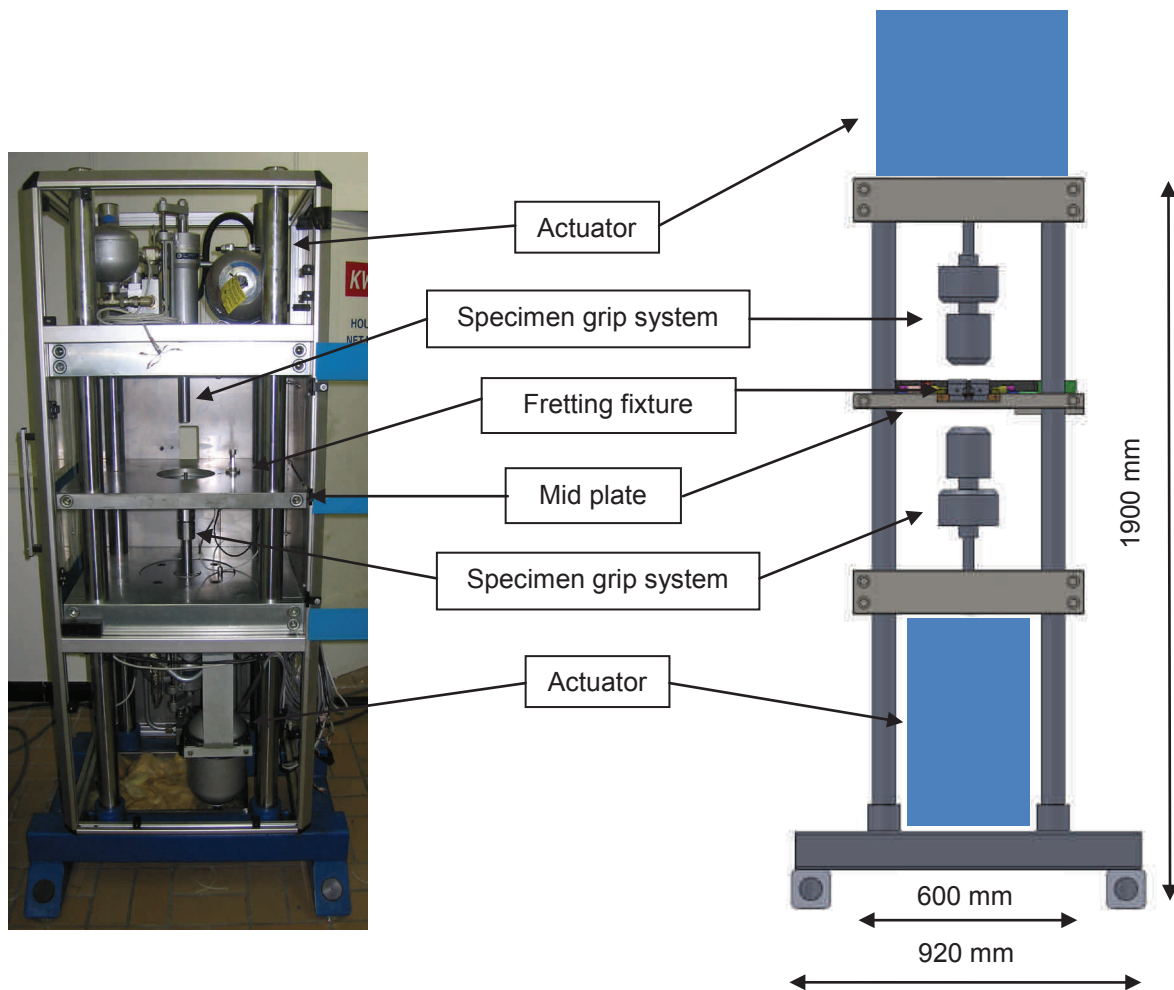
Figure 6: General view of the available machine and the future test fixture

The future design is based on an existing construction; a tablet press machine (Figure 6) will be rebuilt and expanded. The frame, the hydraulic group delivering the pressure needed in the actuators and two actuators for the realization of the fatigue load and the global vertical displacement of the test coupon are already available., A third actuator to apply the normal force on the fretting pads, the pad holder system and the test coupon fixtures has to be designed.

4.1 Specimen grip system

The grip systems at the top and the bottom of the framework are similar and consist of a piston, a load cell and wedge grips assembled with appropriate adaptor pieces (Figure 7). Wedge grips ensure proper alignment of the specimen and are self-clamping. The initial gripping force at specimen insertion is applied by means of a spring, during the actual test it is achieved by the wedge effect.
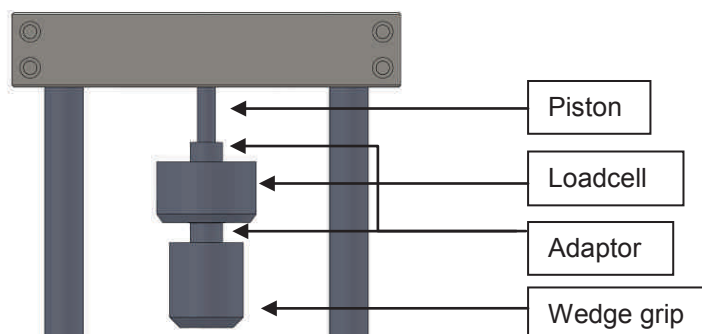
Figure 7: Specimen grip structure

In this application a consideration has to be made between hydraulic and mechanical wedge grips. Hydraulic wedge grips have excellent repeatability as they clamp symmetrical onto the specimen test after test The grips maintain a constant gripping force on the specimen regardless of the test forces acting upon it. This adjustable gripping force prevents damage to the specimen from the grip or specimen slippage during tests. Hydraulic wedge grips can withstand both tensile and compressive forces unlike mechanical wedge grips which can only be used for (static or cyclic) pure tensile loading. Mechanical wedge grips have advantages such as their compact nature and self-tightening behaviour during a tensile test, which avoids slipping of the specimen from its grips. The gripping pressure will be proportional to the tensile force due to the sliding wedges.

4.2   Fretting fixture

A fretting fixture design will consist of several specific parts, including a structure to fix the fretting pads, aligning elements and a construction to load the pads against a flat 'dog bone' tensile test specimen. In order to reach an equal normal force F_N at both sides of the test coupon, whilst limiting the required space and component cost, a spindle or hydraulic piston is directly connected to only one pad. The second pad is connected to the actuator through an U-guidance to apply a similar load to the specimen. Three concepts have been put forward and their feasibility to meet the above mentioned requirements evaluated.

4.2.1   Fretting fixture based on linear guides

A first conceptual design, shown in Figure 8, implements linear guides (in particular full ball types with wide rail) fastened on the mid plate. Linear motion guides are a simple and effective manner to move the pads towards the specimen. The pad holders are mounted on these linear guides. The ability to slide the pad holders backwards improves the visibility of the pad and specimen. The regained space significantly simplifies the removal and replacement of the specimen and the pads. In order to achieve the needed range of results, the height of the linear guidance becomes an obstacle as it increases a lot when the radial clearance decreases to the needed level.

The constant normal force F_N applied through the pads on the 'dog bone' test piece is induced by a spindle which is driven by a gear attached to an electric stepper motor and is measured using a load cell. The spindle will first push the right pad towards the specimen. Once a specific load is reached, the U-guidance (Figure 8) and the spindle housing connected to it, will start moving to the right. In this way, the pad at the left also approaches the specimen and induces an equal load at the specimen's left side. The load cell ensures that the proper contact loads are induced. The use of a spindle with servo control allows to define the position of the pad at all times without the need for an additional extensometer.
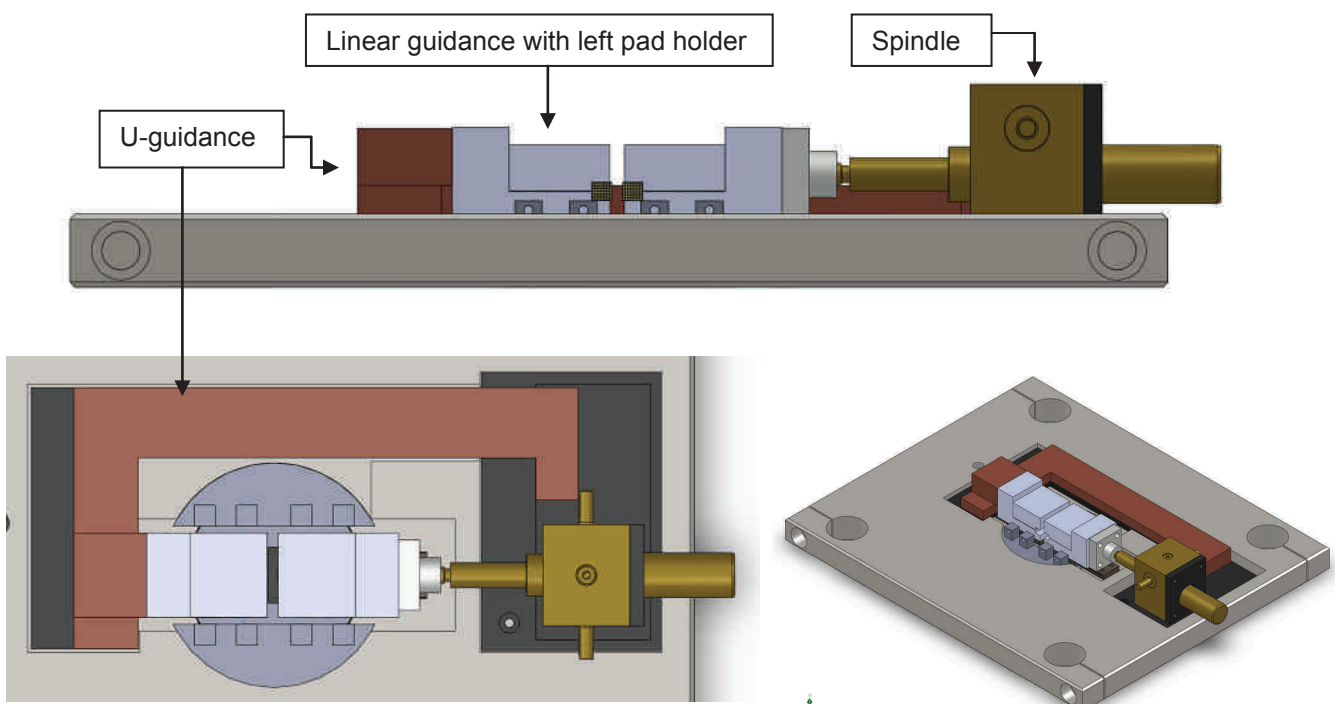
Figure 8: Concept 1: fretting fixture based on linear guides

4.2.2 Fretting fixture based on wedges

In Figure 9 a second conceptual design is depicted. The moveable pad holders are replaced by a structure fixed to the mid plate. The lower plate of the right and left pad holder is made out of one piece so no extra mechanism is needed to align the pad holders relative to each other. In this concept the pads are driven instead of the pad holders. The pad is restrained and guided between a slot in the lower plate and a wedge at the upper side of the pad (Figure 10). Two wedges slide against each other to adjust the clearance. The space between the pad and the lowest wedge is adjustable through two bolts in order to get zero clearance. The contact between pad and guidance causes a friction which is unfavourable for the needed precision movement.
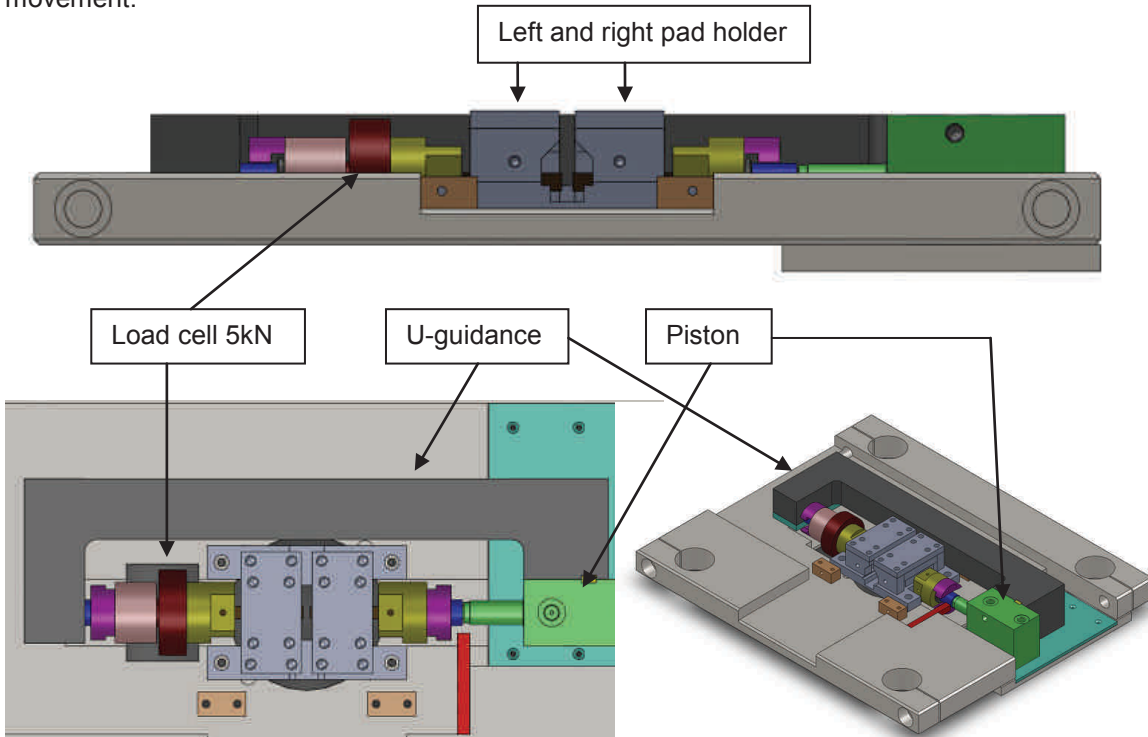
Figure 9: Concept 2: fretting fixture based on wedges
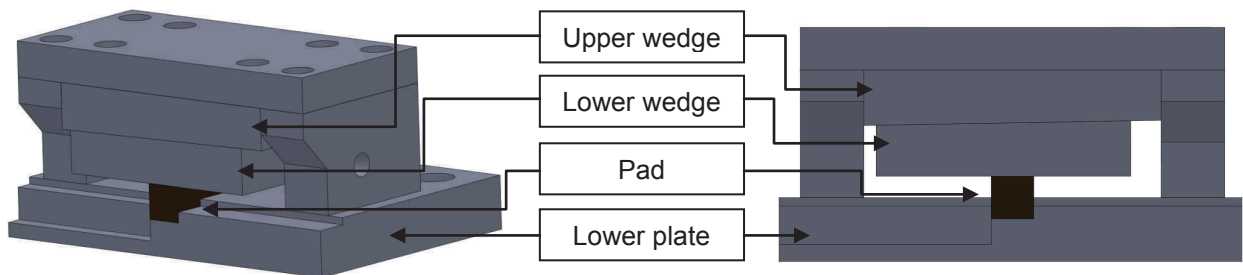
Figure 10: Pad holder system

The back of the pad is clamped into a holding device which is connected to a hydraulic piston. The reason for replacing the spindle of the first design with a piston is to make the fretting structure force controlled instead of displacement controlled. Due to this adaptation the applied normal force can be controlled in closed loop.

Again just one piston is used, the system with the U-guidance (section 4.2.1) is being reused in this design.

4.2.3   Fretting fixture based on a flexure mechanism

A flexure mechanism can be used to overcome the friction problem which is inherent to the construction of the pad holder in the previous concept. Linear guiding is realized by means of parallel leave springs. A schematic presentation is shown in Figure 11. To obtain a parallel displacement u, the stroke has to be small so the transversal displacement can be neglected.
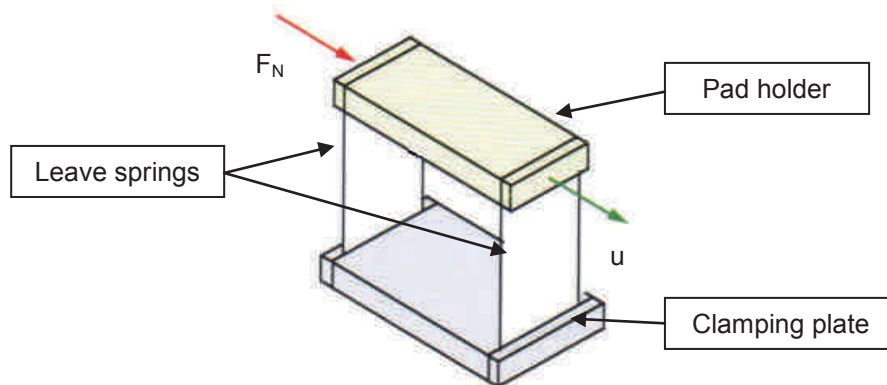
Figure 11: Fretting fixture based on a flexure mechanism [1]

Since the displacement is obtained by elastic deformation, the stroke is limited by the strain at the material's yield point. The stiffness of this system will cause that not all applied normal force F_N is transferred to the test coupon. Since there exists a linear relationship between applied force and displacement of the springs, calibration can avoid this inaccuracy. Unlike the previous design this principle offers the advantage that friction and mechanical play are not applicable. This concept will be developed in detail in the following period of time.

4.3   Instrumentation

The applied dynamic forces are measured by two 50 kN load cells, one on every side assembled between the piston and the wedge grip. The difference between the two registered values results in the sum of the tangential forces F_T among pad and specimen. The resolution of the specimen displacements is in order of 10Hz. A 5 kN load cell is mounted between the fretting pad holding device and the U-guidance of the contact pressure assembly.

The friction force and slip, created by the applied normal force and sliding movement between specimen and pads, are measured by an extensometer. An LVDT measures the position of the axial pistons.

5   CONCLUSIONS

Following a literature study on fretting fatigue and existing test set-ups, some improved conceptual designs have been proposed. Several crucial problems such as fluctuating normal force F_N, low stiffness, poor visibility and controllable slip were found and treated during a thorough evaluation of fretting fixture concepts based on linear guides, wedges and leave springs. Based on this evaluation and an improved understanding of the needs related to testing fretting in combination with fatigue, a third and final concept for controlling the fretting pads is proposed. By making a trade off of the different designs, a detailed final design will be developed. The friction problem encountered in design two can be eliminated using an elastic moveable structure.

The movement of the pad and loading of the test coupon will be realized by a hydraulic cylinder at one side and using a U-guidance to apply an equal force at the other side. Future work consists of finishing the detailed design (components selection, calculations, drawings) and constructing this specific testing device.

6   NOMENCLATURE

F_{fat}	fatigue force	kN
F_N	normal force	kN
F_T	tangential force	kN
d	relative displacement	μm
u	pad displacement	mm

7   ACKNOWLEDGEMENTS

8   REFERENCES

[1] van Beek A., (2009). Advanced engineering design, Delft University of Technology Mechanical Engineering.

[2] Hoeppner DW., C. V, et al. (2000). Fretting Fatigue: Current Technology and Practices, ASTM International.

[3] Majzoobi G.H., et al. (2007). Duplex surface treatments on AL7075-t6 alloy against fretting fatigue behavior by application of titanium coating plus nitriding. Kidlington, ROYAUME-UNI, Elsevier.

[4] [http://www.douwes.nl/dofast/nordlock-werking.htm], 23 december 2010

[5] [http://www.tsb.gc.ca/eng/rapports-reports/rail/2005/r05q0033/r05q0033.asp], 23 december 2010

[6] Aggarwal M. L., R. A. Khan, et al. (2005). "Investigation into the effects of shot peening on the fretting fatigue behaviour of 65Si7 spring steel leaf springs." Proceedings of the Institution of Mechanical Engineers -- Part L -- Journal of Materials: Design & Applications **219**(3): 139-147.

[7] Hoeppner, D. W. and V. Chandrasekaran (1994). "Fretting in orthopaedic implants: A review." Wear **173**(1-2): 189-197.

[8] Liu K. K. and M. R. Hill (2009). "The effects of laser peening and shot peening on fretting fatigue in Ti-6Al-4V coupons." Tribology International **42**(9): 1250-1262.

[9] Buciumeanu M., I. Crudu, et al. "Influence of wear damage on the fretting fatigue life prediction of an Al7175 alloy." International Journal of Fatigue **31**(8-9): 1278-1285.

WEAR OF CONVEYOR CHAINS WITH POLYMER ROLLERS

V. Kerremans[1], T. Rolly[1], P. De Baets[1], J. De Pauw[1], J. Sukumaran[1] and Y. Perez Delgado[1]

[1] Ghent University, Laboratory Soete, Belgium

Abstract   Roller conveyor chains are common used to transport goods in production lines or assembly lines, such as pallets, cars or steel coils. They are sometimes used in severe environments, soiled with water, foreign particles, chemicals or other contaminants. Normal use will result in wear of the components of the chain which can lead to unexpected failure and costly production downtime. Today, few literature on the wear of conveyor chain is available and there are almost no reliable test-rigs to generate and measure chain wear in a reproducible manner. In this research the different components of conveyor chains and the loading conditions are described. Additionally, the applications and (dis)advantages of chains with polymer rollers are discussed. The chain wear mechanisms found in literature are listed. Abrasive and adhesive wear between pin, bushing, roller and track are discussed. From the contact mechanics of the chain and pressure-velocity limit of the roller materials, the design constraints for the laboratory test-rig were derived. The capabilities and working principles of the developed test-rig are explained in this paper.

Keywords wear, conveyor chain, polymer rollers, test rig design

1   INTRODUCTION

Roller conveyor chains are generally used in production or assembly lines where individual large objects need to be conveyed. Typical applications of roller conveyors are carrier conveyors for the transport of steel coils in a steel plant or slat conveyors that carry objects. A slat conveyor consists of two or more endless strands of chain with attached non interlocking slats or metal flights to carry the material. Other examples are conveying pallets, tree-stumps or even whole cars. Wheeled cars, for example, can be carried by the chain but can also be pulled by the chain. Applications can be divided in two basic conveying modes [1]:

- The material is supported and carried entirely by the chain and attachments.
- The chain does not support the material, but it is pushed, pulled or scraped.

Roller conveyor chains differ from transmission roller chains such as a bicycle chain, which is used to transfer torque instead of conveying goods. Conveyor chains have a large pitch which is efficient in bridging large distances with fewer shackles, they generally have thicker side plates and rollers with large diameter. Therefore they can withstand higher tensile and shock loads than transmission chains. Furthermore they can bear large amounts of wear before breakage occurs. On the other hand, roller conveyor chains have a necessary clearance that easily becomes contaminated with particles from the conveyed material.
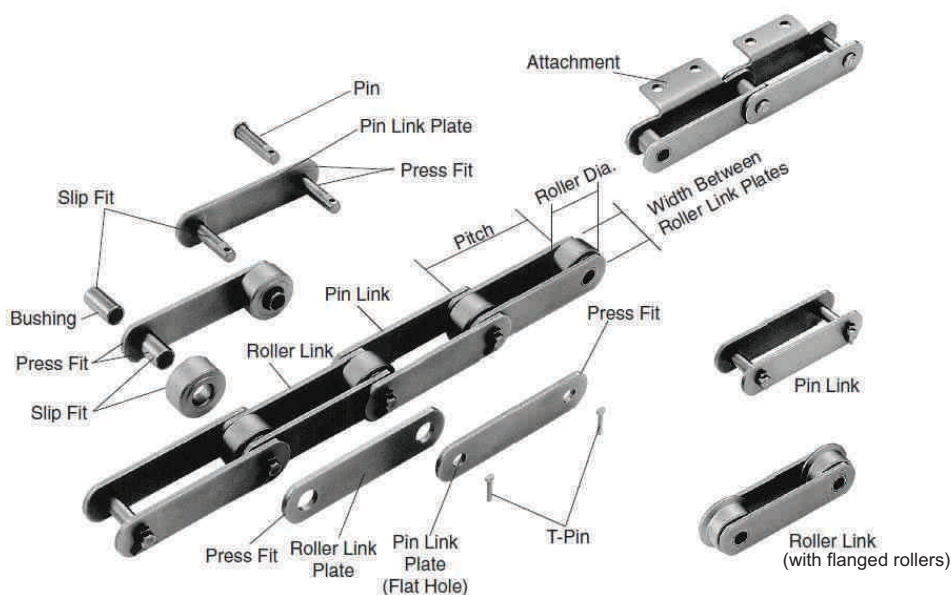

Figure 1: Basic structure of a conveyor chain [2]

A typical conveyor chain is constructed with two different types of shackles: the roller link (or inner link) and the pin link (or outer link), see Figure 1. The roller link consists of two steel bushings who are press-fitted inside the roller link plates, while the pin link consists out of two steel pins press-fitted inside the pin link plates. To prevent disengaging of plates and pins, riveted pins or t-pins (as shown) are used.

Conveyor chains can be loaded in two ways: the force can be applied on the side plates by use of attachments which are connected to the side plates, see Figure 1. Alternately the force can be applied on the pins. Therefore hollow pins and axles instead of solid pins (as shown) are used. The rollers transfer the normal force, due to the weight of the conveyed objects, to the track. The driving sprocket, exerts a force on the chain to pull the load, this results in a tensile force inside the chain which must be large enough to overcome the sliding friction between roller/bushing and the rolling friction between roller/track. Additionally the chain is prestressed by the sprockets, this will result in a raise of tensile force. To transfer this tensile force from one shackle to another, bushing and pin will act together as a bearing. The mechanics of these contacts are further discussed in section 2.1.

The use of chains with polymer rollers is gaining importance. In a water treatment plant, for example, lubrication is unwanted for environmental reasons. Other applications can be found in food industry and pharmaceutical industry, where contamination of the product with oil of the chain is unwanted. Chains with polymer rollers are capable of working without any lubrication, have good corrosion resistance, run quieter and weigh less than chains with steel rollers. The disadvantages of polymer rollers in comparison with steel rollers are: the lower heat resistance due to softening or even melting of the polymer, the lower yield strength and the water absorption of the polymer [1, 2]. Polymer rollers are often placed on a stainless steel chain, for example austenitic RVS 304, to obtain a chain that is entirely corrosion resistant. Different polymer materials are frequently used for the rollers: PA6/6, POM-C, POM-H, PEEK and patented polymers especially developed for chain manufacturers. For example IGUS Iglidur by Renold Chain [3, 4] or VRP(U)-series by Tsubaki [5]. To compare the suitability of different polymers, the pressure velocity limits (Pv-limits) are shown in Figure 2 using a logarithmic scale. Notice that PEEK rollers can withstand the highest contact pressures and sliding speeds. On the other hand, PEEK is more expensive than POM or PA rollers and has a higher friction coefficient and specific wear rate than POM or PA, see Figure 3.

Few literature on the wear of polymer roller conveyor chain is available, this research will study the wear behaviour of chains with polymer rollers. There are almost no reliable test-rigs available to generate and measure chain wear in a reproducible manner. Therefore a test-rig was designed, the required capabilities of this set-up are discussed in section 2.3.
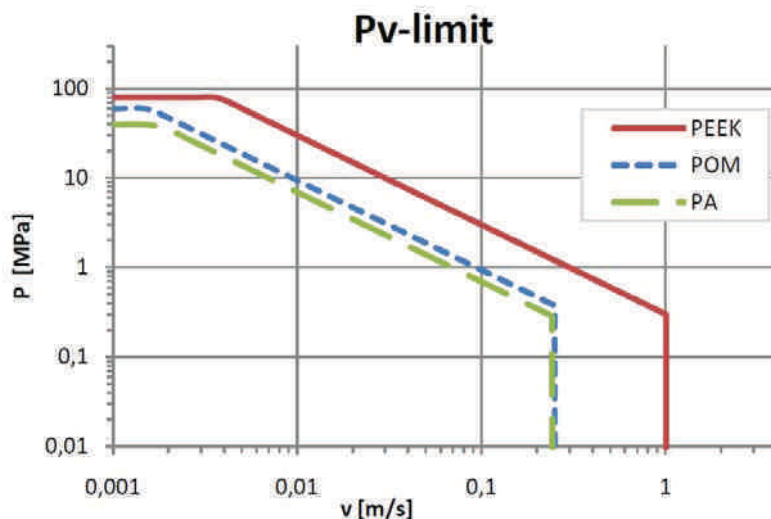
Figure 2: Pv-limit diagram of common polymers [6-10]
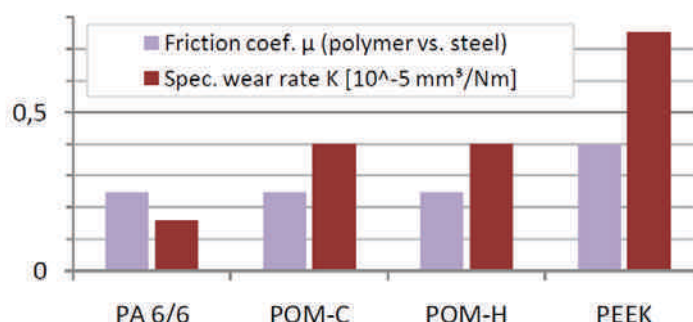
Figure 3: Friction coefficient & specific wear rate of different polymers [6-9]

2   STUDY OF CONVEYOR CHAINS WITH POLYMER ROLLERS

2.1   Contact mechanics

2.1.1   Overview of forces acting in conveyor roller chains

In this section, the contact mechanics are studied of a conveyor roller chain that transports pallets which are carried entirely by the chain. The chain is rolling over a track from left to right, see Figure 4. The weight of the pallets is applied on the pins of the chain, resulting in a normal force N_{02} on each pin. A tensile force F_t is exerted on the chain by the sprockets. This tensile force F_t will be transferred from the inner link to the outer link by bushing and pin acting together as a bearing. The normal force N_{02} is transferred from pin to bushing and than from bushing to track through roller. Notice that pin and bushing have a small clearance resulting in eccentricity e_{23}. Analogous, bushing and roller have a small eccentricity e_{34} (exaggerated on drawing).
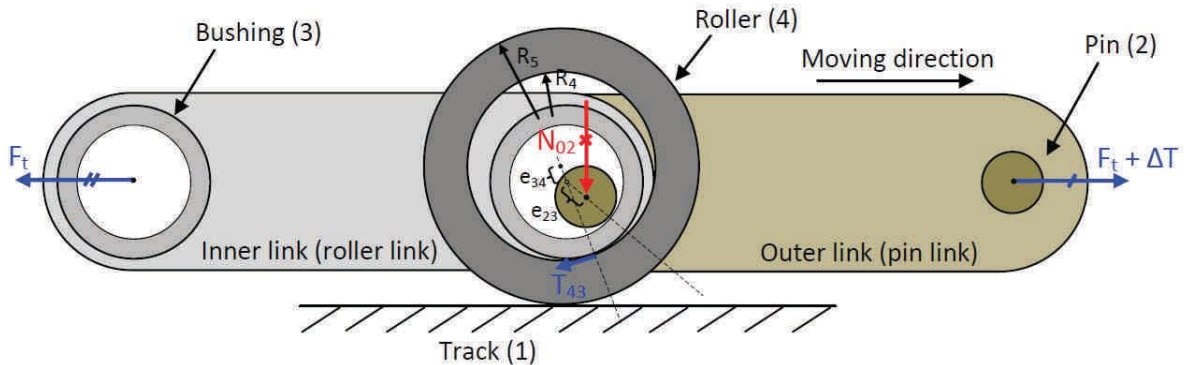
Figure 4: Section view of a roller conveyor chain with exaggerated clearances

The sliding contact between roller and bushing is discussed in section 2.1.2, while the rolling contact between roller and track is discussed in 2.1.3.

2.1.2   Sliding contact between bushing and roller

To calculate the maximum load for this conform bushing/roller contact, we can assume that the contact zone will be a line with finite width. This is called a Hertzian line contact. The pressure distribution is half-elliptic. The maximum Hertzian pressure p_{max} is indicated on Figure 5. Notice that it is higher than the mean contact pressure p_{mean}.
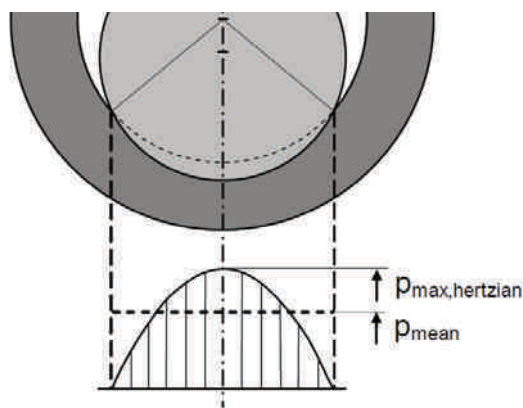
Figure 5: Hertzian pressure distribution in roller/bushing contact [10].

The contact between roller and bushing is a pure sliding contact. As the roller slides over the bush, a tangential force T_{43} appears on the bushing. It engages tangential to the bushing and roller and opposes the movement of the chain. The force T_{34} (=$-T_{43}$) acts on the bushing but is not shown in Figure 4. The friction coefficient μ_{slide} applies at the bushing/roller contact face and needs to be scaled with their diameters to obtain the equivalent coefficient of friction for the bushing/roller contact. This is calculated in equation 1 [1, 11]. Notice that when assuming rollers with the same inner radius R_4, the rollers with a larger outer radius R_5 have a mechanic advantage on rollers with a smaller outer radius because their resulting equivalent coefficient of friction $\mu_{slide,equiv.}$ will be lower.

$$\mu_{slide,equiv.} = \mu_{slide} \cdot \frac{R_4}{R_5} \tag{1}$$

2.1.3 Rolling contact between roller and track

The contact between roller and track can also be described as a Hertzian line contact and pressure distribution is shown in Figure 6.
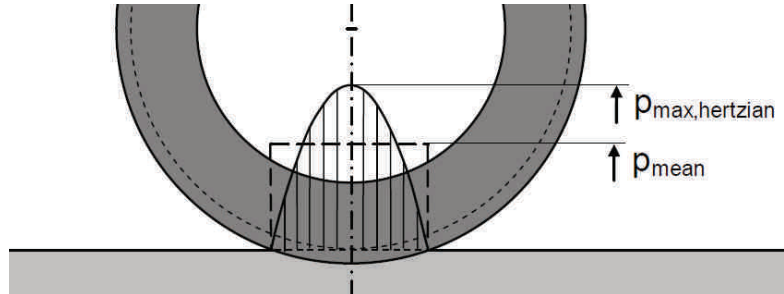
Figure 6: Hertzian pressure distribution in roller/track contact [10].

The contact between roller and track is a pure rolling contact. Although there is some rolling friction, due to hysteresis and micro-slip: When rolling, the polymer roller and track will continually be indented at the front and will elastically recover from the rear. A small fraction of the energy needed to indent is not recovered during the materials relaxation, this is called hysteresis. Under the influence of load, roller and track will deform elastically. The curved contact length of the roller reduces in length, while it increases for the track. The opposing strains at both surfaces result in micro-slip [10].

The dimensionless rolling resistance coefficient μ_{rol} is calculated in equation 2, where b is the rolling resistance coefficient of the materials. For a polymer roller on steel track, μ_{rol} is about 0,07 [5].

$$\mu_{rol} = \frac{b}{R_5} \tag{2}$$

The overall coefficient of friction μ_{total} for the chain is calculated in equation (3). It includes both sliding and rolling friction effects [1, 11].

$$\mu_{total} = \mu_{slide,equiv.} + \mu_{rol} = \mu_{slide} \cdot \frac{R_4}{R_5} + \frac{b}{R_5} \tag{3}$$

The additional pulling force on the chain due to both sliding and rolling friction can be calculated using equation (4):

$$\Delta T = \mu_{total} \cdot N_{02} = \left(\mu_{slide} \cdot \frac{R_4}{R_5} + \frac{b}{R_5} \right) \cdot N_{02} \tag{4}$$

2.2 Wear in conveyor chains

2.2.1 General overview of wear mechanisms in conveyor chains

In materials science, wear can be defined as a process where interaction of the surfaces or bounding faces of a solid with its working environment results in erosion of the material [12]. To study the wear of conveyor roller chains, it is important to know which wear mechanisms can occur. The conveyor chain wear mechanisms found in literature were listed and sorted into a tree-structure, see Figure 7 [2, 13, 14].

This research will only focus on tribological failure because a conveyor roller chain system that is well designed will fail due to tribological wear. Tribological wear can be monitored so that the chain can be replaced before breakage occurs. The most common wear mechanisms in chains with polymer rollers are: adhesive wear, abrasive wear, impact with sprocket and softening of the polymer due to heat generation. They are discussed in the next sections. Failure due to plastic deformation or fracture will occur suddenly and does not evolve gradually. Therefore it should always be avoided by choosing the load- and safety

factor for the chain sufficiently large [1]. Corrosion failure can be reduced by choosing the right materials and/or coatings for the chain, given the working environment [15-17].
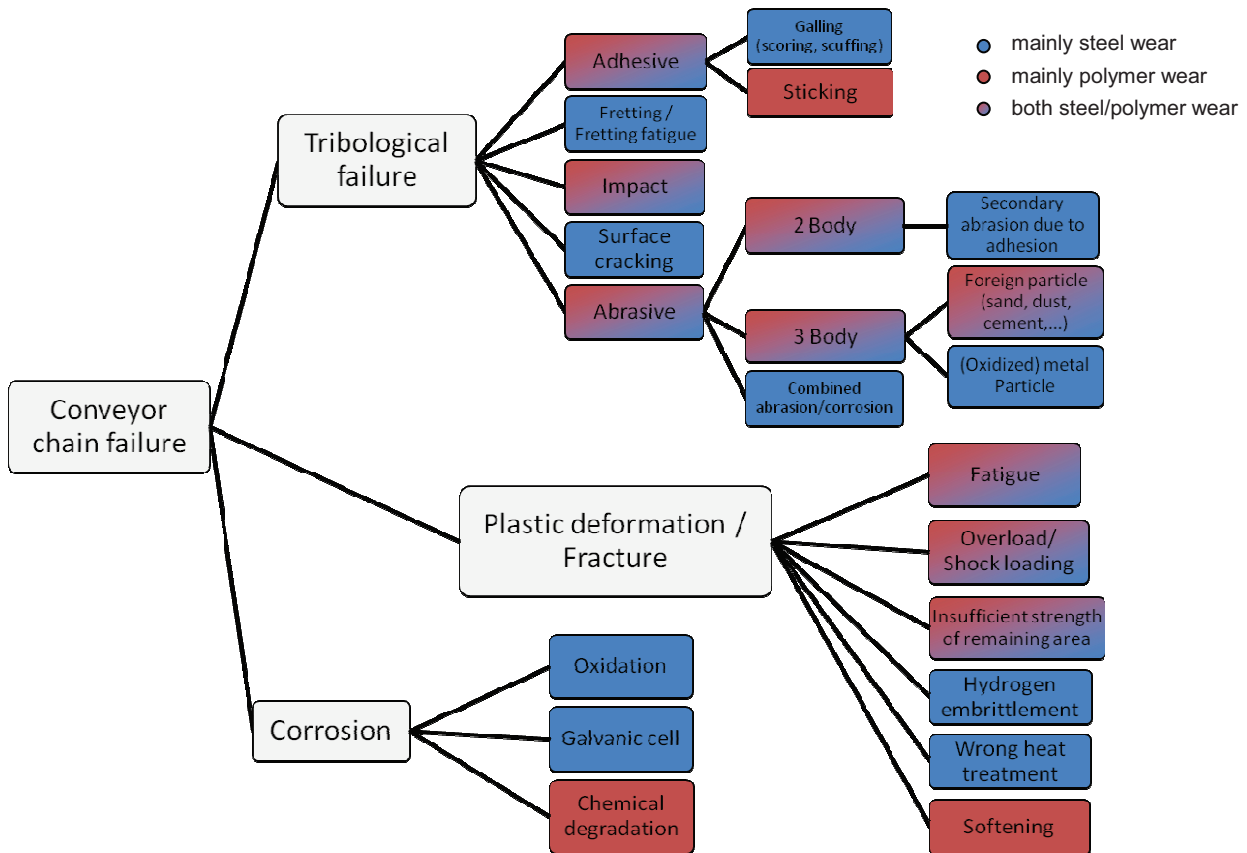
Figure 7: Wear mechanisms ocurring in conveyor chains

2.2.2   Adhesive wear

Adhesive wear occurs when strong adhesive bonding between interacting asperities causes micro-welding. In a continuous movement, junctions shear off whereby material may transfer from one surface to the mating surface [10]. For unlubricated conveyor chains, adhesive wear is expected to occur between roller/bushing and roller/track. Galling and sticking are forms of adhesive wear. With steel-on-steel contact, galling is expected and for polymer-on-steel contact sticking of the polymer to the steel counter surface might occur.

Galling is defined as local welding of both surfaces, immediately followed by breaking of the surfaces. This will occur if the operating conditions exceed the maximum speed and/or load. Especially when the lubrication mechanism does not remove the developed heat fast enough. Galling can occur at low speeds and destroy the contact surface.

Sticking is defined as local melting of one surface to another surface. Because of the heat, the polymer roller can stick to the steel bushing resulting in roller blockage.

2.2.3   Abrasive wear

Abrasive wear occurs in two modes which are referred to as two-body and three-body abrasive wear. Two-body abrasion refers to a hard, rough surface, of which the asperity summits plough into the relative softer counter surface. The effect of abrasion is comparable with a 'micro-cutting process'. Three-body abrasion refers to hard particles between two sliding surfaces participating to the ploughing of at least one of the surfaces. Two-body abrasion may result in three body abrasion when hard wear particles are formed that subsequently contribute to the wear process, see Figure 8. Especially for materials with large difference in relative hardness. In this research, for steel vs. polymer, abrasive wear is expected to be high [10].

In conveyer chains with polymer rollers, both two-body and three-body abrasive wear is expected to occur. Sand, dust or other particles can get between the roller/bushing contact and get embedded in the polymer,

enlarging ploughing and increasing friction. In some cases, particles can act as rolling elements and thus reducing friction. Particle geometry and size are important parameters together with the properties of the polymer.
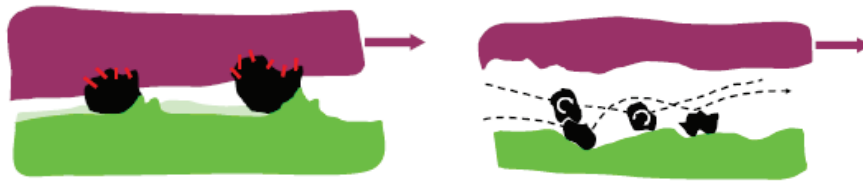
Figure 8: Two-body abrasion (left) and three-body abrasion (right) [18]

2.2.4 Impact of roller with sprocket

If a sprocket drives the chain and takes up a roller of the chain, this roller impacts against the tooth of the sprocket and is lifted due to the polygonal shape of the sprocket, this is called the polygonal effect. The impact increases with decreasing number of sprocket teeth, increasing conveying speed and increasing tensile load inside the chain. Both the roller and sprocket tooth surface can deteriorate due to impact fatigue.

2.2.5 Softening of the polymer

Softening of the polymer under load occurs when the deflection temperature is reached. This will change the material properties such as: tensile strength, hardness, sticking properties,... The softening temperature for thermoplastics is lower than the melting point. For example, the melting point of POM-H lies around 175°C, while the deflection temperature at 1,8 MPa is around 121°C [6].

2.3 Experimental set-up

Today, there are almost no reliable test-rigs available to generate and measure conveyor chain wear in a reproducible manner. A literature search revealed the following full scale test-rigs [14, 19]:

A first test rig was designed by the Central Electricity Generating Board to investigate the wear of a pin-bush chain used to lift control rods in a nuclear plant [14]. This test-rig is not designed to test roller chains.

The Chemnitz University also has some test-rigs, but mainly to investigate flat-top conveyors which do not have rollers [19]. These tests set-ups are not suitable for the testing of conveyor chains with polymer rollers.

Further, the use of the twin-disc test to investigate the roller/track wear and the pin-on-ring test to investigate bushing/roller wear was considered. But these tests were found to focus too much on the material level and not representative for the real working conditions of roller conveyor chains. Therefore a new test-rig was designed, the design constraints are discussed in section 2.3.1.

2.3.1 Design constraints

To study the wear in roller conveyor chains with polymer rollers, different conveying velocity and loading conditions have to be simulated. Therefore the test rig should allow regulation of the conveying speed, tensile force inside the chain and normal load on the rollers. Different sizes of sprockets can be used to investigate the influence of the polygonal effect or to use chains with smaller or larger pitch. The sprocket diameter can vary between 129 mm and 300 mm.

To determine the range for the conveying speed, two different sources are used. According to the Standard handbook of chain, a speed range for conveyor chains between 0,025 m/s and 0,762 m/s is commonly used [1]. In the Tsubaki engineering manual, the usable speed range speed range is between 0,25 m/s and 2 m/s [5]. Therefore, 2 m/s is chosen as an upper limit for the conveyor chain speed.

From the conveyor chain speed range and sprocket diameters, the required motor speed is determined. For the set-up a 4-pole induction motor with a rated speed of 1450 rpm is used. It is powered by a variable frequency drive (5-100 Hz). Then a planetary gearbox is required with a speed reduction of 9,8. This results in a lower velocity limit of the chain of 0,1 m/s. For testing at lower speeds, another gearbox is required which has a speed reduction of 40. With this gearbox, the lowest possible chain speed is 0,025m/s. These speed ranges are shown in Figure 9. Notice that the velocities in Figure 9 are for the sliding speed of roller/bushing interface. To relate this to actual conveying speeds of the chain, the velocities of the graph have to be multiplied with ratio R_5/R_4. Typical values for this ratio R_5/R_4 are 2 or lower.

The maximum roller load for the polymer rollers is derived from the pv-limit diagram in Figure 9. Assume that a chain with PEEK rollers is used (R_4=15mm, R_5=40mm, roller width=10mm). The maximum roller load is than 1200 N per roller which results in a maximum Hertzian pressure of 20 MPa in the roller/bushing contact and 80 MPa in the roller/track interface [10]. This chain has a pitch of 50,8 mm thus 9 rollers will be in contact with the 500 mm long track. This results in a total normal force F_n of 10,8 kN that has to be applied on the chain.

The motor for the test-rig should deliver 2 kW of shaft power. If an efficiency of 50% for the reduction and sprockets is taken into account, the following motor power limit is obtained, shown in Figure 9. Note that it lies above the pv-limit of the polymers. The working area of the test-rig, obtained by the constraints above, is grey coloured.

The test-rig is designed to simulate tribological failure of the chain, breakage of the chain should never occur. In normal conditions the working load, this is the tensile force inside the chain, is generally taken 1/8 of the breaking load. For use in abrasive and unlubricated conditions, load factors up to 1/18 of the breaking load are used [2, 11]. In this test set-up, a tensile force up to 1/5 of the breaking load is used to generate sufficient quick wear. The maximum tensile force that thus must be applied is 20 kN.
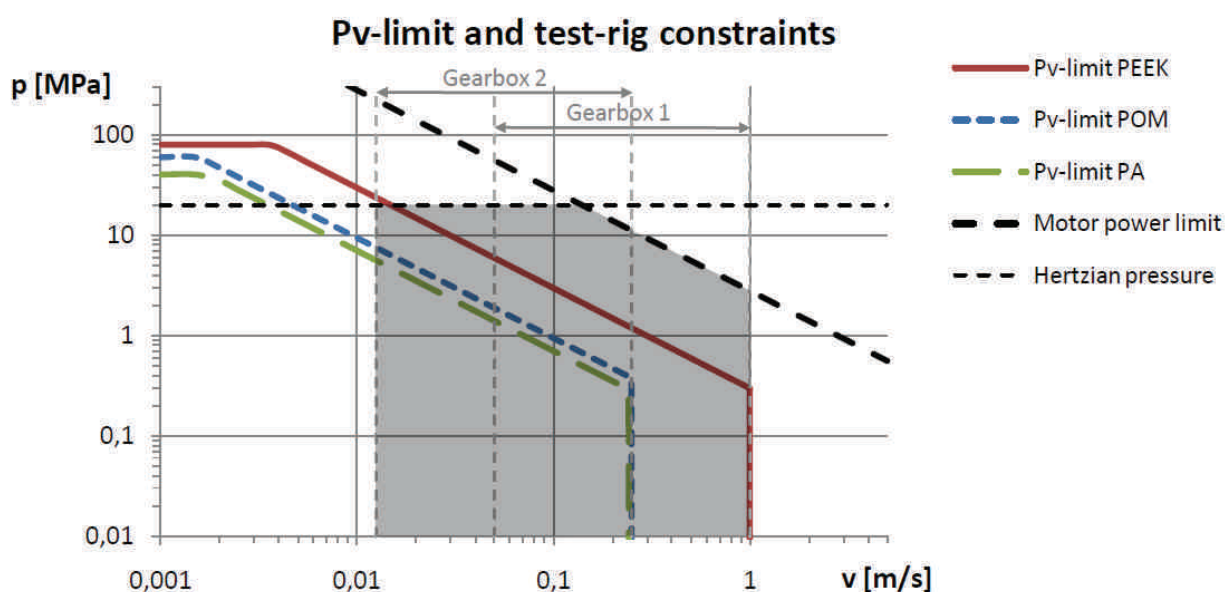
Figure 9: Pressure velocity limit of different polymers and test-rig limitations

2.3.2 Design of the experimental set-up

The experimental set-up allows testing of different types of conveyor chains. It is possible to independently regulate the conveying speed, tensile force inside the chain F_t and normal load F_n applied on the rollers. Sprocket diameters from 129 mm to 300 mm can be tested. The design is shown in Figure 10.

The mechanism to apply tensile force on the chain is *green coloured.* The maximum force that needs to be applied is 20 kN. A pneumatic piston cannot directly deliver this force. Therefore, a lever mechanism with a ratio of 1/5 is used. The pneumatic piston should then deliver 4 kN, which is possible. This force, produced by the piston, is transferred by the lever mechanism to the take-up units and than to the take-up shaft. The take-up units allow displacement of the shaft up to 2% elongation of the chain. Sprockets are clamped on the take-up shaft and transfer the tensile force to the conveyor chains. On the other side of the test-rig, the driving shaft is supported by two fixed plummer-block bearing units. The driving shaft is driven by a motor and planetary gear box (not shown).

The *red coloured section* shows how the normal force is applied to the conveyor chains, see Figure 10. The maximum normal force F_n that can be applied is 10,8 kN. This force is delivered by a pneumatic piston and is transferred to the upper running surface and then to the rollers of the middle conveyor chain. The loading principle of the chain is shown in Figure 11: The chain for testing is in the middle, it is supported by two chains, one on each side. The supporting chains are connected with the middle chain by means of distance bushings and bolts and transfer the normal load to the lower running surfaces. The supporting chains do not contribute to the tensile strength of the middle chain because their outer side plates are removed. They only exist of inner shackles which function as support rollers.

The running surfaces are interchangeable to test different track materials. The distance between the running surfaces can be adjusted to the dimensions of the chains. This is possible by displacing the supports of the tracks along the vertical slots in the chassis. Additionally the configuration of the running surfaces can be altered (not shown) so that one track is on the bottom and the two supporting tracks are on top.
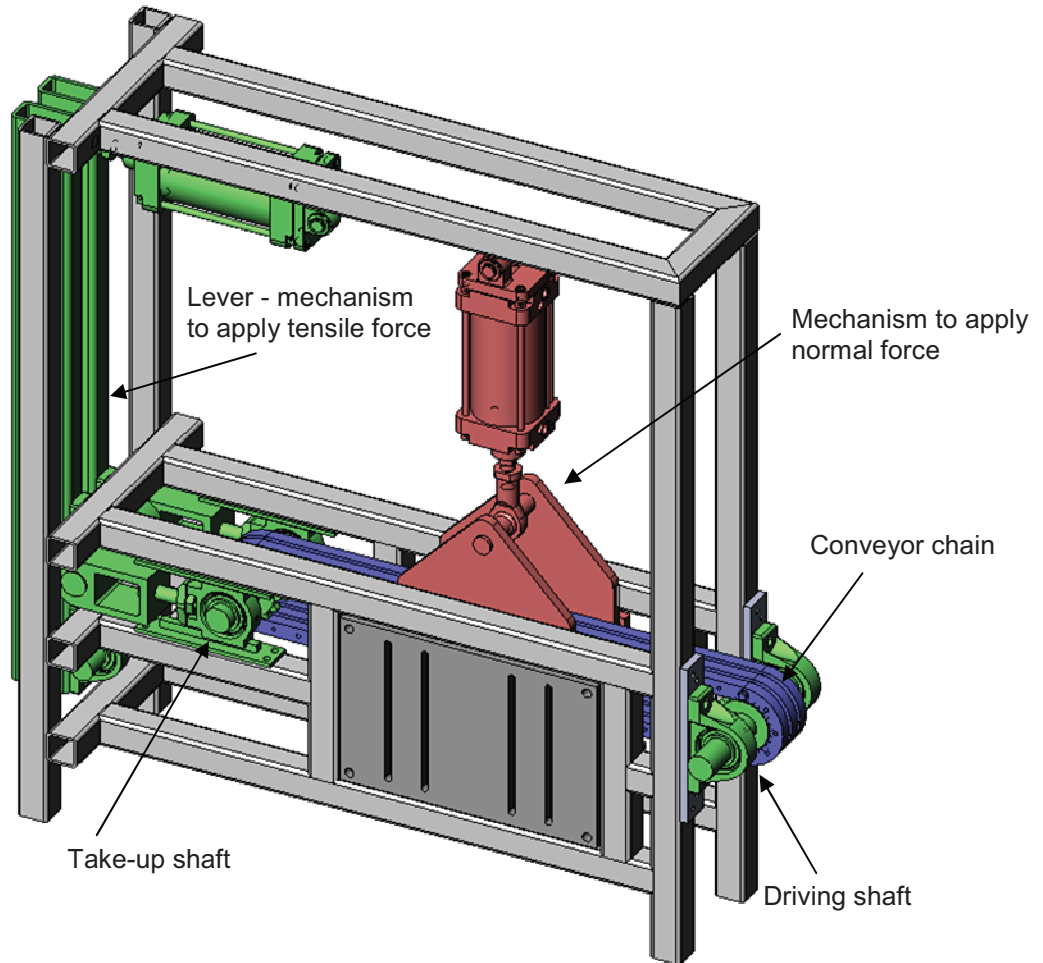
Figure 10: CAD-drawing of the designed test-rig
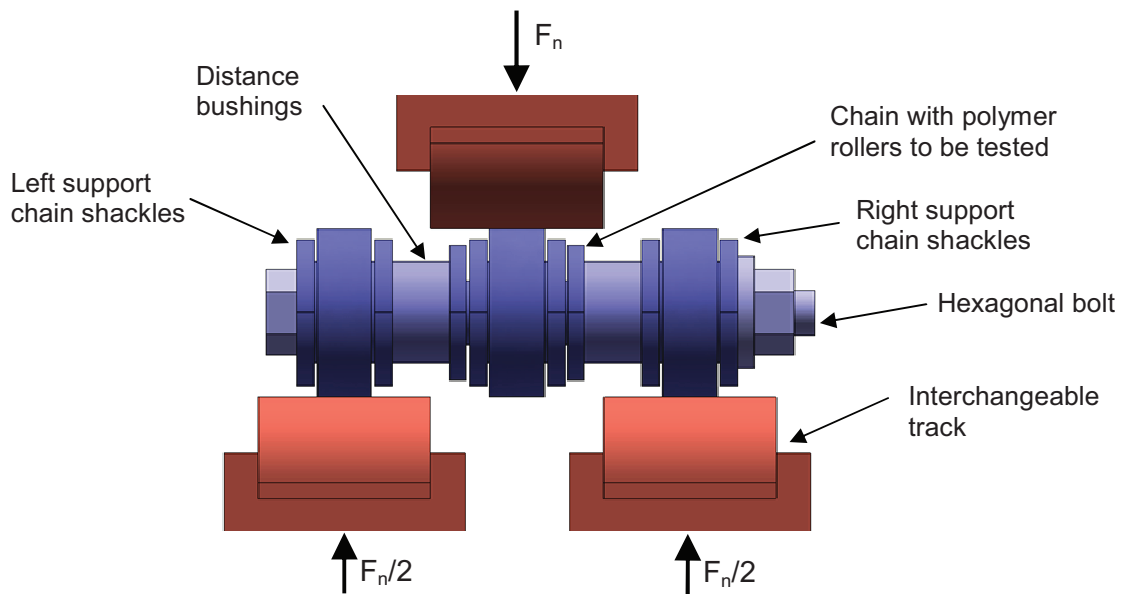
Figure 11: Loading principle of the chain

2.3.3 Instrumentation

Sensors will be placed on the test-rig to measure the applied forces and occurred wear. To accurately measure the tensile force, a load cell is placed between the lever and take-up units. To measure the applied normal force a load cell is applied between the cylinder and its support. To monitor the elongation of the chain, a linear variable differential transformer (LVDT) is used. An optical measuring device is used to measure the change in diameter due to wear of the polymer rollers. The signals from the instruments are captured by a DAQ-card and processed using a PC. Off-line measurements are performed before and after testing to measure the dimensions of the chain components, surface roughness and hardness.

3   CONCLUSIONS

Conveyor chains with polymer rollers are widely used. Mostly because they are capable of working without any lubrication and have good corrosion resistance. From the study of the contact mechanics in a chain, the sliding contact between roller/bushing and rolling contact between roller and track were found to be the most wear critical areas. The wear mechanisms occurring with conveyor chain were listed. For conveyor chains with polymer rollers, the expected wear mechanisms are adhesive wear, abrasive wear, impact with sprocket and softening of the polymer due to heat generation. Existing test-rigs were found not suitable to examine the wear of conveyor chains with polymer rollers. Therefore a new test-rig was designed. The design constraints for the normal load and conveying velocity were obtained from the pressure-velocity limit of frequently used polymers. The breaking load of the chain was used to determine the tensile force in chain. Experiments performed on this test-rig will give better correspondence with the wear mechanisms occurring in real conveyor chain applications.

4   NOMENCLATURE

p	pressure	MPa
v	velocity	m/s
μ	coefficient of friction	-
K	specific wear rate	mm³/Nm
F_t	tensile force inside chain	N
F_n	normal force applied on chain	N
ΔT	additional tensile force due to resistance	N
O_i	origin of local coordinate system of component i	-
e_{ij}	eccentricity of component i versus j	m
F_{ij}	force from component i on j	N
T_{ij}	tangential force of component i on j	N
N_{ij}	normal force of component i on j	N
R_i	radius of circle i	m
b	rolling resistance coefficient	mm

5   ACKNOWLEDGEMENTS

6   REFERENCES

[1]   American Chain Association, J. Wright, *Standard Handbook of Chains - Chains for Power Transmission and Material Handling, Second Edition*: CRC Press, 2006.

[2]   U.S. Tsubaki, Kyosuke Otoshi, *The complete guide to chain*, 1997.

[3]   Renold, "Renold Syno," Wythenshawe, Manchester, 2010
       URL: http://www.renold.com/Products/TransmissionChainSprockets/RenoldSyno.asp.

[4]   Igus, "Iglidur - application examples - conveyor chains," Köln, Germany, 2010
       URL: http://www.igus.com/wpck/default.aspx?PageName=APP_TRANSPORTCHAIN&CL=GB-en.

[5]   Tsubakimoto chain co., *Lambda chain*. Japan, 2009.

[6]   Matweb.com material property data, "DuPont Delrin Acetal, homopolymer, unfilled, extruded," 2010.

[7]   Matweb.com material property data, "Quadrant EPP Acetron GP Acetal, unfilled, porosity-free copolymer acetal, extruded," 2010.

[8]   Matweb.com material property data, "Quadrant EPP 101 Nylon66, unfilled, extruded," 2010.

[9]   Matweb.com material property data, "Quadrant EPP Ketron PEEK 1000 Polyetheretherkethone, unfilled, extruded," 2010.

[10]   A. van Beek, *Advanced engineering design - Lifetime performance and reliability*: TU Delft, 2009.

[11]   Renold, "Renold Conveyor Chain Catalogue," Wythenshawe, Manchester, 2010
       URL: http://www.renold.com/Support/Catalogue_Download/Chain-Literature.asp.

[12]   Wikipedia, "Wear," Wikimedia Foundation, Inc., 2010
       URL: http://en.wikipedia.org/wiki/Wear.

[13]   Renold, "Renold Chain Troubleshooter," Wythenshawe, Manchester, 2010
       URL: http://www.renold.com/Support/Chain_Troubleshooter.asp.

[14]   S. J. Radcliffe, "Wear mechanisms in unlubricated chains," *Tribology International,* vol. 14, pp. 263-269, 1981.

[15]   P. K. D. J. S. Burnell-Gray, *Surface engineering casebook: solutions to wear and wear-related failures*: Woodhead publishing limited, 1996.

[16]   C. R. F. Azevedo, D. Magarotto, and A. P. Tschiptschin, "Embrittlement of case hardened steel chain link," *Engineering Failure Analysis,* vol. 16, pp. 2311-2317, Oct 2009.

[17]   R. E. Melchers, T. Moan, and Z. Gao, "Corrosion of working chains continuously immersed in seawater," *Journal of Marine Science and Technology,* vol. 12, pp. 102-110, Jun 2007.

[18]   P. de Baets, *Slides of the course: Machine design*. Ghent: University of Ghent, 2010.

[19]   Technische Universität Chemnitz - Fakultät für maschinenbau, "Kettenprüfstände," Chemnitz, Germany, 2010
       URL: http://www.tu-chemnitz.de/projekt/Gleitketten/KZT/ps_kettenpruefstaende.php.

ABRASIVE WEAR OF LINK CHAINS

D. Van Steenkiste, S. Plasschaert, P. De Baets, J. De Pauw,
Y. Perez Delgado and J. Sukumaran

Ghent University, Laboratory Soete, Belgium

Abstract   Link chains are widely used in many different sectors of industry, for example in hoist applications, marine applications, manure chains in agricultural applications, snow chains for cars or even as a bicycle lock. A more specific application is the tickler chain, where the link chain is used to drag over the seabed in order to increase the catch rate. In this case the link chain is subjected to extreme abrasive wear due to the sand and seawater environment. Fracture of these chains causes serious economical damage due to downtime and especially production loss. The main objective of this research is to quantify the most important wear mechanisms that act on a link chain, and with that knowledge to try to design and build a reliable test rig that simulates abrasive wear of tickler chains. With these simulation results the chain parameters, such as geometry and material, can be improved in order to decrease the wear rate.

Keywords link chain, tickler chain, three-body abrasive wear, sand and seawater environment

1   INTRODUCTION

Chains are extensively used in many different sectors of industry. According to their intended use there exist two major chain types. The first type is designed for transferring power in machines, so the links need to mesh with the teeth of the sprockets. A well known example is the roller chain, which is used to drive the wheels in a bicycle. The second major type is designed for lifting, pulling or securing. Such link chains consist of a moving series of interconnected links or shackles, which are often torus-shaped and usually made of metal. These chains are used in bicycle locks, anchor chains, hoists, etc.

It is a well-known problem that link chains are susceptible to wear. Due to the applied normal force and the relative movement between the shackles the chain wears out. This wear leads to thickness reduction of the shackles, resulting in a loss of strength. This can cause chain fracture, to detrimental effect. For example, if the lifting chains of a hoist break dangerous situations could occur. For this reason they should be inspected thoroughly.

In marine industries the wear is not only caused by the relative movement of the shackles. Foreign particles from the general environment, like sand and small fragments of rocks, accelerate the wear mechanism. An example of the extreme wear on marine chains is shown in Figure 1. This chain was employed as a tickler chain in beam trawling, as shown in Figure 2. Several tickler chains and a fishing net are attached to a beam which drags over the seabed pulled by a fishing vessel. The chains plough through the seabed in order to scare the flatfish and drag them into the fishing net. Fracture of these chains causes serious economical damage due to downtime and production loss.
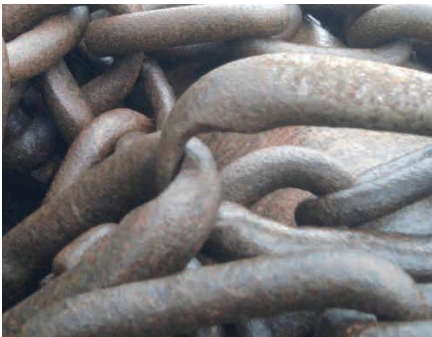

Figure 1: abrasive wear of link chains [1]

Figure 2: small model of a beam equipped with tickler chains [1]

In order to investigate abrasive wear some test rigs have been developed [2-4]. As these test rigs do not include the geometry of the wear contact, a reliable test rig to measure the wear of link chains doesn't exist yet. Furthermore there are no norms available. The main objective of this master thesis is to quantify the most important wear mechanisms that act on a link chain, and with those results try to design and build a reliable test rig that simulates abrasive wear of tickler chains. With these simulation results the chain parameters, such as geometry and material, can be improved in order to decrease the wear rate.

2   ANALYSIS OF WEAR ON LINK CHAINS

2.1   Chain wear mechanisms

To get a clear view of the different kinds of wear that can occur on a shackle, the most important wear mechanisms are shown in Figure 3. These wear mechanisms that act on the shackles can be divided in one-body, two-body and three-body wear, depending on the number of working bodies in the mechanism [5].

Figure 3: chain wear mechanisms

The most important one-body wear mechanism is particle erosion. In this wear mechanism little particles collide against the shackle itself. Because of the high amount of collisions, wear occurs. This kind of wear depends on several factors, such as the shackle hardness and the impact velocity of the colliding particles. A better known example is sandblasting, which is in fact controlled particle erosion.

For two-body wear there is a difference between abrasive and adhesive wear. Abrasive two-body wear occurs when a hard object ploughs through a softer object, due to an applied normal force and the relative movement of these objects. For chains in the marine industry this wear mechanism occurs as contact guidance wear, when the chains rub over the seabed. Adhesive two-body wear occurs between similar materials when there is a high contact load combined with a small contact surface. Because of the very high contact pressures micro-welding of the roughness peaks is possible. This in combination with the relative movement will cause surface degradation. For link chains this wear mechanism can take place in the shackle contact.

During three-body abrasive wear, a hard particle comes in between two objects. Due to the relative movement of these objects and an applied normal force the hard particle acts as a cutting material. For link chains this wear mechanism occurs in the shackle contact, when sand and fragments of rocks get lodged in between the two shackles. When this foreign particle is harder than the shackles the wear rate increases significantly.

Another wear mechanism that can occur is corrosive wear due to the environment. For marine applications the chains are in seawater, which causes corrosive wear. This corrosive wear in combination with one of the other chain wear mechanisms creates excessive chain wear, which reduces the chain life significantly.

2.2 Environmental influences

Previous work on three-body abrasive wear of ductile metals concluded that the influence of the environment is very important, especially if the wear takes place under wet circumstances [2]. These three-body wear tests were carried out on a commercial lapping and polishing machine with different particle sizes and under wet or dry conditions.

Table 1 shows the difference in wear rate under different test conditions. Examination of the wear surfaces after dry tests suggested that the dominant wear type was three-body abrasive wear. For a particle size of 7µm under wet circumstances the three-body abrasive wear was considerably reduced. In this case the particles are no longer cutting in the surface, but they are rolling due to the hydrodynamic lift of the water. For the same wet test conditions with the larger particles of 60µm, the main observed damage mode was three-body abrasive wear. In this case the water acts as a lubricant, so the abrasive particles can cut very easily in the soft metal. This phenomenon increases the wear rate significantly compared to the dry circumstances. It can be compared with a milling process where some cutting oil is added in order to increase machinability.

Table 1: difference in wear rate under wet and dry three-body conditions [2]

	Dry circumstances	Wet circumstances Particle size: 7µm	Wet circumstances Particle size: 60µm
Three- body abrasive wear: sliding and cutting of the particles	Dominant wear type	Rolling of particles due to hydrodynamic lift	Dominant wear type
Friction	High	Reduced by water	Reduced by water
Wear rate	Medium	Low	High

Figure 4 shows the difference in wear rate for three-body abrasive wear of mild steel and particles of 60 µm under wet and dry conditions. It has been observed that the wear rate in the wet condition is much higher than in the dry condition for a high specific load. For marine applications the chains are embedded in a sandy environment (particle size +/- 60µm) and surrounded with seawater, so this observed phenomenon could explain why the link chains in the marine industry wear out extremely fast.

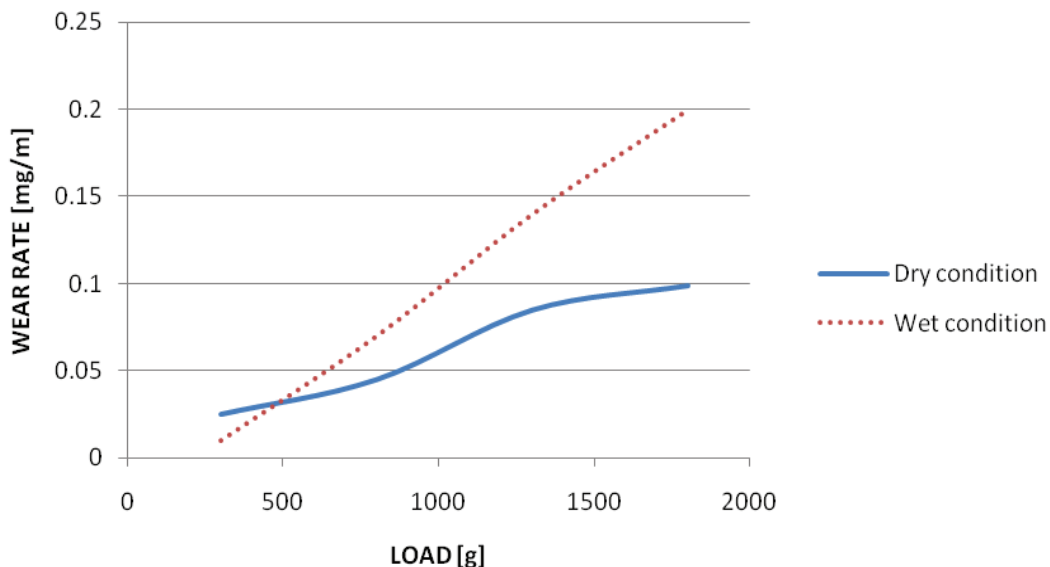Figure 4: Difference in wear rate of mild steel under wet and dry conditions with particle size 60µm [2]

3   TEST RIG

3.1   Existing wear tests

Figure 5 shows a well known pin on disk test. The pin on disc tester consists of a pin which is pressed against a rotating disc that contains the test material. The pin can be stationary or moved forward and backward, in order to create a spiral path. The normal load, rotational speed, and the wear track diameter can be set by the user in order to examine different test conditions. This standard test can be used to examine the two-body contact guidance wear on the outside of a shackle. The shackle should be mounted on the pin and then be pressed against the rotating disc that contains the sand particles. This would then be an easily set up extended application of the standard pin on disk tester in order to observe the two-body contact guidance wear. When the wear rate of a rougher surface needs to be quantified, for example a seabed full of stones, a variant of the pin on disk tester can be used. This type of tester is shown in Figure 6, where a metal sample is pressed against a rotating container which holds gravel or rocks.
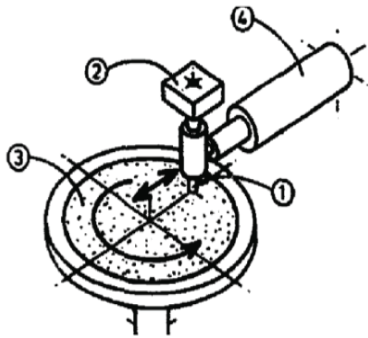
Figure 5: metal pin rubbed along spiral path across silicon carbide paper [4]

Figure 6: metal pin pressed against different kinds of gravel [3]

In recent years some small scale test rigs were designed at Laboratory Soete [6-9]. Four groups of four students were asked to build a test rig that simulated the wear of a tickler chain. Three test rigs used a closed chain cycle, as shown in Figure 7. In this case the chain is closed and is placed around a set of rotating wheels. One wheel is driven by a motor which lets the chain drag through a container filled with sand. With this type of test both two-body contact guidance and three-body shackle contact wear can be inspected. Another test rig used an open chain cycle, as shown in Figure 8. Three shackles are tensioned by a dead weight and eccentrically connected by a rod to a rotating disk. This ensures that the shackles move continuously up and down into a sand and seawater environment. This type of test rig focuses on three-body shackle contact wear, contact guidance wear cannot be evaluated.

Figure 7: closed chain cycle test rig developed at Laboratory Soete [7]

Figure 8: open chain cycle test rig developed at Laboratory Soete [8]

The main advantages and disadvantages of these two types of test rigs are summarized in Table 2. The main drawback of the closed chain cycle is the non-universality. Each different chain type and/or chain size requires a different set of rotating wheels, driving wheel and a connecting link. These test rigs are also heavily subjected to wear, which is not intended with a test rig. Despite these disadvantages both contact guidance and shackle contact wear can be evaluated in one single test rig, which is a great advantage. The biggest advantage of the open chain cycle test rig is the universality. The setup makes it possible to easily mount a different chain type and/or size. The test rig is also less subjected to wear and quite simple to construct.

Table 2: main advantages and disadvantages of test rigs designed at Laboratory Soete

	Closed chain cycle	Open chain cycle
Pro	- Both contact guidance and shackle contact wear	- Universal: easily mount different chain type and/or size
		- Simple
		- Test bench less subjected to wear
Contra	- Not universal: different chain types and/or sizes need different rotating wheels	- Only shackle contact wear
		- Reality?
	- High wear rate of rotating wheels	
	- Connecting link not always available	

3.2 Concepts

An important requirement of the test rig is that different parameters like shackle size, applied force, abrasive medium, etc. can easily be changed. For this reason the closed chain cycle test rig, as mentioned in paragraph 3.1, does not meet the requirements. The open chain cycle is a universal test rig concept, so it is quite obvious that this setup was chosen as a starting point. Because the two-body contact guidance wear can be examined with a simple pin on disk tester, the new test rig needs to focus on the three-body shackle contact wear. With this knowledge several test rig concepts were developed.

3.2.1 Generation of a running wave

The first concept was to generate a running wave in the chain, as shown in Figure 9. A running wave introduces relative movement of the shackles, which causes the three-body shackle contact wear in combination with a sand- and seawater environment. The wave is generated with a common crankshaft mechanism, while the required abrasive medium is transported by a screw of Archimedes.
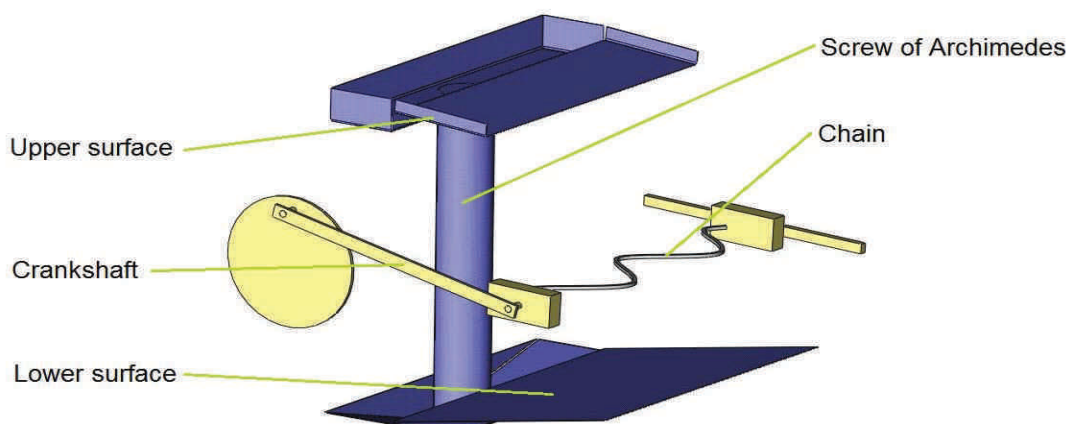
Figure 9: generation of a running wave

A big advantage of this concept is the good shackle movement that is introduced by the wave. Also the contact guidance wear can be inspected when the wave is generated on a plate. The main disadvantage is that the control of the different parameters is very difficult. For example, the applied force in the chain depends on the acceleration of the chain caused by the running wave, which is different for each shackle. Continuous wear measurement is also nearly impossible.

3.2.2 Torsional motion in shackles

Figure 10 shows the second concept which introduces a torsional motion in the chain. Three shackles of a link chain are clamped in between a fixed and a pulling axle. A rotating shaft is connected by two crankshaft mechanisms to these axles, which are pivoting. Because these axles are pivoting in the opposite direction, torsional motion is generated between the clamped shackles.
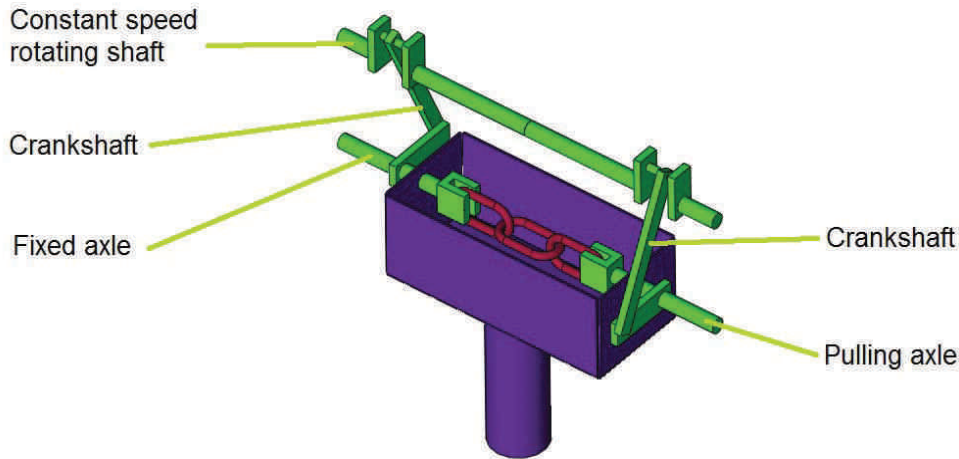
Figure 10: torsion in shackles

The main drawback of this test rig would be the introduced movement of the shackles, which is for small displacements of the crankshaft a pure micro-slip motion. Continuous wear measurement is possible by placing an LVDT on the pulling axle, which will move when the chain wears out.

3.2.3 Focus on shackle contact

The third concept consists of only two shackles that are tensioned by a dead weight, as shown in Figure 11. One shackle is connected to a rotating disk by a ball-joint, while the other one is fixed. This fixed shackle is prevented from rotating, so that it can only move in the direction of the applied force. For this type of test rig there are two possibilities: a vertical or a horizontal setup. In the vertical position (Figure 11, left) both shackles could be immersed in a sand and seawater environment. For the horizontal position (Figure 11, right) an external sand supply must be provided.
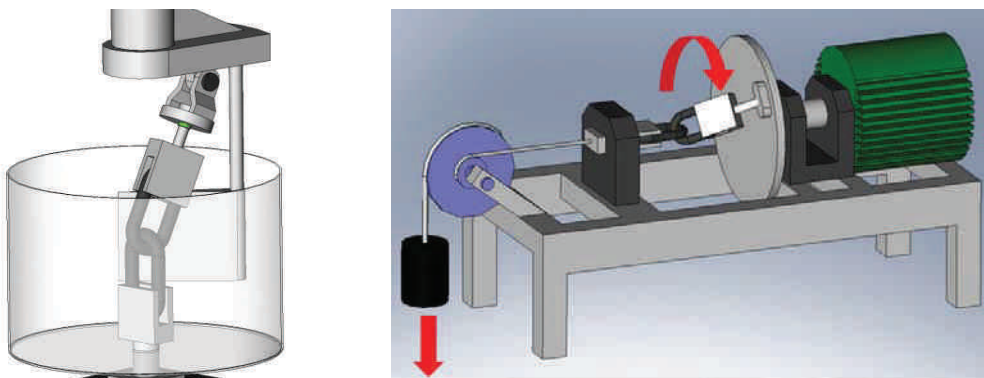
Figure 11: focus on shackle contact wear

The greatest advantage of this test rig concept is the probable high wear rate caused by the introduced rotating shackle motion. In this case continuous wear measurement is possible by placing an LVDT on the fixed shackle, which will pick up the displacement caused by the chain wear. For the vertical setup the abrasive medium can be held in a container. The main drawback of this solution is that the sand and seawater will not be continuously refreshed. In the case of the horizontal setup an external sand supply is necessary.

3.3 Link chain test rig developed at Laboratory Soete

The final test rig that was developed at Laboratory Soete is based on the concept from paragraph 3.2.3. This setup focuses on the three-body shackle contact wear, as the two-body contact guidance wear can be tested on a standard pin on disk tester. A detailed Solidworks-model of the complete test rig is shown in Figure 12. A horizontal setup was chosen (also shown in Figure 11), so an external sand supply is necessary.
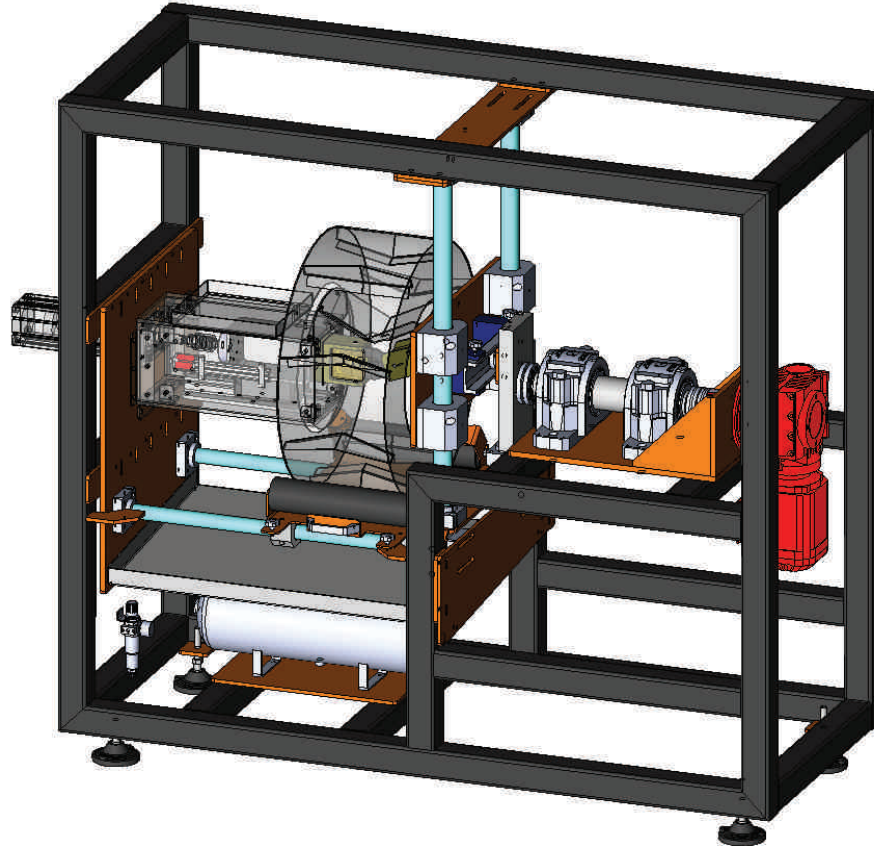
Figure 12: Solidworks-model of the test rig for link chains

The test setup can apply two different shackle motions, so that two different three-body shackle contact wear cases can be investigated. In the first case a circular shackle motion is introduced. One shackle of the link chain is fixed, while the other one makes a circular motion at contact speed. With a little modification a second type of motion, the plane motion, can be executed. In this case the motion-free shackle moves in a plane, so another wear surface is introduced. The additional effect of shackle-to-shackle impact on the three-body wear of the shackles can also be investigated. In this case the force is continuously applied and removed, so the shackles will impact with each other while they are in an abrasive environment. The design specifications of the test rig are summarized in Table 3. In the next paragraphs these different setups will be explained more in detail.

Table 3: design specifications of the test rig

Test rig for link chains: design specifications
Three-body shackle contact wear: - circular motion
- plane motion
- impact on shackle contact
Shackle sizes: d11-s33, d16-s45, d18-s64, d26-s92 (d=diameter, s=pitch)
Maximum tensioning force: 10kN
Continuous sand and seawater supply
Continuous measurement: - applied force
- displacement of the fixed shackle: wear investigation

3.3.1   Circular motion

Figure 13 shows a detail of the test rig set up for investigating circular motion. The fixed shackle is placed in a holder which is mounted on a linear guidance rail. This prevents the shackle from rotating, but allows a certain movement in the direction of the applied force. This tensional force is established by a high force pneumatic cylinder, which is connected to the fixed shackle by the linear guidance rail. On this linear guidance rail a load cell and an LVDT are mounted, so both the force and the displacement of the fixed shackle can be continuously measured. On the other side the rotating shackle is placed in a holder, which is eccentrically connected by a thrust bearing to a rotating shaft. This shaft is driven by a worm-wormgear motor reductor.
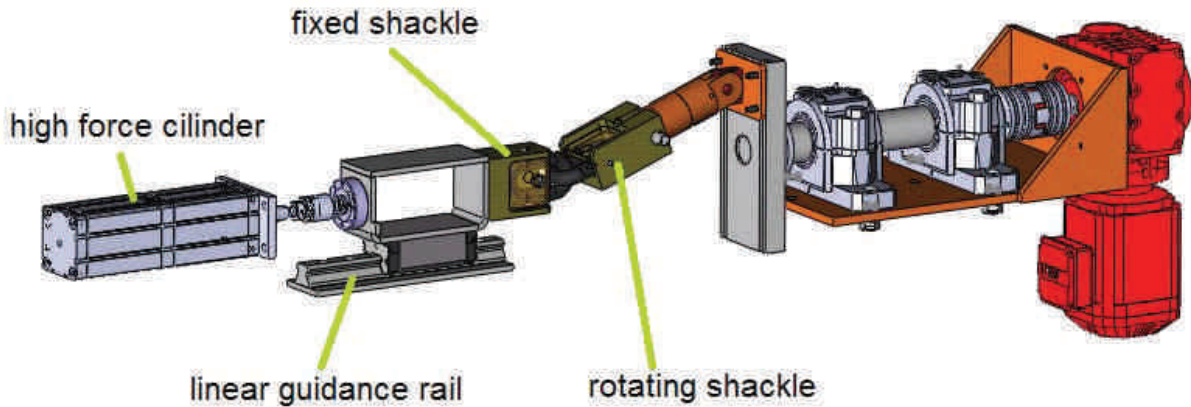
Figure 13: circular motion

3.3.2   Plane motion

For the second type of motion, the plane motion, a detail of the test rig is shown in Figure 14. The fixed shackle is connected to the pneumatic cylinder in exactly the same way as in the case of the circular motion. The only difference is the connection of the motion-free shackle to the motor. This shackle is now connected to a plate, which is placed on a linear guidance system. This plate performs a linear back and forth motion by an eccentric mechanism, which is driven by the motor reductor.
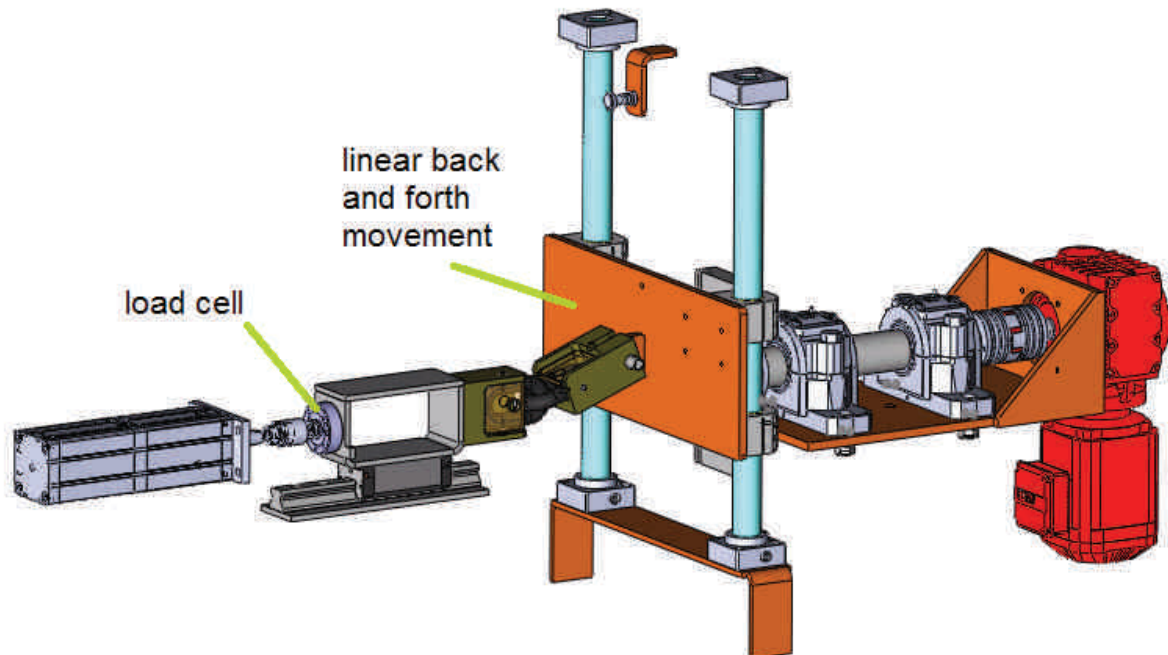
Figure 14: plane movement

3.3.3 *Sand supply*

As already mentioned in paragraph 3.3, an external sand and seawater supply is necessary to provide an abrasive environment around the mounted shackles. This is provided by a 'sand mill', from which the design is based on a concrete mixer. Figure 15 shows the 'sand mill' more in detail. The mixer, which is placed on a linear guidance system, is driven by a drum motor so it could rotate around its center. After it is filled with sand and seawater a homogeneous mixture is transported to the top, where it falls down into a funnel (not shown in Figure 15). This funnel guides the mixture to the desired location, so a continuous sand and seawater supply around the shackle contact is established.
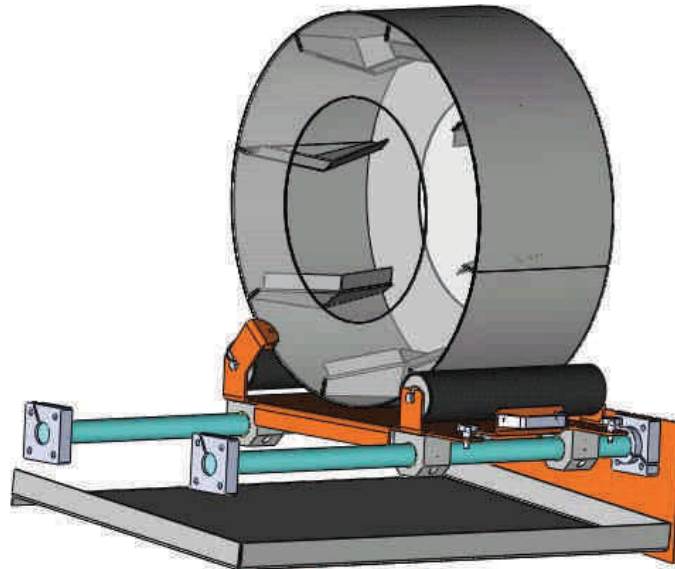
Figure 15: sand supply

4   CONCLUSIONS

The most important link chain wear mechanisms were identified and compared, showing that the two-body contact guidance wear and the three-body shackle contact wear are the most important ones for the link chain. Because the contact guidance wear can be easily investigated with a standard pin on disk tester, the new test rig should focus on the abrasive three-body shackle contact wear. With this knowledge a new test rig has been developed, in order to simulate the wear of a link chain. In the near future the test rig will be constructed so that multiple tests on link chains can be performed. With these simulation results the chain parameters, such as geometry and material, could potentially be improved in order to decrease the wear rate.

5   ACKNOWLEDGEMENTS

The authors would like to acknowledge the support of the ILVO Ostend. They provided the necessary data of the tickler chains (tensional force, dimensions, first estimation of the wear rate).

6   REFERENCES

1.   Plasschaert, S. and D. Van Steenkiste, *Visit ILVO Oostende.* 2010.
2.   Bingley, M.S. and S. Schnee, *A study of the mechanisms of abrasive wear for ductile metals under wet and dry three-body conditions.* Wear, 2005. **258**(1-4): p. 50-61.
3.   Terva, J., et al., *Abrasive wear of steel against gravel with different rock-steel combinations.* Wear, 2009. **267**(11): p. 1821-1831.
4.   Torrance, A.A. and T.R. Buckley, *A slip-line field model of abrasive wear.* Wear, 1996. **196**(1-2): p. 35-45.
5.   van Beek, A., *Advanced Engineering Design.* 2009. 517.
6.   Byltiauw, M., et al., *Simulatie Kettingslijtage.* Vakoverschrijdend project 2008-2009.
7.   De Witte, T., et al., *Simulatieopstelling voor kettingslijtage.* Vakoverschrijdend project, 2008-2009.
8.   Maselyne, J., et al., *Simulatie van slijtage van kettingen in abrasieve omstandigheden.* Vakoverschrijdend project, 2008-2009.
9.   Vanhulsel, P., et al., *Simulatie slijtage van kettingen.* Vakoverschrijdend project, 2008-2009.

IMPLEMENTATION OF AN UNLOADING COMPLIANCE PROCEDURE FOR MEASUREMENT OF CRACK GROWTH IN PIPELINE STEEL

K. Van Minnebruggen[1], D. Van Puyvelde[1], W. De Waele[1], M. Verstraete[1], S. Hertelé[1,2], R. Denys[1]

[1] Ghent University, Laboratory Soete, Belgium
[2] FWO (Flanders Research Foundation) aspirant

Abstract As the demand for fossil fuels increases, pipelines are constructed in inhospitable areas. Under these conditions, not only the strength but also the deformability of the pipelines becomes crucial. A strain based design (SBD) procedure needs to be established. Traditional stress based approaches to evaluate defect tolerance lead to conservative predictions. There is a need to accurately define the fracture toughness of the pipeline steel and assess the criticality of weld defects under strain based conditions. This paper focuses on the implementation of the unloading compliance method to determine stable crack growth. The standardized test procedure described in ASTM E1820 is applied. This method is a handy tool to obtain the J-resistance curves which can forecast ductile failure in pipeline girth welds. Preliminary experiments have been performed on Single Edge Notch Bend (SENB) specimens of plain pipe metal. Using the implemented procedure, it was possible to obtain a good fit between calculated and measured crack size. The most important result is the smoothness of the calculated crack growth and the rather monotonic increase of crack size. Since testing on SENB is well known to provide conservative measurements, Single Edge Notch Tension (SENT) specimens will be evaluated in future work.

Keywords Strain based design, Unloading Compliance method, crack growth, resistance curve

1   INTRODUCTION

Conventional pipeline design is based on a so-called stress design approach, which limits the applied stress to a prescribed fraction of the material's minimum specified yield strength. Recently built pipelines often have to traverse challenging environments, featuring hazards such as permafrost, seismic, land slide prone terrains, or require operations with extreme thermal/pressure fluctuations [1]. These situations could cause a longitudinal plastic deformation beyond the pipe's yield strain allowed by the limits in the commonly used design codes and standards [2, 3]. Therefore, a strain based design approach, which allows a certain amount of plastic strain, is more suitable. This is particularly true for applications where the loading is displacement controlled and the maximum resulting strain is bounded. For example, such displacement controlled plastic straining of pipes occurs in pipe reeling and laying [4].

Welding pipes together unavoidably involves the presence of weld defects. It is not possible to detect or accurately size all defects with non-destructive inspection, and due to economical reasons these cannot all be repaired. Moreover, some defects can possibly be tolerated based on fracture mechanics assumptions. To determine a maximum allowable defect size,   accurate knowledge of material properties, and specifically fracture toughness is needed. In strain based conditions, the defective weld will be subjected to high plastic strains and ductile tearing will inevitably occur. For such problems the fracture resistance curve, i.e. the relation of toughness versus ductile crack growth, has to be determined. A material's fracture resistance curve displays the energy needed (*J*-integral) for a certain crack extension (Δa). This curve can be combined with the crack driving force (CDF) curve. The CDF expresses the applied energy for varying crack lengths at a given load level (displacement or force). This CDF curve can be determined by either finite element analysis (FEA) or analytical solutions [5, 6]. A comparison of both curves results in the maximum applicable load before unstable failure occurs. In Figure 1 this maximum load corresponds to the load level P_3.

This paper focuses on the experimental determination of ductile crack growth and resistance curves. Preliminary Single Edge Notch Bend (SENB) tests have been performed on plain pipe material. Although these tests are widely known to give over conservative predictions when applied to pipeline design [7, 8], the economical benefits in terms of test rig capacity and needed material make the SENB test very suitable for the evaluation of the implemented method for characterization of ductile crack growth.
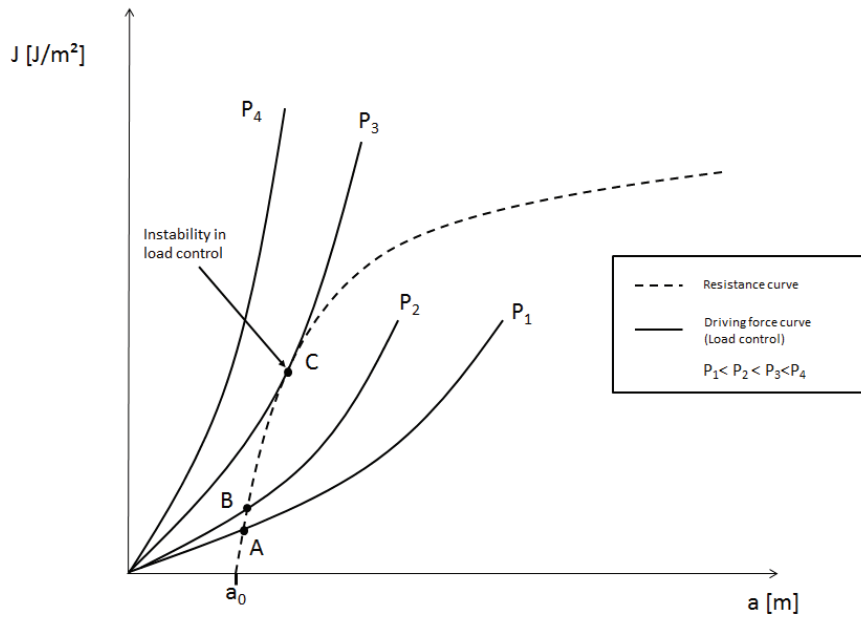
Figure 1: Fracture resistance curve (dashed line) and crack driving force curves (full lines) to determine the maximum allowable load.

2   THE UNLOADING COMPLIANCE PROCEDURE

Several methods are available to determine ductile crack growth, for example the potential drop method [9] or the silicone replica technique [10]. Another frequently used technique is the unloading compliance (UC) method. This standardized method is explained in detail in the following subparagraphs.

2.1   Background

The compliance, C, can be defined as the inverse slope of the elastic unloading part on the load vs. displacement curve, shown in Figure 2.
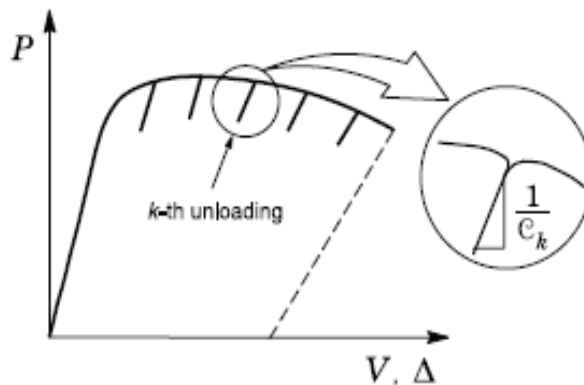
Figure 2: The compliance at the k-th unloading cycle [11].

By partially unloading the specimen at a certain deformation level, it is possible to calculate the slope of the load versus displacement curve at this elastic unloading part. The inverse of this slope is defined as the compliance. The displacement used in the load vs. displacement curve can be defined either as the load-line displacement (LLD or Δ) or as the crack mouth opening displacement (CMOD or V).

When the crack grows, the stiffness will reduce, resulting in an increase of compliance. Therefore, the evolution of this parameter is unambiguously associated with the increase of crack depth. Furthermore, the area below the load-displacement curve determines the stored energy, the J-integral. Both crack length and J-integral can then be used to construct the material's fracture resistance curve [11].

2.2 Testing procedure

2.2.1 ASTM E-1820

An UC procedure for SENB tests is described in the ASTM E1820 standard [12]. This procedure can be divided in five steps, described below.

The first step, is the fatigue pre-cracking of the specimen to obtain a realistic initial crack geometry with a very sharp crack tip. Fatigue pre-cracking is done by cyclically three point bending a bluntly notched specimen according to the standard BS 7448-1 [13].

The next step is the quasi-static loading of the specimen up to an initial force, P_m, within three minutes. This initial force is calculated by:

$$P_m = \frac{0,5\ B\ b_0^2 \sigma_Y}{1000\ S} \tag{1}$$

Where B, b_0 and S are shown in Figure 6, and:

$$\sigma_Y = \frac{\sigma_{UTS} + \sigma_{YS}}{2} \tag{2}$$

The third step consists of three or more (to get an indication of statistical scatter) quasi-static unloading/loading cycles in the elastic zone. Based hereon the initial crack length can be determined, which will be validated after opening the specimen once the test is completely finished. More elastic cycles will improve the accuracy and will provide a reliable value for the measurement errors.

The fourth step consists of a number of quasi-static unloading/loading cycles in the plastic zone. Each cycle is performed at the next initially determined CMOD value. These unloading cycles will later be used to determine the ductile crack extension. One such cycle in the plastic regime exists of CMOD growth, relaxation of the specimen, unloading of the specimen and reloading stages. Between the unloading and reloading part it is possible to add a short pause.

A detailed description of the parameters determining the unloading cycles are described in the next paragraph.

The final step is to open the specimen and to determine the actual initial crack size, a_0, and the actual final crack size, a_{fin}. The crack lengths are measured at nine equally spaced points. No individual initial crack value shall differ from the mean by more than ±0.002W. The average of the two near-surface measurements must be combined with the other seven crack length measurements to calculate the total average:

$$a = \frac{1}{8}\left[\frac{a_1 + a_9}{2} + \sum_2^8 a_i\right] \tag{3}$$

Where a_i is the measured crack length at point i.

Choice of variables

This paragraph describes the most important variable parameters, which are left to the experience of the user. The parameter values used in this work are stated.

Range of unloading: ΔP (Figure 3), The range for the unloading/loading cycle should be large enough to accurately determine the slope. Therefore a range of $0.5\ P_m$ is used, a smaller range could give more inaccurate results.

Increment size CMOD: ΔCMOD (Figure 3), Between each plastic cycle there is a CMOD increment. A minimum of 8 cycles is required before reaching maximum force. Because it is difficult to accurately determine the resistance curve for small crack growth, initially a small CMOD step is needed. But, to limit the time for tests which reach a large eventual CMOD, it is advisable to increase the increment size with a factor of two after every ten cycles.

> For the test described in §3, following settings were used: three groups of ten cycles using a ΔCMOD step of respectively 0.04mm, 0.08mm and 0.16mm. The last group uses a ΔCMOD step of 0.32mm up to the end of the test.
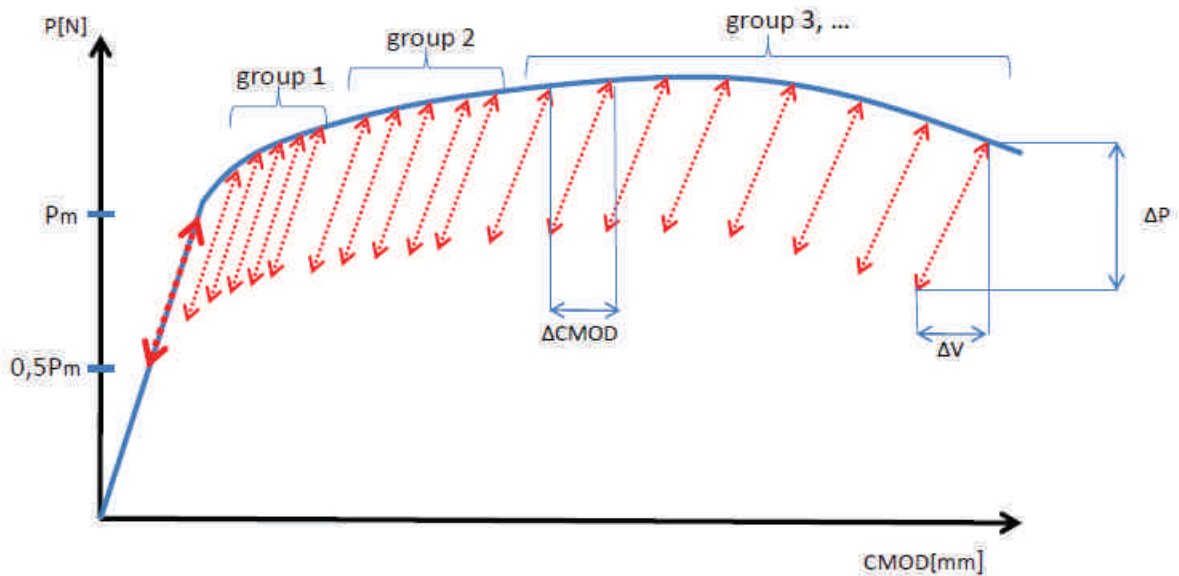
Figure 3: Illustration of unloading range *ΔP*, step size ΔCMOD and cycle division.

Speed of unloading/loading: By reducing the speed of one cycle, the measurement will be more accurate, but a maximum cycle time of 10 minutes must be met.

The speed is also variable during the test. During the elastic regime (step 3) and the following first two groups, the speeds of loading and unloading equal 0.12mm/min. For the further continuation of the test, the speed is doubled. In the first case, the average cycle time varies between 3 and 7 minutes, while the second approximately halves this value.

Pauses: A number of pauses can be implemented. At first, after the growth of the CMOD, a relaxation time is needed to avoid nonlinearity in the unloading slope. Two options are available for this relaxation. First, the specimen can be kept at a constant displacement. Alternatively, the force can be kept constant. Since this last option could possibly cause an unstable fracture, constant displacement is chosen. The length of this relaxation period depends on the used material [12]. For the pipeline steel used (see §3), a delay of 15 seconds was used. In a preliminary test a relaxation time of 30 seconds was used (Figure 4). The force relaxation during the first 15 seconds, $ΔP_1$, is significantly larger than during the following 15 seconds, $ΔP_2$. Therefore the relaxation time was set to 15 seconds to reduce the overall cycle time.

Figure 4: Force versus time graph with indication of 30s relaxation time and dominant procedure steps.

A second pause is introduced after unloading (hold at P_{unload}) to achieve a stable measurement of the minimum force. As shown in Figure 4, this pause is set at 10 seconds because the force does not change significantly.
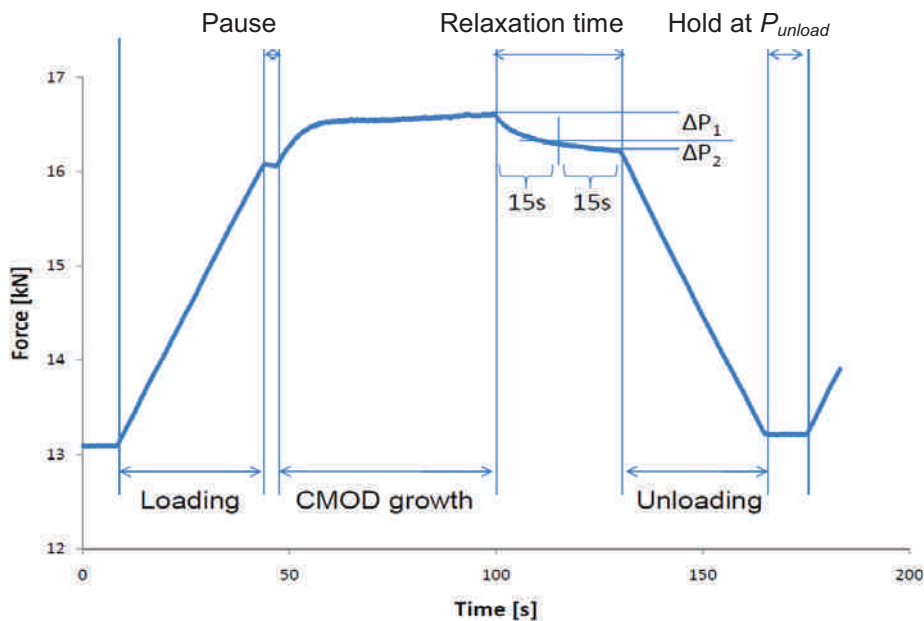
A last pause which can be introduced is a small pause after the loading. This pause is introduced for the stability of the controlling software. A couple of seconds will be sufficient.

2.3   Crack growth analysis

After performing this procedure, a graph analogue to the one shown in Figure 2 is obtained. Using these data, the compliance can be determined at every unloading cycle, indicated by C_k for the k-th cycle. For every cycle the maximum and minimum CMOD are determined. Afterwards, a mid-range of 75% of the partial unloading is kept to fit a linear function (equation 4) to the unload/load part. Figure 5 shows an example of this linear fit performed on a detail of the results shown in Figure 7.

$$force = a_k * CMOD + b_k \tag{4}$$

Since a_k represents the slope ($\Delta P/\Delta V$ in Figure 3) of the elastic unloading, the compliance C_k is the inverse of a_k. The compliance will be determined for both the loading and unloading stage, and are noted as respectively $C_{k,loading}$ and $C_{k,unloading}$. Based on these values an average compliance is then calculated:

$$C_{k,avg} = \frac{1}{2}(C_{k,loading} + C_{k,unloading}) \tag{5}$$
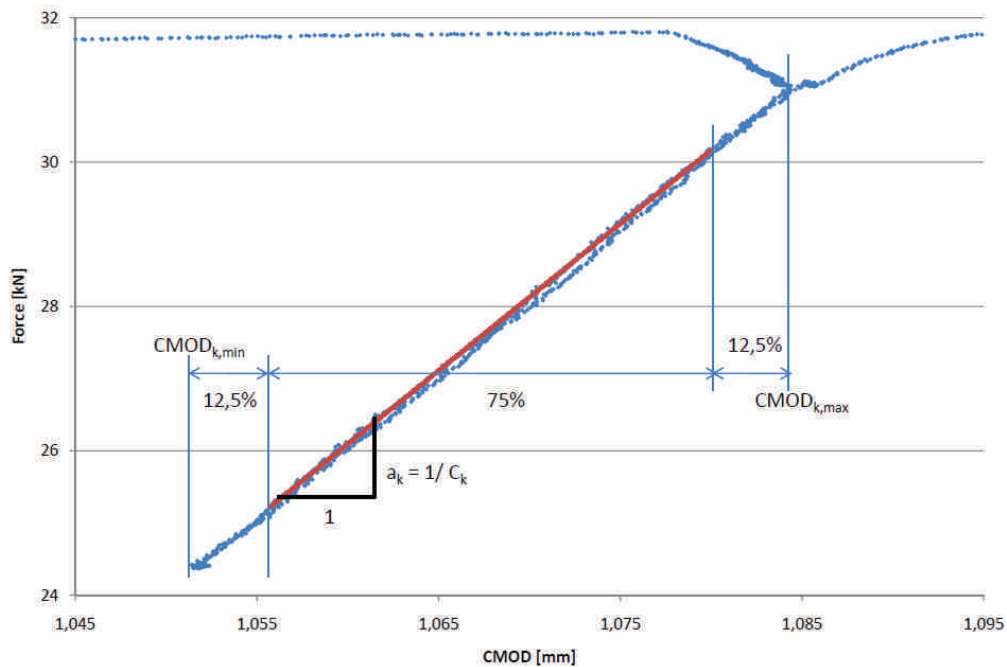
Figure 5: Detail of figure 7, with illustration of the linear fit to the elastic unloading.

In order to relate the compliance to an effective crack length, the following equation described in the ASTM procedure, is applied:

$$\frac{a_k}{W} = [0,999748 - 3,9504u + 2,9821u^2 - 3,21408u^3 + 51,51564u^4 - 113,031u^5] \tag{6}$$

with:

$$u = \frac{1}{\left[\dfrac{B_e\ W\ E\ C_k}{S/4}\right]^{1/2} + 1} \tag{7}$$

Where $B_e = B - (B - B_N)^2/B$ is the effective width and B_N the net width of the specimen. B_N equals B in absence of side grooves.

2.4   Determination of J-integral

The stored energy can be divided in an elastic and plastic part, respectively J_{el} and J_{pl}:

$$J = J_{el} + J_{pl} \tag{8}$$

where J_{el} is given by:

$$J_{el} = \frac{K_I^2}{E'} \tag{9}$$

With $E' = E/(1-v^2)$ for plane strain conditions.

The plastic component is related to the area under the load vs. displacement curve (A_{pl}) and the geometry of the specimen (B_N and $b_k = W - a_k$). This plastic component is defined by the following equation:

$$J_{pl} = \frac{\eta_{pl} A_{pl}}{B_N b_k} \tag{10}$$

The η-factor relates to the specimen geometry and loading condition. For a SENB test specimen this factor can be calculated as follows:

$$\eta_{pl(k)} = 3.667 - 2.199 \left(\frac{a_i}{W}\right) + 0.437 \left(\frac{a_i}{W}\right)^2 \tag{11}$$

3   EXPERIMENTS

3.1 Specimen and test description

The above procedure has been applied for SENB specimens, with global dimensions as shown in Figure 6. The material tested is a plain pipeline steel of grade X65. During the test, the CMOD has been measured with a clip gauge.
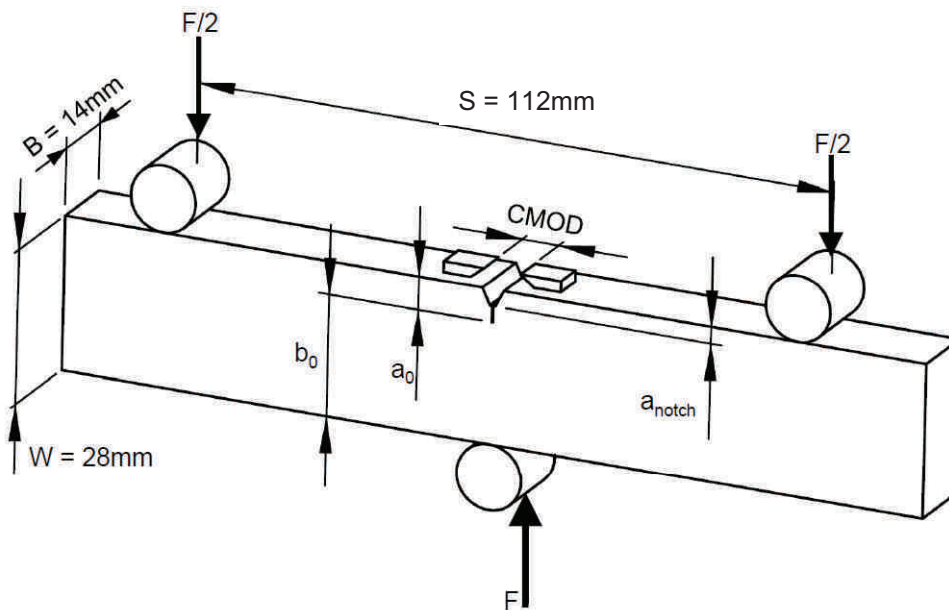
Figure 6: SENB test-specimen with basic dimensions.

During the experiments, the force and CMOD signals have been logged. The force displayed in the figures has a positive value even though it was a compressive force. Force versus CMOD measured during a representative experiment on a SENB specimen (Figure 6) with a_0 equal to 7mm is displayed in Figure 7. The two irregularities near the end of the experiment have been caused by subsequent pop-ins of the crack.
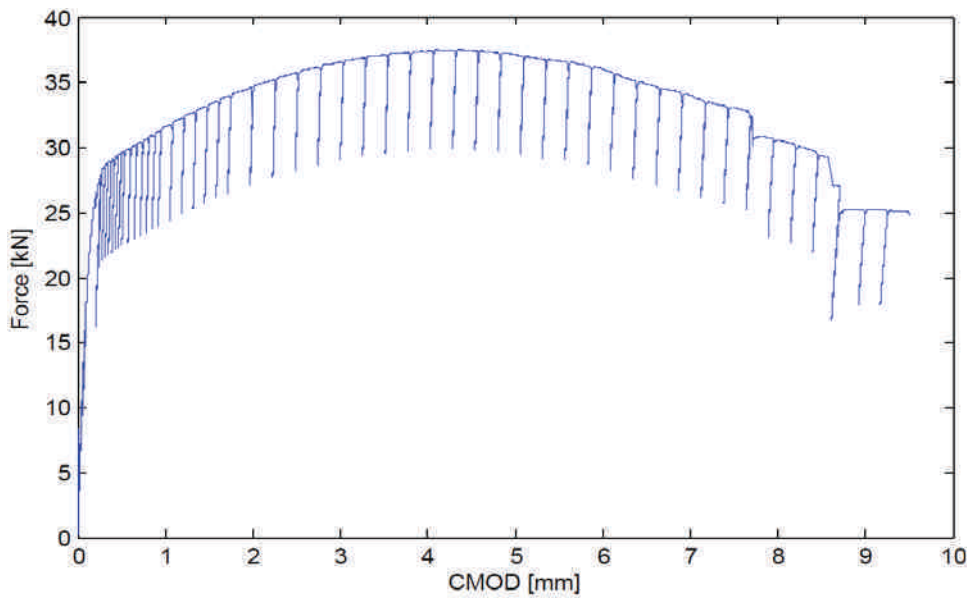
Figure 7: Load versus CMOD graph for a SENB-specimen test.

The unloading compliances C_k and crack length a_k are calculated as described in §2.3. Next the J-integral can be calculated according to §2.4. Once both crack growth and *J*-integral are known, the *J*-resistance curve can be constructed (Figure 8).

3.2 Discussion

The calculated average crack lengths are shown in Figure 8, in function of the unloading cycle number. Remark that the first six cycles took place in the elastic region, in order to estimate the initial crack size. Since no crack growth is expected during the elastic unloading cycles, the values for these first six compliances should be equal. Nevertheless, some scatter on the data is present. This scatter has been used to calculate a standard deviation which can be plotted to the distribution of the fracture resistance curve with a 95% probability. The most important observation is the smoothness of the calculated crack growth and the rather monotonic increase of crack length. This indicates the correctness of the procedure.
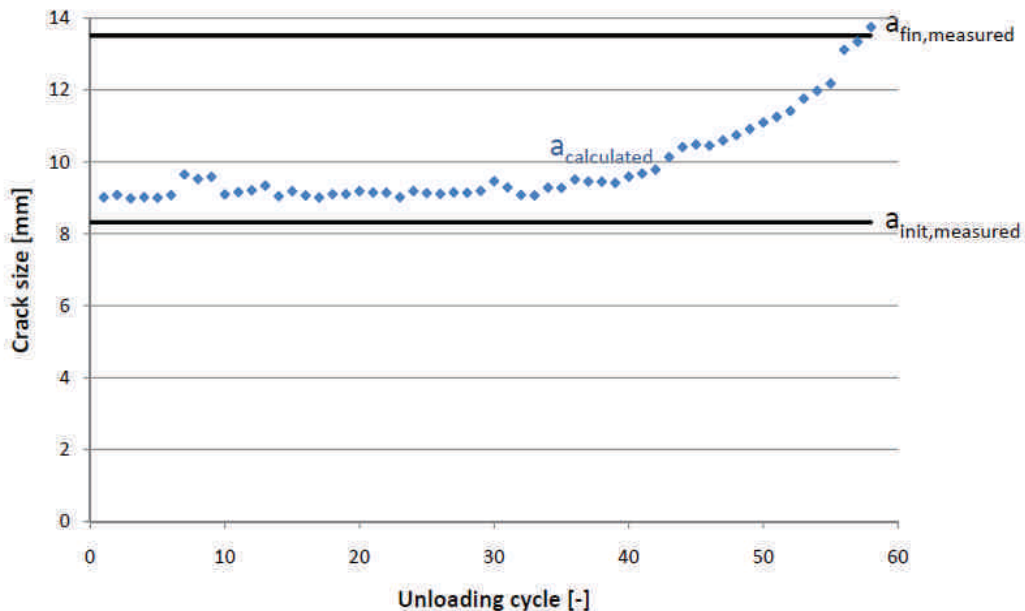
Figure 8: Calculated average crack size with indication of initial and final measured crack size.

The fracture resistance curve, showing calculated *J-integral* in function of calculated average crack growth, is shown in Figure 9. A best of the data is applied and yields the following analytical description:

$$J = 2154\,\Delta a^{0.457}$$

(12)
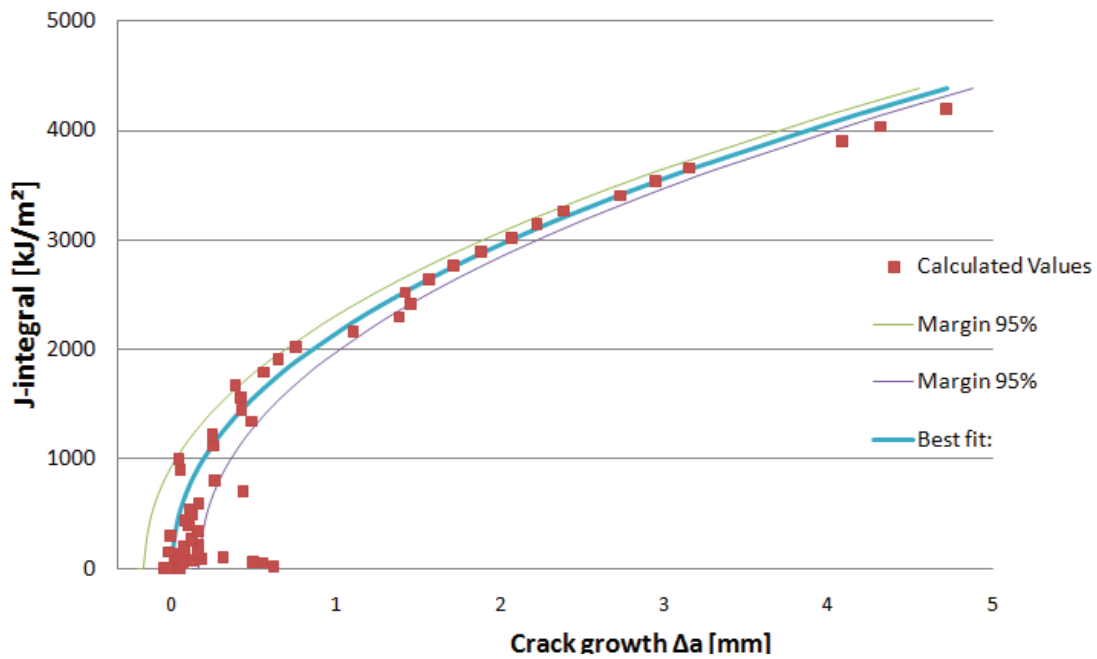
Figure 9: The fracture resistance curve with indication of a probability margin of 95%.

To evaluate the UC method, the calculated initial and final crack lengths are compared to the actual values. This comparison is performed after breaking the tested specimen in a brittle way by cooling them with liquid nitrogen. In Figure 10 a photograph of the broken SENB specimen is shown with the measure grid used to determine the initial and final crack length. Both lengths are determined with the nine points method described in §2.2.1.

It is clear that the fatigue crack line is not completely straight. The same problem occurs for the final crack size after ductile tearing. The main reason for the curved crack front is the increased constraint at the centre of the specimen. A possible solution to this problem could be the application of side grooves. According to the ASTM standard these side grooves promote a uniform crack growth [12].

Figure 10 shows the individual values of the nine measure points for the initial crack and final crack and for each side of the crack front. Their mean values were calculated with equation 3. The initial crack has an average length of 8.3 mm and the final crack an average length of 13.5 mm.
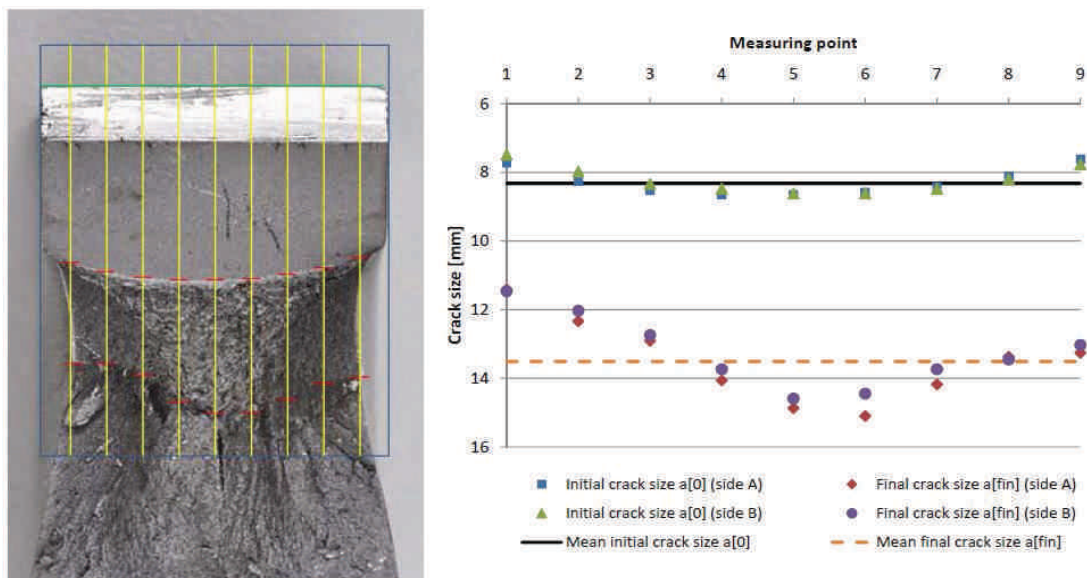
Figure 10: Determination of true crack size

These values are now compared to the ones calculated by the unloading compliance method (Figure 8). The first 6 unloading cycles yield the initial crack length, which is 9.0 mm. This is a difference of 0.7 mm compared to the measured value. This difference is attributed to the invalidity of the formulas (equations 6 and 11) because $a_0/W < 0.45$. The final values on the other hand are very similar, here the formulas are valid. The very curved crack front can also introduce a significant error in the measured final crack length, as described in §2.2.1.

4   CONCLUSION

The unloading compliance method has been implemented and shows to be a powerful technique to estimate the ductile crack length extension in a precise way. Furthermore, the *J*-integral can be calculated by this method. This makes it possible to determine the fracture resistance curve by combining the above two variables. One should take a number of parameters (such as hold times and range of unloading) into account. Improper parameter settings could influence the accuracy of the calculations. For example, a larger unloading range enables a better slope determination, and the relaxation time after CMOD growth is needed for avoiding nonlinearity in the unloading slope.

The results of preliminary experiments on SENB specimens (pipeline material) show a significant deviation of the crack fronts from a straight line. It is preferred to have a straight crack extension to obtain an unambiguous crack measurement. This could possibly be achieved when side grooves are used. In future work, more experiments will be executed on SENB and SENT specimens. The influence of side grooves will also be evaluated.

5   NOMENCLATURE

W	specimen thickness	mm	σ_{UTS}	ultimate tensile strength	Mpa
B	specimen width	mm	σ_{YS}	yield strength	Mpa
B_N	Net width of the specimen	mm	K_I	Stress intensity factor, mode I	$N/m^{3/2}$
a	crack size	mm	P_{min}	Minimal precracking force	kN
a_0	initial remaining crack size	mm	P_{max}	Maximal precracking force	kN
a_{fin}	final crack size	mm	P_m	Basic loading force	kN
S	support span	mm	E	Young's modulus	Gpa
b	remaining ligament	mm	v	Poisson's ratio	-
b_0	initial remaining ligament	mm	J_{el}	elastic part of J-integral	kJ/m²
			J_{pl}	plastic part of J-integral	kJ/m²

6   ACKNOWLEDGEMENTS

7   REFERENCES

1.   Lillig, D.B., *The First (2007) ISOPE strain-based design symposium – A Review*, in *International Offshore and Polar Engineering Conference*. 2008: Vancouver, Canada.
2.   Denys, R.M., et al., *EPRG Tier 2 guidelines for the assessment of defects in transmission pipeline girth welds*, in *International Pipeline Conference*. 2010: Calgary, Canada.
3.   API-1104, *Welding of pipelines and related facilities*. 2001, American Petroleum Institute.
4.   Mohr, W., *Strain-based design of pipelines*. 2003, EWI.
5.   Hertelé, S., et al., *Limit load and reference stress for curved wide plates*, in *International Pipeline Conference*. 2010: Calgary, Canada.
6.   Minnaar, K., et al., *Predictive FEA Modeling of Pressurized Full-Scale tests*, in *International Offshore and Polar Engineering Conference*. 2007: Lisbon, Portugal.
7.   Nyhus, B., M.L. Polanco, and O. Orjasaether, *SENT Specimens an Alternative to SENB Specimens for Fracture Mechanics Testing of Pipelines.* ASME Conference Proceedings, 2003. **2003**(36835): p. 259-266.

8. Pisarski, H.G. and C.M. Wignall, *Fracture Toughness Estimation for Pipeline Girth Welds.* ASME Conference Proceedings, 2002. **2002**(36207): p. 1607-1611.
9. Wilkowski, G., et al., *Using D-C electric potential for crack initiation / growth monitoring during testing of weld metal fracture specimens*, in *Pipeline Technology Conference*. 2009: Ostend, Belgium.
10. Ostby, E., *Fracture control – offshore pipelines JIP: Results from large scale testing of the effect of biaxial loading on the strain capacity of pipes with defects*, in *International Offshore and Polar Engineering Conference*. 2007: Lisbon, Portugal.
11. Cravero, S. and C. Ruggieri, *Estimation procedure of j-resistance curves for se(t) fracture specimens using unloading compliance.* Engineering Fracture Mechanics, 2007. **74**(17): p. 2735-2757.
12. ASTM-E1820, *Standard test method for measuring of fracture toughness.* 2006, American Society for Testing and Materials.
13. BS-7448-1, *Fracture mechanics toughness tests. Method for determination of Klc, critical CTOD and critical J values of metallic materials*. 1991, British Standard Institution. p. 48.

FAILURE BEHAVIOUR OF PRELOADED API LINE PIPE THREADED CONNECTIONS

J. Seys, K. Roeygens, J. Van Wittenberghe, T. Galle, P. De Baets and W. De Waele

Ghent University, Laboratory Soete, Belgium

Abstract – This paper reports on numerical and experimental work concerning the fatigue behaviour and sealing capacity of threaded pipe connections (1" API Line Pipe). Numerical simulations are performed using Abaqus® in combination with ThreadGen©. The fatigue life of a thick-walled standard coupling is determined using a four-point bending test. The corresponding S-N curve is compared to results of previous work on thin-walled specimens. It can be concluded that the standard thick-walled connection has a higher fatigue life than thin-walled ones. In future work, the prediction of fatigue life using established multi-axial criteria will be evaluated. Further, the sealing capacity of several couplings will be investigated by submitting them to different combinations of internal pressure and axial force. Hereto, a specific test setup is designed. The results will then be presented as a test load envelope [1].

Keywords – Threaded connections, API, fatigue, four-point bending, sealing limit, test load envelope, finite element analysis

1 INTRODUCTION

Threaded pipe couplings for joining tubular pipes have been used extensively in applications such as down hole casing, drill pipe strings and TLP tendons. An API line pipe connection consists of a male member, also known as the pin, which is made up into a female part, also known as the box. They have the advantage that they can be easily coupled and uncoupled. In offshore applications, connections can be subjected to cyclic loads, e.g. when drilling deviated wells or due to movement of oil platforms. In case of risers and drill pipes, fatigue is one of the most important failure modes. Since the highest stress concentration occurs at the root of the last engaged thread (LET, Figure 1) of the pin, fatigue cracks commonly initiate at this location. However, the fundamental knowledge on the actual crack initiation and propagation is still inadequate. To that purpose, studies of the fracture surface, based on the beach marking technique, will be carried out. Apart from fatigue, the thread sealing performance of thin- and thick-walled connections will also be investigated.

Threaded connections can be divided in two main categories, standard connections and premium connections. Standard API line pipe, casing and tubing connections are defined by the API 5B and API 5L specifications [2, 3]. Premium connections are designed to have a better fatigue strength and/or optimised sealing properties [4-7].

In this study, fatigue performance is experimentally evaluated using a four-point bending fatigue setup. The number of cycles which the coupling can sustain at a specified stress ratio and amplitude will be determined to develop S-N curves. Numerical simulations are carried out using the commercial software package Abaqus 6.10®. The input and output processing are automated by ThreadGen©, software developed at Ghent University. Results will be compared with previous work on thin-walled (pin thickness = 3,4 mm) standard and modified connections [4, 5]. An objective of this research is to determine the influence of the pin stiffness by carrying out research on thick-walled (pin thickness = 4,5mm) connections.

In future work, sealing performance will be examined by submitting the connection to load envelope tests as defined in ISO 13679 [1]. Test procedures for connection application level 1 (CAL 1) expose the connection to cyclical loads, including internal and external (water) pressure, and axial tension and compression. Failure occurs when the connection experiences leakage or a loss of structural integrity.

The ultimate goal of this research is to give guidance on coupling designs with an optimum combination of sealing capacity and resistance to fatigue failure.

2   FATIGUE BEHAVIOUR

2.1   Finite element modelling

To simulate the structural behaviour of threaded connections, a 2D axisymmetric model is used [8]. The model of the standardized API line pipe connection is shown in Figure 1(a). The connection has a nominal size of 1" according to the API 5B specifications. Other important properties for the thick-walled pin are listed in Figure 1(b).

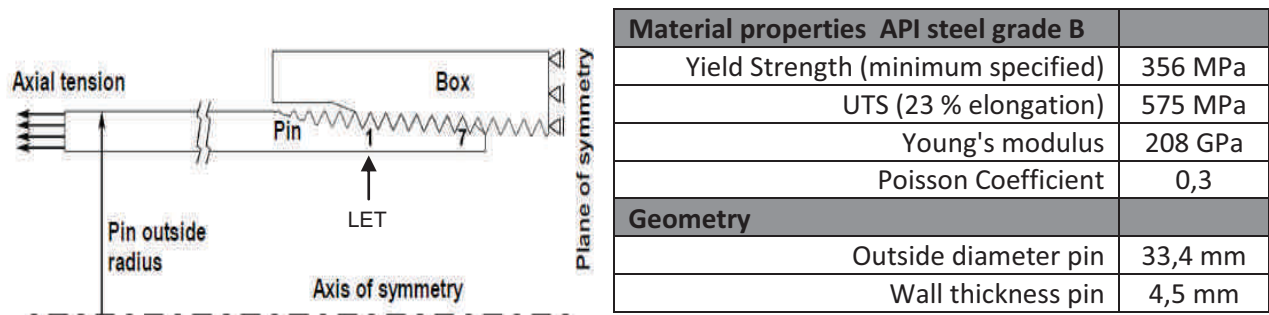| Material properties API steel grade B	
Yield Strength (minimum specified)	356 MPa
UTS (23 % elongation)	575 MPa
Young's modulus	208 GPa
Poisson Coefficient	0,3
Geometry	
Outside diameter pin	33,4 mm
Wall thickness pin	4,5 mm

Figure 1: a) 2D axisymmetric model of an API Line Pipe coupling, b) material properties and geometry

The analyses are carried out using the software ABAQUS® 6.10 and ThreadGen [9]. A fine mesh was seeded along the pin thread roots, since it is known that those locations are most susceptible for fatigue crack initiation. Hereto, four node bilinear axisymmetric quadrilateral elements with reduced integration (CAX4R) are used.

The finite element analysis consists of two consecutive load steps:

- To maintain a sealed and secured connection, the tapered members are preloaded with a make-up torque. For a thick-walled pin this corresponds with 2 make-up turns on top of a hand-tight situation. This is modelled by an initial overlap of the threads of pin and box.

- During the second step, an additional axial tensile stress up to 150 MPa is applied. The highest stress concentration appears, as already mentioned, at the root of the LET of the pin. This is mainly caused by an uneven distribution of the axial forces over the engaged threads.

The LET is the most common place where fatigue cracks initiate. When trying to improve the fatigue life of a threaded connection, one should try to obtain a more uniform load distribution and hence have a lower load and stress intensity factor at the LET. In previous research, this was attempted by a stiffness reduction of the box. However, it was found that it is not possible to simply state that a more uniform load distribution leads to longer fatigue life. Indeed, experiments on couplings with a reduced box wall thickness of 2mm did not reveal a longer fatigue life despite a more uniform load distribution (Figure 2) [4].

The load distribution of a standard thick-walled coupling is also included in Figure 2. The relative thread load reaches its maximum at the LET, which is the same as for a thin-walled coupling with a -5 mm recess, but has a less uniform distribution than the coupling with a reduced box wall thickness of 2mm. This result does not allow us to make correct fatigue life predictions, since experiments on standard thick-walled coupling resulted in the best fatigue life so far (see 2.2 Fatigue experiments).
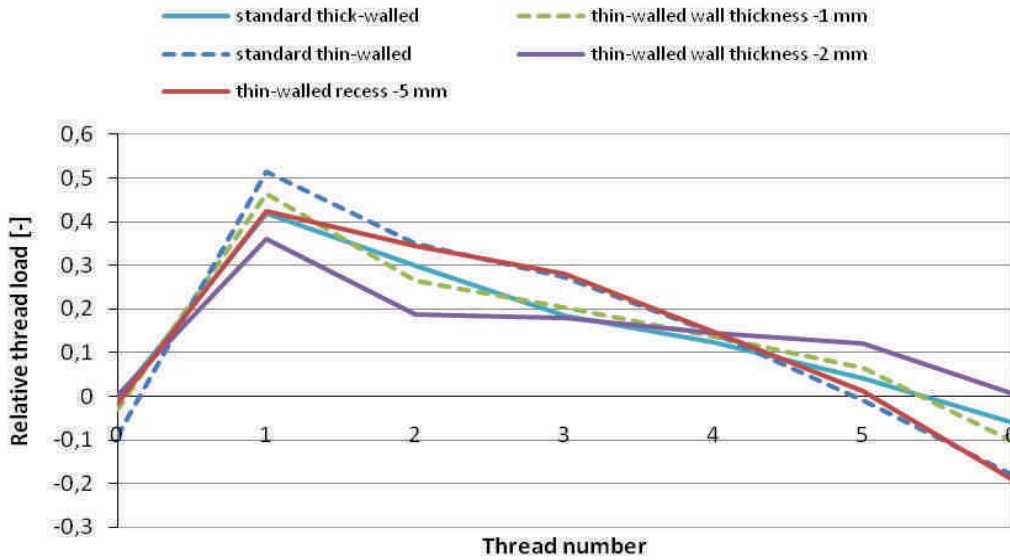
Figure 2: Thread load distribution (make-up and axial tension of 150 MPa) of standard and premium connections

It is well-known that stress multi-axiality plays an important role in fatigue life evaluation. For this reason, both the axial stress distribution and the tri-axiality (defined as in equation (1) [10]), are investigated.

$$R_v = \frac{2}{3}(1 + v) + 3(1 - 2v)\frac{\sigma_h^2}{\sigma_{vm}^2} \qquad (1)$$

In this equation σ_h is the hydrostatic pressure, σ_{vm} the von Mises equivalent stress and v the Poisson's ratio. A high tri-axiality has a positive influence on the fatigue resistance. Hydrostatic pressure has no effect on the occurrence of yielding. The greater the hydrostatic pressure compared to the von Mises stress, the smaller the deviatoric stress components that determine yielding behaviour. The axial stress and hydrostatic pressure of a thick walled standard connection are shown in Figure 3.

Figure 3: Stresses in a standard thick walled coupling subjected to make-up and axial tension of 150MPa
a) axial stress, b) hydrostatic pressure

Unlike Figure 3(a), where the tensile stresses are positive, in Figure 3(b) the compressive stresses are positive. It can be seen that at the LET, due to the high stress concentration, there is a high axial stress exceeding by far the 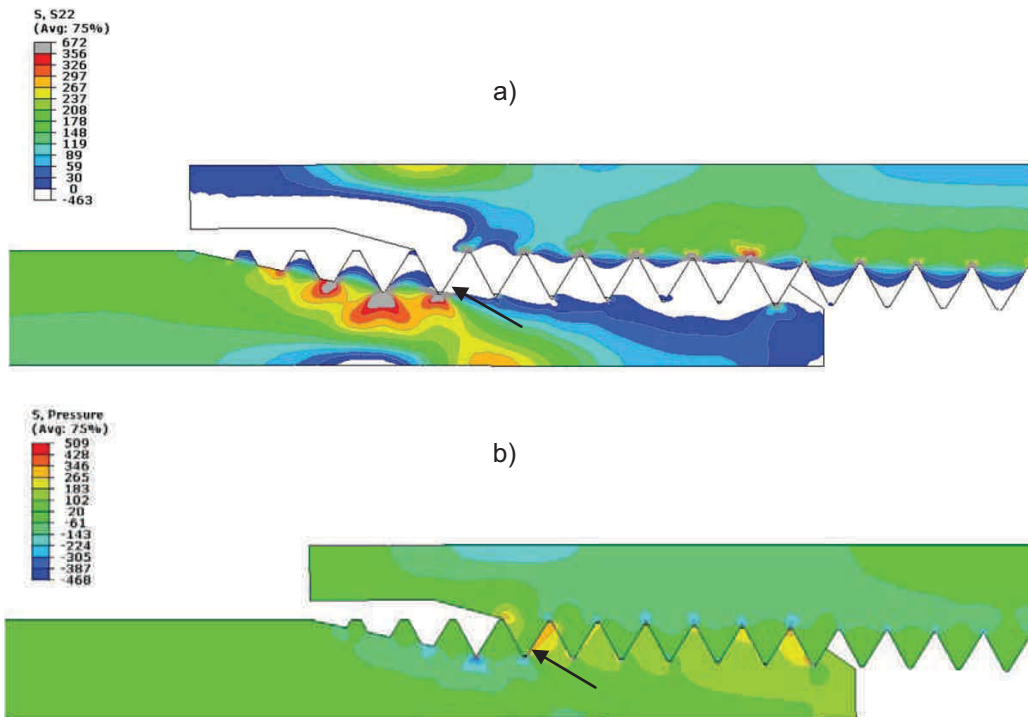minimum specified yield strength of 356 MPa. There is also a high hydrostatic pressure (negative so tensile stress) which gives in equation (1) a high value for the tri-axiality.

However, more research is necessary to provide a correlation with fatigue life. To this end, the multi-axial fatigue criterion (equation(2)) demonstrated in [6] will be used:

$$N_f = \frac{\Delta\sigma_{eq}^{-(\beta+m)} R_V^{-\beta/2}}{A(\beta+m+1)} \qquad (2)$$

In this equation, A and β are damage parameters and material constants, m is the strain hardening exponent of the coupling material ($m = 9.52$), $\Delta\sigma_{eq}$ is the difference between the maximum and minimum von Mises equivalent stress during a load cycle and R_V is the tri-axiality function as given in equation (1).

Previous research [6] showed that β 0 and (β + m)>0. As a result, high tri-axiality in combination with low von Mises stress amplitude results in high fatigue life prediction.

In Table 1, the values for different stresses at the root of the LET are listed. These have been determined by calculating their mean value along two fixed paths at the root of the LET (see Figure 4 &5). The different connections are organized by increasing fatigue life.

The path along the edge gives hopeful results. The standard thick-walled coupling shows a high tri-axiality in combination with a low von Mises stress (so also a low $\Delta\sigma_{eq}$). The thin-walled coupling with a reduced box wall thickness of 2 mm has a high tri-axiality, but experiences a high von Mises stress. So, even though no real fatigue life predictions are made, a trend arises between the multi-axial fatigue criterion and fatigue life. An additional improvement to determine stress values at the root of the LET might be to integrate over a well chosen area instead of integrating along a line path.
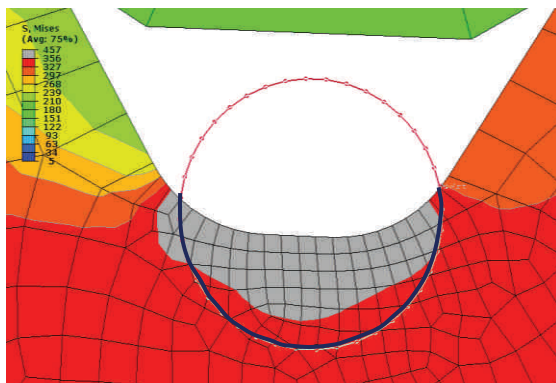
Figure 4: Circular path
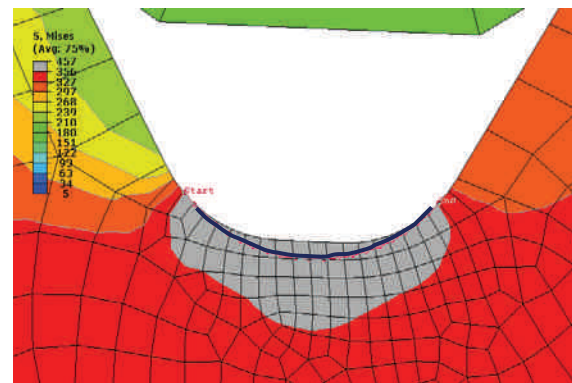
Figure 5: Path along edge

	Axial stresses		Von Mises stresses		Tri-axiality	
	circle	edge	circle	edge	circle	edge
Standard thin-walled	476	446	390	440	0,56	0,45
Thin-walled WT-2	541	451	390	453	1,00	0,48
Thin-walled WT-1	447	420	363	417	0,57	0,44
Thin-walled recess-5	473	438	389	437	0,58	0,45
Standard thick-walled	443	411	350	362	0,69	0,50

Table 1 : Stresses (MPa) and tri-axiality (-) at the root of the LET

2.2   Fatigue experiments

Fatigue performance is experimentally evaluated using a four-point bending setup (Figure 6), which ensures equal loads at both coupling ends. Tests are carried out under load control with a load ratio $R = 0,1$ and at a testing frequency of 15 Hz. When a fatigue crack grows through the wall thickness of a pipe, the applied internal pressure of 3.5 bar drops and the test is stopped.
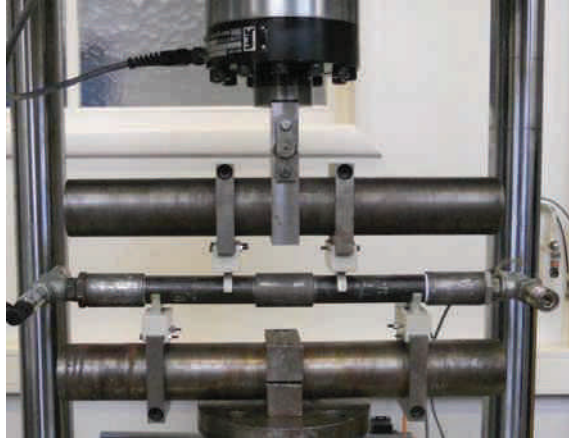
Figure 6: Four-point bending fatigue setup

Twelve tests on 1" thick-walled API line pipe couplings have been carried out. One specimen, loaded with a stress amplitude of 12,5% of the minimum specified yield strength, did not fail after 3 million cycles. The corresponding S-N curves are shown in Figure 7. The mean S-N curve is the best least-squares fit of all data points (equation 3). The design curve is equal to the mean curve minus two standard deviations. A fatigue limit of 2 million cycles is put forward.

$$S_a = 247{,}35 \cdot N^{-0{,}202} \tag{3}$$
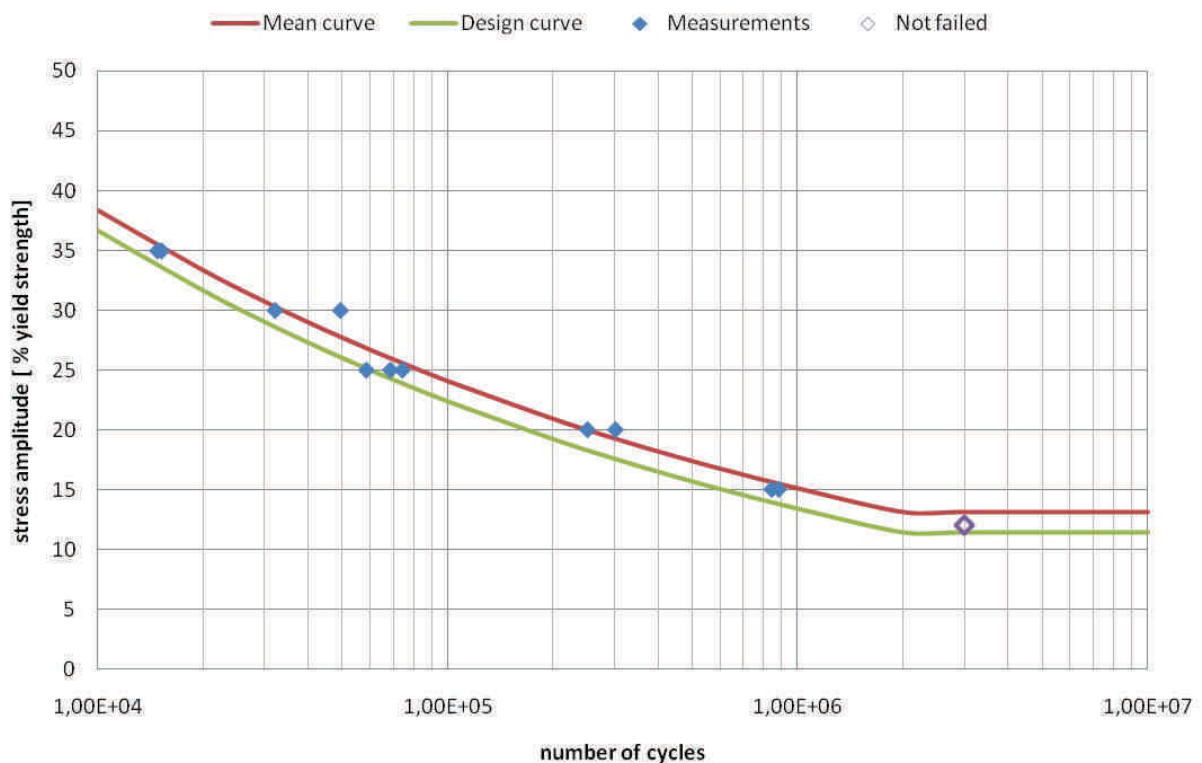
Figure 7: Experimentally determined S-N curves for standard 1" thick-walled API Line Pipe couplings.

In the figure below, the mean curve is compared with results for thin-walled standard and premium connections [4, 5]. The thick-walled connection shows an overall higher fatigue life. A pin with higher stiffness results in a better distribution of stresses.
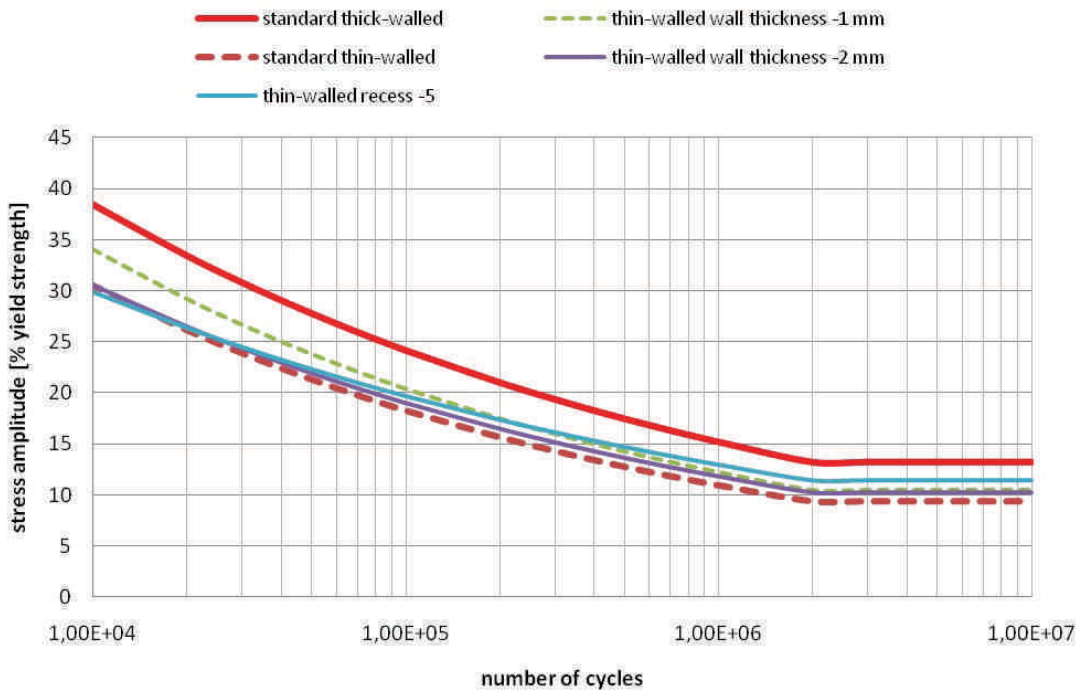
Figure 8: Comparison of S-N curves obtained for a standard thick-walled and for standard and premium thin-walled API Line Pipe couplings (1").

3 SEALING CAPACITY OF AN API LINE PIPE CONNECTION

3.1 Test load envelope

A connection's test load envelope is an indication of its sealing capacity. The envelope defines the boundaries of the combination of loads (axial force and internal pressure) within which the connection will maintain its structural and sealing integrity. Detailed procedures for testing are prescribed in the international standard ISO13679 [1]. The purpose of future research is to experimentally determine quadrant I and II of the test load envelope. Figure 9 shows an example of a test load envelope for a connection rated less than pipe body, which is the case for API line pipe.

Key
1   100 % VME pipe body yield envelope
2   100 % connection test load envelope
3   100 % API collapse
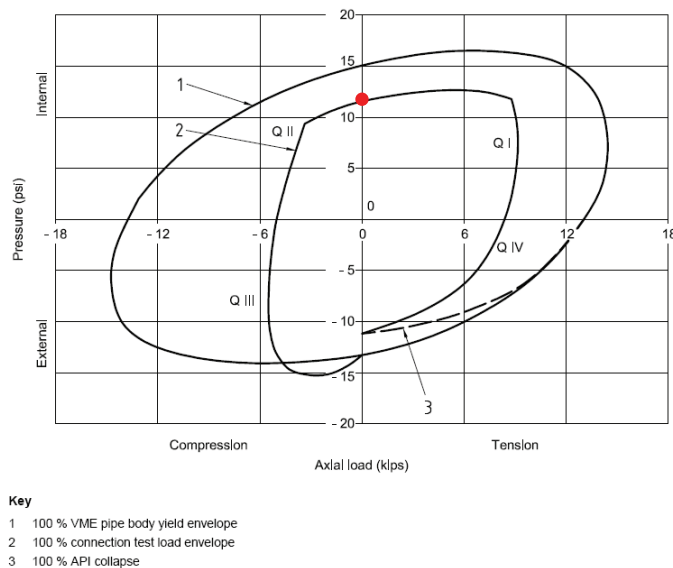
Figure 9: Test load envelope

The red point on the test load envelope will be determined by just increasing internal pressure (without axial load) until leakage or loss of structural integrity occurs (possibly up to 600 bar [11]). Other well-chosen combinations of internal pressure and axial force will be determined by carrying out experiments on the setup described in the next section.

3.2   Test setup

The test setup can be divided into two main parts, related to internal pressure and axial load. First, there is a supply pump to establish a water pressure (up to 600 bar) in the pipe connection. The corresponding pressures will be registered by a digital pressure sensor. Secondly, the pipe connection is mounted in a servo-hydraulic testing machine by means of specially designed adaptor pieces suited for both tension and compression. Deformations of the test coupon will be measured by strain gauges and digital image correlation. A schematic section of the setup can be seen below in Figure 10.
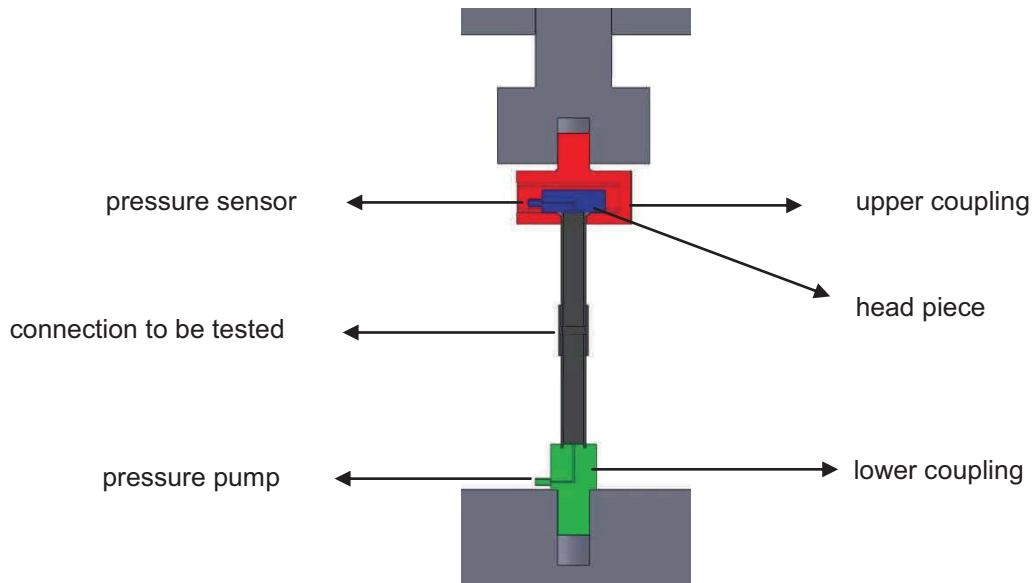
Figure 10: Section view leakage test setup

4   CONCLUSIONS

A 1" thick walled standard API Line Pipe coupling has a higher fatigue life as compared to standard and premium thinner walled connections. Numerical simulations have been performed in order to explain this experimental observation in a fundamental way. First evaluations of stress distribution over the connection and stress tri-axiality do not provide satisfying results. In the future the multi-axiality around the thread root will be studied in more detail using well-established multi-axial fatigue criteria.

A design for a leakage test setup is conceived and will be used to carry out experiments to determine the test load envelopes of different coupling configurations.

Further research should result in clear guidance on how to design threaded couplings with an optimal combination of sealing capacity and fatigue resistance.

5   NOMENCLATURE

API	American Petroleum Institute
CAL	Connection application level
LET	Last Engaged Thread
N_f	Fatigue life
R	Load ratio
R_v	Tri-axiality
$\Delta\sigma_{eq}$	difference between the max. and min. von Mises equivalent stress during a load cycle
S_a	Stress amplitude
TLP	Tension Leg Platform
v	Poisson's ratio
σ_{vm}	Von Mises stress
σ_h	Hydrostatic pressure

6 ACKNOWLEDGEMENTS

7 REFERENCES

[1]   ISO 13679, "Petroleum and gas industries - Procedures for testing tubing and casing connections," 2006.

[2]   API Specification 5B, "Specifications for Threading, Gauging and Thread Inspection of Casing, Tubing and Line Pipe Threads (U.S. Customary Units)," Fourteenth ed, A. P. Institute, Ed., 1996.

[3]   API Specification 5L, "Specifications for Line Pipe," Forty-second ed, A. P. Institute, Ed., 2000.

[4]   J. De Pauw, "Experimenteel onderzoek op geschroefde buisverbindingen," in *Mechanische constructie en productie* Gent: Universiteit Gent, 2009.

[5]   B. Meertens, "Experimenteel onderzoek naar het vermoeiingsgedrag van geschroefde buisverbindingen," in *Mechanische constructie en productie* Gent: Universiteit Gent, 2010.

[6]   J. Van Wittenberghe, J. De Pauw, P. De Baets, W. De Waele, M.A. Wahab, G. De Roeck, "Experimental determination of the fatigue life of modified threaded pipe couplings," *Procedia Engineering,* vol. 2(1), pp. 1849-1858, 2010.

[7]   M. Sugino, K. Nakamura and S. Yamaguchi,Sumitomo Metal Industries Ltd?, D. Daly, G. Briquet and E. Verger, Vallourec Mannesmann Oil & Gas, " Development of an Innovative High-performance Premium Threaded Connection for OCTG, Offshore Technology Conference, Houston, Texas, USA, 3-6 May, 2010

[8]   J. Van Wittenberghe, J. De Pauw, P. De Baets, W. De Waele, " Fatigue life assessment of preloaded API Line Pipe threaded connections", Fatigue design, Cetim, Senlis, France, 25-26 November, 2009

[9]   J. Van Wittenberghe, P. De Baets, W. De Waele, "Modelling of preloaded threaded pipe connections", Proc. of the 8th Nat. Congress on Theor. and App. Mechanics, 149-156, 2009.

[10]   M.M. Abdel Wahab, A.I. Ashcroft, A.D. Crocombe, S.J. Shax, "Prediction of fatigue tresholds in adhesively bonded joints using damage mechanics and fracture mechanics, J. Adhesion Sci. Technol., 15(7), 763-781, 2001

[11]   API 5C3 (ISO 10400), "Petroleum and natural gas industries - Formulae and calculation for casing, tubing, drill pipe and line pipe properties," 1993.

VALIDATION OF A WIDE PLATE FINITE ELEMENT MODEL USING DIGITAL IMAGE CORRELATION

K. De Keyser[1], F. Van Acker[1], S. Hertelé[2], M. Verstraete[3], W. De Waele[3], R. Denys[3]

[1] Ghent University, Belgium
[2] FWO Aspirant, Ghent University, Laboratory Soete, Belgium
[3] Ghent University, Laboratory Soete, Belgium

Abstract To investigate the influence of global plastic deformations on girth weld defect tolerance in pipelines, a parametric finite element model has been developed. This paper provides an experimental validation of the model. It describes the test setup and instrumentation used for the evaluation of plastic strain fields around a notch in a tension loaded non-welded X65 mini wide plate. LVDT measurements and digital image correlation (DIC) results are compared to each other and to the results of finite element simulations. Whereas some deviation is observed owing to unavoidable experimental uncertainties and limitations of finite element modelling, the overall correspondence is more than satisfying.

Keywords digital image correlation, unloading compliance, strain concentration, mini wide plate, finite element method

1   INTRODUCTION

As energy consumption is still increasing, more and more oil and gas sources are exploited in less accessible areas like arctic regions. Pipelines, connecting these sources with civilization, need to cross harsh environments and are thereby subjected to large deformations, for instance due to earthquakes or ground settlements [1]. These deformations exceed the deformations anticipated in stress-based design, usually limited to a maximum longitudinal strain of 0.5% [2]. For this reason, a so-called strain-based design is preferred over a traditional stress-based design.

An important aspect of this design methodology is that strain should not be concentrated in certain critical regions of the welded pipe. As weld flaws are inevitable, large strains must be avoided in their surroundings to prevent crack initiation and (un)stable growth.

Research at Laboratory Soete is focused on the deformation capacity and defect tolerance of pipeline girth welds in the context of strain-based design approach. This experimental based research is performed using so-called curved wide plate (CWP) tests. This can be described as a tensile test on a cut-out from a real pipeline, including a defective girth weld.

Recently, a parametric finite element (FE) model was developed, but experimental validation is required. Since CWP tests are expensive and large equipment is required, smaller test coupons, further called mini wide plates (MWP), offer satisfying accuracy and make tensile testing more convenient.

In this paper, such a mini wide plate test is thoroughly evaluated. The first section discusses the preparation of the specimen, the equipment and instrumentation that was used and the execution of the test. Afterwards, different measurement results are interpreted and compared to results of finite element simulations.

2   PREPARATION AND EXECUTION OF THE TEST

2.1   Specimen

A mini wide plate specimen was cut from an API 5L [3] X65 flat steel plate of 14.6 mm nominal thickness. A 25 mm long by 3 mm deep semi-elliptical surface crack was milled in the centre of the MWP. Blocks were welded to each specimen end for mounting purposes (Figure 1). The dimensions of the specimen are indicated in Figure 2.
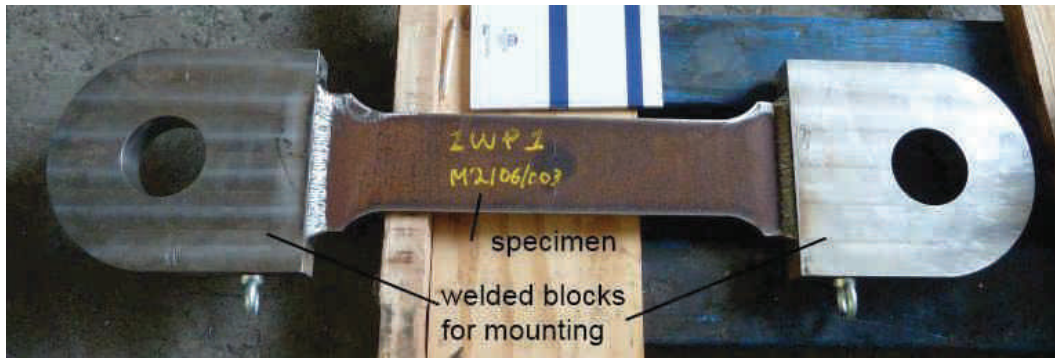
Figure 1: Test specimen with mounting blocks

2.2 Material

The stress-strain relation (average of 6 tensile tests) of the pipeline steel in the longitudinal direction is shown in Figure 3. The plate material exhibits discontinuous yielding behaviour with a pronounced Lüders plateau. The main tensile characteristics are listed in Table 1. Note that the yield-to-tensile stress ratio (*Y/T-ratio*) is defined as the ratio between 0.2% proof stress $R_{p0.2}$ and ultimate tensile stress R_m.

Table 1: Mechanical properties of API 5L X65 pipeline steel

upper yield point R_e	455.0MPa		ultimate tensile stress R_m	537.4 MPa
proof stress $R_{p0.2}$	433.5 MPa		uniform elongation e_m	16.1%
0.5% strain offset $R_{t0.5}$	433.5 MPa		yield-to-tensile ratio $R_{p0.2}/R_m$	0.83
Lüders elongation $e_{Lüders}$	2.62%			
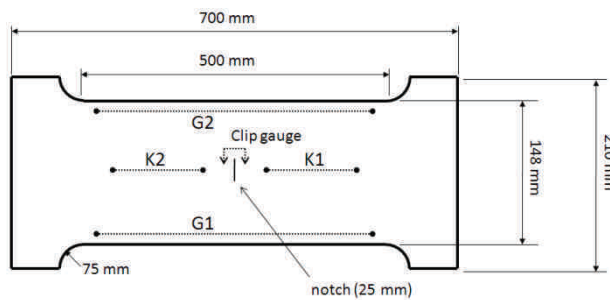
Figure 2: Geometry and mounting positions of measurement devices (figure not to scale)
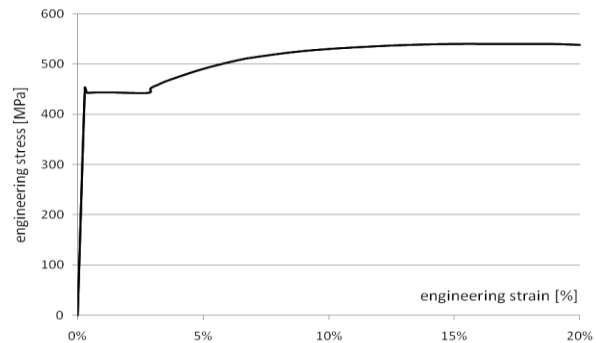
Figure 3: Longitudinal stress-strain curve of the material

For optical strain measurements, a randomly distributed speckle pattern was applied on the notched side of the specimen. The speckle pattern was obtained from a uniform layer of white spraying paint covered with spots of black lacquer paint. This pattern allows the Digital Image Correlation (DIC) camera system to track different regions of the MWP during the experiment. More information on this system is given in section 2.3.3. To avoid crumbling of the paint layer during the test, the corrosion layer on the specimen was removed in advance.

2.3 Test rig and measurement equipment

2.3.1 MTS test rig

A servo-hydraulic MTS universal test rig was used for this experiment. The system can exert a maximum force of 2500 kN and a maximum piston displacement of 150mm.

2.3.2 LVDTs and clip gauge

To measure the deformation at different locations of the specimen, 4 LVDTs were mounted on the backside of the specimen according to the UGent guidelines for CWP testing [4]. Two of them with gauge length 108 mm (K1 and K2) were located in the gross section of the specimen, away from the notch. The two other LVDTs (G1 and G2), with gauge length 388 mm, measured the elongation of the full prismatic section, traversing the defected section. Their position is indicated in Figure 2.

A clip gauge was put over the notch to measure the crack mouth opening displacement (CMOD).

2.3.3 DIC camera system

Digital Image Correlation (DIC) is an optical method in which the movement of speckle dots is tracked to calculate their displacement. From this displacement, strain fields on the surface of the specimen can be determined. In this experiment, a setup of two cameras is used to allow 3D vision, so out-of-plane deformations (eg. necking) of the specimen can be evaluated as well. Both cameras are synchronized and take one picture of 5Mpx every 10 seconds. A laptop with control and processing software also recorded the analogous force signal to allow for synchronization of the DIC and LabVIEW measurements.

A crucial element in the DIC technique is the size of the speckle dots. Dots should not be too small for the cameras to detect them. If they are too large, however, calculation accuracy is reduced. The speckle pattern shown in Figure 4 and Figure 5 did not introduce any correlation issues. The strain resolution was of the magnitude 0.1% strain.
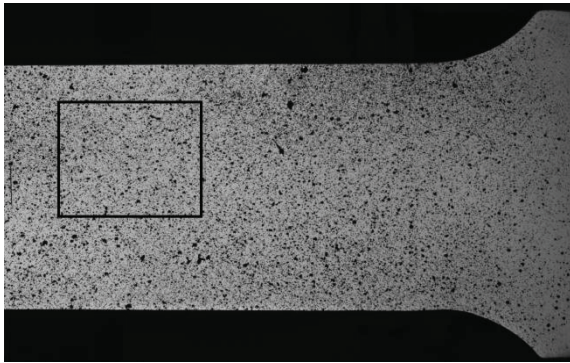
Figure 4: View of speckle pattern on half of the MWP specimen
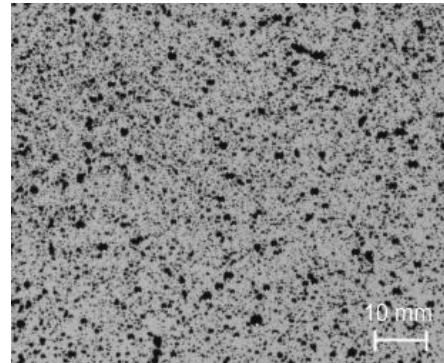
Figure 5: Detailed view of Figure 4.

2.4 Software

A LabVIEW program was developed to control the test rig. The software defines whether the test rig should load or unload the specimen or hold it in a fixed position, based upon measurements of CMOD and applied force. In fact, a simple tensile test would suffice to validate the FEM model, but it was opted to follow the unloading compliance method [5]. Unloading compliance is a technique whereby the specimen is sequentially loaded and unloaded, first in the elastic region, then in the plastic region. In the latter case, the unloading decision is based on a constant increment of CMOD. When plotting applied force as a function of CMOD, as in Figure 6, different loading and unloading cycles can be seen. From the slope evolution of the unloading and reloading cycles, crack size can be determined.
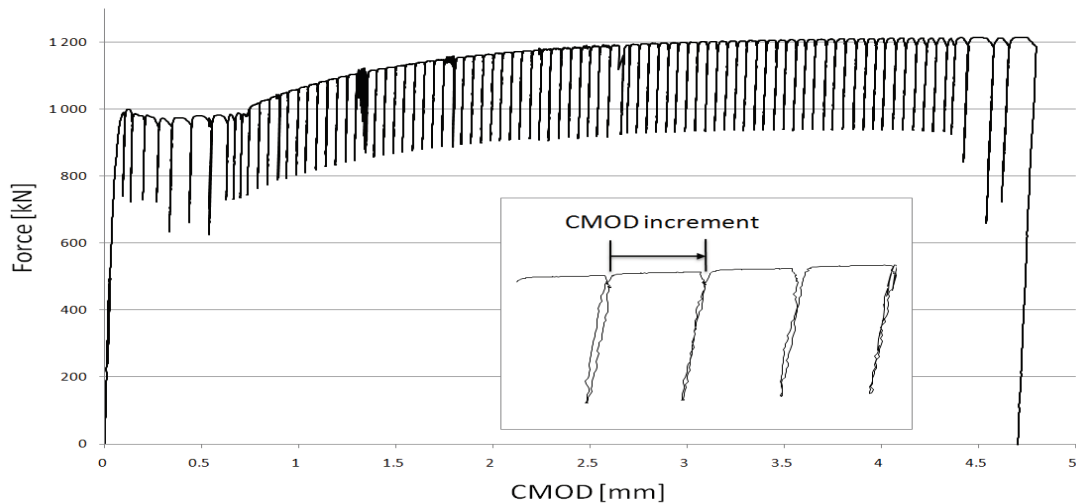
Figure 6: Force with respect to CMOD

The software provides a parametric input of characteristics related to the unloading compliance cycles, for instance the required CMOD increment between two cycles. When the program is started, it runs through a state diagram, defining different cases of how the controller should behave. Depending on the obtained force or CMOD, the software deliberately switches between cases. When detecting failure, all case decisions are overruled by a safety mechanism and the test specimen is unloaded. The use of a state diagram makes the software robust as decisions are not influenced by irrelevant measurements.

All LVDT displacements, CMOD, force and piston displacement have been monitored in the LabVIEW software and logged into a database at a rate of 10 Hz.

2.5 Execution of the test

No significant problems were recorded except for some temporary malfunctioning of the hydraulic valves, which caused an oscillating force (see Figure 6 around 1.3 mm CMOD). Because of a too small CMOD increment setting, as much as 85 cycles were executed. Eventually, it was chosen to end the test when CMOD started increasing drastically, announcing a necking phenomenon in the defective section (net section collapse). A maximum piston displacement of 77.6 mm and force of 1215 kN were measured. The CMOD eventually obtained was 4.8 mm.

2.6 Post-mortem analysis

After testing the specimen, a macro section of the notch region was cut out (Figure 7). This section indicates a stable crack extension of 2 mm in the through-thickness direction, and confirms necking in the defective section.

Figure 7: Macro section of the notch

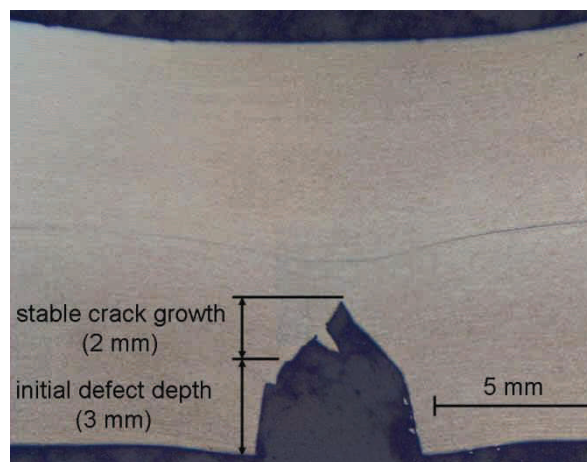## 3   FINITE ELEMENT MODEL

A parametric finite element model of a curved wide plate has been previously developed at Laboratory Soete. Mesh density was defined according to an existing mesh convergence study. This resulted in the mesh shown in Figure 8 and Figure 9. Clamped boundary conditions were imposed at the end nodes of two rigid blocks, attached to the actual wide plate specimen.

The stress-strain curve before necking was converted from engineering values to true stress and true strain. For the curve after necking, the approach recommended in [6] was followed. This method calculates a weighted-average of an upper and lower bound. The upper bound is a linear extrapolation, the lower bound a power law extrapolation. A weight factor between the two curves should be iteratively defined to match experimental results, and was chosen 0.5 in this case.
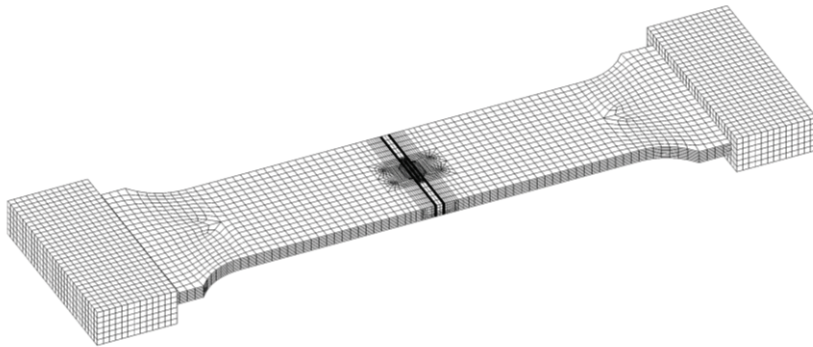
Figure 8: Global FE model (geometry and mesh) of the specimen
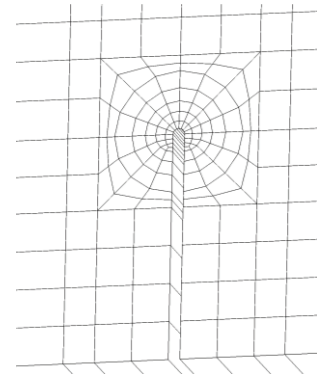
Figure 9: Detailed view of the mesh at the notch region

4   DISCUSSION

4.1   Comparison of DIC and LVDT measurements

To validate the strain field calculations by the DIC software, engineering strain was compared with the strain calculated from the LVDT elongation measurements. Because both datasets described the same experiment, displacement of the pistons was chosen as the common basis for the comparison. The plots in Figure 10 and Figure 11 display the engineering strain measured at the two small LVDTs, K1 and K2.
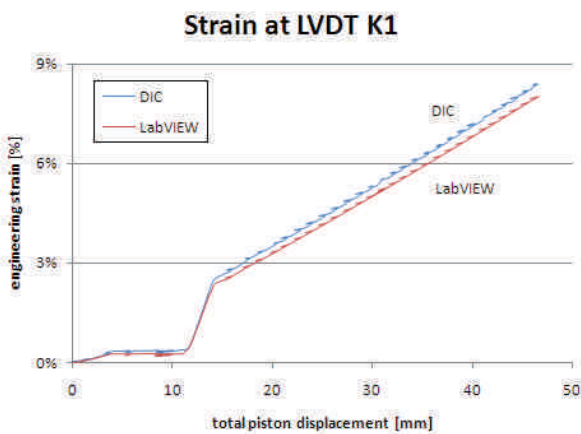
Figure 10: Engineering strain calculated by DIC and measured by LVDT K1
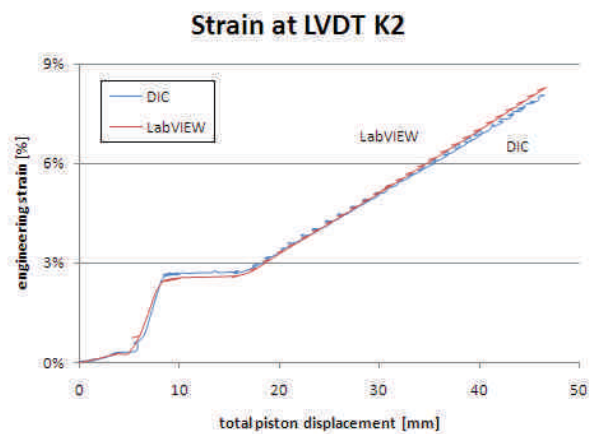
Figure 11: Engineering strain calculated by DIC and measured by LVDT K2

When the piston displacement reached about 45 mm, the boundaries of the LVDTs linear operation range were exceeded, so comparison is limited to this area. The small ripples visible on the curves are caused by the unloading compliance cycles. It can be seen that both strain measurements are in (very) good agreement. The correspondence with the large LVDTs (G1 and G2), which did not saturate, is excellent (Figure 12 and Figure 13). The small "hooks" at the right top corner indicate unloading at the end of the test.
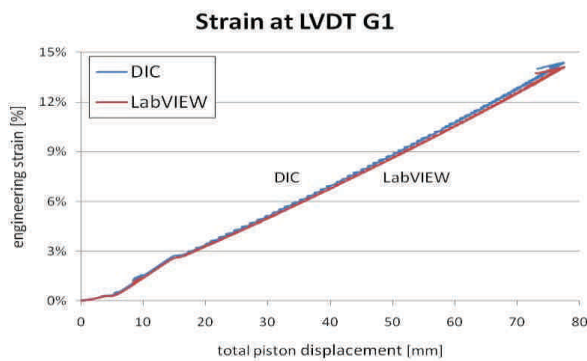
Strain at LVDT G1

Figure 12: Engineering strain calculated by DIC and measured by LabVIEW at LVDT G1

Strain at LVDT G2

Figure 13: Engineering strain calculated by DIC and measured by LabVIEW at LVDT G2

A detailed view of the K1 and K2 engineering strains at both sides of the notch is shown in Figure 14. The large increments of the strain calculated from both LVDT measurements are caused by the Lüders behaviour of the material. The first region experiencing Lüders behaviour is the K2 region. Roughly between 1000 seconds and 1250 seconds, the material at the K2 side yields while the strain at the K1 region remains constant. From 2750 seconds to 3000 seconds, the behaviour is opposite. In the interval between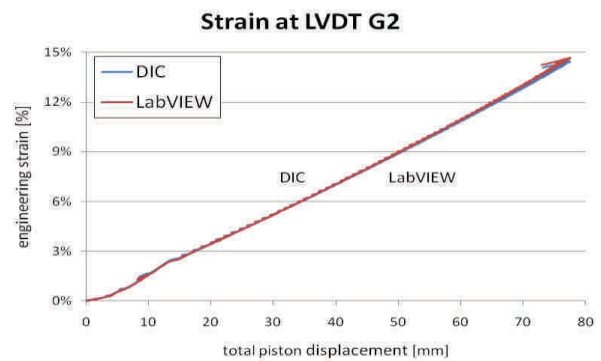 these periods, the region around the crack yields. Although this is a small region, it took a long time before the Lüders yielding ended due to a large number of unloading cycles. If the material around the crack is yielding, a CMOD increment is easily obtained, causing the system to hold, unload, hold and load again. The CMOD curve in Figure 14 illustrates this behaviour. CMOD increases in steps when the material around the crack is yielding, while remaining constant when the K2 and K1 zones yield.
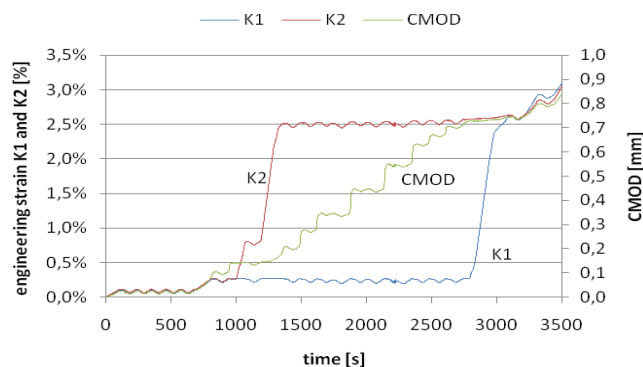
Figure 14: Detailed view of Lüders behaviour at both sides of the specimen

4.2   Comparison of FEM results with DIC measurements

Comparison of the numerical and experimental results is far from straightforward. First, the experiment followed the unloading compliance procedure with loading and unloading cycles, while ABAQUS simulates a monotonically increasing tensile load. Second, the finite element model predicted symmetrical results while small natural variations in material and geometrical properties caused an asymmetrical Lüders yielding. Third, the specimen's mounting blocks elastically deform during the test while modelled as rigid blocks in ABAQUS. Due to this and initial backlash in the test rig, a comparison based on total (piston) displacement is not possible. Fourth, crack growth, and subsequent influence on the strain fields, was not modelled in ABAQUS. Because of these reasons, the engineering strain fields of the simulation were compared to those of the DIC measurement at frames corresponding to a fixed and limited LVDT strain, more specifically the frames corresponding to LVDT strains ε_{K1} of 4% and 7%. With these values, the Lüders behaviour is avoided and the ductile crack extension can be assumed negligible.

Inspection of the contour plots of the first principle strain (Figure 15 and Figure 16) yields a good agreement (both qualitative and quantitative) between the calculated and measured results. It should be noted that ABAQUS plots logarithmic strain while the DIC-software plots Lagrange strain. However, the difference between both is small. An expected X-shaped strain concentration around the notch is visible on both plots. Figure 17 and Figure 18 are plots of the strain values along the paths defined in Figure 15 and Figure 16. ABAQUS successfully predicted strain hotspots in front of the shoulders, which may harm the capability of LVDT measurements to indicate a far-field uniform strain. In the experiment, the hotspot at the right side of the notch was more pronounced than the left one. ABAQUS overestimates this hotspot in Figure 17,

whereas it is underestimated in Figure 18. This indicates that the experiment is prone to inevitable coincidences and natural effects which are not (or even cannot be) accounted for in the simulation. Nevertheless, a more than satisfactory overall agreement is observed between the experimental and the simulated results.
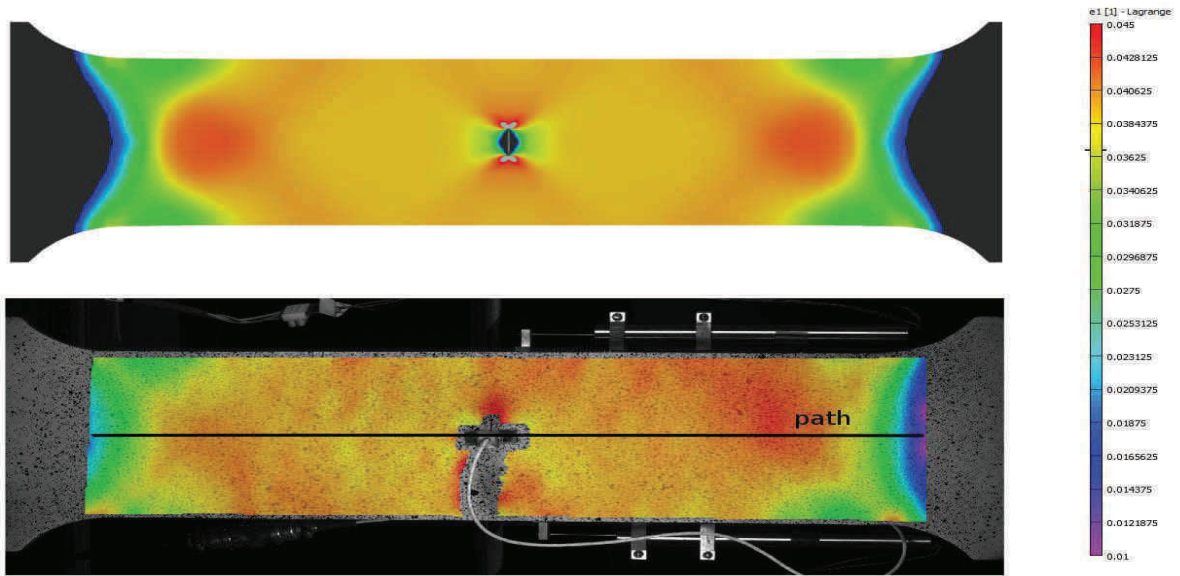
Figure 15: First principal strain for ε_{K1} = 4%
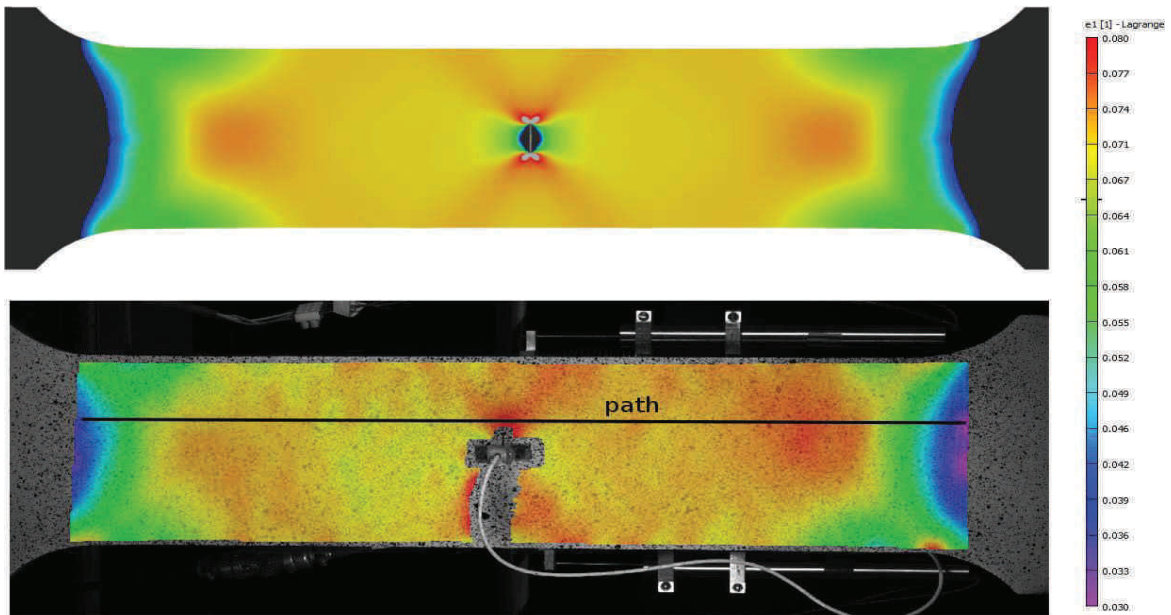
Figure 16: First principal strain for ε_{K1} = 7%
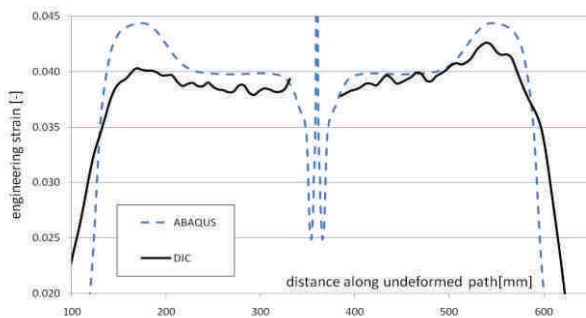
Figure 17: First principal strain along path for ε_{K1} = 4%
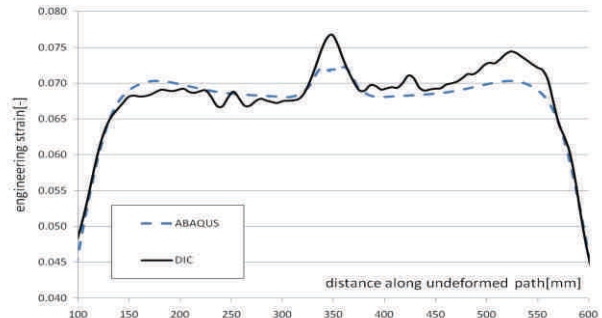
Figure 18: First principal strain along path for ε_{K1} = 7%

5   CONCLUSIONS

The optical strain measurement (DIC) results show good accordance with the LVDT measurement results. Although comparison on the small LVDTs was limited to a maximum strain of 8%, there seems to be a very good similarity between the measurements. The major advantage of the DIC system is that it provides strain field output of the whole surface of the specimen. A disadvantage is the time-consuming and sensitive procedure required to speckle the specimen.

The ABAQUS finite element model predicts the MWP's strain fields fairly well for strains higher than the maximum Lüders strain. Further, crack growth is not yet implemented in the model, so application of the current model at large strains, where ductile crack extension has a significant influence, is discouraged as well.

Although no correlation problems were noted, more accurate DIC results might be obtained when an optimized speckle pattern is applied to the specimen. A study on the influence of the speckle size and how to create speckles in a controlled manner is suggested.

6   NOMENCLATURE

DIC	Digital Image Correlation
CMOD	Crack Mouth Opening Displacement
CWP	Curved Wide Plate
LVDT	Linear Variable Displacement Transducer
MWP	Mini Wide Plate
UC	Unloading Compliance

7   ACKNOWLEDGEMENTS

8   REFERENCES

[1] J. Rupert, G.Tart, Pipeline geohazards unique to northern climates, Proceedings of the 8th International Pipeline Conference, Calgary, Alberta, Canada, 2006.

[2] W. Mohr, Strain-based design of pipelines, October 2003. EWI Report Project No.45892GTH.

[3] API 5L, Specification for Line Pipe, 42nd edition, American Petroleum Institute, 2000.

[4] R. Denys, A. Lefevre, UGent guidelines for curved wide plate testing, Proceedings of the 5th Pipeline Technology Conference, Ostend, Belgium, 2009.

[5] S. Cravero, C. Ruggieri, Estimation procedure of J-resistance curves for SE(T) fracture specimens using unloading compliance, Engineering Fracture Mechanics, 74, 2735-2757, 2007.

[6] Y.Ling, Uniaxial True Stress-Strain after Necking, AMP Journal of Technology, 5, 37-48, 1996.

CHARACTERISATION OF A RESONANT BENDING FATIGUE TEST SETUP FOR PIPES

J. Claeys[1], J. Van Wittenberghe[2], P. De Baets[2] and W. De Waele[2]

[1] Ghent University, Belgium
[2] Ghent University, laboratory Soete, Belgium

Abstract This paper discusses the resonant bending fatigue test setup designed at laboratory Soete for full-scale fatigue tests on pipes. Following an enumeration of other types of fatigue test setups an attempt is made to characterise the resonant bending machine. The characterisation is obtained by conducting different tests on a steel pipe of grade API X65. Concordance between measured and calculated stresses and influence of excentre position on stress amplitude is discussed. High frequencies and small power input make this test setup very effective. The analytical model correctly predicts the measured stresses and a stress versus excentre curve is obtained. However not yet fully defined, it gives a first indication for the excentre position when preparing for a fatigue test.

Keywords Resonant bending fatigue, stress amplitude, X65 pipe, full-scale

1   INTRODUCTION

Pipes used in offshore applications often fail prematurely under cyclic loads of which the maximum stress value is lower than the upper tensile strength of the material. This phenomenon is called fatigue. Especially at welded or threaded pipe joints, which act as stress raisers, a fatigue crack can initiate. It goes without saying that accurate prediction of the fatigue life of these structures is important. In this paper the characterisation of the resonant bending fatigue test setup build at laboratory Soete is discussed.

As a first part of this paper different setups to perform full-scale fatigue tests are discussed. Axial cyclic loading, 4 point-, rotating and resonant bending. The two last setups give rise to the same stress state in the pipe joint or weld and will therefore be jointly discussed.

The characterisation of the laboratory Soete setup will commence with strain gauge measurements. These will confirm the match between the analytical model discussed in [1] and the reality. The influence of different excentre positions on the stress amplitude will be handled as well. All test are done on a seamless steel tube of 4,8 m length, 324 mm diameter, 12,7 mm thickness and grade API X65.

2   FULL-SCALE FATIGUE TEST SETUPS

2.1   Axial fatigue

The principle of axial fatigue is illustrated in Figure 1. A cyclic axial force is applied which gives rise to cyclic axial stresses according to equation *(1)*. A setup for large diameter pipes can be found at Stress Engineering Services [2]. This machine applies its load according to $R = \sigma_{min}/\sigma_{max} = 0$ and its main characteristics are summarized in Table 1. Note that very high forces need to be applied to exert relatively low stresses. This method however causes a uniform stress distribution throughout the thickness of the pipe *(1)* which can be necessary to accurately predict fatigue life in certain applications (e.g. structural columns).
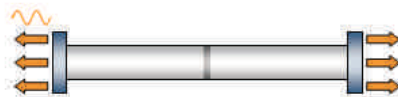
Figure 1: Axial fatigue

$$\sigma \approx \frac{F}{\pi D_o t} \tag{1}$$

2.2 Four point bending fatigue

The schematics of a 4 point bending test setup are given in Figure 2. This test is widely used to determine fatigue life of risers and columns. The cyclic load is now exerted perpendicular to the pipe.
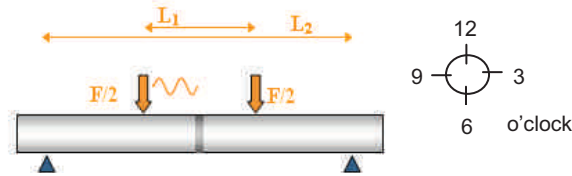
Figure 2: 4 point bending fatigue

Details of two setups have been found in literature. One setup was used to apply loads to relatively small diameter pipes with a load ratio $R = -1$ [3] and the second one for larger diameter pipes but with a load ratio $R \approx 0$ [4]. The characteristics of both setups are again given in Table 1.

In between the load points the bending moment remains constant. The pipe undergoes a cyclic load with a stress amplitude at the outer fibres at 6 and 12 o' clock calculated according to the formulas *(2,3,4)* in case of $R = -1$. Hence there are some important differences with the axial fatigue setup. The stress is not divided uniformly throughout the thickness and not all points on the circumference see the same load.

$$M = F\ (L_2\text{-}L_1)\ /2 \tag{2}$$

$$\sigma = \frac{MD_o}{2I} \tag{3}$$

$$I = \frac{\pi}{64}(D_o^{\ 4} - D_i^{\ 4}) \tag{4}$$

2.3 Rotating and resonant bending fatigue

2.3.1 Rotating bending fatigue

A constant load is applied perpendicular to the pipe which is rotated to introduce time dependency. The same formulas *(2,3,4)* can be applied for this setup. Again a constant bending moment is obtained in between the load points. The only difference is that every point at the outer fibre will now be subjected to the same cyclic stresses, shifted in time. Given that the joint is placed at the centre of the setup, it will be subjected to exact the same stress state as in a resonant bending fatigue setup (Figure 3).
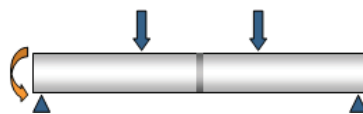
Figure 3: Rotating bending fatigue

Two setups were found in literature. In the first, build and designed by Petrobras and Coppe, an additional axial load can be superimposed to the bending moment. It is suitable for relatively small diameters [5].The second is used to test larger diameter pipes and was constructed by the University of Oklahoma [6, 7]. An additional axial load can be superimposed here as well. Notice that applying an additional axial force does not have any effect on the oscillating character of the stresses. It results in a non zero mean stress and allows testing with different load ratios. The characteristics are given in Table 1 where reported working values are listed for the second setup whereas actual maximum capacity values are listed in all other cases.

2.3.2 Resonant bending fatigue

As an example of a resonant bending fatigue setup the laboratory Soete machine, which is the subject of this paper, is discussed (Figure 4). Similar setups are used at Stress Engineering Services[8, 9], TWI

[10, 11] and EWI [12]. The pipe is excitated according to its first eigenmode by means of a rotating excentric mass. In the absence of axial preload the stress ratio is thus $R = -1$. Again, every point at the outer fibre sees the same cyclic stresses shifted in time. However, an area where the bending moment is constant (as is the case in the rotating bending setup), does not exist anymore. A more detailed description of this setup can be found in [1].

As can be seen in Figure 5, the bending moment is now a fluent line which reaches its maximum at the centre of the tube while the supports are positioned at the nodes of the pipe's first bending mode. The previous remark that the joint at the centre of the tube will be subjected to the same cyclic stresses as in the rotating bending test setup is thus confirmed. Given that the same stress amplitude is constructed. A certain stress amplitude is constructed by altering the position of the excentric mass. The characteristics of our resonant bending fatigue machine are also given in Table 1. The pipe is pressurized with water to lower the eigen frequency and to detect fracture as pressure drops. Due to this pressure, a small axial preload is applied.
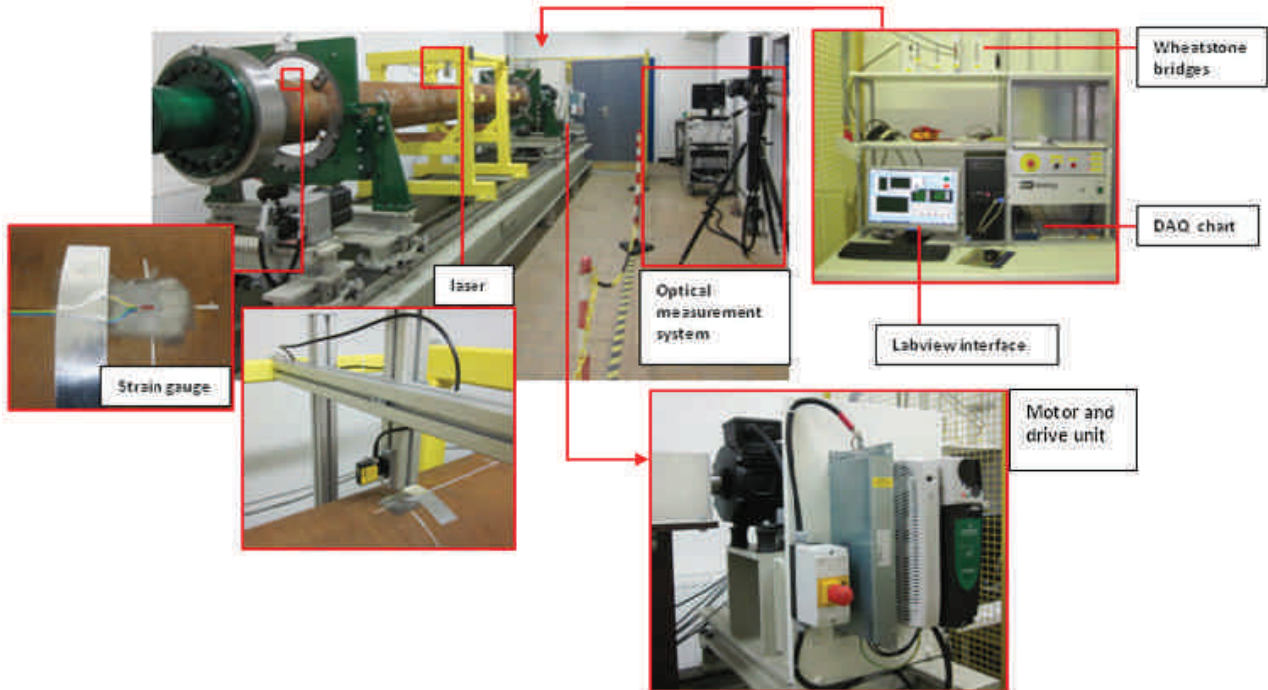
Figure 4: Labo Soete resonant bending fatigue test setup
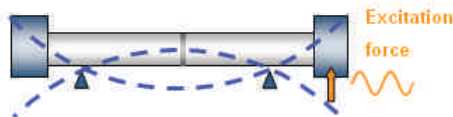
Figure 5: Resonant bending fatigue

Setup	D_o (mm)	L (m)	t (mm)	F (kN)	M (kNm)	σ_{max} (MPa)	f (Hz)
Axial fatigue [2]	351-813	4,5-9,1	11,1-25,4	185	/	15,1	1,0
4 point bending							
$R = -1$ [3]	114,3	1,2	8,6	/	66,3	944,8	0,1
$R \approx 0$ [4]	273,1	4,5	14,3	/	179,0	125,0	0,1
Rotating bending							
[5]	324	6,0	9,5	2000	600,0	1043,6	5,0-15,0
[6,7]	610	9,14	25,4	5780	451,0-995,0	69,0-152,0	2,0
Resonant bending [1]	152,4-508,0	3,7-5,7	40-5,7	/	/	175,0	20-40

Table 1: Characteristics of test setups reported in literature

The advantages of the resonant bending machine when compared to rotating bending setups are the higher possible testing frequencies and the smaller power usage. The resonant bending setup uses between 0,33 kW and 5,9 kW and is driven by a motor with a nominal power of 7,5 kW whilst the rotating bending setup needs a motor of 22,4 kW nominal power for a test with a lower maximum stress and at a reduced testing speed [6, 7].

3 FURTHER CHARACTERISATION OF THE LABORATORY SOETE RESONANT BENDING FATIGUE TEST SETUP

3.1 Stress amplitude

3.1.1 Theoretical versus measured stresses

A semi-analytical theoretical model has been developed to predict the pipe's deflection and stress amplitude at the pipe's mid section, in function of different characteristics of the setup [1]. Predicted stress amplitudes are compared with experimentally determined values derived from strain gauge measurements at the mid- section of the pipe. This is illustrated for a 75° excentre position in Figure 6.
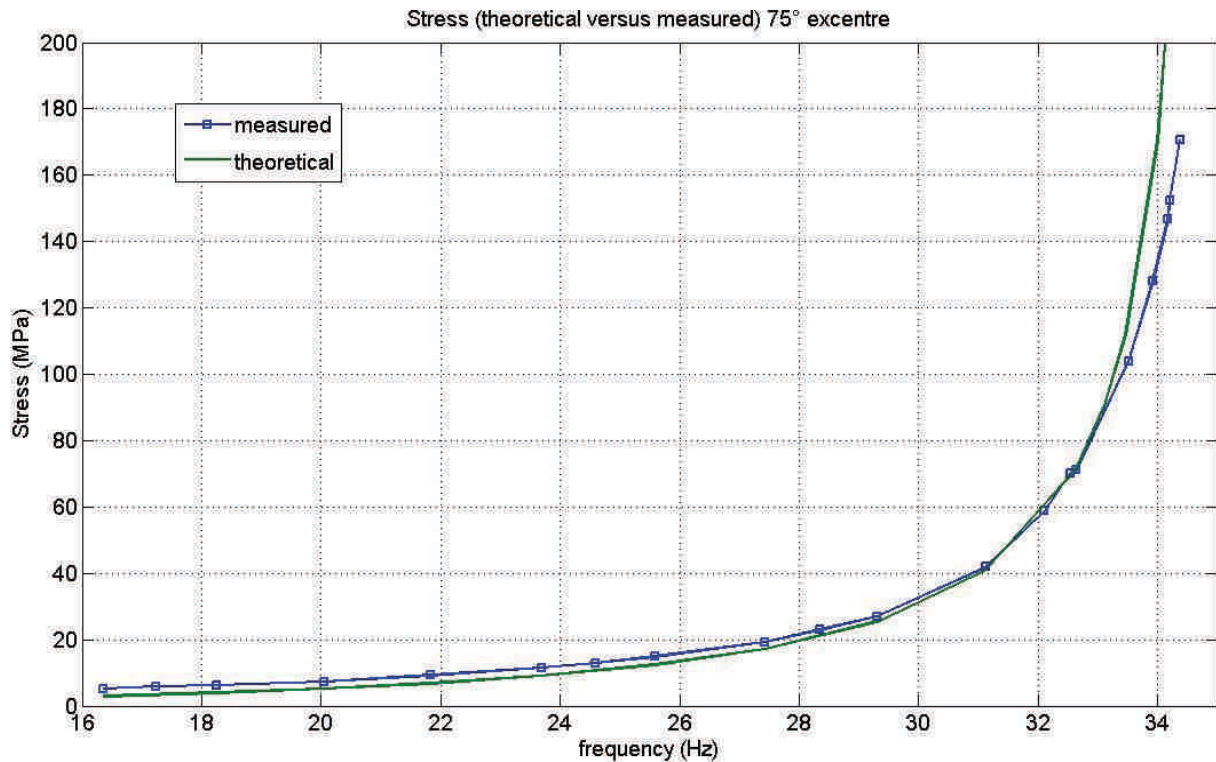
Figure 6: Theoretical versus measured stress amplitude

A good correspondence between the measured and theoretical stress values is observed, except for the higher frequencies. This is explained by the damping effect which is not accounted for by the theoretical model.

3.1.2 Influence of varying excentre position

The influence of altering the excentre position is measured with five strain gauges mounted at symmetrical positions with respect to the mid-section (Figure 7).
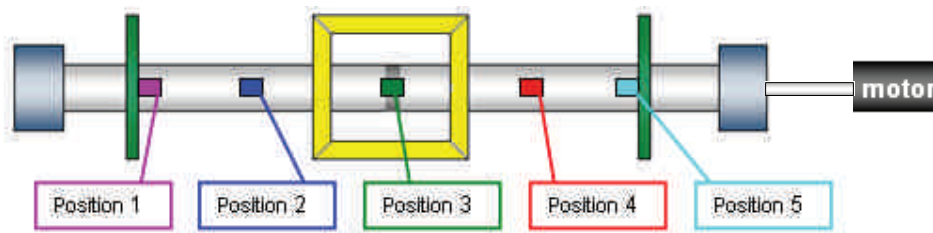
Figure 7: Position strain gauges (top view setup)

In Figure 8 the results of the strain gauge measurements corresponding to one particular excentre position (60°) are illustrated. The strains are recalculated to overall stress by multiplying with the *E* modulus of the pipe metal.
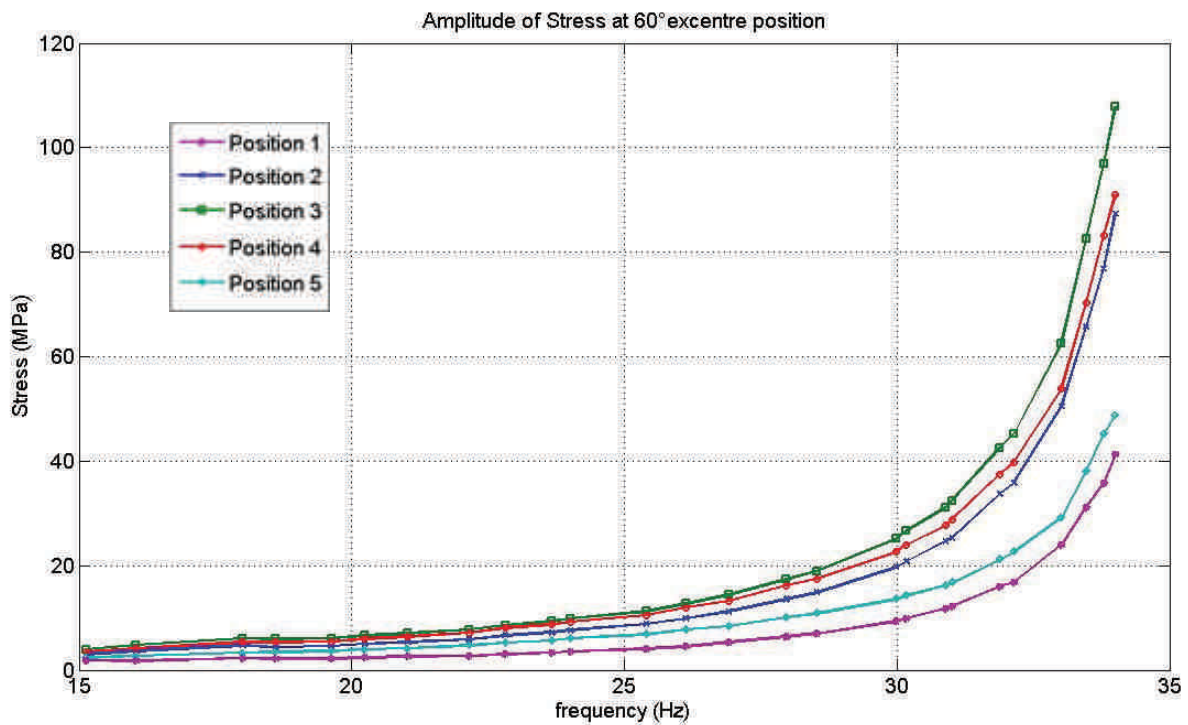
Figure 8: Stress amplitude at 60° excentre position, calculated from strain gauge measurements

The asymmetry in the setup due to the presence of the motor at the right end is clearly visible. This results in higher stresses at positions 5 and 4 when compared to positions 1 and 2, completely according to expectations. In a future development a comparison between the experimentally asymmetry (Figure 8) and the theoretical asymmetry that is taken into account in the semi-analytical model will be made. Furthermore, equivalent graphs can be build for each excentre position thus evaluating the influence of an excentre position alteration.

The machine excentre design is illustrated in Figure 9. The force exerted on the pipe varies from zero at 0° excentre position to *2F* at 180° degrees excentre position according to the formula given in *(5)* where α equals the excentre position. This force is proportional to the stress amplitude in the pipe. Thus a fitting between these curves and the stress data measured at the centre of the pipe for different excentre positions can be used to determine the constants *C(F)* in *(6)*.

Measurements for 20° up to 125° are illustrated for various frequencies (Figure 10). By taking the logarithmic value of the different constants used to fit the cosinus function given in *(6)* to the results, an estimation can be made of the constant to be used for plotting the stress amplitude versus excentre position curve at the upper frequency of 34,4 Hz which corresponds to 98% of the pipe's resonance frequency.
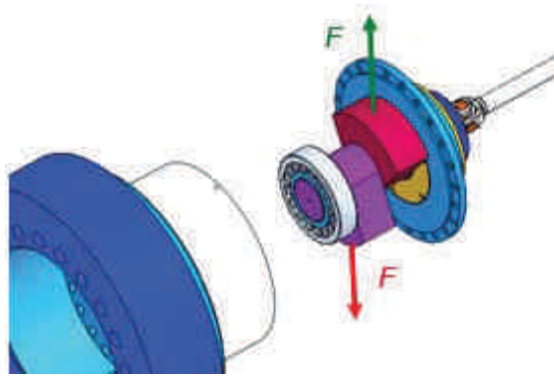
Figure 9: Forces at excentre position 0°

$$Force = 2F\cos(\frac{180° - \alpha}{2}) \quad (5)$$

$$\sigma = C(F)\cos(\frac{180° - \alpha}{2}) \quad (6)$$
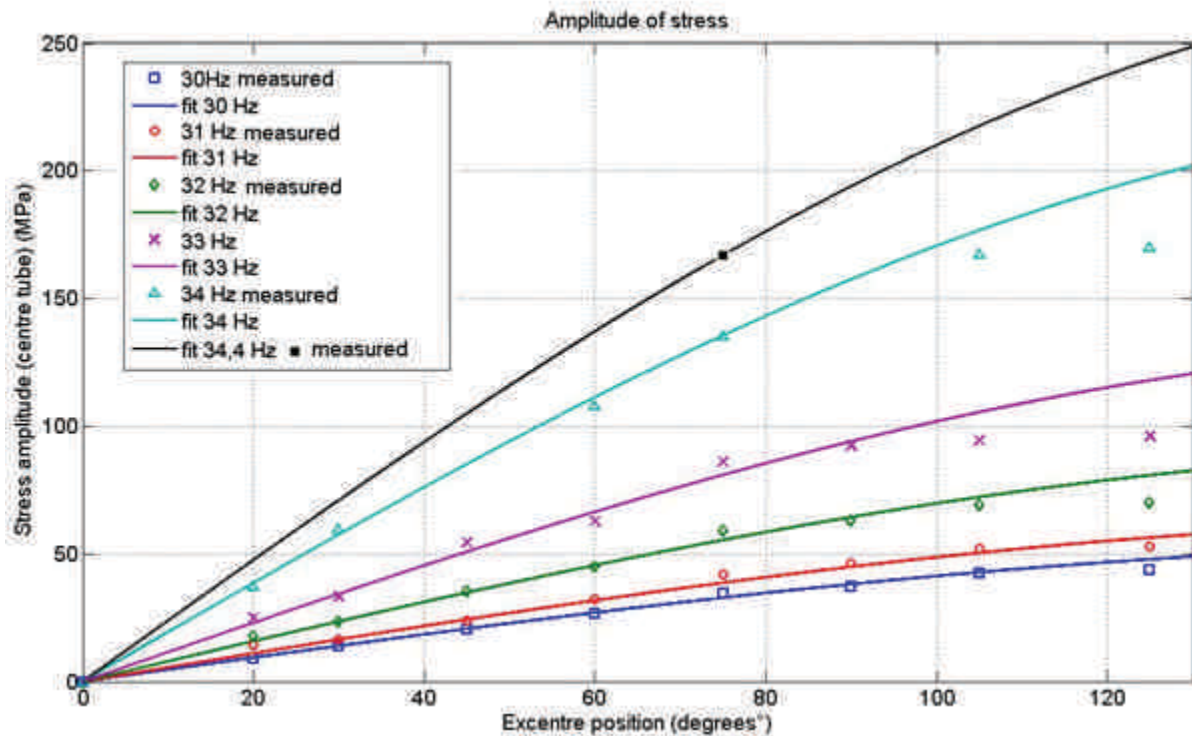
Figure 10: Stress amplitude at the centre of the tube for different excentre positions

When taking back Figure 6 it is seen that for an excentre position of 75° this upper black curve indeed gives a correct approximation of the stress. However further evaluation of this diagram is necessary. For instance the non correspondence between the measured and theoretical values at high excentre positions needs to be examined.

4   CONCLUSIONS

- A comparison of different alternatives to perform full scale pipe fatigue tests has been performed. Different test methods result in different stresses at the centre of the pipe. Compared to rotating bending, resonant bending fatigue tests show the advantages of higher testing frequency and smaller power usage.

- As concluded by J. Van Wittenberghe in [1], the analytical model proves to be accurate. This was evaluated by means of strain gauge measurements. Further evaluation is necessary to evaluate if the analytical model also correctly accounts for the asymmetry in the setup.

- An attempt was made to display the influence of excentre position on stress amplitude at the mid-section of the tube. If the non correspondence between measured and theoretical values for excentre positions larger than 90° will be explained in the future, this graph will prove useful when setting up a fatigue test. It makes it possible to predict in advance which excentre position needs to be installed to exert a certain fatigue stress.

5   NOMENCLATURE

σ	stress	MPa
R	load ratio	
F	force	N
D_o	outer diameter	m
D_i	inner diameter	m
L	length	m
t	wall thickness	m
f	frequency	Hz
M	moment	Nm
I	area moment of inertia	m^4
α	excentre position	degrees

6   ACKNOWLEDGEMENTS

7   REFERENCES

[1]   J. Van Wittenberghe, P. De Baets, W. De Waele, W. Ost, M. Verstraete, and S. Hertelé, "Pipe resonant bending fatigue test setup with optical measuring sysytem," *Proceedings of the 8th International Pipeline Conference, IPC2010,* September 27-October 1 2010.

[2]   SES, "fatigue testing," Stress Engineering Services INC. vol. 2010, 11/1/2010, available; http://www.stress.com/servicetier3.php?sid=11&pid=186 [accessed 11/6/2010].

[3]   K. Hasegawa, K. Sakata, K. Miyazaki, and S. Kanno, "Fatigue strength for pipes with allowable flaws and design fatigue curve," *International Journal of Pressure Vessels and Piping,* vol. 79, pp. 37-44, Jan 2002.

[4]   A. Lefevre, M. Waaijenberg, E. Aylwin, and H. M. Triel, "Defect propagation from fatigue loading in 13% Cr pipelines," *Pipeline Technology Conference, Ostend, 12-14 October 2009,* 2009.

[5]   G. F. Miscow, P. E. V. de Miranda, T. A. Netto, and J. C. R. Placido, "Techniques to characterize fatigue behaviour of full size drill pipes and small scale samples," *International Journal of Fatigue,* vol. 26, pp. 575-584, Jun 2004.

[6]   A. H. Varma, B. W. Russell, and B. Wallace, "Large-scale rotating bending fatigue tests for offshore pipe connections," *Experimental Mechanics,* vol. 37, pp. 147-153, Jun 1997.

[7]   A. H. Varma, A. K. Salecha, B. Wallace, and B. W. Russell, "Flexural fatigue behavior of threaded connections for large diameter pipes," *Experimental Mechanics,* vol. 42, pp. 1-7, Mar 2002.

[8]   N. J. Santi, "Premium & Semi-premium Connections Design Optimization for Varied Drilling with Casing Applications," *OTC Offshore Technology Conference,* vol. 17221, 2005.

[9]   SES, "Full Scale Fatigue Testing," *Stress Engineering Services Inc.,* 2000.

[10]   P. Edmundson, "Variable amplitude fatigue testing of full-scale pipe joints," *Connect,* November 2009.

[11]   G. R. Razmjoo, "Fatigue performance of corrosion resistant steel catenary risers," *TWI PR5473-2,* 2001.

[12]   A. E. Adams, "Full Scale Fatigue Testing," *EWI Tech Brief,* 2007.

GROOVE DESIGN FOR FORM FIT JOINTS MADE BY ELECTROMAGNETIC PULSE CRIMPING

P. Vanhulsel[1], M. Van Wonterghem[1], W. De Waele[2] and K. Faes[3]

[1] Ghent University, Belgium
[2] Ghent University, Laboratory Soete, Belgium
[3] Belgian Welding Institute, Belgium

Abstract The electromagnetic pulse process can be an alternative for many conventional production processes. It can be used for perforating, cutting, welding, forming and crimping. In this thesis, the latter will be investigated in detail, with the emphasis on tubular joints bearing axial tension and/or torsion loading.
To get acquainted with the subject, first a literature study was performed concerning the general principles of electromagnetic pulse crimping. Because a new field shaper had to be designed, literature on this topic was also consulted. Finally, the design and use of grooves in crimp joints was studied. It has been reported that an inner piece (mandrel) with additional grooves in the joining zone significantly increases the strength of a crimped joint [1]. However, the information on electromagnetic pulse crimping with a mandrel with more than one groove is very limited. Therefore one of the main goals of this thesis is to determine an optimal design for a mandrel with two grooves used for axially loaded joints. A combination of finite element simulations and experiments was used to draw preliminary conclusions involving the double groove design. In a later stage torsional joints will be designed and suitable filler materials to realize leak proof joints will be evaluated.

1   ELECTROMAGNETIC PULSE CRIMPING

Previous studies conducted by the Belgian Welding Institute (BWI) have shown promising results for the electromagnetic pulse welding process. As an alternative for the welding, magnetic pulse crimping can increase the applicability of the process, on the condition that the current shortcomings of the crimping process can be resolved (no clear guidelines for the groove design and the crimp joints are not gas-tight). The goal of the research is to make the magnetic pulse crimping a valuable, more robust and economically attractive alternative joining process.

1.1   General principles

Figure 1 schematically shows the layout of the magnetic pulse process. A capacitor bank is charged to the desired energy level by setting the correct voltage level using the machine's control unit. The energized capacitor bank is then discharged by flipping over a high current switch. This results in a damped oscillating current that flows through the coil, generating an intense transient magnetic field in it [2].

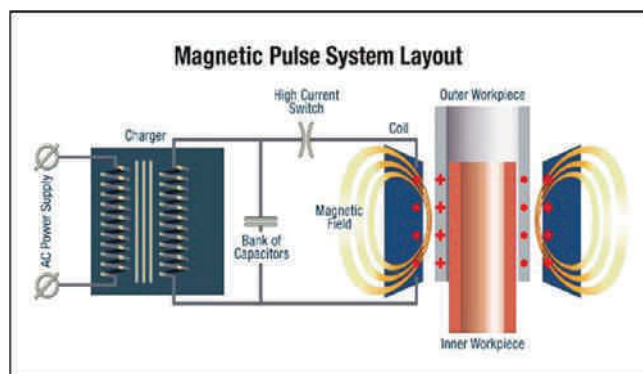Figure 1: Schematic illustration of the magnetic pulse processs [3]

According to Lenz's law, eddy currents are induced in the surface layer of the outer workpiece (flyer tube). This is the so-called skin effect. The depth below the surface of the conductor at which the current density decays to a fraction $\frac{1}{e}$ of the current density at the surface is called the skin depth and can be calculated as [4]:

$$\delta = \sqrt{\frac{2\rho}{\omega\mu}}$$

(1)

With: ρ = resistivity of conductor [Ωm]
         ω = angular frequency of the current [Hz]
         μ = absolute magnetic permeability of the conductor [Hm^{-1}]

As can be seen from the above equation, the skin depth varies with the inverse square root of the angular frequency of the current. Because the flyer tube is hollow, it is important that the frequency is high enough, so that the skin depth is smaller than its wall thickness. In that case the electromagnetic field is shielded by this flyer tube. If this is not the case, the induced magnetic field will be less effective and lead to limited deformation.

The eddy currents flow in such a direction that an induced magnetic field is created that initially shields the workpiece from the magnetic field inside the coil. During the proceeding of the process, the skin depth increases and the magnetic field penetrates the workpiece wall. The resulting pressure pulse acts orthogonally on the magnetic field inside the coil, and the Lorentz repulsion force causes the tube to repel away from the coil. When this force is greater than the workpiece material's yield strength, permanent plastic deformation occurs [2, 5].

The electromechanical forming process differs from conventional forming processes because it is environmental friendly, uses high strain rates and requires low maintenance. This new type of processing can be very interesting for several industries and therefore more applied research is required to obtain reliable data. The machine being used for the experiments is Pulsar's MPW 50 25 Magnetic Pulse System. With an output voltage range of 0-19 kV it is possible to perform experiments on difficult materials such as steel, which has a low electric conductivity compared to aluminium [6].

1.2   Field shaper design

Usually a multi-turn coil is used to induce the magnetic field. To protect this coil from high repulsion forces and to focus the widely spread current, a field shaper (FS) is used [7]. Field shapers can also homogenize and significantly increase the magnetic pressure in the work zone as can be seen in Figure 2. The tube experiences a bigger radial pressure at the ends because the coil length (in the case without field shaper) is larger than the axial field shaper length and the tube length. So all the energy left in the outer windings of the coil exerts a great pressure on the tube ends. When the axial length of the field shaper inner zone decreases, the magnetic pressure increases. This is illustrated on Figure 3, which shows some experimentally obtained graphs where F1 is the field shaper with the smallest working area. This observation can be explained by assuming that magnetic field lines penetrating in a smaller area of the tube impose a stronger magnetic field (and thus higher pressure) in that area [8].
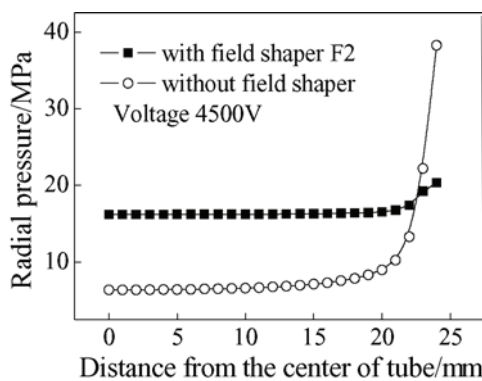
Figure 2: Homogenization effect of FS [8]
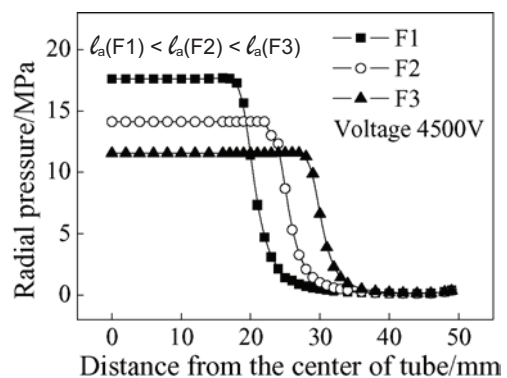
Figure 3: Increasing magnetic pressure effect of FS [8]

In the design of a field shaper, two main parameters need to be considered: its material and its geometry. As for the material, a good electrical conductivity and a high mechanical endurance against pulse loads and thermal shocks is required. As for the geometry, several contradictory demands need to be taken into account: the desired size and shape of the work zone, high stiffness, minimising mechanical and thermal stress (concentrations) and optimising energy coupling efficiency [7].

Optimising the efficiency is very important for reducing energy costs, which might be significant in case of bulk production. Unavoidable losses, like thermal and inductive losses, give rise to the potential problem of

a low energy transfer efficiency. To investigate the efficiency of several shapes the finite element software FEMM (Finite Element Method Magnetics) can be used. A major drawback is the 2D characterization of the model, which can lead to inaccurate results [4].

Despite the inherent decrease in efficiency, the field shaper's geometrical design is chosen to suit the specific size and shape of the working zone. The field shaper stiffness is derived from electro-magnetic force considerations. By cutting a radial slit into the field shaper and decreasing the axial length of the field shaper, the current density increases resulting in a higher magnetic pressure in the work zone [9].
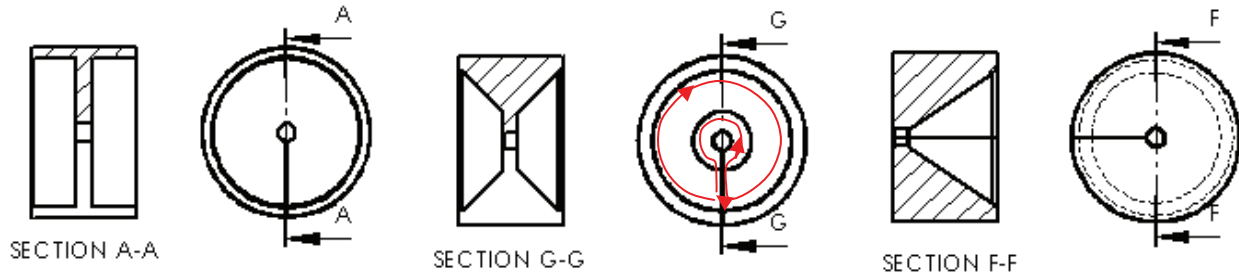
Figure 4: Three different geometrical designs of a field shaper

Figure 4 shows three possible geometrical designs of a field shaper. On the illustration of design G a current line is drawn. It can be seen that due to the presence of a radial slit, the current flows in the high density area around the work zone. It has been proven that design A creates the highest coupling efficiency but provides the least mechanical strength and cracking will easily occur at the stress concentrations in the sharp corners. The efficiency of design G only differs with 5% from that of design A and has better mechanical strength. Design G is the most widely used shape for a field shaper [7]. Design F could be a good alternative because it combines a rectangular shape (less current losses and thus better coupling efficiency) with a conical shape (better mechanical performance). Because the magnetic pulse process deals with high pressures, the asymmetry of this last design will result in an asymmetrical distribution of stresses in the field shaper leading to reduced fatigue endurance.

Two field shapers have been developed according to design G in Figure 4 to perform experimental research on the crimp joint. One field shaper is made of CuCrZr, has an inner diameter of 50 mm and an axial length of 30 mm. The other field shaper is made of CuCoBe, has an inner diameter of 18 mm and an axial length of 20 mm.

2   JOINT DESIGN

2.1   Interference versus form fit

For electromagnetic crimping, two mechanisms are of importance:

1. **Interference fit**: the flyer tube undergoes severe plastic deformation and the mandrel undergoes global elastic deformation. Once the crimping is done and the (electromagnetic) forces decrease, the mandrel wants to return to its original shape (elastic relaxation). This motion is restrained by the plastically deformed flyer tube. As a result, interference stresses are generated between both joining partners.
2. **Form fit**: the flyer tube is forced into an undercut (e.g. a groove), which is applied in the mandrel . The joint strength is thus the result of mechanical interlock.

2.1.1   Interference fit

The strength of the interference fit strongly depends on 3 factors: the residual stresses in the workpieces, the friction between both parts and the interaction area.

On the one hand, the residual stresses depend on strength and stiffness properties of both components. It is favourable to use a mandrel material of higher strength and stiffness than the tube material. Then the elastic recovery of the mandrel is higher, which leads to a higher radial reaction force and a higher pull-out strength of the joint [5].
On the other hand, the residual stresses also depend on the compression velocity. A higher velocity will lead to a higher kinetic energy at the time of impact and will realize a higher compression of the mandrel, which increases the radial reaction force and therefore realizes a higher pull-out strength. A higher compression velocity can be reached by setting a higher charging voltage or by having an initial gap between both joining partners (because then there is the possibility for acceleration, but it should be noted

that the initial gap cannot be too large, because then the acceleration will have switched to deceleration by the time the flyer tube impacts on the mandrel) [10].

The second factor that is of importance is the static friction coefficient between the materials of the outer tube and the mandrel. In Table 1 the values are giving for combinations which will be investigated in this thesis.

Joined materials	μ_s
steel-steel	0.74
aluminum-steel	0.61

Table 1: Static friction coefficients for the investigated material combinations [11]

The third important factor is the interaction area, which depends on the roughness of the parts and the size of the contact zone.
An increasing roughness of the surfaces will lead to a microscopic form fit and a higher percentage of interaction area in the joints and consequently higher pull-out strengths [5].
A larger contact area will lead to stronger joints (assuming that the other factors remain constant). For tubular joints, the diameter of the mandrel and the length of the contact zone are the two parameters which determine the size of the contact area. The diameter of the mandrel is in most cases a fixed parameter determined by the application, but the length of the contact zone (the overlap length) is a parameter which can be varied when designing connections. A large length is desirable, but of course a good balance needs to be found between increasing the length (leading to a higher pull-out strength) and the inherent higher cost (more material, larger machine, more energy) [2].

It should also be noted that an interference fit developed by impact eliminates the potential for fretting (this is wear due to microscopic movements in the interference fit during its operation) [12].

2.1.2 Form fits

To determine the optimal shape of the groove, three options have been evaluated: triangular, circular and rectangular grooves. Joints with triangular grooves were always found to be the weakest. The explanation is that for triangular grooves the angle α (see the radioscopic pictures after deformation in Figure 5) is greater than for rectangular or circular grooves. This results in a lower degree of tube deformation at the groove edge, and thus a lower tensile force is required to initiate pull-out of the tube material from the groove. The circular grooves have a smaller resulting angle α than the rectangular ones, but these last still have a larger pull-out strength because of the larger amount of shearing of the tube. This locks the tube better in place, and thus higher joint strength can be expected. This has been experimentally verified in [1].
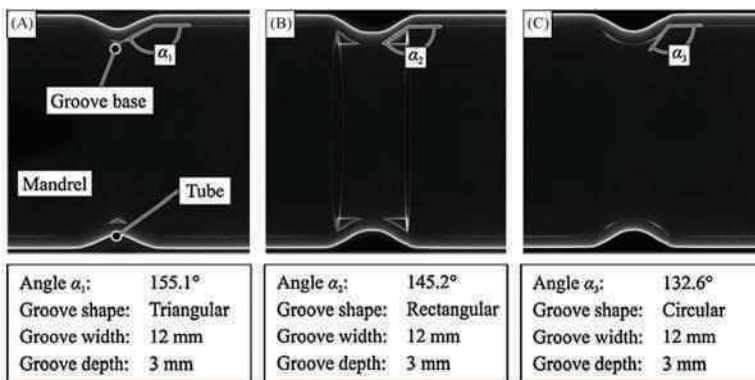
Figure 5: Triangular, rectangular and circular grooves [1]
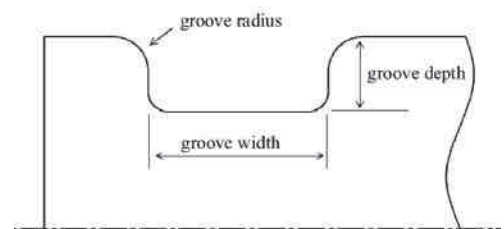
Figure 6: Rectangular groove parameters [13]

The performance of the rectangular groove strongly depends on 3 factors: the groove depth, the groove width and the groove radii (Figure 6).

Deeper grooves will lead to higher joint strengths [14-15], but a too deep groove will lead to a decrease in strength as a result of shearing at the groove edges [16].

For the groove width, it was first believed that a narrow groove would lead to high joint strengths [14-15]. This was later revised because an increasing width leads to a larger contact area at the base of the groove. A larger interference fit and a stronger joint strength will thus be obtained. Again, there is a limit to the dimension, because a too wide groove will lead to wrinkling of the tube which clearly has a negative effect

on joint strength [16]. Furthermore an economical factor comes into play, because a larger width requires more overlap (more material) and a higher energy.

A smaller edge radius at the top of the groove leads to a higher joint strength, but a too small radius leads to increased shearing at the edge and negatively affects the joint strength [16].

Additional grooves in the joining zone will significantly increase the strength of a form fit connection[1]. To verify this statement, a few experiments were performed in a preceding thesis. Joints were produced using mandrels with two grooves and evaluated by tensile testing [13].

The above discussions clearly illustrate the need for more and in-depth theoretical and experimental research activities with respect to the design of mandrel grooves for optimal joint performance.

2.2   Finite element analysis

Finite element simulations of a tensile loaded joint have been performed using the software ABAQUS. The main goal is to get confirmation that a second groove will increase the load bearing capacity of an axially loaded joint. Hereto the magnitude and distribution of the stresses and deformations in both components are studied in detail.

An axisymmetric model consisting of a steel mandrel with two grooves (with a groove width and depth of respectively 13 mm and 2 mm, separated 10 mm apart) and an aluminium tube (with a wall thickness of 1,5 mm and with its assumed deformed shape obtained after crimping) was built. Linear elastic material behaviour is assumed. The static friction coefficient between steel and aluminium (see Table 1) was used to define the interaction between both parts. The mandrel was clamped at the bottom and an upwards displacement was imposed at the tube end. The resulting stress distribution in the axial direction obtained for a representative simulation can be seen in Figure 7. In the unloaded condition, the aluminium tube makes contact with the mandrel at the bottom of both grooves.
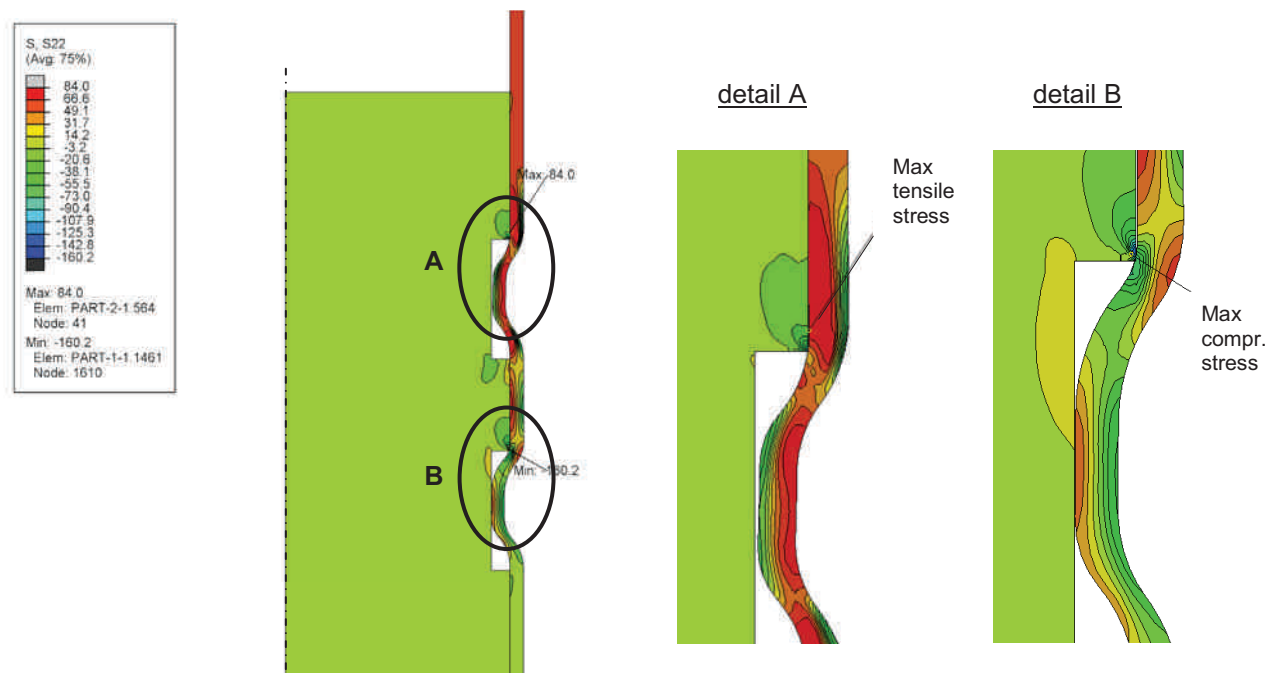
Figure 7: Stress distribution in a tensile loaded joint with a double grooved mandrel

The simulation results revealed that a clearance appeared at the bottom of the first groove during the tensile loading (Figure 7A). As a consequence, the tube is pulled out of the first groove and the mechanical interlock behind the upper corner of the second groove becomes the most important mechanism that prevents the tube from sliding off the mandrel. The highest compression stress in the mandrel can therefore be found at this corner (Figure 7B). The highest tensile stress is found in the tube near the upper corner of the first groove (Figure 7A).

Based on these conclusions, the joint design can be further optimized. The edge radius of the upper corner of the first groove is made larger and this groove is made less deep, in order to prevent early localized shearing of the tube. Also, the first groove is made wider to obtain a larger contact area at the base of the first groove, thus creating a stronger interference fit that will longer withstand pull-out. The second groove is deeper than the first groove and the edge radius of the upper corner is made larger to optimize the form fit

and joint strength. In order to verify these conclusions through experiments, tensile tests were done on both a mandrel with two equal grooves and a mandrel with the proposed optimized grooves, and the results were compared (see section 2.3). More finite element simulations to optimize the groove design will be done in the future.

2.3 Experimental research

2.3.1 Double grooved mandrel

To verify the finite element results, two different types of steel mandrels (with an outer diameter of 46,8 mm) were made: one with two equal grooves and one with optimized grooves that were proposed in section 2.5 (Figure 8a and Figure 9a). An aluminium tube with an outer diameter of 50 mm and a wall thickness of 1,5 mm was crimped on the mandrels. Experimentally it was determined that a charging voltage of 12,6 kV resulted in a good deformation of the tube into the grooves, as can be seen on longitudinal cross sections (Figure 8b and Figure 9b). It should be noted that the radial clearance between the tube and the mandrel is due to the elastic recovery (removal of the residual stresses) when the joints are cut through.
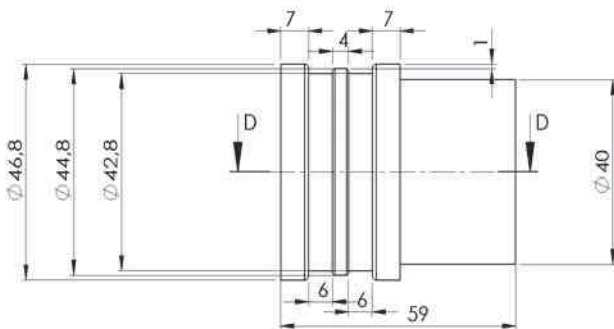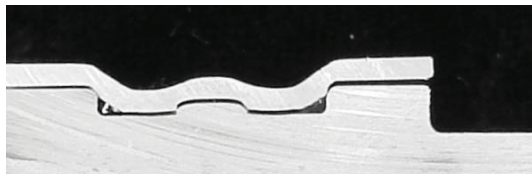
Figure 8: Mandrel with two equal grooves
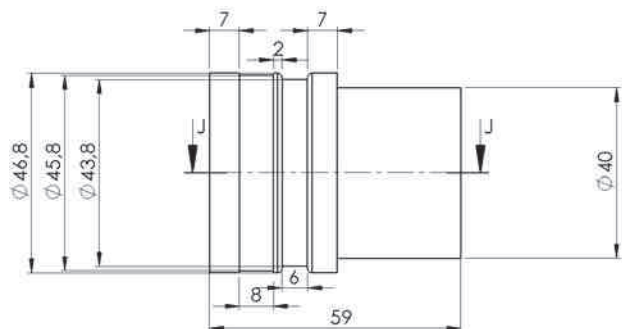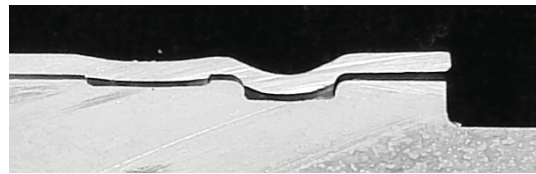
Figure 9: Mandrel with optmized grooves

Tensile tests were done on tubular base material and on the crimped joints. The base material had a tensile strength of 56,1 kN. The joint design with two equal grooves had a pull-out strength of 45,4 kN, whereas the joint design with optimized grooves had a much higher pull-out strength of 53,8 kN. All tested joints failed at the position where the finite element simulation predicted the highest tensile stresses in the tube (Figure 10).

The results from the finite element simulations were confirmed, but further optimization of the grooves is necessary in order to get the pull-out strength closer to the strength of the base material. An optimal joint would be stronger than the base material.

Figure 10: Specimen after tensile test: joint failure occurs due to shearing at the upper edge of the first groove

Figure 11: Mandrel with sharp edges cuts the tube

More experiments were done to investigate the influence of the groove radii. As expected it can be concluded that sharp edges combined with deep grooves should not be used in the joint design, because the mandrel then acts as a cutting tool (Figure 11).

Table 2 shows the parameters used for all the experiments. Groove 1 is the groove near the mandrel's end, which is to be chosen long and shallow. The shallower the groove, the smaller the edge radius can be without cutting the tube. Specimen H has the highest tensile strength, but the grooves still need further optimization to create a joint which is stronger than the base material.

sample name	groove 1				middle			groove 2				tensile strength [kN]
	radius	width	depth	radius	width	depth	radius	width	depth	radius	
A	1	6	3,5	1	4	1	1	6	3,5	1	39,94
B	0	6	3,5	0	4	1	0	6	3,5	0	23,25
C	1	6	2	1	4	0	1	6	3	1	39,26
D	1	8	1,5	1	4	0	1	4	2,5	1	41,66
E	1	6	2	0,5	4	1	0,5	6	2	1	45,41
F	0	6	2	0	4	1	0	6	2	0	47,98
G	0,5	6	1	0	4	0,5	1	6	2	1	37,89
H	0	8	0,5	0	2	0	1	6	1,5	1	53,83

Table 2: Results of the experiments with different configurations for the double groove mandrel

2.3.2   Industrial case study based on a single groove

The industrial case study is a steel to steel joint based on a single groove design. Both pieces are made of the same carbon steel and their dimensions are shown in Figure 12. Crimping experiments are performed to gain more insight in magnetic pulse forming of steel and on the effect of changing overlap lengths. The joint performance and quality will be evaluated by means of tensile tests and macroscopic examination of cross sections. A field shaper with inner diameter of 18 mm and axial length of 20 mm is used. Figure 12 clarifies the set up and indicates the three parameters that will be varied during the experiment: overlap length of field shaper and tube, overlap length of tube and mandrel, and the length of the rod end.
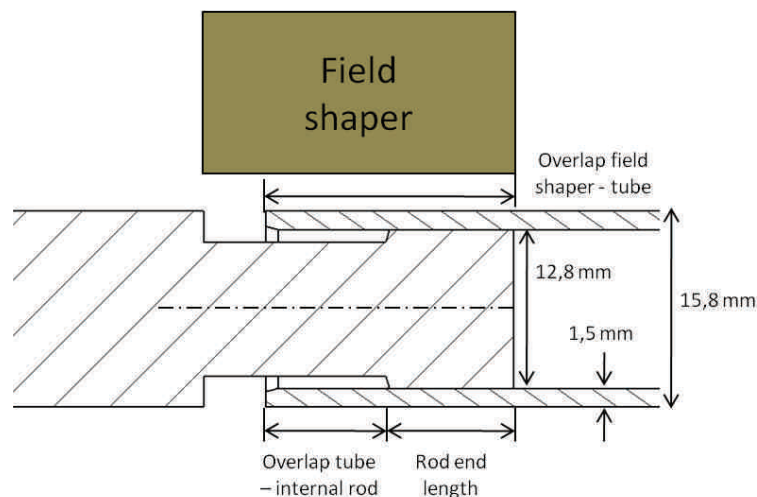
Figure 12: Industrial case study: axially loaded steel to steel crimp joint

For the first test series, the charging voltage of the machine was set to 10 kV. Visual inspection revealed that there was hardly any deformation, so the charging voltage was increased to 15 kV. Now the flyer tube was deformed but there was still a clearance between the mandrel's groove bottom and the deformed tube. Following, the maximum charging voltage (19 kV) was used to obtain a satisfactory result. Additional experiments at three distinct charging voltages between 15 kV and 19 kV were performed. Table 3 gives an overview of all performed experiments and the corresponding parameters. Every combination of process parameters is tested at least twice. The table also lists the evaluation methods and the available results of tensile tests. Eccentricity will be measured for several crimped joints:. the specimen will be clamped on a lathe and during rotating a dial test indicator will measure errors on the eccentricity.

Series	Charging voltage [kV]	Overlap field shaper - tube [mm]	Rod end length [mm]	Overlap tube - internal rod [mm]	Investigation method	Axial tensile load [kN]
1	15	15	10	10	Eccentricity + tensile test	
	16	15	10	10	Eccentricity + tensile test	
	17	15	10	10	Eccentricity + tensile test	
	18	15	10	10	Eccentricity + tensile test	
	19	15	10	10	Eccentricity + tensile test	
	19	15	10	10	Tensile test	30,7
	19	10	10	10	Tensile test	33,3
2	19	10	10	5	Eccentricity + cross section	
	19	10	10	5	Eccentricity + tensile test	
	19	10	10	5	Eccentricity + tensile test	
3	19	8	10	3	Eccentricity + cross section	
	19	8	10	3	Eccentricity + tensile test	
	19	8	10	3	Eccentricity + tensile test	
4	19	8,5	5	5	Cross section	
	19	8,5	5	5	Tensile test	25,8
	19	8,5	5	5	Tensile test	

Table 3: Overview of test parameters and evaluation methods used for the industrial case study

Most of the evaluations are still in process, so it is not yet possible to formulate clear conclusions.. However, the tensile test results obtained so far are promising. Reducing the overlap length of the field shaper and the tube, increased the strength of the joint from 30,7 kN to 33,3 kN. This can be explained by noticing that reducing the working area, results in a stronger magnetic pressure (as already discussed in paragraph 2.2) and increasing joint strength.

Figure 13 shows a cross section of a specimen from the fourth series, where localized thinning and shearing can be clearly seen at the edge of the mandrel. However, during the tensile test on that sample, the tube slid off the mandrel instead of breaking (which was the case for the other samples, Figure 15). Figure 14 shows the four visible cracks in the tube, each under an angle of 90 degrees. This is a natural consequence of the radial pressure working on the tube during its sliding.
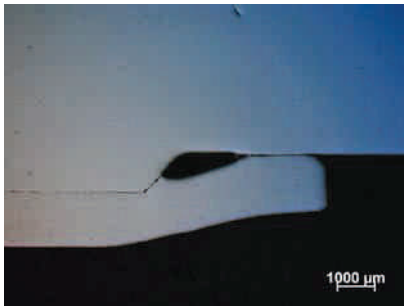
Figure 13: Cross section illustrating localized thinning and shearing of the tube

Figure 14: Tube with 4 cracks as a result of radial forces during relative sliding in the tensile test

Figure 15: Shearing of tube metal during tensile test

3   CONCLUSIONS

From literature, it was concluded that a rectangular shaped groove results in a strong axial joint. Adding a second groove may have a positive influence on the joint strength. Finite element analyse shows a clear contribution of a second groove. Based on the simulations an optimal design is proposed and tested.

The experiments on a double grooved mandrel confirmed the assumption that an optimized groove design consists of a first groove which is less deep and wider than the second groove. The tensile strength of the designed crimp joint is however still lower than the tensile strength of the base material. Thus further optimization of the grooves' dimensions is needed. Experiments also showed that if the groove radius is too small compared to its depth, the mandrel's edge will cut the tube. Further optimization of the double groove design will be done based on a combination of simulations and experiments.

The industrial case study of a steel to steel joint showed that for this material combination, a large voltage is needed in order to get a good joint. A joint strength higher than the base material was accomplished. Macroscopic images showed that a too sharp edge of the mandrel causes localized shearing and thinning of the tube. If the groove depth is small, the tube rather slips than shears at the edge, causing a weaker joint strength. In case of slipping, failure occurs by cracking of the tubular part More tensile tests and eccentricity measurements still need to be performed.

Based on the obtained results and a more experiment trials, process windows will be developed. A process window is a tool that can be used by an operator to easily determine the minimal charging voltage that is needed to obtain a sound joint for a given groove design.

By using axial groove cuts in the surface of the mandrel, a torque crimp joint can be designed. The influence of the axial groove parameters will be evaluated using the same approach as for the tension loaded crimp joints.

The suitability of different filler materials (rubber and solder) to be used in the magnetic pulse process and realize gas-tight crimp joints will be experimentally evaluated. Rubber sealing rings can be compressed easily and are widely used for various applications. Solder metals deform easily and can therefore fill the open areas without using too much energy.
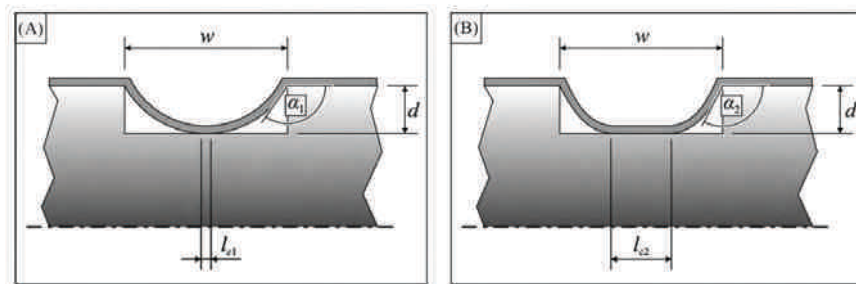
Figure 16: (A) connection with minimal needed voltage, (B) connection with a larger voltage than is minimally needed [1]

4 ACKNOWLEDGEMENTS

5 REFERENCES

[1]   Weddeling, C., Woodward,S.,Marré,M.,Nellesen,J.,Psyk,V.,Tekkaya,E.,Tillmann,W., *Influence of groove characteristics on strength of form-fit joints.* Journal of Materials Processing Technology, 2010.

[2]   Dehra, M.S., *High velocity formability and factors affecting it*, in *Materials Science and Engineering*. 2006, Ohio State University. p. 336.

[3]   *Innovative electromagnetic high-velocity welding techniques*. 2008; Available from: http://www.bil-ibs.be/NL/Onderzoek/Beelden/MPWeld.jpg.

[4]   Bahmani, M.A., K. Niayesh, and A. Karimi, *3D Simulation of magnetic field distribution in electromagnetic forming systems with field-shaper.* Journal of Materials Processing Technology, 2009. **209**(5): p. 2295-2301.

[5]   Hammers, T., et al., *Influence of Mandrel's Surface and Material on the Mechanical Properties of Joints Produced by Electromagnetic Compression.* Steel Research International, 2009. **80**(5): p. 366-375.

[6]   Pulsar, *Manual MPW 50 25 Magnetic Pulse System*.

[7]   Wilson, M.N., Srivastava,K.D., *Design of efficient flux concentrators for pulsed high magnetic fields*, in *The review of scientific instruments*. 1965: Berkshire, England.

[8]   Haiping, Y., et al., *Effect of field shaper on magnetic pressure in electromagnetic forming.* Journal of Materials Processing Technology, 2005. **168**(2): p. 245-249.

[9]   Pulsar (2008) *Coil/field shaper designing (company guidelines)*.

[10]   Schulze, V., Barreiro, P., Löhe,D., *Investigation of the Influence of Process Parameters on the Structure and the Mechanical Properties of Joints Produced by Electromagnetic Compression.* Advanced Materials Research, 2006. **10**: p. 79-88.

[11]   *Friction coefficients*. Available from:
         http://www.engineershandbook.com/Tables/frictioncoefficients.htm.
[12]   Eguia, I., Zhang, P., Daehn G.S., *Improved crimp joining of aluminium tubes onto mandrels with undulating surfaces*, in *Proceedings of the 1st International Conference on High Speed Forming*. March 31 –April 1 2004: Dortmund, Germany. p. Pages 161 - 170.
[13]   Broekaert, F., De Ketele,M., *An exploratory study into the feasibility of magnetic pulse forming*, in *Mechanical construction and production*. 2009, Gent. p. 284.
[14]   Bühler, H., von Finckenstein, E., *Fügen durch Magnetumformung.* Werkstatt und Betrieb 101, 1968: p. 671-675.
[15]   Golavashchenko, S. *Methodology of design of pulsed electromagnetic joining of tubes*. in *Proceedings of the TMS Symposium "Innovations in Processing and Manufacturing of Sheet Materials"*. 2001. New Orleans,LA,USA.
[16]   Park, Y., Kim, H. , Oh, S., *Design of axial/torque joints made by electromagnetic forming.* Thin-walled structures 43, 2005: p. 826-844.

LME SUSCEPTIBILITY OF GALVANISED WELDED STRUCTURES OF HIGH STRENGTH STEELS

M. Vermeersch[1], W. De Waele[2], N. Van Caenegem[3]

[1]Ghent University, Belgium
[2]Ghent University, Laboratory Soete, Belgium
[3]Ghent University and Belgian Welding Institute, Belgium

Abstract Hot dip galvanizing is a very popular and well known process in corrosion protection of steel. However, very occasionally, cracks appear on structures when they leave the zinc bath. The responsible crack phenomenon appears to be liquid metal embrittlement. This phenomenon is already known for a long time, but it is still not yet fully understood. The lack of fundamental theoretical knowledge and the absence of accurate models to predict liquid metal embrittlement oblige engineers to set up extensive test programs to determine an area of process parameters in which safe design is guaranteed. A qualitative understanding of the various influencing parameters during galvanizing is necessary to explain the occurrence of liquid metal embrittlement. This knowledge is also helpful to design an experimental test set up and procedure for evaluating the influence of one parameter where the effect of other parameters should remain constant. This master thesis deals with the occurrence of liquid metal embrittlement when galvanizing welded high strength steels. This paper gives an overview of the most important process parameters and gives a short description of possible future experimental work.

Keywords liquid metal embrittlement, LME, welding, high strength steel

1   INTRODUCTION

Hot dip galvanizing is a process in which a zinc coating is applied on a steel specimen. This metallic layer, which is metallurgically bonded with the steel substrate provides an excellent protection against corrosion. The zinc coating is applied by immersing the steel in a bath of zinc (450°C / 840 F). Considering the large amounts of steel structures that fail due to oxidation, corrosion protection is of great economical interest. A zinc layer provides three levels of protection. The first is the physical barrier that separates the steel from oxidation agents. Another protection level is the galvanic protection. The zinc acts as a sacrificial anode that makes iron oxidation impossible when the Zn layer is damaged. A final level of protection is offered by the zinc oxides that cover defects in the zinc layer. These three levels of protection make galvanizing more advantageous than painting, which only offers barrier protection.

The hot dip galvanizing process was patented in 1837 [1] and became widely used during the 20th century. The first ASTM standard concerning galvanizing dates from 1928 (ASTM Standard A 123, currently listed as "Standard specification for zinc (hot-dip galvanized) coatings on iron and steel" [2]). Since then, standards, practices and guides have been developed to avoid significant problems due to the galvanizing process. Nowadays almost all problems occurring after hot dip galvanizing are found to be due to misunderstanding of those codes [2]. However, during the last decades, cracks in galvanized steel have been sporadically reported. Those cracks originated at flame cut edges, welds or heavily cold formed parts. Examination of the cracks showed that they occurred due to liquid metal embrittlement (LME). This phenomenon is also called liquid metal assisted cracking (LMAC) or liquid metal induced cracking (LMIC) or liquid metal induced embrittlement (LMIE).
Welds in galvanized structures have been found to severely increase the LME susceptibility. Using high strength steels in galvanized structures also seemed to be detrimental to avoid LME cracking. In this master thesis, the LME susceptibility of welded high strength steels (Q&T and TMCP) will be investigated.

2   LIQUID METAL EMBRITTLEMENT (LME)

2.1   Introduction to LME

The failure process during liquid metal embrittlement is not yet fully understood. Hence, lots of definitions and models have been proposed to define and explain the phenomenon [3]. One of those definitions describes liquid metal embrittlement as "a mechanism one in which the ductility of a solid metal is reduced

by surface contact with a liquid metal" [4]. Despite the lack of fundamental knowledge of the failure process, the relative importance of influencing process parameters has been mapped in various research projects.

Liquid metal embrittlement was found to require an embrittling agent (in particular, the liquid zinc bath), a normally ductile embrittled metal and a force field at the time and place of the embrittling contact [2]. Cracks that occurred after retaining the steel part from a zinc bath are always intergranular [5].

The embrittling process during hot dip galvanizing is governed by lots of parameters, each of which cause a modification in at least one of the four influencing aspects which are represented in figure 1. The first aspect is the mechanical and metallurgical condition of the steel. The second is the environment, e.g. composition and temperature of the zinc bath. The third aspect is the acting forces, both residual and external ones. The last aspect represents the influence of time, which refers to the immersion time.
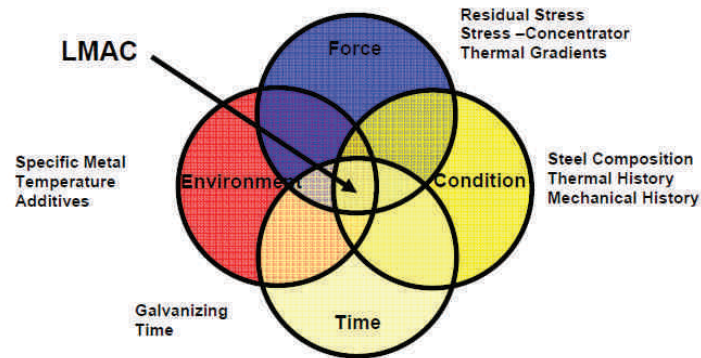
Figure 1. Aspects influencing LME [6]

2.2   Specificity of LME

Liquid metal embrittlement can only occur in particular combinations of solid and liquid metals. The solid should be sufficiently wetted by the liquid metal. Solid-liquid metal couples that form intermetallic compounds, usually do not show liquid metal embrittlement. The steel–zinc contact however is characterised by such compounds, as can be seen in figure 2. Research in specificity of liquid metal embrittlement showed that the Fe-Zn couple was not susceptible to liquid metal embrittlement.[7] Nonetheless the cracks found after galvanizing are clearly due to liquid metal embrittlement.
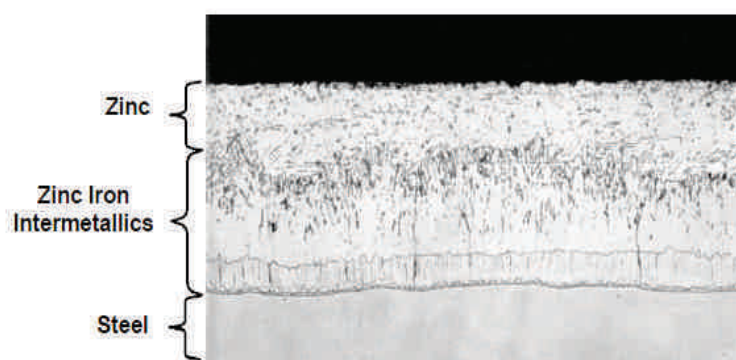
Figure 2. Typical galvanizing microstructure [2]

This seems to be contradictory, but can be explained when considering other elements apart from zinc that are used in a zinc bath. To obtain a smooth zinc surface after galvanizing, some elements are added to the zinc, amongst which are Pb, Sn and Bi. As can be seen on the EDX-analysis of a crack tip [6], the concentration of those elements at the crack tip has increased significantly compared to those in the zinc bath. These elements are known to sufficiently wet steel surfaces and thus show more liquid metal susceptibility compared to pure liquid zinc. They also have much lower melting temperatures than zinc.
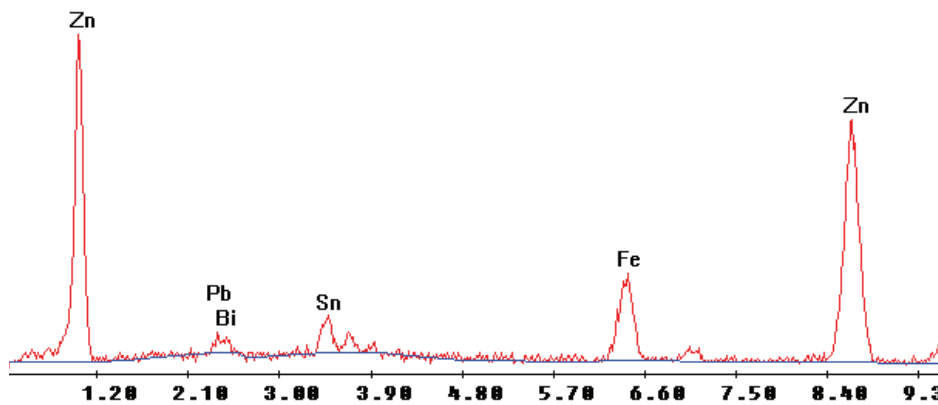
Figure 3. EDX analysis at crack tip [6]

2.3   Model for liquid metal embrittlement during galvanizing

Given the melting temperature and steel wettability of the afore mentioned additives, a model was proposed for cracking during galvanizing [2]. When the steel is immersed in the zinc, a reaction occurs between the steel and zinc, and intermetallic compounds are formed. The low melting temperature additives cannot participate and are banned from the reaction surface. Because zinc is consumed, the concentration of the additives near the steel surface increases and a thin layer is formed that separates the intermetallic compounds from the rest of the zinc bath. This layer prohibits uncontrolled growth of the intermetallic layers, what leads to a smooth surface.

However, when the liquid metal penetrates existing cracks, rejection of the afore mentioned additives is prohibited by the intermetallic layer that formed at the crack root. The liquid metal in the crack becomes trapped. The zinc continues to be consumed to form intermetallic compounds. A melting pool is formed in the crack and contains high concentrations of Pb, Sn and Bi which have not yet solidified because of their low melting temperatures. The remaining liquid metal is known to show a very high susceptibility to liquid metal embrittlement in combination with steel. The crack will propagate when enough stress is applied.

3   FORMER RESEARCH RESULTS

As mentioned before, the LME phenomenon is not yet fully understood. Theoretical insight of the metallurgical process is impeded by some factors. First of all, because of all the additives in the zinc bath, the growth of the zinc layer is not governed anymore by the simple binary Fe-Zn phase diagram. Secondly, different reactions take place at the same time: the wetting of the surface, dissolution of steel by zinc, isothermal solidification of intermetallic compounds, solid state diffusional phase transformations, and solidification of liquid zinc alloy. Moreover, those reactions all have a high reaction speed [8] .

Due to the lack of fundamental understanding, one cannot make theoretically based predictions regarding the exact influence of process parameters. This means that extensive testing is necessary to confine the limiting design properties that should not be exceeded in safe design.

3.1   Stress-strain behavior in liquid zinc

The first experimental programs about LME during galvanizing were started in the early eighties. Kikuchi investigated the LME susceptibility of steel by doing tensile tests on unnotched specimens in a zinc bath [9]. Figure 4 shows the resulting stress/strain curves. As can be seen on this figure, the steel shows a loss of some of its mechanical properties (as stiffness and strength). When tensile tests are done in the zinc bath, the resulting stress-strain curve follows the corresponding curve measured on a specimen tested in air at the same temperature. However when a certain threshold stress/strain is reached the curve drops down, the steel shows sudden fracture. This threshold stress always exceeds the yield stress. This observation cannot be extrapolated to other metal couples showing LME [10]. In actual structures, stress concentrations such as grain boundaries, second phase particles and notches are capable of producing localised plastic deformation sufficient to cause LME cracking, and general plasticity is not essential [11]. When no brittle fracture occurs, all mechanical properties recover when cooled to room temperature after galvanizing [12].

Not only strength (YS and UTS) and stiffness decrease when tested at elevated temperatures. Other research programs also found a detrimental effect on toughness [12][13]. However, all properties fully recover after galvanizing (when no LME has occurred).
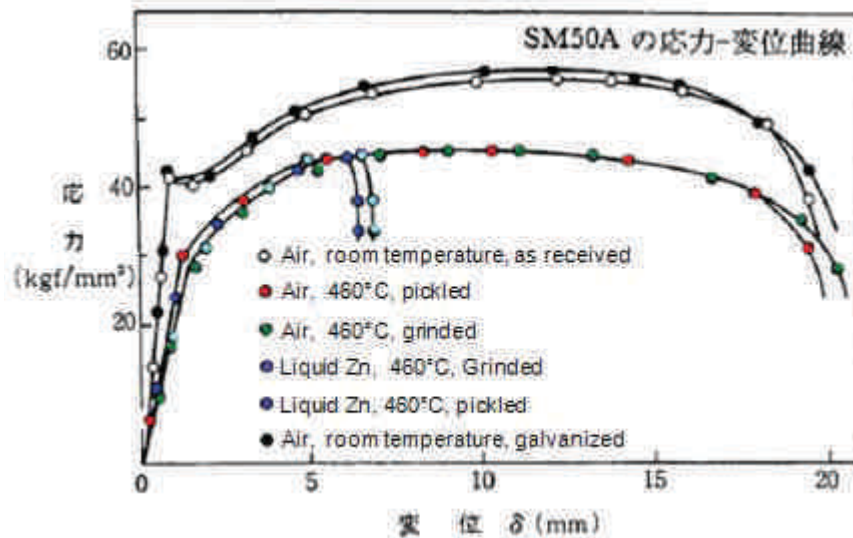
Figure 4. Stress/strain curves obtained from tensile tests [9]

3.2 Stresses induced during the galvanizing process

As mentioned before, stress is a predominant factor in LME initiation. Hence it is essential to know and understand the processes which cause stresses that can trigger LME initiation. Between dipping in the zinc bath and withdrawal, the temperature of the steel changes from the ambient temperature above the bath to the liquid zinc temperature and then back again. This temperature variation causes thermal gradients in the steel which induce stresses. The level of these stresses is a function of several parameters, of which the most important ones are [8]: the dipping and withdrawal speed and angle, the structure geometry and the bath composition (influence on the heat transfer rate at the solid liquid contact surface [2]). Preheating the steel can lower thermal gradients, as can lowering the bath temperature.

These stresses can accurately be modeled with finite element simulations [12]. The results however are only valid for one combination of the influencing parameters described above and the simulations are rather time consuming. Nonetheless such simulations can give insights in the relative importance of the parameters. The European test program "Failure mechanisms during galvanising" [12] did some extensive research on those parameters.

3.3 Stresses in galvanized structures induced by manufacturing

Several manufacturing processes are known to introduce residual stresses in structures. The stresses result from cold working or thermal processes (e.g. flame cutting and welding). Residual stresses can be detrimental regarding to LME.

3.4 Hydrogen embrittlement

In industrial galvanizing, the structures are chemically cleaned by pickling and fluxing before entering the zinc bath. These processes are known to introduce significant hydrogen concentrations on the surface (figure 5). This might increase the susceptibility to hydrogen embrittlement during galvanizing. However all test programs regarding hydrogen embrittlement concluded that the H concentrations didn't cause cracking except for steels with tensile strengths > 800 MPa [12][13]. These tests were performed with smooth steel specimens. However when manufacturing processes result in high local hardness, hydrogen embrittlement can become a problem. This local hardness can be induced by welding, flame cutting or severe cold working. Especially the welding process is known to introduce hydrogen microcracks, when executed in suboptimal conditions [14]. It is recommended not to exceed hardness values above a certain threshold

(±300 HV) [15],[2]. Several guides and standards have been written, e.g. EN 1011-2, that can be followed in order to avoid hydrogen induced cracking [15] .
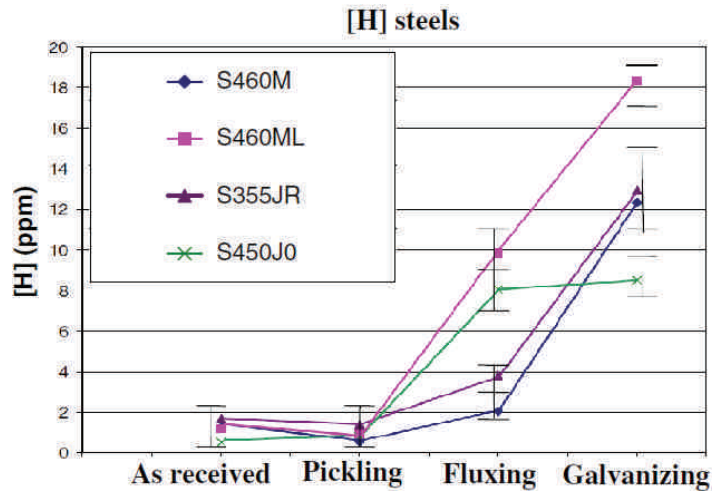

Figure 5. Evolution of hydrogen concentration on the steel surface[16]

3.5   Influence of steel microstructure

The microstructure of the steel surface also has a strong influence on the liquid metal susceptibility. Some researchers linked the susceptibility to the carbon equivalent value (CEV) which is generally used in welding practices. They proposed a CEV limiting value that should not be exceeded in safe design [14]. This value however is no "condition sine qua non" to allow safe design, as there are lots of other influencing parameters.

Not only the overall steel composition is important, also the metallurgical structure of the steel (e.g. grain size, apparent phases,…) is decisive for liquid metal embrittlement. This metallurgical state of the surface can be severely altered by welding processes. Therefore welding parameters as cooling rate and welding material should be chosen carefully.

4   FUTURE WORK

The final goal of this thesis is to define a restricted area in which galvanizing process parameters can vary ensuring a safe design of high strength steel welds. Though the obtained results are, strictly taken, only valid for the used steels and zinc baths, extrapolating the results will certainly improve qualitative understanding in the behaviour of welded high strength steels in general.

In the test procedure, the welding of the steel will be simulated by imposing a temperature cycle on the test specimens. This cycle will result in a certain metallurgical state. This state will approach the one of the HAZ of the base material after an actual welding process in which the same temperature cycle is imposed.

After the welding simulations, the specimens need to be cleaned, before entering the zinc bath. When using different cleaning methods one can evaluate their influence, e.g. chemical cleaning which can cause hydrogen embrittlement versus mechanical cleaning methods like sand blasting.

To evaluate the LME susceptibility the specimens finally need to be stressed in a liquid zinc environment. The necessary equipment to perform traditional tensile tests in a zinc bath, is currently not available at the laboratory. However there are three alternative solutions

1) Tensile tests can be done in cooperation with the university FH Esslingen, Germany

2) A simple small scale test setup can be designed that allows testing at the galvanizing company Galvapower in Dendermonde, Belgium

3) The test specimens can be galvanized without implied stresses and can afterwards be tested with test equipment which allows testing at elevated temperatures. In this case, the testing temperature would be the one of the zinc bath.

5   ACKNOWLEDGEMENTS

6   REFERENCES

[1] Specification of a patent granted for a process for protecting articles made of iron or steel from oxidation. Granted to M. Sorel, of the city of Paris in the kingdom of France. December 1837. , American railroad journal – volume 7, 116-119, 183

[2] Kinstler T. J., Current knowledge of the cracking of steels during galvanizing, Galvascience LLC

[3] Coen G. Mechanical behavior of structural steels in liquid lead-bismuth, for ADS nuclear facilities, 2008

[4] Joseph, B., Picat, M., and Barbier, F., "Liquid Metal Embrittlement: A state-of-the-art appraisal, The European Physical Journal, Applied Physics, Volume 5, 19-31, 1998

[5] Feldmann M., Pinger T. Schäfer D., Sedlacek G., New rules in DASt-Richtlinie 022 for avoiding liquid metal assisted cracking (LMAC) of prefabricated structural steel components during hot-dip galvanizing, 2009

[6] Vervisch A., Liquid Metal Embrittlement in the heat affected zone of welded high strength steel during batch hot dip galvanizing – Influence of steel composition and microstructure, 2009

[7] Fernades P.J.L., Jones D.R.H, Specificity in liquid metal induced embrittlement, *Engineering Failure Analysis,* Vol 3, No. 4, 299-302, 1996

[8] A.R. Marder, The metallurgy of zinc coated steel, Progress in Materials Science 45, 191-271, 2000

[9] M. Kikuchi, Liquid metal embrittlement of steels during hot dip galvanizing, Tetsu to Hagane, (Iron and Steel) Volume 68, Number 14, 1870-1879, 1982

[10] Ho-Seok Nam, Srolovitz D. J., Effect of marererial properties on liquid metal embrittlement in AL-Ga system, Acta Materialia 57, 1546–1553, 2009

[11] Fernades P.J.L., Jones D.R.H, Clegg R.E., Failure by liquid metal induced embrittlement, Engineering Failure Analysis, Vol. i, No. 1, 51-63, 1994

[12] Failure mechanisms during galvanizing, 2008

[13] Effect of Galvanizing on High Performance Steels and their weldments - Summary of the IZA ZC-21 Project, 2009

[14] James M.N., Designing against LMAC in galvanised steel structures, Engineering Failure Analysis 16, 1051–1061, 2009

[15] Mraz L., Lesay J., Problems with reliability and safety of hot dip galvanized steel structures, Soldagem & inspecao Volume 14 Issue: 2, 184-190, 2009

[16] Carpio J., Casado J.A. , Ivarez J.A. A, Gutierrez-Solana F., Environmental factors in failure during structural steel hot-dip galvanizing, Engineering Failure Analysis 16, 585–595, 2009

FRICTION WELDING OF STEEL TO CERAMIC

P. Rombaut[1], W. De Waele[2] and K. Faes[3]

[1] Ghent University, Belgium
[2] Ghent University, Laboratory Soete, Belgium
[3] Belgian Welding Institute, Belgium

Abstract

The goal of this paper is to give a clear summary of the literature review performed during the master thesis on friction welding on dissimilar materials. Of main interest for this work is the welding of steel to a ceramic material such as alumina (Al_2O_3). Because of the difficulties involved in producing a sound weld for this material combination, not a lot of literature is available on this topic. This paper starts with a discussion on the basics of friction welding and typical problems encountered in welding of steel to ceramic.

Almost all research articles that have been found in open literature state that welding steel to a ceramic is nearly impossible without using an interlayer consisting of a compatible metal. The most frequently reported type of weld is steel to alumina with an aluminium interlayer. For this reason the literature study included in this thesis, also focuses on friction welding of aluminium to steel and aluminium to ceramic. A detailed explanation will be given for the most challenging difficulties like the creation of a brittle intermetallic compound layer in a steel-aluminium weld interface and the creation of fatal thermally induced stresses in an aluminium-ceramic weld interface. Both of these problems must be dealt with in order to produce a strong bond. A redesigned rotary friction welding machine is currently being assembled and will be used for the experimental part of this research.

Keywords friction welding, ceramics, steel, aluminium

1   INTRODUCTION

The main objective of the thesis is to investigate the possibility of joining dissimilar materials by means of friction welding. The material combination that will be studied in detail consists of steel and ceramic material. At first, a literature study has been conducted to get a basic understanding of the principles of friction welding, and of the physical phenomena which are important in welding steel to ceramics. This specific material combination is relatively new, but has a lot of potential applications in today's industry.

In the modern industry, there is a constant drive to make everything lighter, stronger and more durable. The studied material combination combines the strength, high ductility and toughness, and adaptability of steel with the advantages of technical ceramics, such as high hardness, wear resistance, chemical inertness, corrosion resistance, low thermal expansion coefficient and resistance to high temperatures. This ensemble of properties is especially useful in area's like the automotive, aerospace, electronics, and nuclear industries.

Friction welding is a solid state welding process that allows joining of specific material combinations which are considered unweldable by conventional techniques. In order to produce a friction weld, the two components are forced to rotate against each other (friction phase), thereby generating heat at the interface. Once the desired upset length or process time has been reached, the rubbing motion stops (braking phase), the pressure rises (swelling time) and the components are pressed against each other (forging phase) until they are cooled down. The main variables in friction welding are the rotational speed, the axial forces during the friction and forging phases, and the welding time. The typical relationship of these characteristics is shown in Fig. 1 which illustrates a direct drive friction welding process.
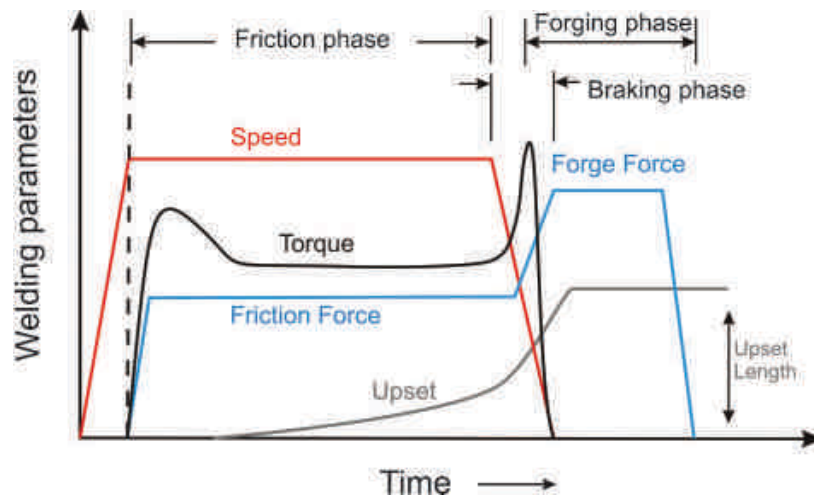
Fig. 1: Variation of the welding parameters with time in direct drive friction welding. (2)

In order to make such a weld, a rotary friction welding machine has been redesigned (see Fig. 2) (2) to meet the specific demands of the material combination steel – ceramic. The final goal of this thesis is to use this machine to make successful welds between metal and ceramic bars and to investigate the integrity and strength of this weld by means of microscopic examination and fracture tests.
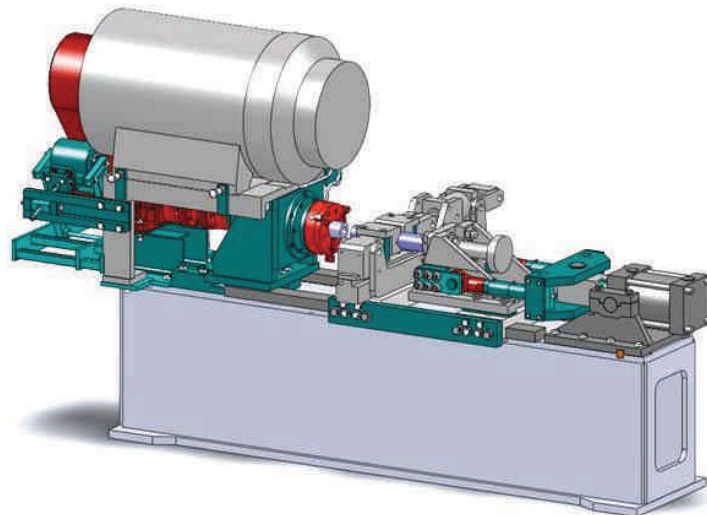
Fig. 2: Redesign of the rotary friction welding machine (2)

2   CHALLENGES IN FRICTION WELDING OF CERAMIC TO STEEL

It is not straightforward to make a sound and strong bond between a ceramic material and steel. Sometimes the joint will prematurely break at the interface or in an adjacent area in the ceramic material [(4) (5)]. This mostly happens during the cooling down phase when cracks initiate and propagate, or during post-welding mechanical treatments. The reasons for this observed fracture behaviour can be attributed to differences in thermal and mechanical properties and in the crystallographic structures of the two materials.

There are three major causes related to the welding problems observed for this material combination:
*   There is an important difference in the type of atomic bond between a ceramic and steel. Bonding in ceramics is mainly of an ionic or covalent nature (and usually a hybrid of these), while metals have a metallic bonding character.
*   There is often a very big difference in thermal expansion between the two materials. Ceramics typically have a much lower thermal expansion coefficient. When the two parts cool down after welding, this induces thermal stresses at the weld interface which could lead to cracking.
*   The brittle and porous nature of ceramics makes it very hard to absorb production defects. The strength of a ceramic is highly dependent of its grain size and surface roughness. (6)

Despite these problems, joints between steel and ceramics have already been realized successfully trough rotary friction welding [(3) (5)]. Fig. 9 shows that alumina (Al_2O_3) and mild steel rods were successfully joined using friction welding at a rotational speed of 900 rpm. However a 1 mm thick aluminum sheet has been used as soft interlayer (5).

Fig. 3: Successful friction welds of alumina to mild steel (5)

A successful joint almost always contains a stress-relieving metallic interlayer that absorbs the stresses caused by the thermal expansion difference of the two base materials. The aluminum interlayer has been found to be an essential intermediate medium in the formation of a sound joint between alumina and mild steel. It acts as a ductile buffer which is capable of absorbing deformations and stresses related to the high temperature gradient during the cooling phase (5).

Because of the third type of material that is introduced in the welding process, the weld geometry becomes even more complex. The bond now consists of two weld interfaces, namely a steel/aluminium and an aluminium/alumina weld interface. Both of these interfaces need to be free of defects and have a maximum strength in order to optimize the total bond strength.

3   FRICTION WELDING OF ALUMINIUM TO STEEL

3.1   Difficulties

Joining of aluminium to steel is not easy for the following reasons (6):

- Much higher melting points of steels compared to aluminium alloys.
- Difference between the thermal expansion coefficients of steel and aluminium.
- The very tenacious superficial oxide film on aluminium alloy, which interferes with the achievement of a metal-to-metal contact at the interface.
- The formation of brittle intermetallic compounds (IMC).

The most serious of these problems is the formation of brittle intermetallic compounds (IMC) resulting from the reaction of Al with Fe. In particular, fusion welding involves the formation of large amounts of intermetallic compounds in the weld metal because the steel and the aluminium alloy are mixed in the liquid state. This material combination is therefore considered to be unsuitable for fusion welding. Friction welding is a process most widely used for joining of dissimilar metals, and for aluminium to steel in particular, because of its high productivity and reliability of the joint performance in addition to the controllability of the formation of the IMC layer. The following paragraph discusses the formation of IMC layers in more detail.

3.2   Occurrence and growth of the intermetallic compounds in rotary friction welding

Tylecote (7) stated that the formation of Al-Fe intermetallic compounds at the weld interface causes a serious reduction of the joint strength. Wallach and Elliot (8) (9) suggested by reviewing previous papers that a reduction of the joint strength only occurred when the thickness of the IMC layer exceeded about 1 µm. They also suggested that the addition of Mg to the aluminium alloy enhances the growth of the IMC layer and reduces the joint strength, whilst Si addition retards the growth of the IMC layer and thus improves the joint strength.

In order to get an improved insight in the growth of the intermetallic compound layer, Yamamoto et al. (10) (11) (12). investigated the nano-scale microstructures of the friction weld interface of aluminium alloys (A5052, A5083 and A1070) to low carbon steel (S10C). For all these weld trials, the tensile strength of the joint had a common tendency to first increase with friction time up to a maximum value, and then to decrease with a further increase in friction time (see Fig. 4). The maximum joint strength obtained, was approximately equal to the tensile strength of the (weakest) base material.
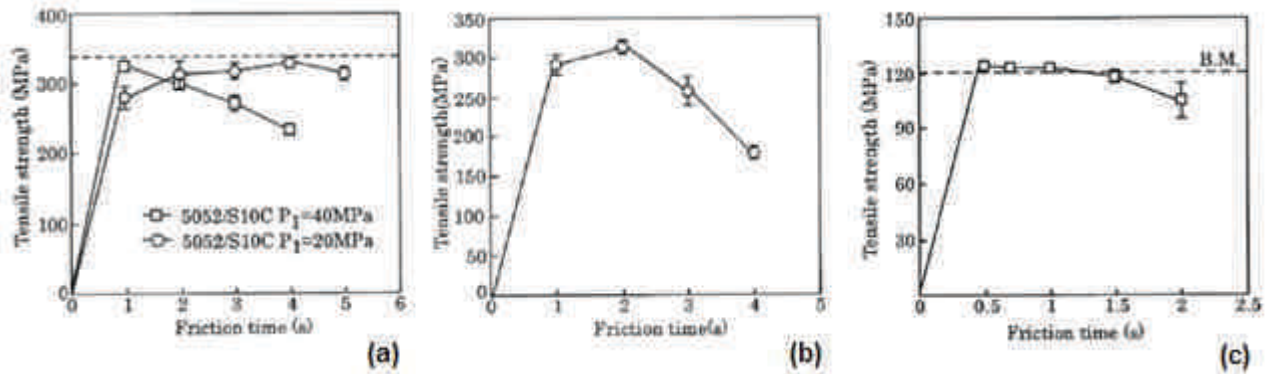
Fig. 4: Tensile strength vs. friction time for friction welds of steel S10C to aluminium alloys A5052 (a), A5083 (b) and A1070 (c). P_1 resembles the friction pressure during the friction phase.

3.2.1 Al-oxide layer

Observations of the fracture surfaces and interfacial microstructures suggest that an Al-oxide film of ~10 μm thickness was present at the joint interface for the shorter friction times (i.e. when the tensile strength increased with friction time, see Fig. 4). The tensile cracks of the test specimens propagated along this oxide film.

Probably this Al-oxide layer originated from the superficial oxide film that gives the Al alloy corrosive resistant properties. Oxide contamination in the interface reduces the quality of the weld. This may be explained in terms of interface impurities, which do not permit a close contact between the base materials, which is necessary to obtain full bonding (13).

3.2.2 The Al-Fe IMC layer

When the friction time was longer than the one corresponding to the maximum joint strength (see Fig. 4), the Al-oxide film at the interface was not longer observed. The tensile cracks of the test specimens propagated through the IMC layer, which occupied almost the whole area of the interface. The relation between the tensile strength of the joints and the thickness of the IMC layer is shown in Fig. 5 for the three material combinations.

Fig. 5: Relations between the tensile strength and the thickness of the IMC layer for the A5052/S10C, A5083/S10C, and A1070/S10C joints.

The tensile strength of the joints which fractured in the IMC layer was found to decrease with an increasing thickness of the IMC layer. This thickness increased almost proportionally to friction time at a rate depending on the kind of Al alloy. An increase in the friction pressure was found to enhance the growth rate of the IMC layer. It is clear that in order to produce a sound weld with optimal strength, the thickness of the IMC layer has to be controlle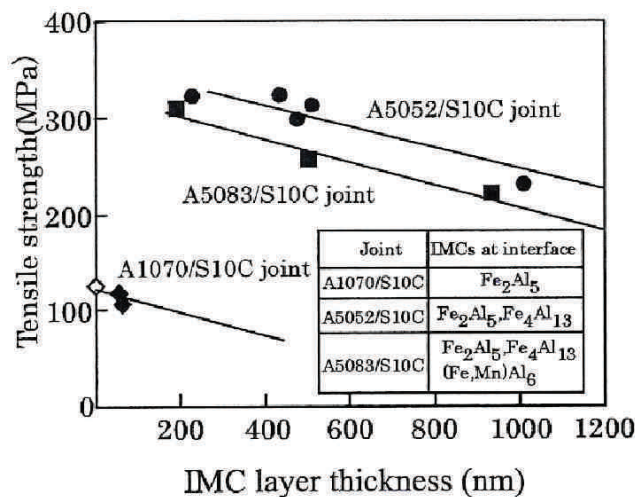d to stay within certain limits. Although the presence of a small amount of intermetallic components seem to be favourable for the weld quality, the thickness of the IMC layer must not exceed the proposed thickness of 1 µm.

Typical IMC layers observed in the joints of steel to A5052 and A5083 Al alloy and to A1070 pure aluminium, are shown in Fig. 6 (a), (b), and (c), respectively.
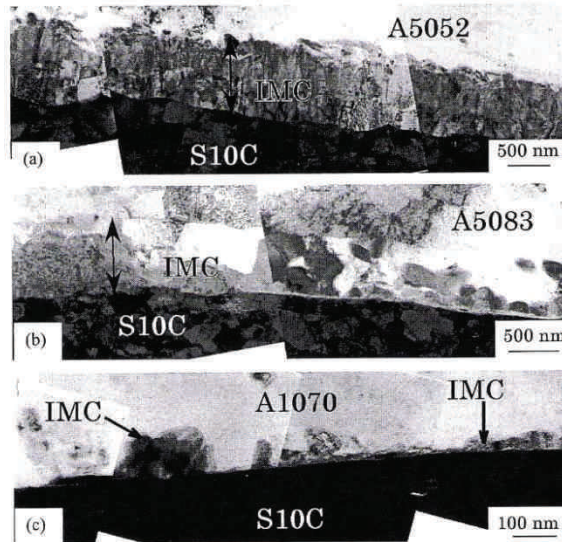
Fig. 6: IMC layers observed at friction-bonded interfaces: (a)A5052/S10C joint (P_1=40MPa, t_1=4s), (b) A5083/S10C joint (P_1=40MPa, t_1=3s), and (c) A1070/S10C joint (P_1=20MPa, t_1=2s). t_1 resembles the duration of the friction phase.

3.2.3 $MgAl_2O_4$ oxide layer

When the friction time was at its maximum (see Fig. 4), a magnesium-aluminium-oxide layer ($MgAl_2O_4$) was formed in addition to the intermetallic compounds. The A5083/S10C joint reached much lower tensile strength than that estimated from the IMC layer thickness and using the relation shown in Fig. 4. This result suggests that the $MgAl_2O_4$ layer impaired the joint strength more seriously than the IMC layer. The presence of this layer can be considered as a cause for the decrease in joint strength when the friction time further increases.

In order to confirm this assumption, the cross section of the fractured surface of a joint welded with a high friction time was observed with TEM. The observed microstructure of the fractured surface (A5083 Al-alloy side) is shown in Fig. 7 .
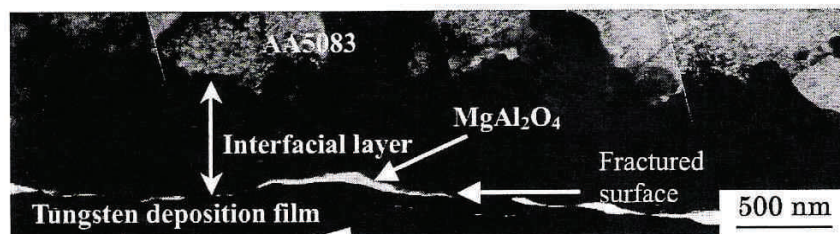
Fig. 7: Fractured surface observed in a joint bonded at friction time of 4 s

This micrograph confirmed that the fracture occurred along the $MgAl_2O_4$ layer, since this layer was observed along the entire fractured surface. For shorter friction times it was observed that the fracture occurred at the Al-oxide layer between the IMC layer and steel substrate (t_1 = 1 s), and along the IMC layer (t_1 = 2 s).

These microstructures can clearly be considered to be critical factors controlling the bond strength of the joints obtained under the given conditions. Since the bond strength was significantly reduced by an increase in friction time from 2 to 4 s, the $MgAl_2O_4$ layer can be regarded as more harmful to the bond strength than the IMC layer.

4   FRICTION WELDING OF ALUMINIUM TO CERAMIC

In order to reach an optimal strength of the weld interface, it is important to keep in mind that the difference in thermal expansion of the two welded pieces needs to be carefully controlled. The stresses induced during cooling down after welding can be sufficient to cause the joint to crack and prematurely fail.

4.1   Thermally induced stresses.

To investigate this phenomenon, Zimmerman et al. (13) (14) and R. Weiss (16) have made various finite element simulations of the heat generation throughout the weld pieces and the contact pressure distributions at the weld interface. The workpieces they used for the experimental validation were rods of 10 mm diameter made of corundum ceramics (97.5% Al_2O_3) and aluminium alloy 6061-T6.

The optimal friction welding conditions that where applied for bonding aluminium alloy 6061-T6 and ceramic Al_2O_3 are given in Table 1 and were originally established by Wlosinski et al. (2004) (14).

Rotational speed (rpm)	14,500
Friction time (ms)	850
Swelling time (ms)	3,500
Pressure in the friction time (MPa)	18
Pressure in the swelling time (MPa)	46
Delay time (ms)	80

Table 1: Friction welding conditions (Wlosinski et al., 2004) (14)

4.1.1   Heating phase.

The temperature distributions at the contact surface for different periods of frictional heating are presented in Fig. 8. Figure 9 shows the temperature distribution in the two joined elements as a function of friction time. It is clear that the temperature is not uniformly distributed over the joint interface. The outer regions of this interface (i.e. the most distant from the axis), remain at a lower temperature for a long time. This might have a negative influence on the quality of the joints in the vicinity of the outer diameter. This is confirmed by observing tensile test specimens, as shown in figure Fig. 11, where the whiter regions represent alumina particles that have been welded to the metal and the more gray regions did not form a strong bond. Also note that a flash is developed in the aluminium workpiece (Fig. 9), which leads to a geometrical discontinuity and stress concentration.
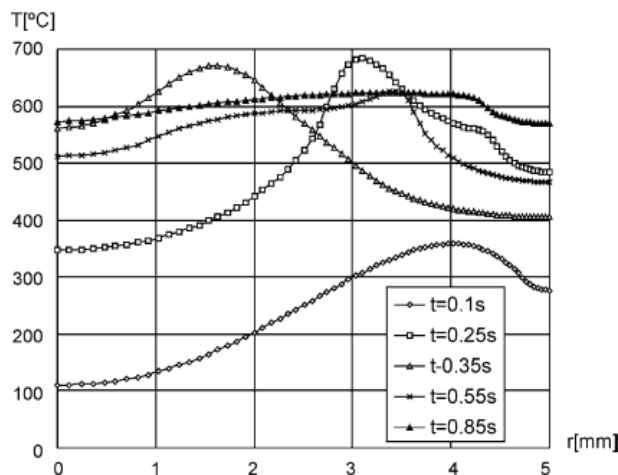
Fig. 8: Temperature variation over the joint interface for selected values of heating time.
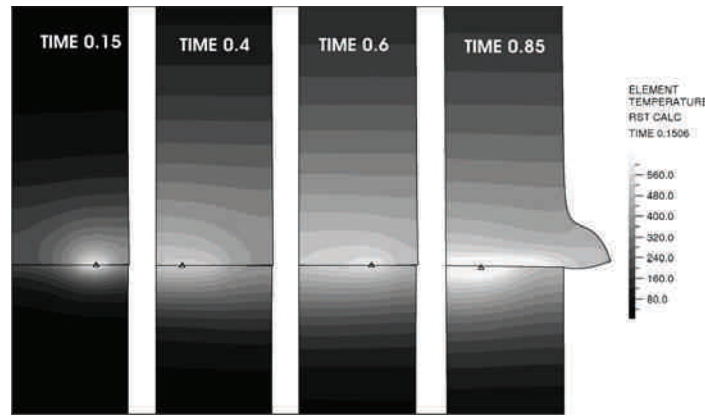
Fig. 9: Temperature distributions in the welded materials for selected values of friction time.

The high temperatures and the applied friction pressure cause local plastic and thermal deformations at the joint interface which mainly occur in the aluminium workpiece. The ceramic does not deform significantly. As a result the actual contact area changes continuously. The heat flux depends on the bearing surface and the temperature dependent friction coefficient. For a heating time of 0.455 s the deformation (scaled up eight times) of the aluminium workpiece near the welding zone and the distribution of temperature and contact forces (dashed area), is shown in Fig. 10.
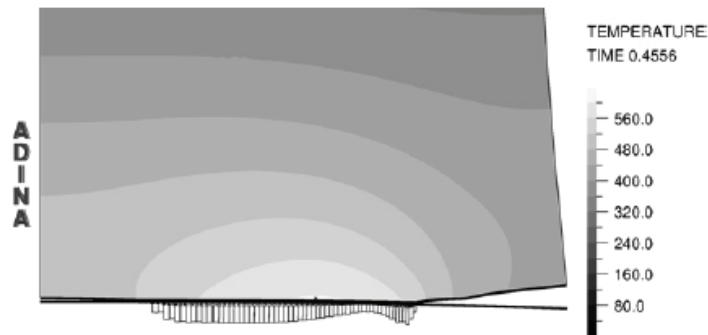
Fig. 10: Deformation of Al in the vicinity of the contact zone scaled up eight times, bands of equal temperature and contact force distribution (time of heating 0.455 s)

The contact pressure distribution is found to be close to uniform only in the last phase of friction. However, the regions most distant from the axis never come into contact during the friction stage. This means that the bond at these regions may be weaker. The pictures of fractured joints after tensile testing confirm this conclusion (Fig. 11).
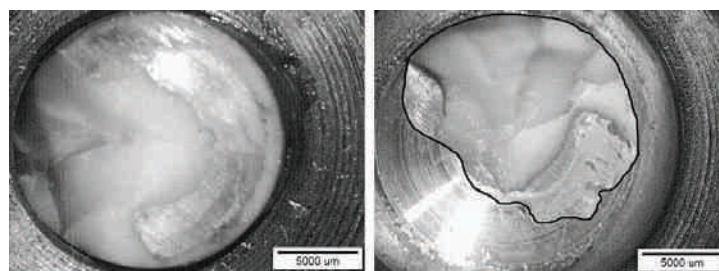
Fig. 11: Pictures of bonds destroyed during tensile tests.

In the friction welding process it is very important to get the surfaces of the two workpieces so close together that atomic forces are applied. In Fig. 12 the contact pressure distribution after the flash formation is presented. This corresponds probably to the period the bond is created. The contact pressure distribution is inhomogeneous, with the smallest values occurring at the outer areas. It means that the closeness of the bonded surfaces is non-uniform. This can also contribute to a weaker joint in the areas most distant from the axis of the welded components.
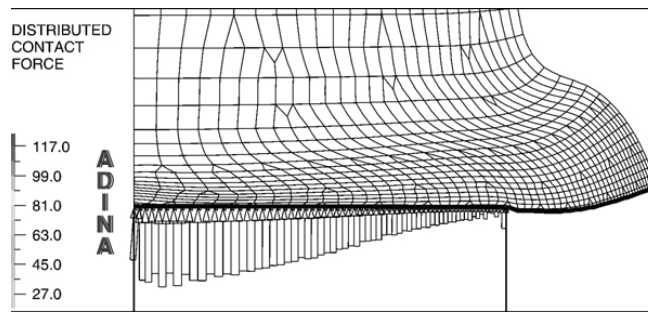
Fig. 12: Pressure distribution on the flat contact surface during the creation of the bond.

4.1.2   The cooling phase.

When the joint is cooled down to ambient temperature after friction welding, the thermal stresses change their signs (from a compressive stress during expansion to a tensile stress during shrinking). The unbeneficial tensile stress area enlarges during the cooling period. As a result residual stresses are generated, which is caused mainly by different physical and mechanical properties of both joined materials. In Fig. 13, calculated residual equivalent stress and axial stress in a ceramic workpiece and in the vicinity of the contact surface are shown, as function of the radial distance. Close to the central axis the equivalent stress reaches its maximum value close to 150MPa. Axial tensile stresses also develop in that region (the maximum value reaches 120MPa). This is harmful for the joint integrity since ceramic materials cannot withstand high tensile loading (and certainly not in the presence of weld impurities or defects). It was indeed observed in the tensile test that the fractured areas of the ceramic (Fig. 11) corresponds with regions of an axial tensile stress appearance. The mechanical tensile strength of the welded joints was about 30MPa.
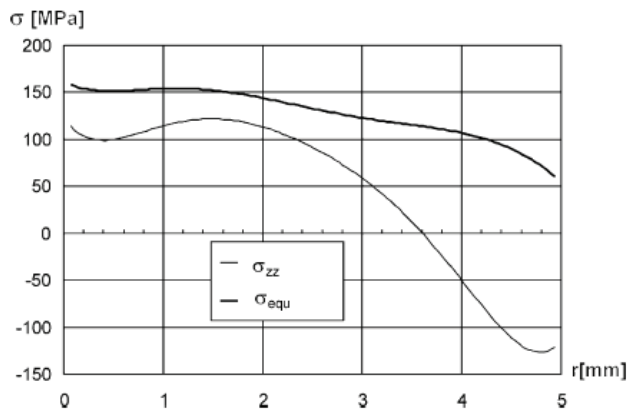
Fig. 13: Residual stress profile in a ceramic workpiece near the bond area obtained by FEM.

5   CONCLUSIONS

The results of this literature study show that there are two major points that are important when it comes to welding steel to a ceramic material.

- The use of an interlayer is necessary to reduce the amount of residual stresses that are induced because of the different thermomechanical properties of the workpiece. Aluminium sheet is a commonly used interlayer.
- Attention is needed to control the creation of a brittle intermetallic compound layer that grows in the aluminium-steel weld interface in proportion to the friction time.

In order to create a bond with maximum strength, these two phenomena will need to be optimized.

Once the new friction welding machine is assembled and operational we can start to put these ideas into practice.

6 NOMENCLATURE

σ	Stress	[MPa]
P_1	Friction pressure	[MPa]
t_1	friction time	[s]

7 ACKNOWLEDGEMENTS

The authors would like to acknowledge the technical staff of the Belgian welding institute and Laboratory Soete for their support in building the rotary friction welding machine..

8 REFERENCES

1. *REVIEW Friction welding – critical assessment of literature.* **Maalekian, M. Graz.** University of Technology : Institute of Materials, Minerals and Mining, 10 09 , 2007, pp. 738-759.
2. **Bart Derynck, Dries Bonte.** *Ontwikkelen van een wrijvingslasmachine voor het verbinden van ongelijksoortige materialen.* Universiteit Gent : s.n., 2010.
3. *THE FRICTION JOINING OF CERAMICS TO METALS.* **ESSA AA, BAHRANI AS.** 2, Dublin, Ireland : ELSEVIER SCIENCE SA LAUSANNE, PO BOX 564, 1001 LAUSANNE 1, SWITZERLAND, 1991, JOURNAL OF MATERIALS PROCESSING TECHNOLOGY , Vol. 26, pp. 133-140. 0924-0136.
4. *Alumina-mild steel friction welded at lower rotational speeds.* **Mohamad Zaky Noh, Luay Bakir Hussain, Zainal Arifin Ahmad.** 1-3, Malaysia : Elsevier B.V., 2007, Journal of Materials Processing Technology, pp. 279-283.
5. *Mechanical behaviour of ceramics.* **DAVIDGE, R.W.** Cambridge : Cambridge University Press, 1987.
6. *Effect of interfacial reaction layer on bond strength of friction-bonded joint of Al alloy to steel.* **Naotsugu Yamamoto, Makoto Takahashi, Masatoshi Aritoshi, Kenji Ikeuchi.** Japan : s.n., 2005. IIW Doc. IX-2190-06.
7. *The solid phase welding of metals.* **Tylecote, R.F.** [ed.] Edward Arnold Ltd. London : s.n., 1968, p. 154.
8. *Joining aluminium to steel Part 1-Diffusion bonding.* **E.R.Wallach, S.Elliott and.** 1981, Metal Construction, pp. 167-171.
9. *Joining aluminium to steel Part 2-Friction bonding.* **E.R.Wallach, S.Elliott and.** 1981, Metal Construction, pp. 221-225.
10. *Effects of interfacial microstructure on friction-bonded strength of low carbon steel to Al-Mg alloy (AA5083).* **Naotsugu Yamamoto, Makoto Takahashi, Masatoshi Aritoshi, Kenji Ikeuchi.** Japan : s.n., 2004, pp. 296-299. IX-2104-04.
11. *Effect of interfacial reaction layer on bond strength of friction-bonded joint of Al alloyto steel.* **Naotsugu Yamamoto, Makoto Takahashi, Masatoshi Aritoshi, Kenji Ikeuchi.** Japan : s.n., 2005. IIW Doc. IX-2190-06.
12. *Formation of Intermetallic Compounds in Friction Bonding of Al Alloys to Steel.* **Naotsugu Yamamoto, Makoto Takahashi, Masatoshi Aritoshi, Kenji Ikeuchi.** Japan : Trans Tech Publications, 2007, Materials Science Forum (Volumes 539 - 543), pp. 3865-3871.
13. *Investigation into the properties of friction-welded aluminium bars.* **Bekir S. Yilbas, Ahmet Z. Sahin, Ali Coban, B.J. Abdul Aleem.** Dhahran, Saudi Arabia : Elsevier science S.A., 1994, Journal of Materials Processing Technology. SSDI 0924-0136(95)01923-3.
14. *Thermo-mechanical and diffusion modelling in the process.* **Jolanta Zimmerman, Wladyslaw Wlosinski, Zdzislaw R. Lindemann.** Warsaw, Poland : Elsevier, 2009, journal of materials processing technology, pp. 1644–1653.
15. *Thermo-mechanical phenomena in the process of friction welding.* **Z. LINDEMANN, K. SKALSKI, W. WŁOSIN´ SKI, and J. ZIMMERMAN.** Warsaw, Poland : s.n., 2006, BULLETIN OF THE POLISH ACADEMY OF SCIENCES.
16. *Residual stresses and strength of friction welded ceramic/metal joints.* **Weiss, R.** Weinheim, Germany : s.n., march 1998, welding research supplement.
17. *Advanced materials & processes inc. metal progress.* 1987.
18. *REVIEW Friction welding – critical assessment of literature.* **Maalekian, M.** Graz University of Technology : s.n., 10 09, 2007, Institute of Materials, Minerals and Mining, pp. 738-759.
19. **Faes, dr. ir. K.** *General introduction to friction welding processes.* [powerpointpresentation – Workshop on friction welding] Gent : Belgian Welding Institute, 2010.
20. **AG, KUKA.** KUKA, sl : sn.
21. *The Effect of Joint Design and Volume Fraction on Friction Welding Properties of A360/SiC (p) Composites.* **C. B. LIN, C. K. MU, W. W. WU AND C. H. HUNG.** Taiwan, P. R. China : Department of Mechanical Engineering, Tamkang University, 1999.
22. **Smet, Jean-Pierre.** *Cursus Materialenleer.* Hoboken : Karel de Grote-Hogeschool Antwerpen, 2008. KdG-IWT-MA-EMEM-08.

23. **Nicholas, M. G.** *Diffusion bonding ceramics with ductile metal interlayers.* Oxfordshire, England : Material Development Division, AERE Harwell, 1986.

24. **Kazakov, N.F.** *Diffusion Bonding of Materials.* [trans.] Boris V. Kuznetsov. Moscow : Mir Publishers Moscow.

MAGNETIC PULSE WELDING: LESSONS TO BE LEARNED FROM EXPLOSIVE WELDING

J. Verstraete[1], W. De Waele[1] and K. Faes[2]

[1] Ghent University, Laboratory Soete, Belgium
[2] Belgian Welding Institute, Belgium

Abstract Almost 50 years after magnetic pulse welding was invented, it is finally finding its way to the private sector, in particular the transportation and refrigeration industries. To support this evolution, more fundamental and applied knowledge on magnetic pulse welding has to be established. Learning from the explosive welding process which is very similar and already thoroughly studied and documented, is one way of achieving this. This paper first discusses why both processes are alike, but not the same. A closer look at the process parameters and especially those of explosive welding learned, that an increasing flyer plate velocity results in a transformation of the bonding interface from smooth to wavy and an increase in hardness at the surfaces of both metals. Welding windows developed for explosive welding are discussed. The reasons for the limitations set to impact angle and collision velocity in a welding window are briefly reviewed. This information can give a hand in the optimization of the parameter settings to achieve sound welds with the magnetic pulse process. To check if a high quality weld is made, several testing methods for both processes are discussed and compared.

Keywords magnetic pulse welding, explosive welding, welding parameters, welding window, quality testing.

1 INTRODUCTION

This paper is part of an ongoing research on magnetic pulse welding and forming of the Belgian Welding Institute in partnership with CEWAC (Centre d'Etude Wallon de l'Assemblage et du Contrôle des Matériaux). This research aims to demonstrate the industrial advantages of this technology.

Magnetic pulse welding (MPW) is a solid state welding process that uses the power of a high energy magnetic field to create a bond. In the case of tubular products, the magnetic field causes the outer workpiece, also called flyer tube, to collapse on to the inner workpiece (Figure 1a). When this collisiontakes place at very high speed, the high pressure impact results in metallic bonding wherein atoms of the two materials are brought into direct contact.
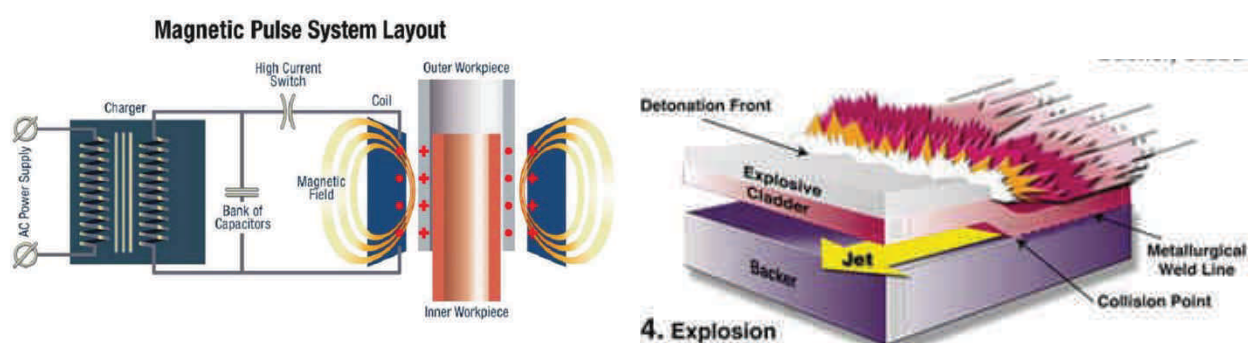
Figure 1: (a) MPW process overview [1] (b) EXW process overview [2]

Explosive welding (EXW) is a solid state welding process as well, but makes use of controlled detonations to force two metals in a high velocity impact, creating a metallic bond (Figure 1b). The bonding principle is thus the same as in magnetic pulse welding although the practical implementation and thereby its applications are different. The explosive welding process was discovered in the late 1950's but was rapidly industrialized worldwide. During the more than 50 years of industrial applications, the process has been continuously improved. This contrary to the MPW process which was discovered a little later but didn't directly find its way to the industry. Therefore it is far less investigated although it has a high potential and some major advantages. MPW is one of the rare processes capable of joining dissimilar metals in a high

volume product environment. Up to now, any joints between round parts such as tube-to-tube joint and tube-to-rod joint are ideal candidates for MPW. MPW can also be applied to non cylindrical workpieces like flat sheets[3]. But this is outside the scope of our research activities. Because the bonding principles are the same for EXW and MPW a good understanding of the MPW process can be derived from an already existing insight on EXW.

2   COMPARISON OF MPW AND EXW

It is generally agreed that the joining mechanism for MPW is the same as for EXW. This cannot only be concluded from the obvious fact that both processes use a high velocity impact to achieve a metallurgic bond. Looking at microscopic images (Figure 2) reveals   the appearance of a similar wavy bonding interface as well. In both processes the formation of a jet takes place at the collision zone. The formation of the jet can be assigned to hydrodynamic material behaviour in the bonding zone. The pressure near the point of collision is so high that the material there behaves like a fluid but incompressible and inviscid. The collision of the metals creates a jet consisting of a mixture of metal ions, air and oxides, ejected from the surfaces of both metals[4]. For explosive welding experiments have pointed out that this jet cleans the surfaces sufficiently before welding. Specific surface preparation is therefore not needed. Experiments with MPW however,   proved that degreasing the workpieces directly before welding has positive   effect in achieving sound welds.[5]
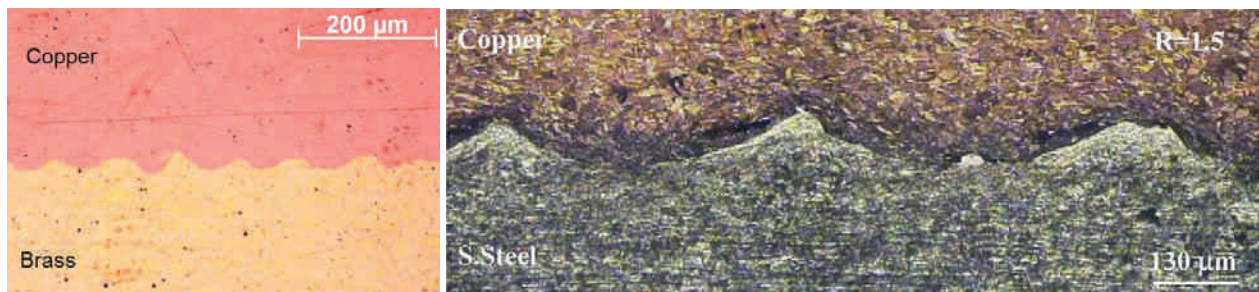

Figure 2: (a) Waviness observed in microscopic images of a MPW interface [6]
(b) and of an EXW interface [7].

The big difference between MPW and EXW lays in the origin of the pressure used to accelerate the flyer plate. For magnetic pulse welding, this is a magnetic field generated by a coil and focused by a field shaper. This field is limited to a small area, of very short duration, clean and safe. The only provision needed to generate it is an electrical current, which is provided by a capacitor bank connected to the electricity net. The capacitor bank charges to a voltage of around 15 to 20 kV, and discharges a current of 150 up to 500 kA with a frequency of roughly 14 kHz [6]. The magnetic field will only generate enough pressure under the condition that the flyer tube is a good electrical conductor. There is a limitation in the size of the coil. This is mainly economical, because a bigger coil needs more energy, enlarging all the equipment. Because MPW is so fast (a weld is produced in less than 100 microseconds [4]), clean and easy (once parameters are defined) it is very suitable for automation.

The explosive welding process makes use of explosives to generate a pressure wave, accelerating the flyer plate. Explosives are cheap, high in energy and there is no real size limitation. The downsides of explosives are that they are dangerous, only trained personnel can handle them, most produce toxic gases and the explosion has to take place in the outside or in a specially designed room that can withstand the pressure. The process can weld cylindrical parts with special setups but the easiest and most used configuration welds flat plates.

This frankly means that MPW is limited to weld large series of thin walled, tubular parts that have a high electrical conductivity and EXW is most convenient to weld thick and large metal plates.

3   WELDING PARAMETERS

3.1   Overview

The welding parameters for MPW and EXW are mostly identical except for those concerning the magnetic field respectively the explosives. In the following table an overview is given of the parameters applied to both processes. Figure 3 shows a schematic overview of the basic parameters.
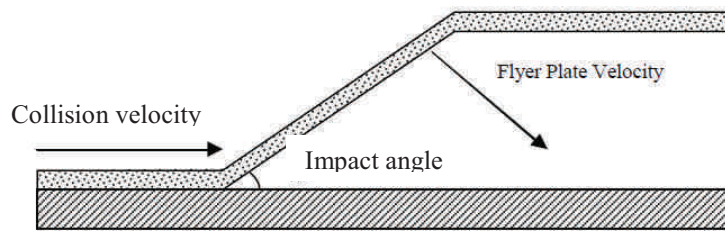
Figure 3: Welding parameters common to MPW and EXW [8]

Impact angle (α)	This is the angle formed by the base plate and the flyer plate on impact. For EXW the impact angle is considered constant whereas for MPW the angle starts small and ends big for a parallel setup of the tubes[6]. The impact angle normally is somewhere between 3° and 30° [9].
Collision velocity (Vc)	This is the speed of the collision point parallel to the base plate. For explosive welding, it is controlled by the detonation velocity, the speed in which the explosive front travels across the layer of explosives. This parameter depends on the type of explosive used. For both processes the collision velocity is in the order of 1500 to 3000 m/s [4]. The collision velocity should remain lower than the sonic velocity of both flyer and base plate.
Flyer velocity (Vf)	This is the speed of the flyer plate. There is a proportional correlation between impact angle, collision and flyer velocity $Vf = Vc * \sin(\alpha)$ [9]. For both processes this speed is around 250 to 500 m/s [4].
Standoff	The standoff distance is the distance between flyer plate and base plate (EXW) or between flyer tube and core (MPW). This standoff distance is generally expressed as a multitude of the flyer plate thickness. It is normally between 0,5 and 3 times the thickness [10]. Because explosion welding can weld thicker plates, the average standoff distance is larger as well.

Specific explosive welding parameters:

Anvil	This is the type of underground the base plate is lying on. The anvil has to make sure the base plate does not move downwards during the explosion. For MPW this translates in the yield strength, stiffness and hardness of the inner part. It can be a solid core or a tube with a mandrel.
Loading ratio	Explosive mass to flyer mass ratio. The higher this ratio, the more explosives used. And thus the more powerful the explosion will be. For MPW this can be compared to the charging voltage and energy level of the machine because these parameters will also influence the force of the magnetic field.

3.2   Influence of process parameters for explosive welding

In several papers ([10],[11],[12]) it is reported that increasing the flyer plate velocity on impact transforms the bonding interface from smooth to wavy. This can be realized in two ways. Increasing the loading ratio increases the pressure the explosion exerts on the flyer plate, thus resulting in a higher acceleration. Increasing the standoff distance gives the flyer plate more time, thus reaching a higher end speed. Note that increasing the standoff distance to much can make the flyer plate decelerate again. Low speeds do not result in a wavy surface (<200m/s). Once waves appear, further increasing the loading rate or the standoff distance increases wave length and amplitude. With increasing flyer plate velocity the following interface types will occur: straight , smooth, small waves, larger waves, waves with vortices, waves with solidified melt pockets and continuous fused layers. The most desirable interface is the wavy or transition bond without any apparent intermetallic layers. It is well known that an intermetallic layer will most probably lower the ductility and cause brittleness [11]. The benefits of the wave formation are: a higher contact surface, higher mobility of atoms and dislocations and effective removal of contaminations. Some research [12, 13] points out however, that the waviness of the interface does not have an effect on shear strength. Sound welds were made without waves in the interface zone as well.

For EXW al three parameters (Vc,Vf, α) are considered constants. This is not the case for MPW as can be concluded from microscopic imagesof the entire length of the weld (Figure 4). A continuous change in waveform (amplitude and period) can be observed and is attributed to variations in flyer velocity and/or impact angle. A detailed analysis of the wave geometry could tell something about the local flyer velocity and impact angle.
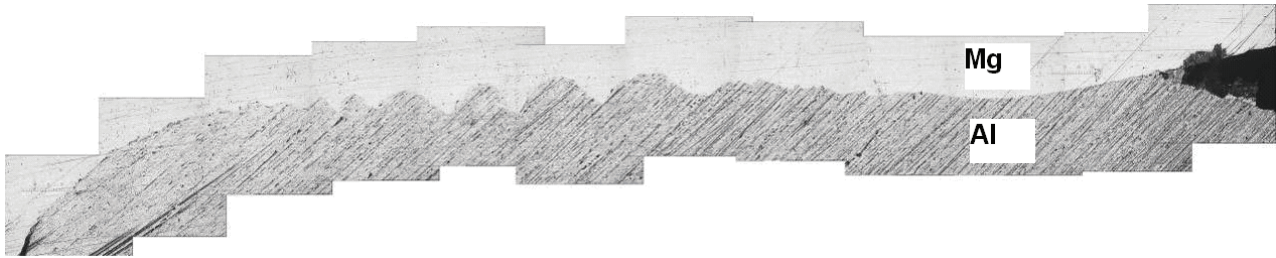
Figure 4: Microscopic image of a MPW over the entire length of the weld [4]

Another effect of increasing the standoff distance is the increase of hardness in the interface layer. Due to plastic deformation, there is always an increase of hardness along the interface layer. The higher the plastic deformation, the higher the increase in hardness (Figure 5a). The measurements also show an increase in hardness on the outer surfaces of the plates. There is a compression here as well due to action – reaction. Analysis of the microstructure of interface layers shows that the grains are elongated in the explosive welding direction (Figure 5b). Heat treatment of the weld zone can recrystallize these grains resulting in a higher shear and bending strength. So far there has been no report of this phenomenon in MPW.
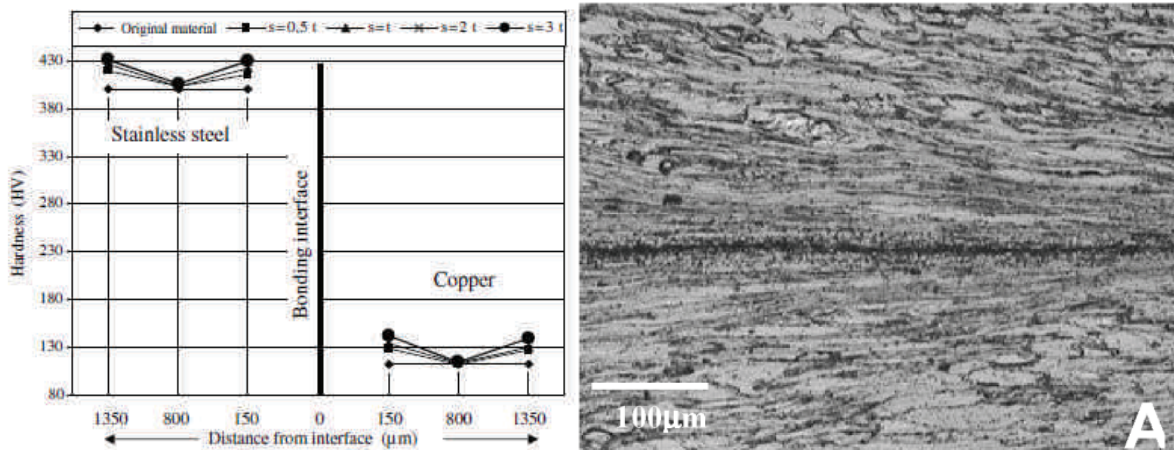
Figure 5 (a) Hardness distribution for a metal couple welded at different standoff distances [10].
(b) microstructure of elongated grains [12]

Besides the loading ratio and the standoff distance some articles also discuss the importance of the anvil. Different anvils are used: sand and steel plates varying in thickness and hardness. The conclusion is that the softer the anvil, the higher the loading ratio needed to establish a sound weld. No welds could be formed for an anvil of sand nor for thin plates[11, 12]. Translated to MPW it is very important that the core material has a hard yield strength and is as stiff and hard as possible, so no bonding energy will be lost in plastic deformation of the core or inner tube. This conclusion was also drawn directly out of several MPW tests reported in [5].

4   WELDING WINDOWS

Welding only takes place if the process parameters or within an optimal range. As stated before, an optimal weld has a wavy or transition bond without intermediate layer. To achieve this, the collision velocity has to be slightly greater than the transition velocity (velocity at which waves start to form) and less than the sonic velocity of the work pieces. The collision velocity has to impart the kinetic energy and fluid behaviour for jet formation and should result in a collision angle corresponding to small wavy interface. Too high velocity could cause interface melting. For explosive welding, these parameters have been studied and resulted in several welding windows such as Figure 6.

Figure 6: Generic welding window[9]

The welding windows normally plot the impact angle in the ordinate and the collision velocity in the abscissa. One of the most important conditions for welding is the formation of a jet. Jetting has to occur at the collision point to achieve welding. In theory if the velocity of the collision point remains subsonic jetting will occur. In practice 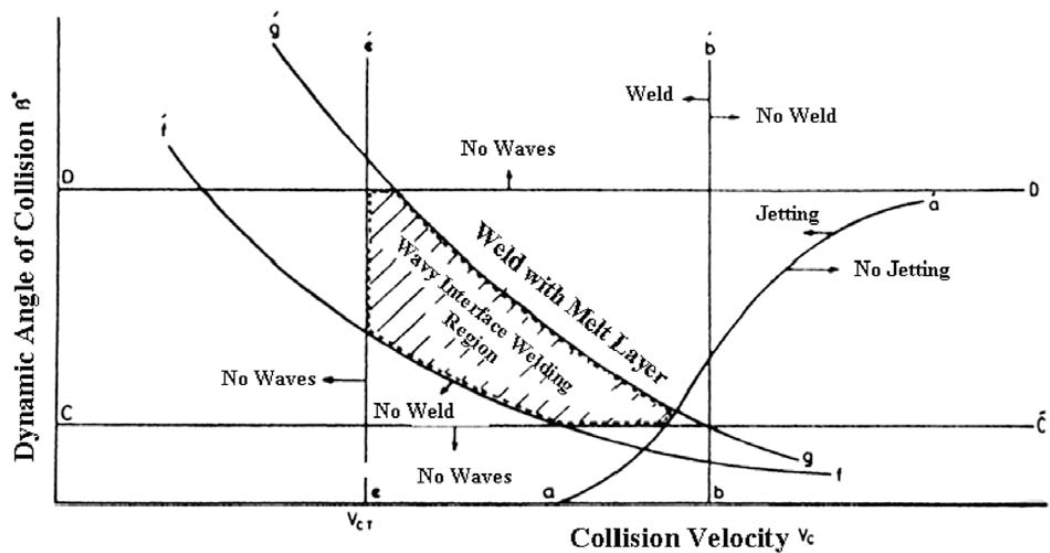however, a minimum angle is required to satisfy the pressure requirement. That is, the pressure must be sufficient to exceed the dynamic elastic limit of the metal to ensure deformation of the metal's surface into jet. In Figure 6 line aa represents the critical impact angle which is necessary for jetting. Line bb represents the upper limit of the collision velocity depending on the sonic velocity in the materials. The lower and upper limits of the impact angle were experimentally determined at around 3° and 30° respectively for a parallel geometry. The line ff counts as the lower limit for welding. Above line gg, interfacial melting will occur. All these lines are material depended and have to be calculated for the specific applications. As can clearly be seen from Figure 6, approaching the upper limit of the collision velocity restricts the choice of other parameters within the welding window [9].

These welding windows are material and geometry dependent and can be used to make a first estimation of the parameter settings for MPW. The downside is that neither of the parameters can easily be measured for MPW. If welding windows have to be developed for MPW alternative parameters should be chosen. Previous work [6, 14] mentions the use of impact angle versus standoff, standoff versus charging voltage, or other possible combinations.

5   WELD QUALITY EVALUATION

Experiments should be performed to determine the weld quality and thus to evaluate the influence of the process parameters. To test an explosive weld, both non destructive and destructive methods are used. Ultrasonic and radiographic inspection are the most widely used non destructive methods for these welds. For MPW, ultrasonic investigation is not straightforward. Because of the cylindrical configuration of the test specimens, it is difficult to realize a good coupling of the sound waves into the test coupons. An advanced radiographic technique is computerised tomography [15]. Preliminary tests [6] indicate that a source with high power is needed to reach the resolution needed to discover the very small weld flaws (Figure 7a). The cylindrical geometry has the benefit that a leak test can easily performed.
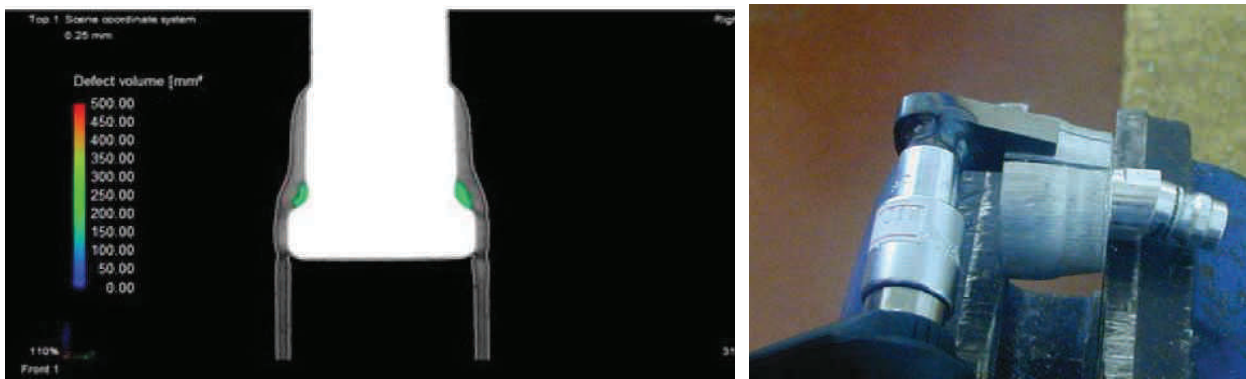
Figure 7 (a) Example of a CT image made of a MP welded specimen [6]
(b) Torque tool being applied on a strip of the weld for a peel test [16]

Because there are not a lot of options for non destructive testing, the majority of tests are of a destructive nature. As can already be concluded from some of the figures, microscopic examination is one of the most important tests which is used for MPW. Next to that fracture tests (tensile, shear, bending), hardness measurements, peeling and chisel tests are an option. Fracture tests are used to evaluate the strength of the weld (i.e. global quality) under load conditions that resemble the in-service loading of the connection. Hardness tests are used to evaluate the presence of hard (and brittle) intermetallic layers (i.e. local quality). A peel test examines the adhesive strength of bonded strips by peeling strips off and recording the required force (Figure 7b). During a chisel test, a chisel is driven into and along the bond interface. The ability of the interface to resist the separating force of the chisel provides an excellent qualitative measure of bond ductility and strength [17]. These tests can also be executed on a circular magnetic pulse welded specimen, but first the flyer tube has to be split in strips [16]. These tests give a characterization of the bonding strength itself. Further tests specifically used for tubular MPW joints are torque tests and tensile or crushing tests [6]. Here the weld strength is compared to the tube strength. If fracture appears in the tube and not in the weld zone, the weld is characterized as sound.

6   CONCLUSIONS

Reported knowledge of EXW has shown to be useful in the understanding of the bonding principles and the influence of several process parameters. Both wavelength and amplitude of the wavy joint interface will increase with increasing flyer velocity. The challenge for MPW is the fact that the parameters (impact angle and flyer velocity) are not constant. This results in a changing interface appearance along the length of the weld. The boundaries of the welding windows for explosive welding learn what happens if velocity or impact angle get too high or low. They can however, only give a first estimation of the parameter settings for MPW because the parameters used in those welding windows are hard to measure and adjust in the MPW process. Concerning the quality evaluation of the welds, the used non-destructive and destructive testing methods for EXW have to be adapted to the tubular shape of the products. Tubular products have the benefit of new possibilities such as leak and torque tests. A concluding remark is that a lot of fundamental knowledge on the magnetic pulse welding process still has to be gathered, but the knowledge gained with the EXW process will make this research advance.

7   ACKNOWLEDGEMENTS

8   REFERENCES

1.   V. Shribman. Magnetic Pulse welding. PULSAR Ltd. Magnetic Pulse Solutions.
2.   *figure: www.dynamicmaterials.com*

3.   Böllinghaus, T., et al., *Manufacturing Engineering*, in *Springer Handbook of Mechanical Engineering*, K.-H. Grote and E.K. Antonsson, Editors. 2009, Springer Berlin Heidelberg. p. 523-785.
4.   Ben-Artzy, A., et al., *Wave formation mechanism in magnetic pulse welding.* International Journal of Impact Engineering, 2010. **37**(4): p. 397-404.

5. Hokari, H., et al., *Magnetic impulse welding of aluminium tube and copper tube with various core materials.* Welding International, 1998. **12**(8): p. 619 - 626.

6. J. Broeckhove, L.W., *Experimental research on magnetic pulse welding of dissimilar metals.* 2010, UGent.

7. Durgutlu, A., B. Gulenc, and F. Findik, *Examination of copper/stainless steel joints formed by explosive welding.* Materials & Design, 2005. **26**(6): p. 497-507.

8. J. B. Perkins, K.L., Z. Akin, Z. Nylund, *Explosive Welding of a 12" x 12" x 0.125" ASTM B152 Copper Plate to a 12" x 12" x 0.5" ASTM A516 Gr70 Normalized Steel Plate.* 2005, Colorado School of Mines.

9. Mousavi, S.A.A.A. and P.F. Sartangi, *Experimental investigation of explosive welding of cp-titanium/AISI 304 stainless steel.* Materials & Design, 2009. **30**(3): p. 459-468.

10. Durgutlu, A., H. Okuyucu, and B. Gulenc, *Investigation of effect of the stand-off distance on interface characteristics of explosively welded copper and stainless steel.* Materials & Design, 2008. **29**(7): p. 1480-1484.

11. Acarer, M., B. Gulenc, and F. Findik, *The influence of some factors on steel/steel bonding quality on there characteristics of explosive welding joints.* Journal of Materials Science, 2004. **39**(21): p. 6457-6466.

12. Acarer, M., B. Gulenc, and F. Findik, *Investigation of explosive welding parameters and their effects on microhardness and shear strength.* Materials & Design, 2003. **24**(8): p. 659-664.

13. Sudarshan, T.S., *Explosive Welding of Metals and Its Application - Crossland,B.* Journal of Metals, 1983. **35**(10): p. 68-68.

14. Loncke, K., *An exploratory study into the feasibility of the magnetic pulse forming process.* 2009, Ghent Univercity.

15. *Computerised Tomography* http://www.ndt-ed.org/EducationResources/CommunityCollege/Radiography/AdvancedTechniques/computedtomography.htm.

16. Shribman., V., *Magnetic pulse welding of automotive HVAC parts.* PULSAR Ltd. Magnetic Pulse Solutions, 2006.

17. *welding technology machines.* http://www.welding-technology-machines.info/index.htm. 2011.

RELIABILITY ANALYSIS OF SEMI-AUTOMATIC TRAIN DOOR SYSTEMS IN SERVICE ON TODAY'S ROLLING STOCK OF THE SNCB

W. Van der Gucht[1], D. Vanwalleghem[1],H. Bonne[2], W. Eeckhout[2], W. De Waele[3], P. De Baets[3]

[1]Ghent University, Belgium
[2] SNCB, Belgium
[3]Ghent University, Laboratorium Soete, Belgium

Abstract This article analyses the reliability of semi-automatic train door systems that are in use on today's rolling stock of the SNCB. For the analysis several databases of the SNCB concerning both operation and maintenance were thoroughly screened. These databases are briefly explained and scaling factors are applied to compare the performance of different series of rolling stock relative to each other. Conclusions are made out of the available data.

Keywords Reliability analysis, rolling stock, SNCB, train door systems

1   INTRODUCTION

The National Railway Company of Belgium (SNCB) [1] experienced that malfunctioning of the entrance doors during the operation of passenger trains is one of the top elements that cause delays. Furthermore, entrance doors can be a source of safety accidents with passengers and/or train crew. In order to understand the source of these problems, a master thesis is performed (at Ghent University in cooperation with the SNCB) on the reliability of train door systems. The purpose of this master thesis is to analyse the reliability and safety performance of different semi-automatic pneumatic door systems in service on the rolling stock of the SNCB. The SNCB deploys different types of rolling stock (e.g. hauled trains, push-pull trains, Electric Multiple Units and Diesel Multiple Units). Each series of rolling stock is referred to with its own abbreviation, found in references [2-4]. Note that EMUs and DMUs consist of multiple coaches with own traction facilities.

The master thesis will also study a reference case on an AM75-77 EMU, shown in Figure 1. This EMU will be modernised in the near future and one of the goals of the master thesis is to give well-founded advice for the optimisation of its door system. This article will quantify the reliability of the door systems based on the already available data at the SNCB.

Figure 1. An AM75-77 EMU

2   ENTRANCE DOOR SYSTEMS

2.1   Different train door systems in service

All train door systems in service on the rolling stock of the SNCB are semi-automatic and electro-pneumatically steered. The different systems can be classified based on their kinematics.
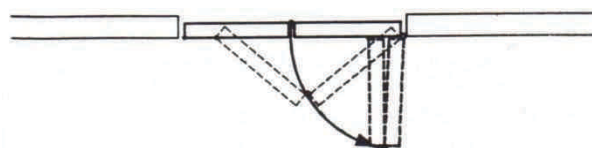
FOLDING DOORS, shown in Figure 2.

Figure 2. Kinematic principle of folding doors

Folding doors are the oldest type of semi-automatic doors in service. They are not suited for speeds above 140 km/h.
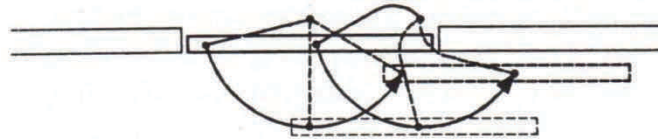
SWING PLUG DOORS, shown in Figure 3.

Figure 3. Kinematic principle of swing plug doors

This type is implemented on AM80-83 EMU and HV M4m, HV M5(m) coaches.

Swing plug doors have a mechanically robust design. However, a violation of the gauge of the infrastructure can occur when they are opened while the train is running in service.

SLIDING PLUG DOORS, shown in Figure 4.

Figure 4. Kinematic principle of Sliding plug doors

This type is implemented on AM75-77, AM86-89 AM96 EMU, AR41 DMU and HV I6, HV I10, HV I11, HV M6 coaches. Sliding plug doors are the most elegant looking doors but are harder to adjust in maintenance. Even during their opening, they do not violate at any time the gauge of the infrastructure.

As mentioned all entrance doors are electro-pneumatically steered. However, two different technologies are used to handle the electric steering.

RELAY TECHNOLOGY, used in older series and implemented on AM62-79, AM75-77, AM80-83, AM86-89 EMU and HV I6, HV I10, HV M4m, HV M5(m) coaches.

THE USE OF (AN) ELECTRONIC CONTROL UNIT(S), used in modern series and implemented on AM96 EMU, AR41 DMU and HVI11, HV M6 coaches.

2.2 Scaling factors

Before starting an analysis on the reliability of the train door systems, we figured out a way to compare the different types. This is necessary because all data we found provide absolute figures. First of all it is necessary to look to these absolute counts, because it means that you can reduce the overall amount of door problems significantly when improving the reliability of the door system that causes most of the problems. However, when comparing different train door systems one needs to consider parameters other than just the number of coaches in use of a series.

For that reason, we developed two scaling factors for every series to compare the relative amounts of data with each other.

The first scaling factor is one that is very often used by the SNCB and is based on the average amount of kilometres that a coach of a series travels during one month. Its mathematical expression is given by eq. (1).

$$\frac{\left(Mean\ \#\ Coaches\ .Mean\ \#\frac{Km}{Coach}\right)_{of\ all\ ser}}{\left(\#\ Coaches\ .\#\frac{Km}{Coach}\right)_{one\ series}} \tag{1}$$

The second scaling factor is one that is created by ourselves and is based on an estimation of the total number of door movements of a train series a day. Its mathematical expression is given by eq. (2).

$$\frac{(Mean\ Theoretical\ \#\ Door\ cycles)_{of\ all\ ser}}{(Mean\ Theoretical\ \#\ Door\ cycles)_{one\ seri}} \tag{2}$$

When the total amount of incidents or problems is multiplied by the appropriate scaling factor for each series, data can be compared.

The numbers used to calculate our scaling factors are given by Table 1.

Series	# Coaches	# Km/Coach (one year)	Theoretical #Door Cycles (2 days)
AM 62-79	585	93.486	287.656
AM 80-83	417	146.746	183.897
AM 75-77	176	123.676	93.016
AM 96	360	213.011	117.197
HV I6	78	89.732	12.324
HV I10	93	63.610	11.036
HV I11	163	306.644	36.981
HV M4m	575	90.491	126.120
HV M5(m)	130	47.535	23.997
HV M6	447	137.607	162.973
AM86-89	102	92.117	49.470
AR 41	185	94.574	59.539

Table 1. Data used to derive scaling factors

3 COLLECTION OF DATA

3.1 Point of view

Any analysis on the reliability and safety of train door systems needs to consider two domains, the commercial operation and the maintenance. This is necessary because a train door system can perform very well during operation in terms of reliability and safety but with high costs in maintenance. For that reason, the different available databases at the SNCB-group are divided according to these two domains.

3.2 Points of attention

The major problem when performing an analysis of train door systems is to collect complete information.

A first challenge is that a train does not stand still. The malfunctioning of a train door can occur anywhere on the railroad network so maintenance personnel cannot get there immediately to make their findings about what went wrong. As an analyst you have to focus on the data of the different following-up systems (of the SNCB) and the testimonials of the train crew. Furthermore, it was only in the early 90's that rolling stock was equipped with a diagnostic system for entrance doors. However no permanent follow-up of the data from these diagnostic systems is done.

A second challenge lies in the fact that the maintenance of the trains, done by SNCB Technics [5], is performed at several maintenance sites across the railroad network. Although the maintenance rules for all the sites are the same, they all have their own interpretations and techniques. For that reason one has to pay attention when comparing maintenance data of several maintenance sites.

A third challenge is the split-up of the SNCB in 2005 in order to meet European legislation [1]. This split-up caused that every division (the operator and the infrastructure manager) wants to manage its own data and tracking system. This leads to a situation in which a 'marriage' between operation and maintenance data is difficult.

A fourth challenge is that historically at the SNCB, the follow-up of EMU, DMU and coaches are different because they have other organisations in charge of maintenance. The non-uniformity in data channels makes the analysis of (similar) train door systems on the SNCB's rolling stock more difficult.

We also have to note that the malfunctioning of train doors is often only the visible symptom of a 'disease'. E.g. a malfunctioning static inverter can cause malfunctioning doors and will thus be wrongly reported as a door. This phenomenon is inevitable and must be kept in mind when analysing train door system problems.

3.3 Databases analyzed

As already mentioned, the data(bases) about the follow-up of door problems will be divided into two domains.

As for the operation, which affects the passengers directly, we analysed four different databases:

'Database Infrabel direction Network' This database keeps record of reports in which all the incidents and accidents that caused a delay of more than five minutes are (briefly) described. It is published as a text document by the direction Network of Infrabel which manages the Belgian railway infrastructure [1]. This document is internally referred as 'de Gazet' and is distributed every working day.

'Database operator SNCB - D43' is a database of complaint documents, filled in by a train attendant, to report an accident or technical failure which affects the safety, passenger comfort or regularity.

'Database operator SNCB - SMS-Averij' is a database based on SMS texting done by a train attendant. This SMS-tool allows a train attendant to report a little accident or technical failure which does not affect the safety, passenger comfort or regularity.

'Database operator SNCB - SafeTrain' is a database that manages all safety-incidents during Belgian railway operation. It was founded to inform a department of the Belgian government.

As for maintenance, we analysed two databases:

'Database operator SNCB - MARS' which stands for MAintenance Rolling Stock is a database that manages maintenance tasks and the (spare) parts of the SNCB's rolling stock.

'Database operator SNCB - Warranty tracking of M6-coaches' is a database unique for the 492 M6 double deck coaches (Figure 5) which are entering the final stage of production and delivery. The database contains all the information of the warranty follow-up of the SNCB's new double deck coaches by their manufacturer Bombardier-Alstom.

Figure 5 A M6 double deck coach

3.4   Fault categories

Different types of faults occur (e.g. a single door can refuse to open or close, all the doors refuse to close,..) and they have different consequences (e.g. a (serious) delay, a cancelled train, a passenger or a member of the train crew being hurt). Therefore it is important to consider fault categories. However not being done in the first part of the master thesis, this issue will be incorporated in the final master thesis text.

3.5   Evaluation period

We opted for an evaluation period of one year starting from July 1st 2009 till June 30th 2010. This time frame is used for every database analysed, unless being stated otherwise.

4   OPERATIONAL DATA ANALYSIS

4.1   Database Infrabel direction Network

As mentioned earlier, Infrabel's database is a text document so it needs to be manually analysed. A **total of 611 incidents concerning entrance doors** were reported. Graph 1 shows the total amount of incidents for each series listed in Infabel's database during the chosen time frame. The graph clearly shows that the M6 coaches and the AM62-79 EMU's cause more delays longer than 5 minutes due to door incidents.
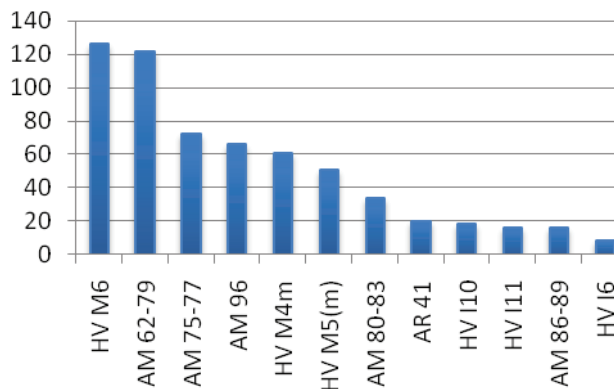
Graph 1. Number of door incidents for each type of train reported in Infrabel's database
(period 01/07/2009 until 30/06/2010 and without scaling)

Graph 2 shows the number of minutes of delay caused by each train series due to door problems over the same period. The **total delay caused by door problems is 29,523 minutes** (approximately 492 hours). In comparison all problems with the rolling stock accounted for a delay of 455,008 minutes in 2009 [6].
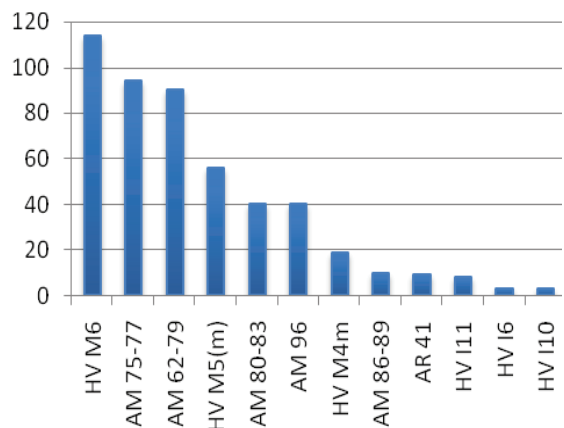
Graph 3 shows the number of cancelled trains due to door problems over the same period **totalising 486 cancelled trains**. This number also includes the indirectly cancelled trains. These are cancelled because another train had door problems and is blocking the track ahead or the train with door problems cannot assure its other services and so on. In comparison a total of 21,556 trains were cancelled in 2009 [6].

By evaluating Graph 2 and Graph 3 we see both HV M6 and AM62-79 coming in front again. We notice that door problems on the older AM62-79 series cause more delay but less cancelled trains contrary to the newer HV M6 series.

The AM75-77 completes the top-three despite its limited number of coaches in use.
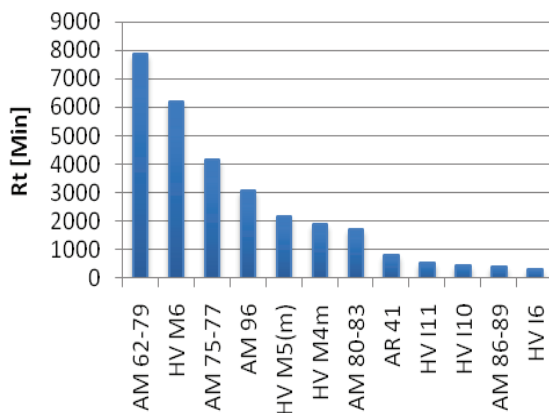
Graph 2. Number of minutes delay due to door problems (period 01/07/2009 – 30/06/2010)

Graph 3. Number of cancelled trains due to door problems (period 01/07/2009 – 30/06/2010)

In order to compare the different train door systems we apply our two scaling factors as earlier mentioned. Graph 4 and Graph 5 show the results.

Both graphs place the HV M5(m) and the HV I10 in the top-three. These two series of coaches mostly provide enhanced supply during peak hour thus not having a lot of kilometres and door movements on their record.

Another thing that we have noticed is that with the introduction of the modernised HV M5 series, named the HV M5m, the number of door incidents reported with the HV M5(m) increased. Possibly there are a few growing pains concerning the door system of the HV M5m. However we did not have the possibilities to distinct whether a HV M5 or a HV M5m was involved in an incident, so we could only make an assumption. This can be subject of further investigation.
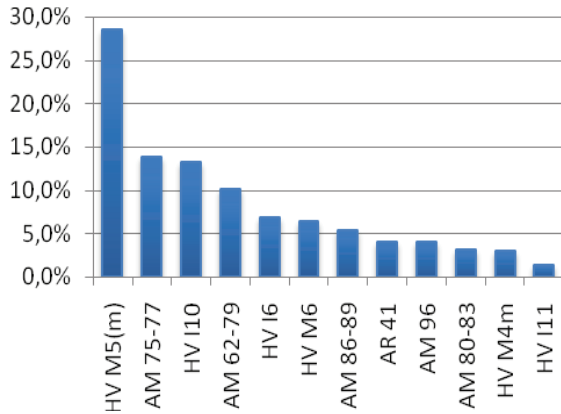
Graph 4. Relative portion of the amount of delay due to door problems for each series by scaling the absolute figures with the first scaling factor.
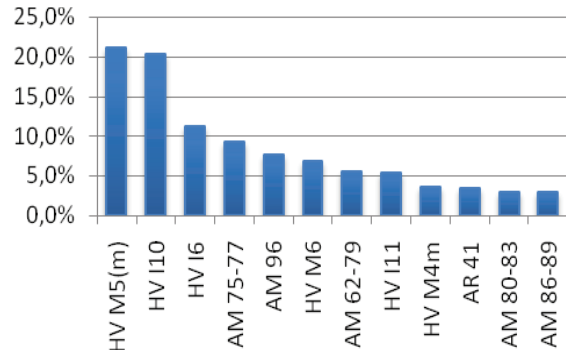
Graph 5. Relative portion of the amount of delay due to door problems for each series by scaling the absolute figures with the second scaling factor.

4.2 Database operator SNCB – D43

The **database of Infrabel** direction Network only reports incidents that cause a delay of more than 5 minutes. The **'D43'** database reports all the incidents seen by the train manager during operation. **Integrating both databases** and taking into account the double counting of incidents, should give a more complete picture of the door 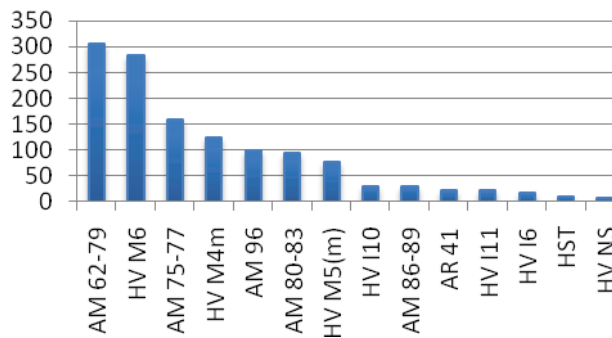reliability in operation. The integration was done over the same time period of one year. In Graph 6 the number of door incidents are shown. We found for the period mentioned a **total of 1,279 incidents**.

Graph 6. Number of door incidents reported by integration of two databases (period 01/07/2009 - 30/06/2010)

The trend seen in Graph 6 is similar as observed in Graph 1, meaning that the application of our scaling factors would give approximately the same results as in the previous paragraph.

4.3 Database operator SNCB – SMS-Averij

Adding the data from 'SMS-Averij' to our own big database would have given us a complete listing of all door incidents that occurred during operation for the period mentioned. However it appears that there are currently two methods used to obtain an extraction out of the 'SMS-Averij' database. The old way (Figure 6) did not allow us to obtain the desired data.

OORSP : IBIS and Stat:Som

| datum	VOER	TRKS	Voorz	OMSCHRIJVING WAUW	WERK	GLDW	UIC	Trst	Teff WRKT
1/02/2010	11704	I10A	N	ok	. . .	. . . .	51881170004-7	FBMZ-M52	0,5

Figure 6. Old extraction out of the 'SMS-Averij' database.

The new one (Figure 7) fulfilled our expectations but we noticed that the system was in a start-up phase for the period requested.

Voertuig						Datum
660	SMS	ACW391	Toegangsdeur	E	IBIS	2/11/2010

Figure 7. New extraction out of the 'SMS-Averij' database.

Therefore we asked more data and only the results of the last obtained month (November 2010) were taken into account. The number of door incidents are shown in Graph 7. When looking at the graph we see approximately the same distribution as in Graph 6 with the exception of the HV M4m which is ranked second. At this moment a possible explanation can be that the HV M4m often has more door problems which do not affect the safety, passenger comfort or regularity.
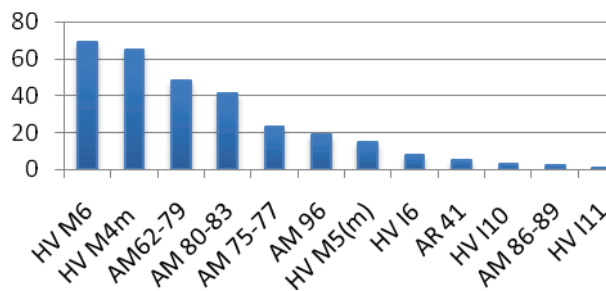
Graph 7. Number of door incidents collected from the new extraction system of 'SMS-Averij'
(period November 2010)

4.4 Database operator SNCB – SafeTrain

The last database we analysed was SafeTrain, in which all safety problems are divided into predefined categories. This database can have some incidents in common with those found in Infrabel's database and database 'D43'. The reason is that a safety problem mostly causes more than five minutes of delay and that the train attendant must always fill in a D43 when such a problem occurs.

The main reason why we wanted to investigate the safety problems related to the entrance doors is to have an idea about how safe the different train door system designs are. This is important because some series (e.g. the M6 double deck coach) have a moveable step or a folding step. These kind of steps can be made bigger because they fold away keeping the limits of the free space profile. A fixed step must be smaller to stay within the gauge of the infrastructure.

The advantage of such a folding step is that they are safer for passengers when boarding, but the mechanism can reduce the reliability when giving direct feedback to the door steering, as experienced with the HV M6.

Although we received a list stating all safety incidents that could involve the entrance doors for the requested period, we did not have the possibilities to identify which series were involved. So the potential of this database had to be left unused.

However as an alternative we searched Infrabel's database for safety related problems during passenger boarding. Table 2 contains the results.

It is clear that no significant difference can be observed between series with or without a folding step. However it is dangerous to make any profound conclusions because of the insufficient amount of data and the influence by many other factors (e.g. weather conditions while boarding, the height of the railway platform).

Type	Number of persons fallen between train and platform	Other incidents	Folding step
AM 80-83	5	0	Partially
M6	2	3	Yes
I11	2	0	Yes
MS 96	0	2	No
M5(m)	1	1	No
AM 62-79	5	1	No
AM 75-77	1	0	No
MW41	2	0	No
Total	17	7	

Table 2. Safety incidents reported in Infrabel's database (period 01/07/2009 until 30/06/2010)

5   MAINTENANCE DATA ANALYSIS

5.1   Database operator SNCB – MARS: hours performed on the maintenance of entrance doors (only 4 series of EMUs)

To get an idea about the requirements concerning maintenance for the different train door systems, we performed an analysis of the maintenance tasks database of MARS. Four series of EMUs were analysed. First the hours spend in maintenance on train doors are evaluated and shown in Graph 8. Maintenance is stated as 'unplanned' when needed to be performed due to an incident during operation.
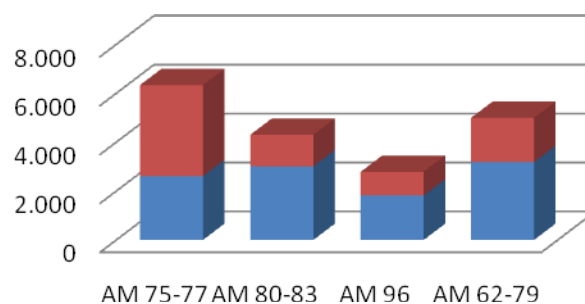
Graph 8. Hours of maintenance spend on the train door system (without scaling) (period 01/07/2009 until 30/06/2010) Legend: **Blue=planned maintenance** and **Red = unplanned maintenance**

To compare the different train door systems on the EMUs we can scale the hours in Graph 8 to obtain the hours of maintenance needed to let a door system perform 1,000,000 cycles or let a coach travel 1,000,000 kilometres. The results are shown in Graph 9 and Graph 10 respectively.
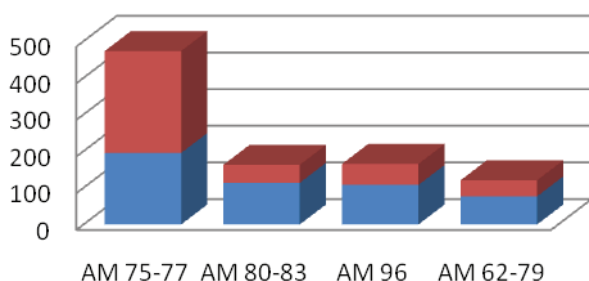
Graph 9. Hours of maintenance on the door system to let one door system perform 1,000,000 cycles. (period 01/07/2009 until 30/06/2010) Legend: **Blue=planned maintenance** and **Red = unplanned maintenance**
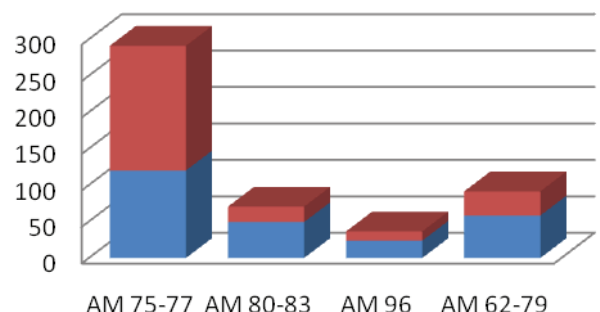
Graph 10. Hours of maintenance on the door system to let one coach travel 1,000,000 kilometres. (period 01/07/2009 until 30/06/2010) Legend: **Blue=planned maintenance** and **Red = unplanned maintenance**

Looking at both graphs we immediately notice that the door system of an AM75-77 EMU requires up to 3 times more maintenance hours which represent a considerable cost. Another remarkable fact is the awkward spread between planned and unplanned maintenance of the door system of an AM75-77 EMU in comparison to the other EMUs. These findings offer opportunities while re-evaluating the door system and its maintenance procedures in the modernisation process of the AM75-77 EMU. By giving its design an upgrade and by revising the maintenance procedures, reduced maintenance costs could be possible. The second conclusion that can be drawn is that both reduction factors give approximately the same results (with the exception of the AM96 EMU which travels a large amount of kilometres).

5.2   Database operator SNCB – MARS: number of maintenance tasks (EMUs+coaches)

Based on the available data a suggestion was made to compare the number of unplanned maintenance tasks of the 4 EMUs to the number of rejections caused by door problems of 4 series of coaches. Graph 11 makes the comparison.
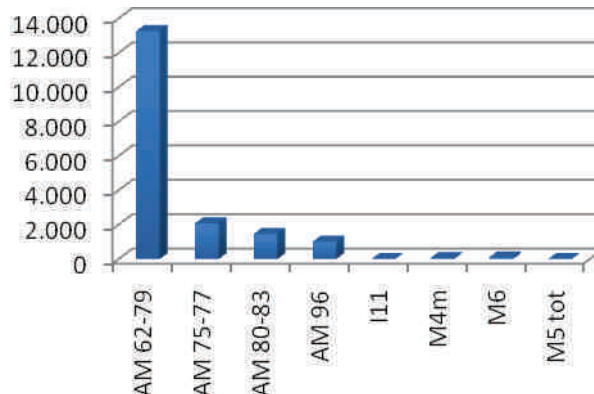
Graph 11. Number of unplanned maintenance tasks of the EMUs compared to number of rejections of coaches both due to door problems. (period 01/07/2009 until 30/06/2010)

Graph 11 has two types of highly unrepresentative data.

First, a lot of unplanned maintenance tasks for the AM62-79 are recorded while Graph 8 does not give an indication in that direction. Therefore it can be useful to examine the maintenance tasks for the AM62-79 series EMU. The AM62-79, also known as 'twins', cover a large family of EMUs divided into multiple series. When we look more in detail to these series (also see [3]), we notice that a very large amount in the unplanned maintenance tasks is coming from the AM62-65 series (Graph 12).
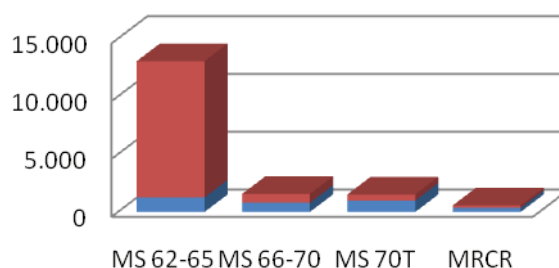
Graph 12. Number of maintenance tasks for the four series in the AM62-79 family. (period 01/07/2009 until 30/06/2010) Legend: **Blue=planned maintenance** and **Red = unplanned maintenance**

Omitting the AM62-79 from Graph 11 results in Graph 13 which gives a more detailed view for the other series.

Second, a huge difference is noticed in numbers between the unplanned maintenance tasks of the EMUs and the rejections of the coaches. This has nothing to do with the door systems of the coaches performing so much better. The only conclusion that can be drawn is that comparing the two different databases is completely meaningless. This leads to the inability to compare similar types of door systems implemented across EMUs and coaches (e.g. the door system of an AM96 EMU and an I11 coach).
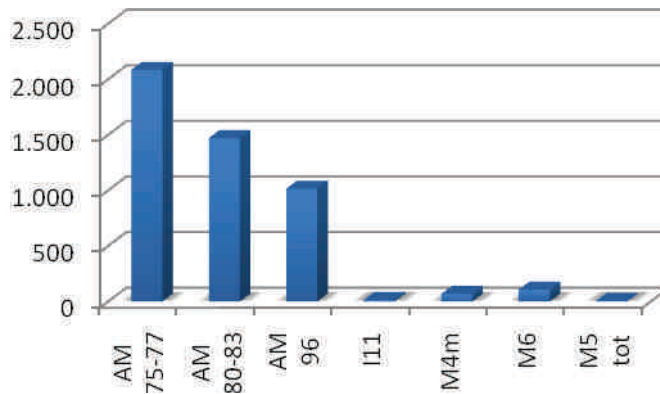
Graph 13. Number of unplanned maintenance tasks of the EMUs compared to number of rejections of coaches both due to door problems (excluding AM62-79) (period 01/07/2009 until 30/06/2010)

5.3   Database operator SNCB – Warranty tracking of M6 double deck coaches

One of the most complete databases available from the operator SNCB is the warranty tracking of SNCB's new M6 double deck coaches. During their warranty period every problem that occurs is mentioned and is included into the warranty tracking system. Every type of problem that occurs receives a certain predefined code. When a new problem category occurs, a new code is generated. Graph 14 and Graph 15 show the top ten ranking for the most common codes in the warranty tracking database of the 'Basic' order and the 'Option' orders of the M6 double deck coaches.
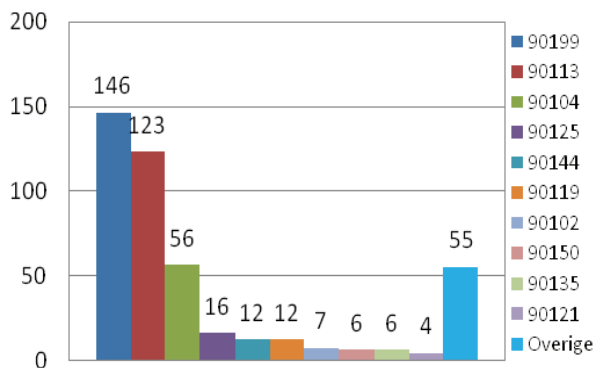
Graph 14. Top 10 of the most common codes for door problems of the first 'Basic' order of 210 M6 double deck coaches. (period 01/07/2009 until 30/06/2010) Note: 'Overige' means 'Balance'

Graph 15. Top 10 of the most common codes for door problems of the 'Option' orders totalizing 282 M6 double deck coaches. (period 01/07/2009 until 30/06/2010) Note: 'Overige' means 'Balance'

Graph 14 indicates that the 'Basic' order had three types of problems that occurred most frequently. As seen in Graph 15, the 'Option' orders are more uniformly s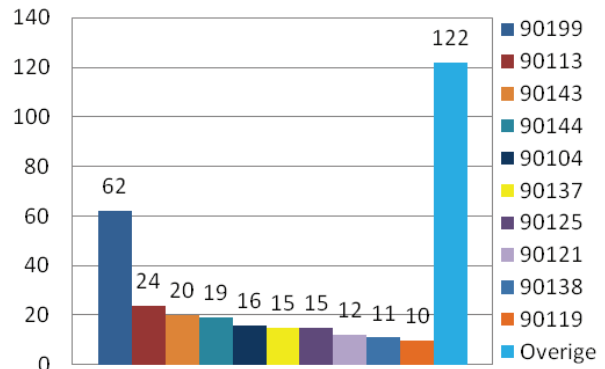pread over all the codes. This means that the manufacturer worked on the severe problems after the delivery of the 'Basic' order. That is the reason why the last column 'Balance' of Graph 15 is that big. All problem types occurred approximately at the same rate. We can also put the numbers for the 'Basic' and 'Option' orders together an look at the monthly spread of the door problems. Graph 16 displays the result.

The follow-up of the door problems of the SNCB's new M6 double deck coach in the warranty tracking system is needed. This is proven by the statistics derived from commercial operation. It can be a tool to increase the reliability of a series of coaches that are very important due to their high capacity and expected lifetime of at least another 30 or 40 years.
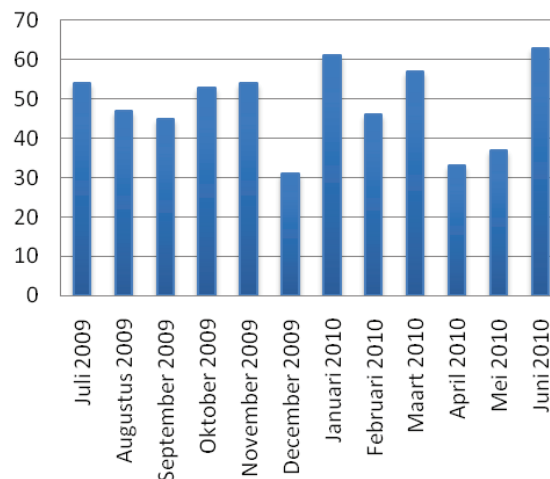
Graph 16. Monthly distribution of door problems of the 'Basic' and 'Option' orders in the warranty tracking system of the M6 double deck coaches. (period 01/07/2009 until 30/06/2010)

6   CONCLUSIONS

An attempt was made to analyse the reliability of the semi-automatic train door systems in use on today's rolling stock of the SNCB. The analysis enclosed both the domains of operation and maintenance. Within the limitations of the databases analysed, following conclusions can be made.

First of all the series AM62-79, AM75-77 and HV M6 face a big part of the door problems during operation. So both the oldest series of rolling stock and the newest series are affected. It has to be noticed that the HV M6 takes the lead in the cancelled trains due to door problems.

Further development of the 'SMS-Averij' tool can provide extra insights with respect to the problems concerning entrance doors.

Series that are only used as supply enhancement during peak moments tend to come on the forefront when data are scaled. Because their usage is limited, one could assume these can be ignored. However a standstill of a train due to technical problems during peak hour can lead to a bottleneck causing a lot of delay for many customers.

There is a potential of reduced maintenance costs when improving the train door system of the AM75-77 EMU during modernisation.

A warranty tracking system for the SNCB's new M6 double deck coaches provides useful technical data if applied correctly.

We can state that a simplified uniform data system for the follow-up of technical systems like train door systems is necessary in a commercial operation environment. The importance of reliable train door systems will only increase with the introduction of the Regional Express Network around Brussels and the growing number of passengers/customers the SNCB has to transport and satisfy.

After the different databases being analysed, the master thesis will mainly study the AM75-77 EMU. Therefore techniques like Fault Tree Analysis and Mean Time Between Failure will be implemented.

7   ACKNOWLEDGEMENTS

The authors would like to acknowledge the help of many people working at the SNCB.

8   REFERENCES

[1]   Wikipedia, t.f.e. National Railway Company of Belgium. Available from:
        http://en.wikipedia.org/wiki/National_Railway_Company_of_Belgium.
[2]   Neef, D.D. Voitures SNCB. Available from: http://www.belrail.be/F/fiches/car/index.php.
[3]   Neef, D.D. Automotrices SNCB. Available from: http://www.belrail.be/F/fiches/emu/index.php.
[4]   Neef, D.D. Autorails SNCB. Available from: http://www.belrail.be/F/fiches/dmu/index.php.
[5]   SNCB. SNCB Technics. Available from:
        http://www.b-rail.be/corporate/F/company/destination_mieux/sncb_technics/index.php.
[6]   Infrabel, N., 'Stiptheid van het treinverkeer' - Jaarverslag 2009. 2010.

MATERIAL SELECTION FOR A NEW TYPE OF FIRE EXTINGUISHER

L. Lambert[1], W. De Waele[1], G. Van De Vijver[2]

[1] Ghent University, Laboratory Soete, Belgium
[2] Optimize Services, Belgium

Abstract

Nowadays safety is a hot topic, damage inflicted to human beings is intolerable. Fire safety is a big concern in industrial areas, but in residential areas a lot less precautions are in place. Therefore a new type of fire extinguisher should be developed that should encourage the installation of fire extinguishers in commercial environments and at home. The design of this fire extinguisher has to answer to a lot of demands. From a legal point of view, the extinguisher has to comply with the PED regulations and the EN 3 standard. Extra demands are, given the purpose, superb performance, great ergonomics and an attractive visual design.

One of the steps in the design process is to make a material selection based on needed and desired properties of materials. Also the possible processes for manufacturing are an important parameter.

Keywords performance index, EN3, PED, materials selection

1   INTRODUCTION

In modern Western society, safety is one of the utmost important issues. Regulations to ensure safety of people and environment are omnipresent. One of the dangers human beings are rather frequently confronted with, is fire. As a result, a lot of safety measures have been developed over the ages. With current fire extinguishers, fires of different natures can be extinguished with a high efficiency, if the size of the fire is not too big.

In industrial environments, regulation dictates a very strict fire prevention policy. In residential areas, however, a lot less precautions are in place. The only safety measures are the conceptual and structural design of the buildings. Although a large percentage of the fires people are confronted with occur at home, most people do not have any fire extinguishing equipment at home. A lot of fires that result in destroying one's belongings and cause a lot of casualties, can be easily controlled, even without training, if a proper extinguisher or fire blanket is present and the fire is noticed in an early stage. Also in commercial environments, (restaurants, stores,…) fire extinguishers are placed out of sight for esthetical and practical reasons.

In order to encourage private consumers to install fire extinguishers at home, developing a new type of fire extinguisher might be a decisive factor. This type has to be highly functional, ergonomic and esthetic. This should lower the threshold for people to place a fire extinguisher in their homes, especially if people are made aware that this greatly reduces the risk of immense fire damage. An attractive design might also encourage restaurants and stores to put fire extinguishers in easily accessible and visible locations to increase safety. Some manufacturers have already developed designer extinguishers, but at the cost of a serious decrease in performance compared to the types developed with focus on performance.

European and national legislation dictates that portable fire extinguishers have to comply with both the pressure equipment directive (PED)[1] and the EN 3 standard [2]. These include an entity of empiric design rules and a series of tests the extinguisher has to pass. Furthermore they limit the types of materials that are allowed for the construction of the portable fire extinguisher. These prescriptions will be limiting factors at several levels of the design.

Improvement of current designs is possible on several aspects. In this study, the most prominent aspect will be using carefully selected materials in an optimized configuration. This might allow the construction of a (super-)lightweight extinguisher, with superior performance, as discussed below. Optimal materials selection and usage might as well make more daring designs possible.

Another important and related challenge will be selecting the most suited manufacturing and assembly processes to produce the device. A critical study has to be performed of the currently used techniques at the production site.

Also the ecologic impact of the design will be taken into account, (recyclability, impact of production on environment,…).

2   CURRENT SITUATION

A typical modern fire extinguisher, (Fig. 1) consists of a steel, (e.g. ST12) cylindrical hull, with a typical thickness of about 1,5 to 2 mm. On the inside of the hull, usually a coating, (epoxy, polyester) is fitted to protect it from corrosion. On the outside, the hull is protected by a layer of paint.

For the production of the hull, a series of processes are used. Starting from steel coils, the two main parts of the hull are deep drawn. Afterwards, these two parts are welded together and the filling opening is cut out and finished by welding in a top part with thread. A metallic tap (brass or chrome), is screwed on. The hose is made of flexible rubber and the nozzle is usually a type of plastic.

1: Hull
2: Paint
3: Coating
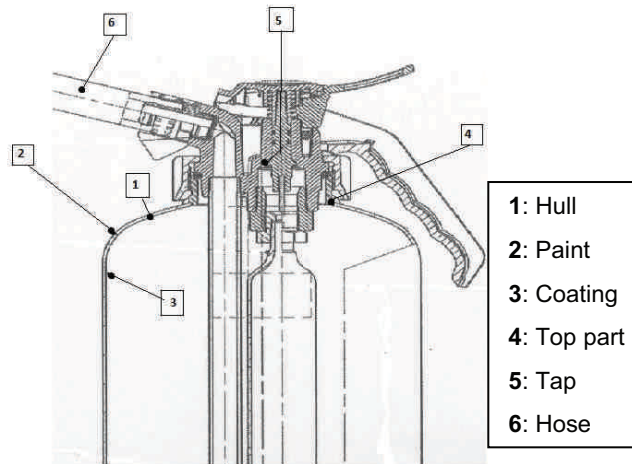4: Top part
5: Tap
6: Hose

Fig. 1 Schematic current design

There are almost no types that deviate from a cylindrical hull form. This form is very robust and is easily constructible.

Based on the fire extinguishing agent, three types of fire extinguishers can be distinguished: CO_2 powder or foam extinguishers. Based on capacity, typical extinguishers contain 3, 6 or 9 litres, (foam) or 3, 6 or 9 kg, (powder). Concerning pressure a distinction can be made between types with stored pressure and with a pressure cartridge.

Considering the purpose or this fire extinguisher, a foam extinguisher with a capacity of 6 litres is the most suiting of these types. In order to simplify efficient inspection, a pressure cartridge is recommendable.

3   BOUNDARY CONDITIONS: DEMANDS & DESIRED PROPERTIES

3.1   Legislation : EN3 & PED

The design of portable fire extinguishers has to comply with European legislation: PED and EN 3 (sections 7 & 8). EN 3 is a European harmonized standard consisting of 10 parts and specifically developed for portable fire extinguishers. PED is a general European directive for pressurized equipment and translated into national legislation [3]. A portable fire extinguisher cannot be placed on the European market before its conformity with legislation has been evaluated by a notified body. In Belgium this is done by ANPI or APRAGAZ.

PED and EN 3 include lists of empirical rules to make sure that any design matching these criteria can be considered a safe device with a required performance level. For the basic design, some important limitations are:

1) Allowed materials

2) Max. weight

3) Min. hull thickness + permissible stress

4) Corrosion resistance

5) Electrical conductivity

6) Mechanical integrity (crushing, impact, …)

Some other basic limitations are practical demands to ensure that easy and safe handling is always guaranteed. With regard to the design aspects discussed in subsequent paragraphs,1), 2) and 3) are considered to be the most relevant qualifications. The weight of a portable fire extinguisher is not allowed to exceed 20kg and a lower weight is always advantageous. The selection of materials according to these criteria will be discussed in section 4.

The minimum hull thickness for portable fire extinguishers with a metallic body, depends on the chosen alloy and is dictated by the standard EN 3 (part 8). For austenitic steel alloys, the minimum thickness (s) is given by equation (6). For all other alloys, the minimum thickness is calculated with equation (7).

$$s = \frac{D}{600} + 0{,}3 \; [mm] \tag{6}$$

$$s = \frac{D}{300} + K \; [mm] \tag{7}$$

where D is the diameter of the hull and K varies from 0,45mm up to 0,7mm, depending on D.

In PED and EN 3, also a series of tests are specified, to which the device has to be submitted. These consist of a crash test, a corrosion test, a creep test, a fatigue test, a pressure test and a burst test.This last test has to guarantee the structural integrity in case of failure. This implies that the failure behaviour of the material may not be characterized by brittle crack. Hence, ductility will be an important parameter of the material selection process. The described pressure test has to be performed at a pressure p≥1,43.PS, where PS is the maximum allowable pressure in the vessel.

3.2   Desired properties

Apart from the demands due to legislation, several material characteristics will be desirable from the viewpoint of the producer and his customers. First of all, the designer or user will favour low weight, low cost, good formability and ductility,…

On the other hand, society in general will be concerned with sustainability and the impact on the environment. In this respect, the recyclability of the materials, the energy cost related to the production of the device, CO_2-exhaust caused by construction and the availability of the selected materials (rare resources) will be important factors. Even the amount of water needed for the production can be used as a criterion. These "environmental costs" should be reduced as much as reasonably possible.

Several degrees of sustainability can be considered. For some materials recycling simply is not an option (e.g. some composites can only be broken down by combustion). For other materials, a distinction will be made between cradle to grave recyclability, where the material is degraded every time it is recycled, and cradle to cradle recyclability [4] where materials can be recycled without degrading. Steel alloys often allow cradle to cradle recycling, which gives them an inherent advantage compared to other materials.

The challenge is to design the device as such, that it complies with both regulations and satisfies as much of the previously mentioned desirable characteristics as possible.

A systematic method to select materials with the desired properties is discussed in section 4.

4   MATERIALS SELECTION

4.1   Procedure

A very effective way to visualize the feasibility of different material types for a certain application, is using so-called 'Materials Selection Charts'. This graphical method was developed by M.F. Ashby and D. Cebon [3]. For a series of materials, a certain material characteristic is displayed in function of a second characteristic. In that way, different zones can be distinguished corresponding to more or less preferable combinations of properties. Examples of meaningful properties were discussed in section 3.2. If a series of charts are compared, one can make an evidence-based selection of the materials to be used.

More often however, a combination of several (sometimes conflicting) properties will be advantageous. In this case it will be difficult to get a conclusive result with Materials Selection Charts. Performance indices [3] allow to quantify the aptitude of materials for certain applications. Depending on the properties that are considered to be most significant, different performance indices can be specified. These indices are obtained by combining certain properties like density, yield strength, cost, … Like this, materials can be

sorted based on increasing or decreasing values of a performance index. Extreme values of performance indices will be associated with very advantageous or disadvantageous combinations of properties.

For the application of a fire extinguisher, different performance indices can be defined. As an illustration, three completely different indices (related to construction, cost and durability) will be discussed in subsequent paragraphs.

4.1.1 Weight

The weight of the hull is an important parameter from the viewpoint of both legislation and customer requirements. For a certain hull geometry with a specified thickness, one can calculate the stresses (σ_{rr} in radial direction and $\sigma_{\theta\theta}$ in circumferential direction) in the hull. For a cylindrical hull for example, this can easily be calculated based on the formulas of Lamé [2],

$$\sigma_{rr} = p \frac{a^2}{a^2 - b^2} \left(1 - \frac{b^2}{r^2}\right)$$

$$\sigma_{\theta\theta} = p \frac{a^2}{a^2 - b^2} \left(1 + \frac{b^2}{r^2}\right) \qquad (1)$$

Where a and b are the inner and outer radius of the cylinder hull and r the radius at which the stress is calculated.

The stress σ_{zz}, as displayed in Fig. 1, is calculated as: $\sigma_{zz} = p \frac{\pi a^2}{\pi b^2 - \pi a^2}$.

For a thin-walled vessel, these equations can be simplified as:

$$\sigma_{\theta\theta} = \frac{pa}{t}$$

$$\sigma_{zz} = \frac{pa}{2t} \qquad (2)$$

Where t is the hull thickness.

For more complicated geometries, it will be difficult to derive an analytical solution for these stress-components and finite element models may have to be used.
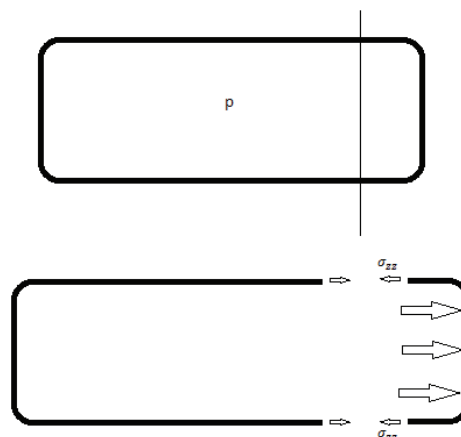
Fig. 2: Axial stress in the cylinder of a thin-walled
pressure vessel.

Using the Von Mises yield criterion (for ductile materials), an equivalent stress can be calculated and compared with the material's yield strength. Taking into account a safety factor, this will allow to determine the minimum required wall thickness. Or, starting from a specified geometry of the hull, one can calculate the minimum required yield stress of the material.

The volume V of material that is used determines the thickness t of the hull. For thin-walled vessels, V and t are directly proportional and the stress in the hull is inversely proportional to t. As a result, there is an inversely proportional link between V and the required yield stress σ_0.

In order to optimize the weight of the hull, this weight is written as a function of the volume V and the density ρ of the materials:

$$W = V.\rho = \frac{1}{c_1 \sigma_0} \rho \qquad (3)$$

where C_1 is a constant and σ_0 the yield stress of the material. A first performance index M_1 can be defined as:

$$M_1 = \frac{\sigma}{\rho}$$ (4)

Materials with a very high index M_1 will allow the lightest construction.

4.1.2   Material cost

The material cost of the hull will also be an important parameter. The total material cost K of the hull is a function of the material cost per unit mass k, the density ρ and the volume V of materials used.

$$K = V\rho k = \frac{1}{C_1 \sigma}\rho k$$ (5)

A second performance index M_2 can be defined as:

$$M_2 = \frac{\sigma}{\rho k}$$ (6)

Materials with a higher M_2-index will possibly allow a cheaper hull. It has to be noted that the considered cost only consists of the material purchase cost. The cost of the processing operations is not taken into account and needs further consideration.

4.1.3   Durability aspect of production

Regarding production, several indices can be defined. The daily costs for producing the components could be brought into account, or even the required investment costs for starting up a new type of manufacturing processes.

In this paper the ecological aspects of the production are taken into account.

A third performance index M_3 is specified as:

$$M_3 = E_{prod} \cdot C_{CO2} \cdot U_w$$ (7)

Where E_{prod} is the embodied energy for primary material production [MJ/kg], C_{CO2} represents the CO_2-exhaust caused by the production process [kg/kg] and U_w is the water usage [l/kg] .

Unlike M_1 and M_2, low values of M_3 will be desirable. The production of materials with a low index M_3 will have a low impact on the environment.

4.1.4   Other indices

Several other performance indices could be specified based on cost considerations or mechanical integrity aspects (resistance to fatigue, corrosion and impact damage). These indices can be used to further eliminate materials, but are not further discussed in this paper.

Also selections can be made by rejecting materials that are (strongly) degraded by recycling, are not biodegradable or by specifying a lower limit for the fraction that is expected to be actually recycled.

4.2   Implementation

.

4.2.1   Primal selection of material classes

Before applying the above discussed methods, one can already determine which classes of materials will be worth considering, based on some of their general characteristics.

Applied to the case of a portable fire extinguisher, this results in the rejection of:

- Ceramics or glasses: since they are very brittle and sometimes porous.
- Magnetic materials: magnetic behaviour is an undesirable property.
- Materials that are not watertight (fibres, particulates, foams,…): the contents of the vessel may not be lost.

This primal selection already greatly reduces the amount of materials that should further be considered. In subsequent paragraphs, materials that didn't pass this first selection are therefore not taken into account.

One can also reflect in advance what kind of materials might have advantageous characteristics for this application and can be expected to survive the following selection.

- Steel alloys might be well worth considering, since they typically have high yield strengths and are available at a relatively low cost.
- Composites might be advantageous, since they have high tensile strengths and low densities.
- Some other metal alloys (Al, Mg, Ti…) might be worth considering, since they have high yield strengths and lower densities than steel.

However, selection of the most feasible material(s) should be based on a systematic and evidence-based approach as described in section 4.1.

4.2.2   Further selection based on materials selection charts and performance indices

In order to come to a profound selection, all needed and desired properties of the materials have to be listed and critically compared.

Software packages, like CES-Edupack [5] have extensive libraries of materials and their properties. This software package is used to develop graphs of the previously discussed parameters. As an illustration, a Materials Selection Chart can be made where yield strength is displayed in function of the material cost per volume. This graph (Fig. 3) is useful to get a clear view on the material costs that can be expected for certain material classes. The straight lines with slope=1 are constant material cost-lines. The difference between two subsequent lines is a factor 10. It is clear that the group of 'Gold, Platinum and Palladium alloys' and the group of 'Tungsten, Tantalum and Zyrconium alloys' will be to expensive for this case. Elastomers and plastics are beneficial from the viewpoint of cost, but have too low strength properties. This graph also shows that the family of steel alloys are, in terms of strength and cost, very advantageous materials.
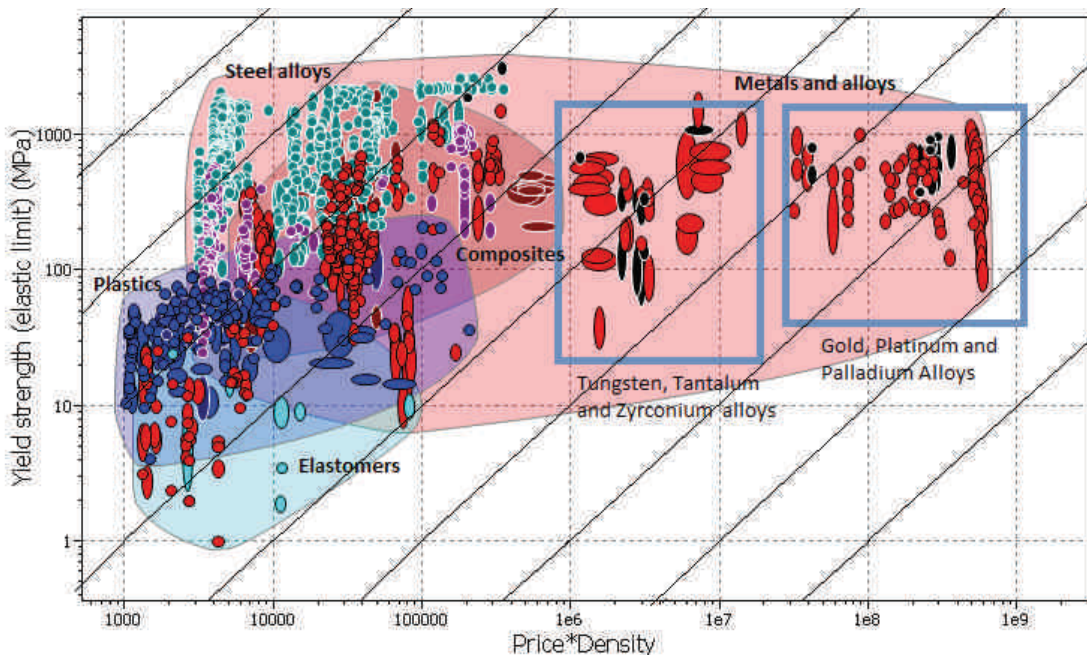

Fig. 3 Materials Selection Chart: evaluation of strength and cost

If performance index M_1 is calculated for the selected materials (section 4.2.1), values ranging from $5*10^{-4}$ kN.m/g up to 1,5kN.m/g are found. As a first selection criterion, a lower limit of 0,1kN.m/g is specified for M_1. The fact that a minimal thickness is required due to legislation is not taken into account. This may reduce the advantage of using materials with extreme high values of performance index M_1.

In a similar way performance index M_2 can be calculated. This parameter varies from $5*10^{-8}$ kN.km/€ up to 0,5 kN.km/€. A lower limit for M_2 is specified at 10^{-2} kN.km/€.

Performance index M_3 varies from 200 L.J/g² up to 10^{15} L.J/g². For this index, an upper limit is specified at 10^5 L.J/g².

The defined limits will greatly reduce the number of materials that should be considered. For this selection, M_1, M_2 and M_3 are displayed respectively in Fig. 4, Fig. 5 and 6. A logarithmic scale is used to get a well-interpretable graph for a very wide range of materials.

It can be noted that M_3 (related to the durability of the production processes) filters out almost all materials except steel alloys. Dozens of steel alloys are selected, while the only other materials that survive the selection are glass fibre reinforced epoxies (composite material).

Most of the steel grades that are selected are tool steel alloys, low alloy steels and carbon steels.
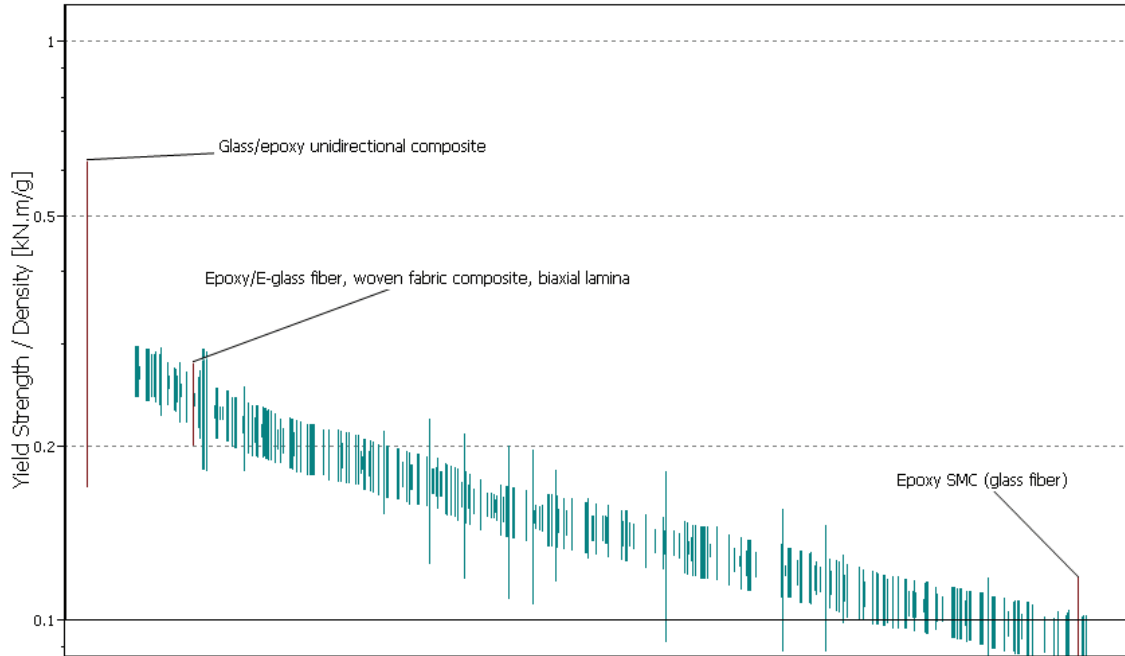

Fig. 4 Performance index M_1

The best result regarding low weight (index M_1) is achieved with a glass/epoxy unidirectional composite, which is amongst others used in hulls of ships. For the selected steel alloys, no consistent trend can be established concerning performance for M_1.
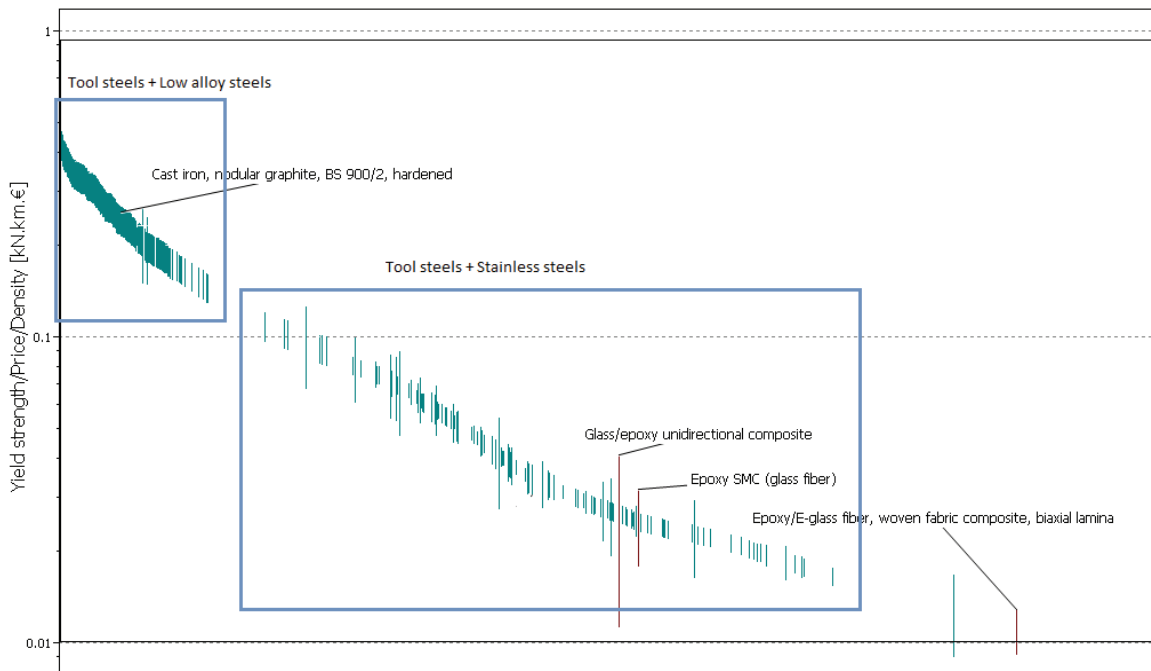

Fig. 5 Performance index M_2

With respect to material cost (index M_2), steel alloys give the best result, and the selected composites are situated closer to the defined lower limit. It should also be noted that the steel alloys with better results for M_1 tend to have a worse M_2-value and vice versa.

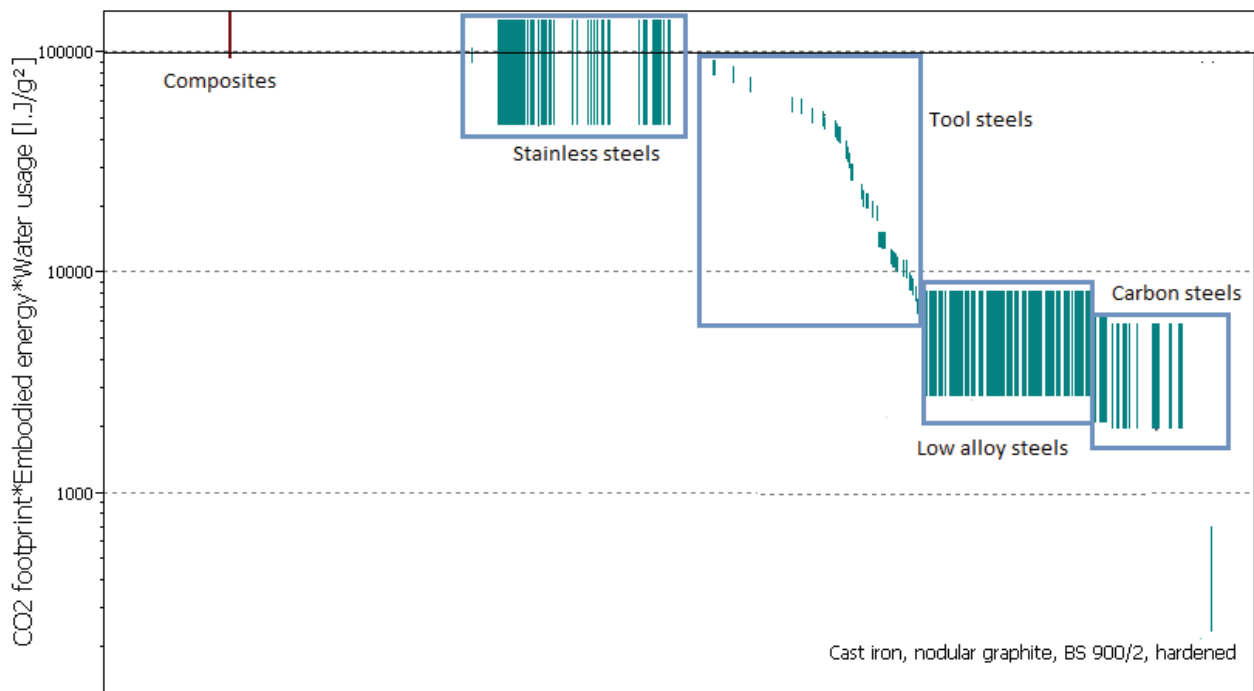This situation could be expected from the start and illustrates the compromise that has to be made.

Fig. 6: Performance index M_3

With regard to durability of production (index M_3), low alloy steels and carbon steels obviously show very good results (Fig. 6). The best result is achieved for a hardened cast iron (nodular graphite, BS 900/2).

When all performance indices are taken into account, the family of low alloy steels appear to be very attractive materials for portable fire extinguishers. Based on the discussed evaluation procedure, the material with the most attractive properties is a low alloy steel, type AISI 9255 (tempered at 205°C and oil quenched)This steel alloy has a yield strength of 1840MPa. For this material M_1=0,3 kN.m/g, M_2=0,5kN.km/€ and M_3 ranges from 500 up to 900 l.J/g². By redefining the upper and lower limits for the performance indices, different results can be obtained.

Only when the weight of the hull is the decisive factor, composites will be considerable. The non-recyclability of most composites is however a great disadvantage that has not yet been taken into account and might exclude composites altogether.

4.3   Low alloy steels

Since low alloy steels seem to be very promising materials for this application, it is useful to take a closer look at this group of materials. Depending on the techniques used to produce the steel and the composition of the alloy, a huge variety of steels can be obtained. Although steel alloys have been the most important engineering materials since about 1800, still a lot of research is performed to develop new steel grades. The microstructures that occur in the steel alloy, (ferrite, martensite, bainite, pearlite, austenite), will determine its properties, such as yield strength, ductility,…

Of course, not all low alloy steels are included in the CES libraries. Some recently developed grades that are worth considering are the Advanced High Strength Steels (AHSS) [8]. These include dual phase steels (DPS), transformation induced phase (TRIP) steels and complex phase steels. All these grades have very advantageous mechanical properties (high strength and good ductililty) and wide processing possibilities. For this kind of application, DPS seem to be well suited [9],[10],[11]. These steel grades typically have a

fine ferrite structure with a second harder phase as strengthener. They are also suitable for deep drawing and other processing techniques (cf.5.2), which makes them very attractive in this context.

AHSS as described by Z. Xiaodong [8] have yield strengths ranging from 400MPa up to 1400MPa, depending (DPS, CPS and TRIP). These steels will not necessarily obtain the highest values for M_1 and/or M_2 , but the advantage in processing abilities might be significant. Also a very good strength-ductility combination is obtained with these steel grades [8]. It has to be noted that the previously defined performance indices are merely an illustration of the possible indices that can be used for the selection process. In order to make a more profound selection, an extensive set of indices has to be evaluated.

As noted in section 4.2.2 the advantage of high M_1 indices will be limited by the minimal thickness required by legislation.

Also the availability of the desired steel grade and the production form (coils,…) is an important issue that should be considered. For DPS, a number of standardized grades are available on a large scale in coils.

5   PROCESSING

5.1   Composites

For composites, the material is immediately produced into the desired component shape.

No forming processes have to be or can be performed afterwards. This has the advantage that almost every shape is possible, and that the material properties can't be deteriorated by the forming process.

On the other hand, a fire extinguisher is not supposed to have an exceptionally complicated form.

The anisotropic behaviour of these materials is a challenge that requires special attention and complicates the design. A lot of composites, like the previously mentioned glass/epoxy types however certainly are a possibility.

The production processes for composites are less suitable for mass production, and in general require more time. Composite pressure vessels are typically constructed with a filament winding on a permanent mould, which is used as an impervious coating for fluids.

5.2   Steel

Steel grades are typically produced in flat sheets and need subsequent forming steps to realize the desired shape. A possibility to avoid secondary forming processes, would be to use casting techniques. For this application however, this will not be advantageous in any way. Casting techniques are in general rather complicated and time consuming. In addition they are certainly not the most evident processes for creating hollow geometries. As a result, cast iron that was mentioned in earlier paragraphs will not be a valuable option.

Starting from a steel plate, a form can be created in several ways: deep drawing, bending, welding, hydroforming,… The feasibility of each of these techniques depends on the specific properties of each steel grade. The strength properties of the processed material will be a lot higher than those of the non-deformed steel due to strain hardening. For a fire extinguisher, the most obvious procedure is to create two shaped parts with deep drawing or hydroforming techniques and join them with a weld in the circumferential direction of the vessel. With hydroforming techniques, some hull geometries can be constructed in one part, which would save a lot of time, although this will reduce the possible geometries.

It is in this prospect that dual phase steels stand out [4], as mentioned in section 4.3. Both hydroforming and deep drawing allow a great variety of shapes, (single and double curved), which ought to be more than enough for any reasonable design of a fire extinguisher. Hydroforming has an extra advantage that it is possible to start from a tube-shaped part , which will need to be deformed less than a part that is constructed from a sheet. These materials are also capable of absorbing high amounts of energy, which can be useful with respect to the earlier mentioned impact tests.

The processing costs for steel will also be lower for steels than for composites, but a high installation cost will be unavoidable.

6   CONCLUSIONS

The development of a new type of fire extinguisher can reduce the risks of fire damage in residential and commercial areas. The design has to comply with regulations and standards (PED and EN3). Further it has to unite several desirable properties, some imposed by society and others desired from a technical point of view. A selection procedure is established by using materials selection charts and performance indices. Three performance indices quantifying the performance of materials regarding weight, cost and impact of the production on the environment have been defined and evaluated. If weight is the decisive factor, glass/epoxy-composites are beneficial, but when other aspects are taken into account, low alloy steels are the materials with the best suited properties. Also when processing possibilities and recyclability are taken into account, steel grades turn out to be very advantageous materials. Dual phase steels are a modern class of low alloy steels with some very attractive properties for this specific application. This will be studied in more detail in the further progress of this work.

7   NOMENCLATURE

a	Internal Diameter Cylinder	mm
b	External Diameter Cylinder	mm
σ	Yield Strength	MPa
W	Weight	kg
V	Volume	m³
ρ	Density	kg/m³
K	Cost	€
k	Cost/weight	€/kg
E_{prod}	Embodied Energy for production	MJ/kg
C_{CO2}	CO_2-exhaust	kg/kg
U_w	Water usage	l/kg

8   REFERENCES

[1]   Directive 97/23/EC of the European Parliament and of the council of 29 May 1997 on the approximation of the laws of the Member States concerning pressure equipment, 2003.

[2]   EN3, Portable fire Extinguishers, 2007.

[3]   Belgisch Staatsblad, 38063-38123, 8-10-1999.

[4]   McDonough, W., Braungart, M., Cradle-to-cradle: Remaking the Way We Make Things, 2002.

[5]   Ashby, M.F., Cebon, D., Materials Selection in Mechanical Design, Euromat, 1993.

[6]   CES Edupack, Granta Design Limited, version 6.0.2.

[7]   Van Paepegem, W., De Waele, W., Mechanica van Materialen, UGENT, 2010.

[8]   Xiaodong, Z., Zhaohui, M., Li,W., Current Status of Advanced High Strength Steel for Auto-making and its Development in Baosteel,

[9]   Vanrostenberghe, S, Goudemez, J., Chiappini, M., Brun, O., Desplaces, G., Bregnon,R., New Steel Grades For Light Weight LPG Cylinders.

[10] Schaeffler, D., Introduction to advanced high-strength steels- Part I, Stamping journal, 2005.

[11] Abedrabbo, N., Mayer, R., Thompson, A., Salisbury,C., Worswick, M., van Riemsdijk, I., Crash response of advanced high-strength steel tubes: Experimental and model, International Journal Of Impact Engineering, 36(8), 1044-1057, 2009.

FAILURE BEHAVIOUR OF A TUMBLE DRYER

S. Droessaert[1], W. De Waele[2], W. De Groote[3], E. Delorge[4]

[1] Ghent University, Belgium
[2] Ghent University, Laboratory Soete, Belgium
[3] Spie Belgium, Piping and Mechanical
[4] Sioen Fibres, Spinning Division, Belgium

Abstract A tumble dryer is a rotating heated vessel used to fulfil a poly-condensation process of PET-granules. This step is very crucial in the entire production process of polymer fibres. System failure, causing production loss, cannot be afforded. Unfortunately, since a couple of years, the reactors suffer from severe cracking at weld details. To find the root cause(s) of this problem a detailed study of the vessel construction, the loads induced during the production process and the cracking has been performed. Hereby the influencing parameters and their importance could be determined. Based on this study it is put forward that fatigue, due to the exceptional translation of the granules in the vessel, is responsible for the cracking of the tumble dryer. Two main loading modes and corresponding crack locations could be determined: a cyclic changing torque causes the cracks on the outside of the vessel while the dynamic play of the moving granules around the heating elements is responsible for the cracks at the inside the tumble dryer. The root cause of the cracking problem has been determined but the actual mechanism causing the cracks, still needs to be quantified.

Keywords Inspection, welding, construction, fatigue, fracture

1   INTRODUCTION [1]

A tumble dryer (Figure 1) is a patented device which is used in the polymer fibre industry. Polymer fibres are produced from PET-chips. However, before this material can be used for the production of fibres, the PET-chips have to undergo a heat treatment which is called a post-condensation process. This is the process that is taking place inside the tumble dryer. During this treatment all impurities are removed and the viscosity of the chips is adapted to meet the requirements of the subsequent process steps.

Figure 1: One of the four tumble dryers (capacity of 44m^3) at the Spinning Division of Sioen Fibres.

Four tumble dryers of this type are continuously in operation at the Spinning Division of Sioen Fibres (Moeskroen, Belgium) to meet the production demand. In the year 2000 the first two smaller units, with a capacity of 36m^3, have been installed. In 2003 there was a production expansion with 2 bigger units each having a capacity of 44m^3. Initially the tumble dryers operated well. As of 2007 the first problems in one of the vessels emerged. At random locations cracks were found in different crucial welds, both at the inside and outside of the vessel. These cracks were systematically resolved but the problem continuously shifted to other sections of the vessel. Constructional adaptation by the supplier did not solve the problems, on the contrary they even worsened the situation. Eventually they even had to undo some of the adaptations. So far no satisfactory solution for the cracking problem has been found. The troubles with the tumble dryers already resulted in a lot of (financial) production losses and a lack of reliability of these important production tools.

The goal of this study is to define the root cause of the observed weld cracks. For this reason a detailed overview of the occurring cracks has been made. Hereby it is important to the crack types, the locations of

the cracks and their time of occurrence. Furthermore a detailed study of the reactor and of the process has been performed in order to define all influencing parameters. Based on these results, the intervening loads (mechanical, thermal, etc.) have been determined. In the near future, a detailed and critical study of the design, material choices and dimensions has to be performed. Both the global design and implementation details will be considered. Based on the final results of this study we will eventually try to provide a technical solution to the problem.

2 SHORT OVERVIEW OF OBSERVED CRACKS

In collaboration with the contractor SPIE, a detailed study has been performed to map the location and the frequency of crack occurrence. A first conclusion is that cracks appear both at the inside and the outside surface of the vessel. The cracks on the outside are situated at the connection of the vessel supports with the axis of the vessel and the connection with the outer shell. All cracks appear at discontinuities of the weld details and thus in a region with high stress concentration. Most of these cracks occur at the transmission side of the tumble dryer. In fact all supports at this side already needed a repair. Failures at the vacuum side only resulted in two repairs at the tip of the shortest supports. Cracks leading to failure of the heating paddles have been observed at almost every weld detail of this element. Figure 2 gives an impression of some important failures.

a) Crack at tip of vessel-support
b) Cracks situated at a heating element
c) Crack of vessel-support at the axe
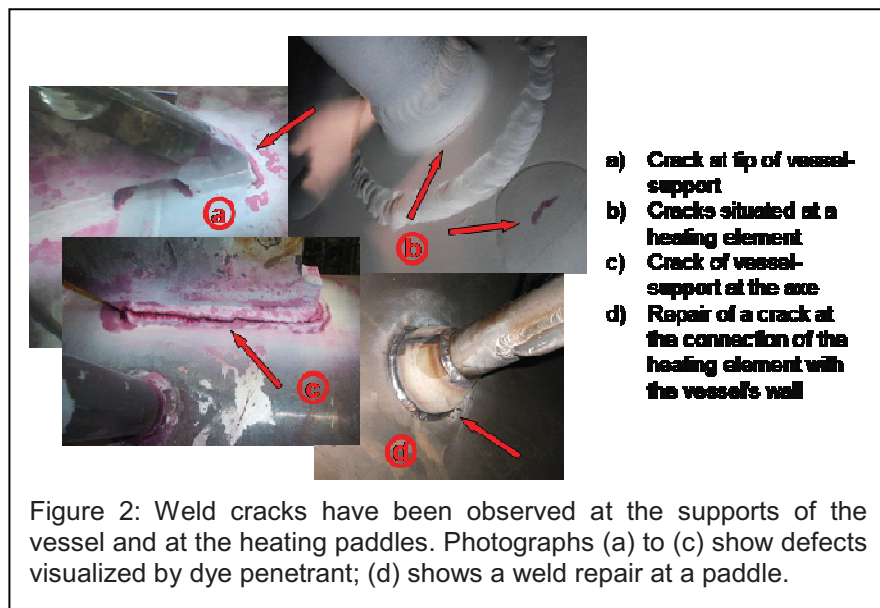d) Repair of a crack at the connection of the heating element with the vessel's wall

Figure 2: Weld cracks have been observed at the supports of the vessel and at the heating paddles. Photographs (a) to (c) show defects visualized by dye penetrant; (d) shows a weld repair at a paddle.

3 STUDY OF THE TUMBLE DRYER

3.1 The production process

Figure 3 represents a schematical overview of this production step. The applied post-condensation process entirely takes place in the tumble dryer which is a double shelled vessel (central part of the figure). Two chambers can be considered: one inner vacuum chamber filled with the PET-chips (in blue) and a surrounding chamber filled with circulating heated oil (in orange).

For heating the vessel's contents, oil with a temperature of maximum 250℃, is pumped into the oil-chamber at a pressure of 2bar. To realise a homogeneous heat distribution throughout the entire vessel an internal heating system consisting of paddles and connected to the oil chamber is installed The maximum heating and cooling speed is limited to 2K/min.

In the first step, the reactor is heated until the vessel temperature reaches 120℃. Then the vessel i s filled up to 75% of its capacity ($V_{load,max}$=33,7m³) with PET-chips (having a cylindrical shape). The ingoing viscosity $Visc._{in}$ of the chips is approximately 0,64dl/g. The pouring weight is about 0,8kg/l which means that 1g counts about 50 chips. The melting temperature T_s of the chips is over 258℃. In the next step the reactor is rotated with a speed of 0,561 rpm. The vessel makes a tumble movement as it rotates around a diagonal of the cylinder. This tumbling movement results in an easeful mixing and homogeneous temperature distribution of the vessel's contents. While rotating the reactor, the temperature is increased up to 170℃.
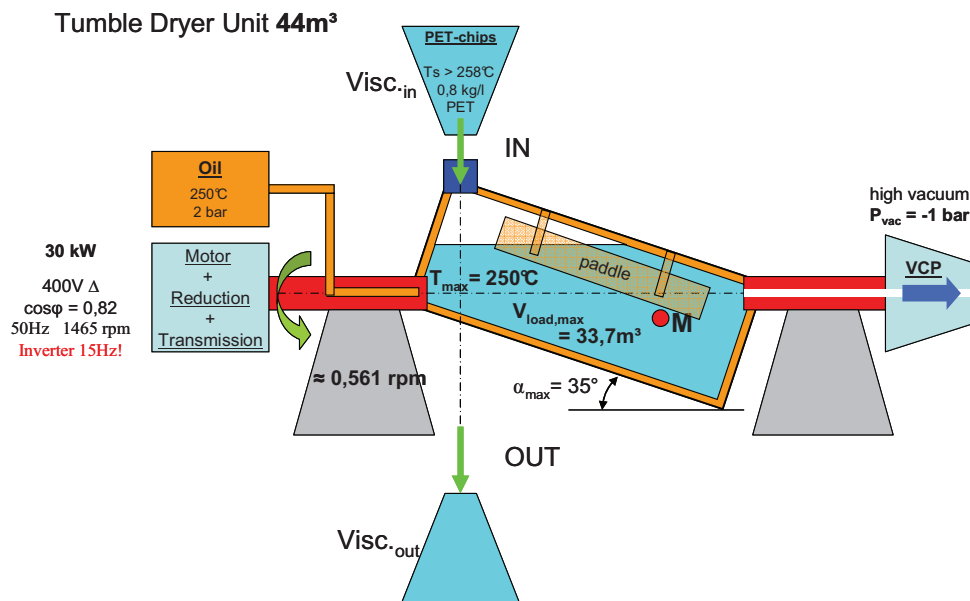
Tumble Dryer Unit **44m³**

Figure 3 : Schematic illustration of the process characteristics

During this stage of the process the vacuum pump is also activated. Thereby the pressure drops to approximately -1 bar. When a homogenous temperature is reached, the reactor is heated up to the final temperature 225℃. Viscosity change starts to take place when a temperature of 185℃ has been reached. The further processing time is a function of the required viscosity. For the treatment of a standard batch a process time of approximately 40 hours has to be taken into account.

3.2   The reactor construction [2][3][6]

Due to the lack of detailed drawings a 3D model was sketched based on an assembly drawing. This model will help to understand the behaviour of the tumble dryer (Figure 4). The working part of the installation is the vessel. This vessel is supported by two axes: one axis driven by a triplex chain and one non-driven axis situated at the vacuum side of the tumble dryer. These axes are carried by two self adjusting cylindrical roller bearings which are installed on the substructure. Six external supporting fins, on both sides of the vessel, are used to connect the vessel with the axes through weld joints. To reduce the thermal losses, the reactor is covered with a layer of isolating material (Figure 1).. Additional supports are present on the inside of the vessel. However, these fixtures are not visible as they are covered with a plate (not shown on the figure). For this reason it is at this moment not certain if these supports are crack free.

Principally the reactor is an assembly of two vessels that have been put together (Figure 5). The inner vessel is completely made of stainless steel. To create a smooth surface on the inside of the inner vessel, a technique with distance tubes has been used to fix both vessels together (Figure 7). Thus all welding operations could be done from the outside of the inner vessel and only a limited amount of welds are visible on the inside. For the outer vessel two different types of steel are used: stainless steel for the cylindrical part and carbon steel for the bottom of the vessel.

The vessels are designed according tot the AD Merkblätter. As is prescribed, the bottom of the vessel is designed according to the German standard DIN 28011 *(AD 2000–Merkblatt, List of all standard, quoted in the AD 2000 body of regulations).* This implies that the vessel consists of a cylindrical part completed by a torispherical head at both sides. The most critical point of such a vessel can be situated at the transition from the cylinder to the end cap. The tension stress in this region increases with a decreasing ratio of the transition radius to the vessel diameter, and with an increasing ratio of the global end bottom radius to the vessel diameter.

The heating system consists of 16 paddles evenly divided along the vessel's circumference. Three hollow tubes connect the heating element to the vessel wall and allow heated oil to flow into the paddles. Each paddle is also connected with every neighbouring element to increase the system's stiffness. The heating element (Figure 8) is an assembly of two plates which are welded together at their sides. To avoid the plates of the heating element to deform due to the internal oil pressure, the plates are connected with small rods, evenly distributed over the heating element.

Throughout the structure, elements made of different materials (carbon steels, stainless steels) have to be welded together. To avoid cracks in such composite welds, a suitable filler material can be selected using for example the Schaeffler diagram, or the WRC–diagram (which is an improved version).
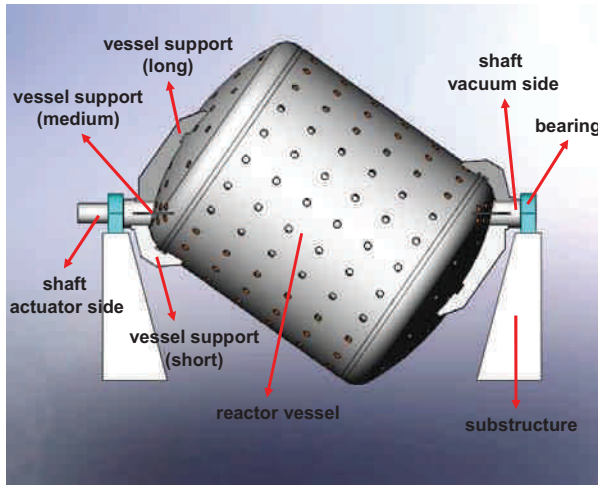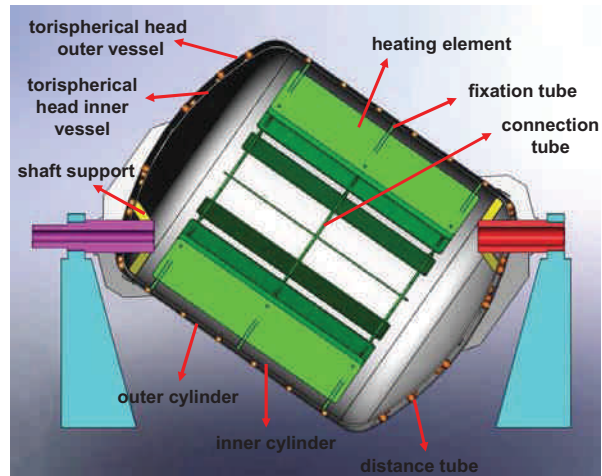

Figure 4: 3D model of the tumble dryer

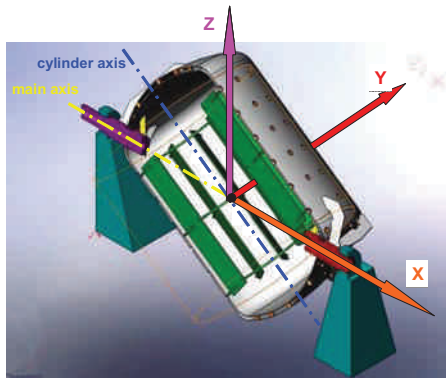Figure 5: Cross section view of the tumble dryer

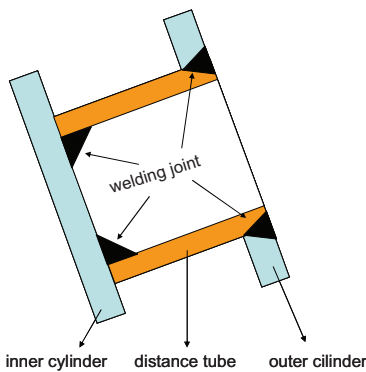Figure 6: Orthogonal trihedron

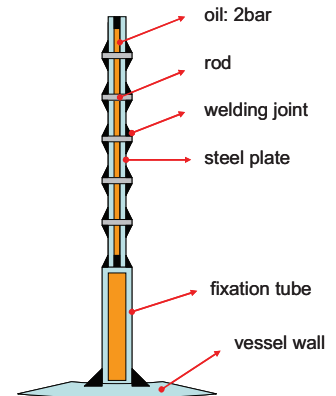Figure 7: Detail of the distance tube connection

Figure 8: Cross section view of a heating element

3.3   Motion study

For describing the reactor's movement, an orthogonal trihedron was introduced as shown in Figure 6. Its origin coincides with the mid-point of the centreline through the shaft of the tumble dryer. Using the XYZ axes, the centreline through the shaft and the vessel's axis of axial symmetry, a simplified representation can be used to render the instantaneous position of the reactor. Projecting the vessel's axis of axial symmetry onto the XY- and XZ-plane, two reference angles can be defined: the tilt angle α and the spiral angle β (Figure 9). The construction of the tumble dryer is choosen in such a way that the centreline through the shaft coincides with a diagonal of the cylinder. The angle between this diagonal and the vessel's axis of axial symmetry is 35°. This implie s that the tilt angle and spiral angle must meet to the following expressions:

$$-35° \leq \alpha, \beta \leq 35° \tag{1}$$

$$| \alpha | + | \beta | = 35° \tag{2}$$

It can be concluded that the introduced system makes it possible to describe unequivocally the vessel's position at any time. Figure 10 shows how the position of the tumble dryer changes during its rotation.
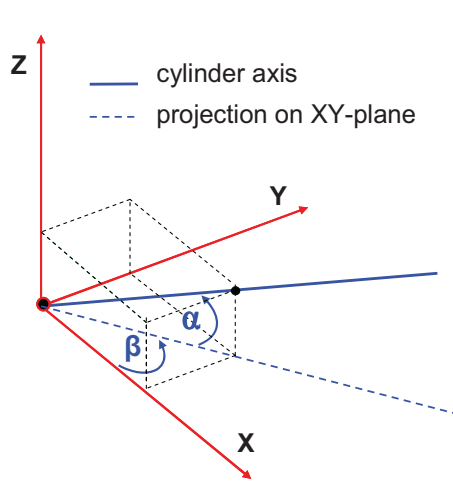
Left turning

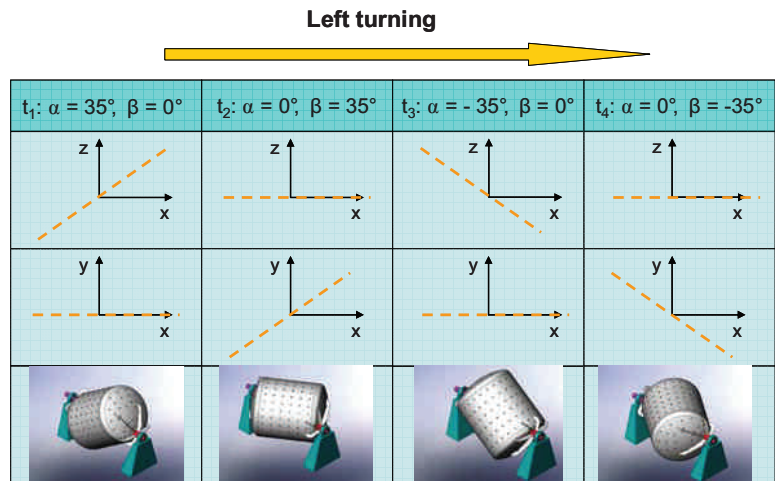Figure 9: Definition of tilt angle (α) and spiral angle (β)

Figure 10: Evolution of the vessel's position

3.4 Analysis of the service loads [4][5][7]

Based on the study of the process shown in Figure 2, five influencing load factors could be distinguished:

a. Net weight of the construction
b. Vacuum pressure inside the reactor
c. Oil pressure between the inner and outer shells
d. Temperature gradients
e. Weight and movement of PET granules

To obtain an improved insight in the mechanical behaviour of the vessel (i.e. its deformations due to the above listed loadings), some simplified preliminary calculations have been made. Therefore the tumble dryer has modelled as a cylindrical tube with a double wall, having the same dimensions as the real vessel.

First the static deflection of the tumble dryer due to the net weight of the construction has been estimated. The net weight can be modelled as an evenly distributed load engaging a beam clamped at both ends beam. Hereby it is assumed that the vessel has a much higher stiffness than the axes. A deflection of 36µm at the connection between the driven axis and the vessel was calculated. Due to the very small relative deflection, the influence of the net weight of the vessel can be neglected.

The study of the effect of the oil pressure and the internal vacuum can be treated together. We first consider the inner cylinder and then the outer one. The influence of the distance tubes has been modelled by replacing them with an uniformly distributed pressure P_R. This pressure was calculated based on the assumption that inner and outer cylinder have the same radial displacement (expression of compatibility). P_R can be found as:

$$P_R = \frac{R_1^2 h_2 \cdot (P+O) + R_2^2 h_1 P}{R_1^2 h_2 + R_2^2 h_1} = 2,514 bar \qquad (3)$$

From this result we can conclude that the inner and outer shells of the vessel clearly interact, an effect that should not be ignored in further calculations. For the radial displacement of the inner shell we find:

$$u_n = \frac{(P_R - P - O) \cdot R_1^2}{2h_1} \cdot \frac{2-v}{E} = -0,0672 mm \qquad (4)$$

Due to the internal vacuum and the oil pressure between the shells, the vessel will shrink with a very small radial displacement of about 67,2 µm.

The temperature of the vessels changes very slowly with a maximum speed of 2K/min. If the reactor is used in a continuous way throughout the year, there are about 219 heating and cooling cycles a year. This means that we can consider the temperature as a static influence. To make a prediction of the expansion of the vessel due to the temperature rise (20℃ => 250 ℃), a linear thermal expansion coefficient α equal to 17.10^{-6}/K has been used. The vessel will increase in length with 150mm while the diameter increases with

about 147mm. At first sight this looks quite large, but it is to be compared with the huge dimensions of the vessel (4,910 m long and 3,800 m in diameter). Though we have to pay attention as the linear expansion coefficients of the inner and outer torispherical head have a different value (respectively 17 and 13,6 10⁻⁶/K). Due to the different thermal expansion coefficients of the two shells, thermally induced stresses can occur. This will be studied in future work.

To determine the influence of the weight and movement of the PET granules, we need another approach. Studying the process on figure 3 reveals that the position of the chips' centre of mass is not displaced symmetrically during the rotational movement. Because the vessel is not filled completely, the centre of mass M will follow a 3 dimensional curve through the vessel. To study this phenomenon we need to know the location of M for every position of the vessel (determined by alpha and beta). The results of these calculations are presented in Figure 11.
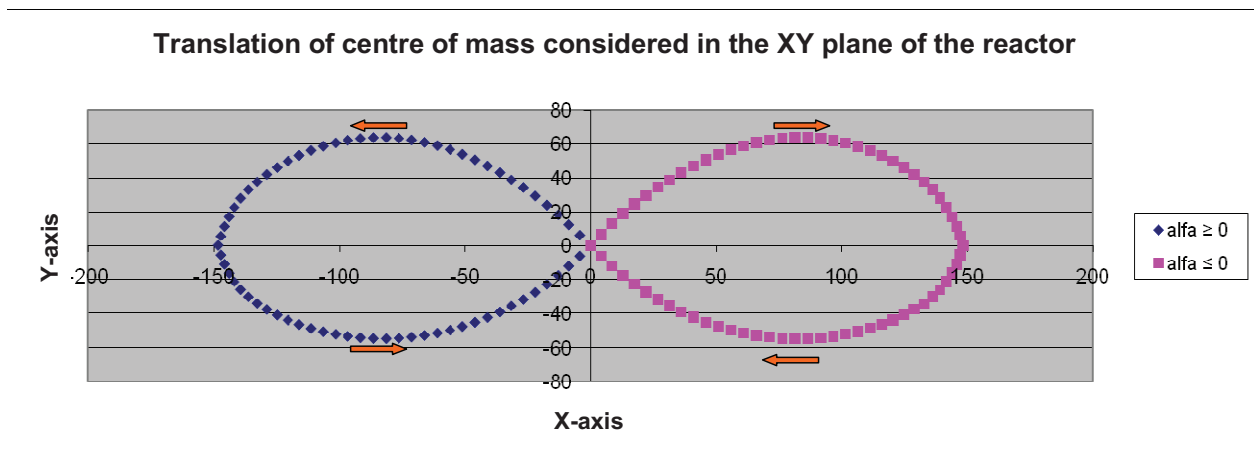

Figure 11: Translation of centre of mass considered in the XY plane of the reactor

It is clear that during one rotational movement the centre of mass describes a "horizontal figure 8" in the XY-plane. This implies that during one rotation the torque-rate changes 4 times. If the Y-coordinate of M has a positive value, the torque is reinforced while a negative value for Y_M results in a drop of the torque. The periodical change of torque in time can be expressed as:

$$T = m_{chips} \cdot 9{,}81 \cdot C \cdot Y_{max} \cdot \sin(\frac{4\pi \cdot 0{,}561}{60}t) = 41{,}655 \cdot \sin(\frac{4\pi \cdot 0{,}561}{60}t) \quad [kNm] \qquad (5)$$

To verify these results, an electrical power measurement of the driving motor has been performed (Figure 12). The calculated profile is adapted with a factor C=0,25 to match with the measurements. This correction was necessary because the flow behaviour of water differs from the behaviour of solid particles due to: friction, bulk density, dilatancy, shape of the particles etc. So we can conclude that the mass displacement of the granules generates a dynamic change of the driving torque. This effect is expected to have a serious impact on the tumble dryers' fatigue endurance live.

The displacement of M in the X-direction will also have a non-negligible and dynamic effect on the amplitude of the tangential force on the axis. This means that the periodical change of amplitude of the tangential power will also affect the system's fatigue endurance live.
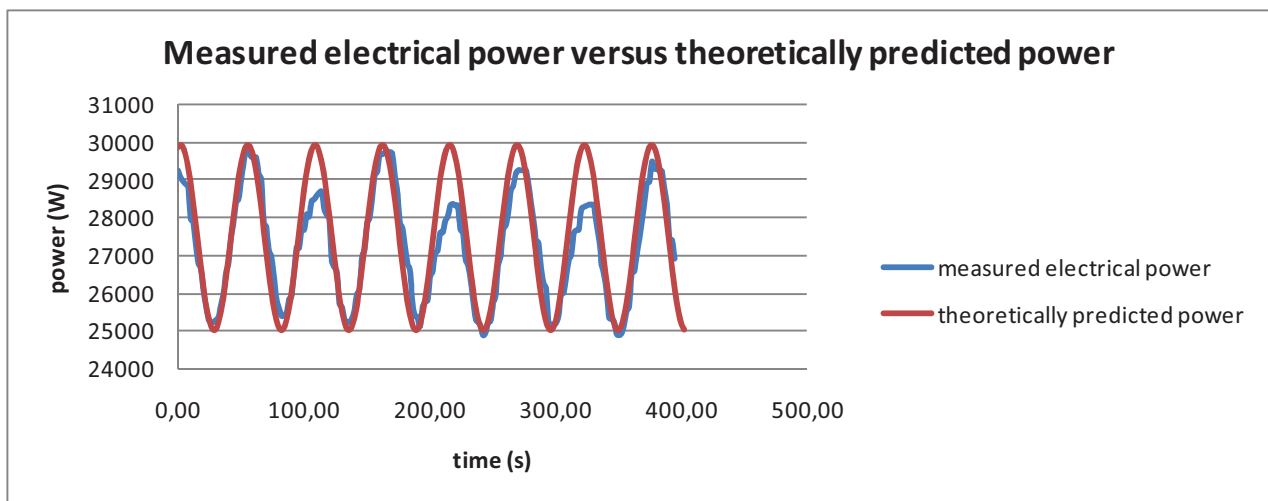
Figure 12: Measured electrical power versus theoretically predicted power

3.5 Further research

To determine the effective torque on the driven axis of the tumble dryer, strain gauge measurements will be performed. This way, one can exclude the influence on torque amplitude allocated to transmission losses. Further, the global stresses and deformations of the vessel and the hotspots of the system (locations with high tensile stresses) will be localized using a FEM–analysis. With these results, fatigue life calculations can be done. Also the dynamic play of the granules around the heating elements will be investigated. The results of this study will be checked to see if they meet the requirements of the applied standards and codes. Further research activities will be performed to find out how the fatigue live of this dynamic system can be improved. Based on these findings technical solutions will be presented.

4 CONCLUSIONS

It can already be established that the dynamic behaviour of the vessel's contents play a decisive role in the (fatigue) cracking of the tumble dryer. Based on the locations and kind of cracks, two critical loading conditions can be determined. The first one is a dynamic torque due to a centre of mass displacement of the granules inside the vessel. This phenomenon mainly causes the cracks observed at the supports on the outside of the vessel. A second critical loading mode can be assigned to the dynamic play of the granules around the heating elements of the vessel and is thereby responsible for the cracks in the welds of the paddles. Summarizing, the weight and movement of the granules can be considered as the main reasons for the vessel failures while all other influencing parameters have a minor or negligible effect.

5 NOMENCLATURE

T	torque	Nm
P	(oil-) pressure	Pa
h	wall thickness	m
E	Young's modulus	N/m²
R	radius cylindrical vessel	m
v	Poisson-ratio	-
t	time	sec.
O	vacuum pressure	Pa
P_R	Reaction Pressure	Pa
u_n	Normal Displacement	m

6 REFERENCES

[1] http://www.ohl-eng.com/en/process/ssp.html 18/09/2010
[2] G. den Ouden, M. Hermans, Welding Technology, VSSD Delft, p152, 2009
[3] D. MUHS, H. WITTEL, M. BECKER, D. JANNASCH, J. VOSSIEK, Roloff/Matek, 4de druk 2007, p581
[4] P. Verleysen, Mechanica van werktuigkundige constructies, Ugent, Toegepaste materiaalwetenschappen, p6.18, 2008-2009.
[5] J.Pollefliet, Elektrische Vermogenscontrole, Vol.2 Elektronische motorcontrole, 6de druk 2de oplage, Academia Press, Gent, 2007
[6] AD 2000 code, technical rules for pressure vessels, July 2003
[7] Richard. G. Holdich, Fundamentals of particle technology, Department of chemical engineering, Loughborough university, U.K., 2002, p363